Frazil Ice Crystal Collisions

Deborah Rhee

St Anne's College

University of Oxford

A thesis submitted for the degree of

Doctor of Philosophy

Michaelmas 2025

Acknowledgements

The first thanks goes to my supervisors Andrew and Ian. Thank you for all of your ideas, advice and the time that you have invested not only into thinking about how to solve the many problems encountered during this PhD but also in developing me as a researcher. Thank you also to Tom Mitchell and Rosie Willatt at UCL for helping me with all the laboratory work and for enabling me to be one of the few people in the 'Icy Maths' group who has actually seen the ice that they research. An additional thank you goes to Andre Souza and Glenn Flierl at MIT for convincing me to give Julia a go and teaching me so much more along the way.

The second thanks goes to all of my colleagues that I have had the pleasure to work alongside over these past four years. Thank you for all the advice at group meetings, and for random conversations down the corridor. A particular thanks goes to my office/corridor mates who have helped solve so many problems, provided excellent study breaks and made AOPP a more joyful environment to be in. A special shout out goes to Charlotte, Bethan, Rosie, Oscar and Jasmeen whose daily company I greatly miss. During my PhD I had the pleasure of spending a few months in America on the WHOI GFD programme and I'm so grateful for all the inspiring people I met there and I'm glad to have seen some of you again at conferences. Particularly, Ellie, thanks for being a wonderful roommate and for all of our not so late night chats.

A third thanks goes to my family. Mum and Dad I'm grateful for your encouragement from a young age for me to keep exploring, trying new things and to keep asking questions. I don't think you expected that would lead me to deciding to spend four years answering one very specific question! I'm grateful for how you've constantly supported through the highs and lows of the last four years, particularly thank you Dad for reading through the thesis to try and spot any typos and Mum for always asking the right questions. Thomas and Ian, among all of the banter I'm thankful to have brothers that I know always have my back. Thank you also to my extended family and to my new family (!). Spending time with you has always been a very welcome change from the pace of Oxford life and your support has been very precious.

During my PhD I have had the pleasure of getting married and it was such a privilege to have so many people that I love from so many different parts and stages of my life in one room. So a big thank you goes to all of you. To my OUTriC friends I'm going to miss training with all of you. To my bridesmaids thank you for being with me through so many highs and lows. To my Pembroke friends thank you for making undergrad such a joy and to Joe P thanks for sticking around to do a PhD (and sorry that you've been demoted from Joe to Joe P). To my physics friends, thanks for all the chats and laughs along the way and in particular Esthy and Georgia thank you for being inspiring women in physics. To my St Cross housemates (Sergio included) thanks for all the food, corridor chats and memorable quotes. To my DTP friends, particularly Hannah, Lewis and Harri. Hannah thank you for all the walks, ice cream and convincing me to try wheelchair basketball when I was injured. Harri and Lewis thanks for being wonderful housemates and my personal bike mechanics. Zelie thank you also for all the early morning cycles, every day that started with a Zelie cycle was a good day. Thank you also to my church family for praying for me, walking alongside me, for so many joyous times studying the Bible and for always pointing me to Jesus. There are too many of you to name but a particular thanks goes to all the people I've shared a Bible study table with over the last four years, to Josh and Fern for the marriage advice, and to Beth, Joseph and Rich for our fortnightly 'life together' evenings and Marisa, Elizabeth, Kelly, Kay and Christy for so many helpful conversations.

Finally, thank you to my husband Joe. I am so incredibly grateful and honoured that you promised me to love me for better for worse, for richer for poorer, in sickness and in health, till death do us part. You have already modelled that in so many ways during my PhD. Thank you for sacrificially loving me in so many ways, particularly in these last few months. Thank you for giving me a much needed sense of perspective, for pointing me to Jesus and for making me laugh so many times. Thank you for being willing to move to the North with me for my post-doc. I'm really excited to see what the next few years hold and I'm so grateful to have you by my side.

I thought at the start of the PhD I would be able to say much more about frazil ice than I can now. Instead, I've discovered that these small crystals are more complex and intriguing then I could have ever have first thought and you can spend over 200 pages writing just about how they collide with each other. This verse from the Bible had been a great encouragement to me "Who can understand how He spreads out the clouds, how He thunders from His pavilion?" (Job 36:29). Spending four years researching frazil ice has demonstrated to me the amazing

creation that I live in, that I will never fully understand and yet I personally know the Creator. I know that He loves me, He sent His Son to die for me and I know that one day I will see Him face to face and I will be able to ask Him all my questions about frazil ice and more.

Abstract

Frazil ice crystals are small, often disk-shaped, millimetre sized crystals that form in supercooled turbulent water. Frazil ice crystals are found in rivers, lakes and the sea. Despite their small size, frazil ice crystals have significant impacts on infrastructure and the climate, in particular through the role frazil ice formation plays in the water transformation processes in coastal polynyas. The processes governing the evolution of a frazil ice crystal population are complex. One of these processes is collisions between frazil ice crystals. It is hypothesised that this process can result in crystal fracture, and is responsible for the rapid increase in the number of frazil ice crystals that has been observed in experiments. Despite its significance, many uncertainties remain about how to parametrise crystal collisions and many key physical processes are unaccounted for. In this thesis we include some of these processes into a model for frazil ice crystal collisions.

Typical models assume that the crystal collision rate can be determined by calculating the number of crystals each frazil ice crystal meets per second as it moves through a fluid. The other crystals are assumed to be stationary and point-like. We develop a model for crystal collisions that accounts for the velocity and finite size of both crystals and better accounts for the cylindrical shape of the crystals. We derive a new method to distribute fractured particles into the crystal population which better accounts for the size difference between the fractured crystal and the original crystal. We also use the lubrication approximation to calculate the hydrodynamic forces on 2D plates and 3D crystals as they approach and find a critical velocity for collision when the crystals approach close to parallel. We also obtain the conditions for fracture of 2D plates by elastic bending.

Including these non-hydrodynamic processes leads to a large increase in the collision rate and a decrease in the mean radius of the crystal population when compared to a typical frazil ice model. Hydrodynamic effects act to reduce the number of collisions. However, there are still discrepancies between our model and experimental results. We hypothesise a main cause of these differences is from neglecting flocculation and assuming that collisions always introduce crystals of the smallest size class. This suggests that future models could be improved by focussing on understanding these processes.

Contents

"Open my eyes that I may see wonderful things in your law."

— Psalm 119:18 NIV

1 Introduction

Contents

1.1 Overview

The cryosphere is one of the five major spheres of the climate system. It plays an important role in the earth system with its huge fresh water reserves, latent heat of phase transitions, greenhouse gases, and unique species (Qin et al., 2020). Numerical models of the cryosphere vary in resolution but all processes on scales smaller than a kilometre are not directly resolved even in fine scale models of the Earth's climate system (Hewitt et al., 2022). However, these processes occurring on much smaller-scales often have climactic significance and may affect model predictions (Hewitt et al., 2022). One of these processes is frazil ice formation

in rivers, lakes and the ocean. Frazil ice has been shown (Nakata et al., 2021; Ohshima et al., 2022; Portela et al., 2022) to impact the global ocean circulation via the role it plays in the water transformation processes occurring off the coast of Antarctica. However, there is still large uncertainty in the approach used to model frazil ice (Souillé et al., 2023). This thesis addresses one aspect of modelling frazil ice: collisions of frazil ice crystals and provides a more physically informed parametrisation for the collision rate.

In this chapter we provide a broad introduction to frazil ice before providing a more detailed background on how crystal collisions are modelled in §2. In the subsequent chapters we discuss the effect of incremental improvements to how crystal collisions are parametrised. In this chapter we begin in §1.2 with a discussion of the physical characteristics of frazil ice crystals and where frazil ice is found, before discussing how it forms in §1.3 and why it is important in §1.4. We then give a broad overview of the existing observations of frazil ice in §1.5 and discuss how it is currently numerically modelled in §1.6 . In §1.7 we then justify why further work needs to be done on crystal collisions and give an overview of the rest of the thesis in §1.8.

1.2 What is frazil ice and where is it found?

Frazil ice typically consists of a suspension of individual sub-millimetre to millimetre-sized crystals in water (Barrette, 2021; Daly, 1984). The crystals may, under certain conditions, coalesce into flocs, slush, and 'pancake ice', and eventually form a floating ice cover (see Figure 1.1). Frazil ice crystals can have dendritic, hexagonal, needle-shaped, and irregular shapes (see Figure 1.2) (Pei et al., 2024; Schneck et al., 2019), but are predominately disc-shaped (Barrette, 2021; Daly, 1984; Martin, 1981).

Frazil ice can be found in rivers, lakes and the ocean (Frazer et al., 2020). In the ocean, frazil is particularly found in leads (long narrow openings in pack ice that form as a result of deformation of the pack ice) and polynyas (large openings in pack ice) (Smith et al., 1990).

Figure 1.1: Frazil ice crystals accumulate as a 'slush' on the surface of the water. Image taken during some laboratory experiments in collaboration with Rosie Willatt and Tom Mitchell at University College London.

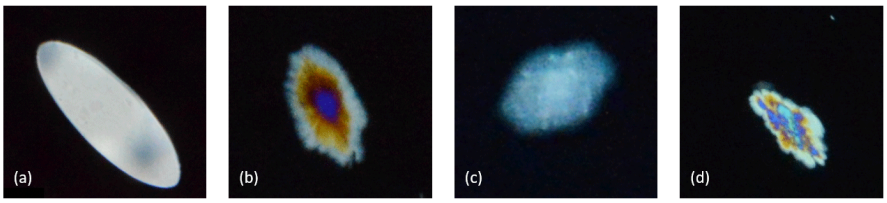

Figure 1.2: © Schneck et al. (2019). Frazil ice crystals can have a) disk, b) dendritic, c) hexagonal or d) irregular shapes.

1.3 How does frazil ice form?

Frazil ice tends to form in a water column that is both supercooled and turbulent (Frazer et al., 2020) as sufficient turbulence is needed to prevent a surface skim of ice from forming (Barrette, 2021).

The mechanism behind the initial seeding process to form frazil ice (known as primary nucleation) is unknown. Homogeneous nucleation (freezing of ice in pure water) only occurs at temperatures of about -40^oC and heterogenous nucleation (where impurities are used as a catalyst) typically requires a supercooling of at least 1^oC, far lower than that observed when frazil ice formation occurs (Daly, 1994). Therefore, it is suggested that frazil ice forms as a result of initial seed crystals, which then multiply by secondary nucleation.

There are a range of possible sources for these seed crystals. Vapour evaporating from the water surface and depositing into ice crystals in the atmosphere which fall back into the water has been observed by Osterkamp (1975). Gosink and Osterkamp (1983) and Martin, 1981 suggested that seeding could also result from bubbles caused by wave breaking: the bubbles burst at the surface where the droplets are ejected into the cold air, freeze and fall back into the water to act as seed crystals. Further, Martin (1981) suggested that crystals could also be introduced into rivers as snow or frost crystals. Evidence for natural seeding comes from finding numerous ice crystals in air samples taken at night above Arctic streams (Martin, 1981). Finally, it has been discovered that water-soluble gas micro-bubbles and cavitation bubbles created by turbulence can also start the processes of frazil ice nucleation (Chen et al., 2023; Zhang et al., 2015).

1.4 Why is frazil ice important?

Frazil ice is important for its effects on infrastructure, the ecosystem and its climactic significance.

Frazil ice that forms in rivers, lakes and canals has been observed to block water intakes (e.g. Daly and Barrette (2023), Daly and Ettema (2006), Ettema et al. (2009), and Gebre et al. (2013)), posing substantial difficulties for hydropower and water-supply facilities. Furthermore, frazil ice may promote ice jamming of a water channel, and consequent flooding if it develops into hanging dams below a stable ice cover (Barrette, 2021). In extreme cases this can halt shipping (Chen et al., 2023).

As well as impacting infrastructure, frazil ice has been observed to affect ecosystems. Frazil ice has been observed to change winter biogeochemical processes in rivers, affecting microbial activity and thus the nitrogen cycle (Opfergelt et al., 2024). Frazil ice also impacts fish habitats and causes them to migrate or redistribute daily (Brown et al., 2011). Finally, frazil ice has been shown to enhance the

entrainment of microplastics into ice (Chen et al., 2023; Kelly et al., 2024) impacting the transport of microplastics and the subsequent effect they have on an ecosystem.

Frazil ice also plays a role in processes impacting the global climate system. When frazil ice forms it releases latent heat into the water column and subsequently when it melts it cools down the water column. In cases where frazil ice forms in saline water, brine rejection during frazil ice formation increases the salinity of the water column (Thompson et al., 2020). Frazil ice is often the dominant type of ice produced in coastal polynyas off the coast of Antarctica (Nakata et al., 2021). Polynyas are focal locations for biological activity and gas and nutrient exchange, allowing enhanced carbon sequestration into the deep ocean by buoyancy driven mixing (Golledge et al., 2025). Further, the production of dense shelf water within polynyas plays a key role in the global thermohaline circulation (Jeong et al., 2023). All of these processes are highly sensitive to the amount of frazil ice produced and how it interacts with the water column (Bradtke and Herman, 2023; Ito et al., 2020).

Frazil ice also forms under ice-shelves in ice-shelf water plumes (Galton-Fenzi et al., 2012). Understanding the melt rate of ice shelves is vital for predicting the future of the Antarctic Ice Sheet (Rosevear et al., 2025), as when ice shelves lose mass they can destabilise the ice sheet (Smith et al., 2020). Therefore, frazil ice is important for understanding the mass balance of ice shelves as freezing is dominated by frazil ice formation, so-called marine ice accretion (Rosevear et al., 2025).

In order to understand how frazil ice impacts all of these processes, a fundamental understanding of the behaviour of frazil ice is required. In particular, how frazil ice crystals nucleate, grow and melt, interact with each other, move through the water column and alter the properties of the water. In order to understand the behaviour of frazil ice, various studies of frazil ice in both the laboratory and in the field have been conducted. Numerical models for frazil ice have been developed informed by these

studies and the physics governing the behaviour of small particles in turbulent water.

In the following sections we shall give a brief overview of the existing observations of frazil ice and the numerical models that have been developed.

1.5 Observations of frazil ice

Frazil ice has been observed both on a large scale with measurements looking at frazil ice distribution and occurrence (e.g. Bradtke and Herman (2023) and Ito et al. (2015, 2020, 2021)) and at a smaller scale looking at individual crystals. A full review of laboratory experiments conducted on frazil ice was done by Barrette (2021). Chen et al. (2023) gives an overview of field observations of frazil ice in freshwater. Fewer field observations have been conducted in saline water (Frazer et al., 2020). Observations have been taken of the air temperature, salinity, flow speed, turbulence intensity and the degree of supercooling alongside the concentration, rise velocity and size distribution of frazil ice crystals. Not all observations have all of this data. Key results are that the number of frazil ice crystals rapidly increases after the initial seeding processes (McFarlane et al., 2015; Schneck et al., 2019) in what is known as a frazil ice explosion (Jones and Wells, 2018). At the same time the temperature of the water increases (McFarlane et al., 2015; Schneck et al., 2019) due to latent heat release from crystal growth. The location of the frazil ice crystals changes with the turbulence. In more quiescent conditions the frazil ice crystals rise to the surface, whilst in more turbulent conditions the crystals are distributed throughout the water column (Ito et al., 2021; Ohshima et al., 2022; Wang and Doering, 2005). A more complete overview of the existing observations of frazil ice crystals that can be used to test numerical frazil ice models is given in §2.2.

1.6 Numerical models of frazil ice

In numerical models, frazil ice crystals are often modelled as disks moving around the water column (Daly, 1984). The volume V_r of a frazil ice crystal with radius r

and thickness w is given by $V_r = \pi r^2 w$. This can also be expressed as $V_r = 2\pi r^3/d$, in terms of the aspect ratio $d = 2r/w$ of the crystal.

As frazil ice crystals move throughout the water column, they grow or melt depending on the water temperature, and in doing so introduce a local heat and salt flux (Heorton et al., 2017). Crystal collisions may result in frazil ice crystals flocculating (joining together) or secondary nucleation, where sections of the crystal fracture and create an additional source of nuclei (Svensson and Omstedt, 1994). A complete model of frazil ice would calculate the motion and growth of each individual crystal as it moves throughout the water column as well as interactions with other crystals. However, due to the high computational cost of doing so and the need to develop a frazil ice parametrisation to inform larger scale models, most frazil ice models evolve a crystal size distribution rather than individual crystals (Souillé et al., 2023).

Many frazil ice models build on the suggestion of Daly (1984), that the change in crystal size distribution can be modelled using a continuity equation (Souillé et al., 2020)),

$$\frac{\partial n_r}{\partial t} + \underbrace{\mathbf{u}\cdot\nabla n_r}_{(1)} - \underbrace{\nabla\cdot(\nu_c \nabla n_r)}_{(2)} = \underbrace{-\frac{\partial}{\partial r}(G n_r)}_{(3)} + \underbrace{(\dot{N}_I + \dot{N}_T)\delta(r - r_c)}_{(4)} - \underbrace{\frac{1}{V_r}\frac{\partial}{\partial r}(F V_r n_r)}_{(5)} - \underbrace{v_g \frac{\partial n_r}{\partial z}}_{(6)}. \quad (1.1)$$

The continuity equation captures (1) advection, (2) diffusion, (3) growth/melt, (4) nucleation, (5) flocculation and (6) gravitational rise of crystals. Here, n_r is the number of crystals per unit length in radius space per unit volume, $\mathbf{u} = \mathbf{u}(\mathbf{r}, t)$ is the fluid velocity at position $\mathbf{r} = (x, y, z)$ and time t, ν_c is the frazil particle diffusivity, G is the growth rate, $\dot{N}_I$ and $\dot{N}_T$ are the respective primary and secondary nucleation rates, F is the flocculation rate, V_r is the volume of a crystal with radius r and v_g is the buoyant rise velocity. It is assumed all crystals nucleate at a radius r_c.

To solve the continuity equation, two different approaches are used. Either the crystals are binned into groups of crystals of a certain size range or a mean crystal size is assumed. Choosing a mean crystal size has the advantage of being a simpler approach, allowing easier understanding of how each of the processes in (1.1) influence the frazil ice population. However, choosing an evolving size distribution allows processes such as crystal rise and nucleation to be more accurately modelled. These approaches are discussed in §2.3 along with the different choices for the parametrisation of growth/melt, nucleation, flocculation and gravitational rise.

1.6.1 Interaction with the water column

Local changes to the water properties due to frazil ice formation have important consequences. They alter the process of buoyancy driven mixing as well as the habitability of the water. In numerical models of frazil ice, the presence of frazil ice is parametrised to alter the water column in several ways. Growing and melting ice crystals alter the density of the water column column, by changing the temperature and salinity of the water and also changing the fraction of the water column that is ice. In fresh water the crystals provide a heat flux (e.g. Wang and Ayala, and and Scott, and Wojciech (2005)) and in saline water a heat flux and a salt flux (e.g. Heorton et al. (2017)). Sufficiently high concentrations of frazil ice increase the effective viscosity of the water (e.g. Ito et al. (2015)). In some numerical models frazil ice crystals exert a drag force on the water as they rise to the surface (e.g. Herman et al., 2020). Finally, in some models frazil ice leads to a decrease in the heat and momentum exchange between the atmosphere and ocean/river (e.g. Herman et al. (2020)).

1.7 Strengths and weaknesses of numerical frazil ice models

Numerical frazil ice models often produce results consistent with those measured in the lab. However, this does not necessarily mean that frazil ice models are predictive (Jones and Wells, 2018). This is particularly true when different processes compete

and have similar impact on the crystal size distribution, meaning that parameters can be tuned so that the model matches the experiment. Therefore, we shall discuss the uncertainties in each of the four terms on the right hand side of the frazil ice continuity equation (1.1).

Much work has been done to parametrise crystal growth (see §2.3.1 and Rees Jones and Wells (2015) for a detailed review). Crystal growth is thought to occur dominantly in the radial direction and increases with the supercooling and size of the crystal. Therefore, there is less uncertainty surrounding the parametrisation of crystal growth (Souillé et al., 2023).

Secondary nucleation and flocculation remain poorly understood (Souillé et al., 2023) and the mechanism of these processes has not been fully understood or replicated (Chen et al., 2023). Many of the important physical processes such as the fracture mechanism and hydrodynamic interactions have been neglected or simplified resulting in the need for fitting parameters to be introduced to match experimental results. This was emphasised by Souillé et al. (2023) who performed an uncertainty analysis of single and multiple-size-class frazil ice models and found that the choice of parametrisation for secondary nucleation and flocculation strongly influenced the evolution of the frazil ice once the supercooling was small.

There are also multiple methods to calculate the rise velocity of the crystals (see §2.3.3 for a detailed review). Some approaches (e.g. Chen et al. (2024)) rely on experimental data from ice-like crystals. Other approaches (e.g. Holland and Feltham (2005), Souillé et al. (2020), and Yang et al. (2023)) rely on a combined experimental and theoretical approach. This means that models use a wide range of expressions for the rise velocity, such that the choice of parametrisation for gravitational removal (Souillé et al., 2023) provides a significant source of uncertainty in frazil ice models.

Given that much uncertainty in frazil ice models comes from the parametrisation for secondary nucleation and flocculation of frazil ice crystals, the focus of this thesis will be on improving parametrisations of these processes which rely on a parametrisation for the frequency of crystal collisions.

1.8 Outline of the thesis

We shall begin in §2 by giving further background on frazil ice, focussing on how frazil ice crystal collisions are parametrised. We shall also discuss how crystal collisions in other settings are parametrised. By comparing the two approaches we will find weaknesses in the current method to parametrise frazil ice crystal collisions which will be addressed in §4 - §8. To test the impact of our changes to the parametrisation of crystal collisions, we shall implement them into a very basic frazil ice model which only includes crystal collisions. This model is introduced in §3 alongside a frazil ice model for a well mixed-layer that will be used in §9 to test the final parametrisation for collisions against experimental data. The improvements to the parametrisation of frazil ice crystal collisions are broadly divided into two halves: in §4 - §6 the improvements focus on the ballistic aspect of the collisions, such as the parametrisation of the relative velocity and the effect of crystal shape. These changes impact how often crystals encounter each other. The improvements in §7-§8 focus on calculating how many of these encounters result in a collision when accounting for hydrodynamic effects.

"In the beginning God created the heavens and the earth."

— Genesis 1:1 NIV

2 Background

Contents

2.1 Overview

The purpose of the thesis is to improve numerical models for frazil ice, with a particular focus on crystal collisions resulting in secondary nucleation and flocculation. We therefore in §2.2 begin by discussing the observations of frazil ice that can be used to test an improved model. We then discuss the different numerical parametrisations of frazil ice processes in §2.3. As the focus of this thesis is on modelling collisions of frazil ice crystals, we also outline the methods currently used to model crystal collisions in other settings in §2.4. In §2.5 we then compare these models to the models typically used for frazil crystal collisions. This enables us to identify weaknesses in the current approach used in frazil ice models, which will be addressed in subsequent chapters.

2.2 Observations of frazil ice

We begin by outlining some of the existing observations of frazil ice. As the focus of this work shall be on improving our fundamental understanding of how frazil ice behaves, we shall here focus on reviewing the measurements that provide data to test simple numerical frazil ice models.

2.2.1 Crystal sizes and size distribution

Sizes of frazil ice crystals measured by photographing the crystals in the laboratory (e.g. Clark and Doering, 2008; McFarlane et al., 2015; Ye et al., 2004) and the field (McFarlane et al., 2017, 2019), at different salinities (Schneck et al., 2019) and levels of turbulence (Clark and Doering, 2008) have all been reported to fit a log-normal distribution (Souillé et al., 2023). A wide range of crystal sizes are reported, with summaries given in McFarlane et al. (2017) and Souillé et al. (2023). The measured diameters of frazil ice crystals ranges from 22 μm to 5.5 mm (McFarlane et al., 2017).

Most frazil ice crystals formed in freshwater are observed to be disk shaped (Barrette, 2021; McFarlane et al., 2015), with aspect ratios ranging from 5 to

100 (Souillé et al., 2023). In saline water disk-shaped crystals still form but qualitative observations show that the individual crystals tend to be more irregularly shaped (Schneck et al., 2019).

2.2.2 Effect of turbulence

The maximum crystal size has been shown to increase with increasing turbulence (Clark and Doering, 2008; McFarlane et al., 2015; Ye et al., 2004) and then decrease again (Clark and Doering, 2008; Ettema et al., 1984; McFarlane et al., 2015)) with the intensity still increasing. It is hypothesized by Clark and Doering (2008) that increasing turbulence intensity allows larger crystals to form due to a higher turbulent energy dissipation rate allowing faster ice growth, until a point when the turbulent eddies physically limit the average size of the crystals because of their relatively weak mechanical strength. Increasing turbulence intensity may also increase the frequency and intensity of crystal collisions, which could also begin to limit the average size of the crystals. Further, the production rate of frazil ice has been measured to increase with wind speed (Naumann et al., 2012; Ushio and Wakatsuchi, 1993) and turbulence (Ettema et al., 1984).

The distribution of frazil ice crystals throughout the water column has been observed to be more uniform at higher turbulence levels (Clark and Doering, 2009). This is potentially due to the velocity of each crystal being dominated by turbulence and not buoyant rise. Increasing the turbulence also prevented the formation of large flocs (Clark and Doering, 2009).

2.2.3 Supercooling history

Figure 2.1 shows measurements of the water temperature (blue line) as a function of time in an experiment with a frazil ice suspension. Initially the water temperature decreases as the water is cooled by the cold air. As the number of frazil ice crystals increases (panel a) and the crystals grow (panel b), the water temperature increases due to latent heat release. Some experiments (see Barrette (2021) for a full list)

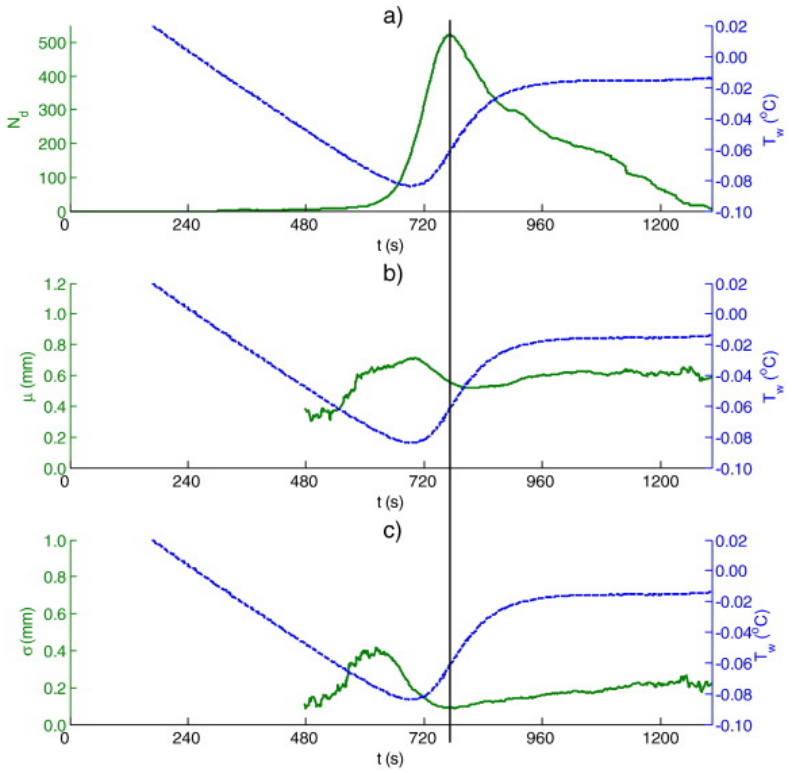

Figure 2.1: From McFarlane et al. (2015). Time series of the water temperature (blue line and right hand scales), along with green curves showing the a) average number of crystals observed in a 35 second window, b) mean crystal diameter μ and c) standard deviation of the crystal diameter.

report a residual supercooling (e.g. Ye et al. (2004)) whilst in other experiments the temperature levelled off at the freezing point (e.g. McFarlane et al. (2015) and Schneck et al. (2019)).

Various measurements have been taken of the concentration of frazil ice as a function of supercooling both in the field (Frazer et al., 2020) and in the laboratory (Clark and Doering, 2008; McFarlane et al., 2015; Schneck et al., 2019). The most useful for validating numerical models are the measurements of the number of crystals, mean and standard deviation of the crystal diameter, and the supercooling over time (McFarlane et al., 2015; Schneck et al., 2019).

In both of the experiments by McFarlane et al. (2015) and Schneck et al. (2019) the mean crystal size is seen to increase and then subsequently decrease until a near-

equilibrium crystal diameter is reached. This is supported by the field observations reported in McFarlane et al. (2017) where it was observed that the mean crystal diameter was larger during the principal supercooling stage, and reached a smaller mean diameter during the residual supercooling phase. Using this data, McFarlane et al. (2015) suggest that larger crystals may be more prone to form frazil flocs or fracture into smaller crystals.

Measurements of the volume concentration of frazil ice have been made in rivers, the sea and the laboratory, with a summary of the results given in McFarlane et al. (2019). Typically volume concentrations of frazil ice range from 10^{-6}-10^{-3} in rivers, 10^{-8}-10^{-4} in the sea (from Frazer et al. (2020)) and 10^{-5}-10^{-2} in the laboratory.

2.2.4 Rise velocity

The rise velocity of different sized frazil ice crystals has also been measured (see McFarlane et al. (2014) for a review). Larger crystals are observed to rise faster.

2.3 Numerical parametrisations of frazil ice processes

We shall now discuss how frazil ice crystals are modelled numerically. As was briefly discussed in §1.6, numerical models for frazil ice solve the continuity equation (1.1) instead of modelling individual frazil ice crystals. Two different approaches are used. Either the crystals are binned into groups of crystals of a certain size range, or a mean crystal size is assumed.

In most models (termed multiple-size-class frazil ice models) (e.g. Heorton et al., 2017; Holland and Feltham, 2005; Souillé et al., 2020; Svensson and Omstedt, 1994), the crystals are binned into groups of crystals of a certain size range, with transfer between bins as a result of growth, secondary nucleation and flocculation/break up. In some models (termed single-size-class frazil ice models) (e.g. Souillé et al., 2023; Yang et al., 2023), a single mean crystal size is assumed. Figure 2.2 illustrates

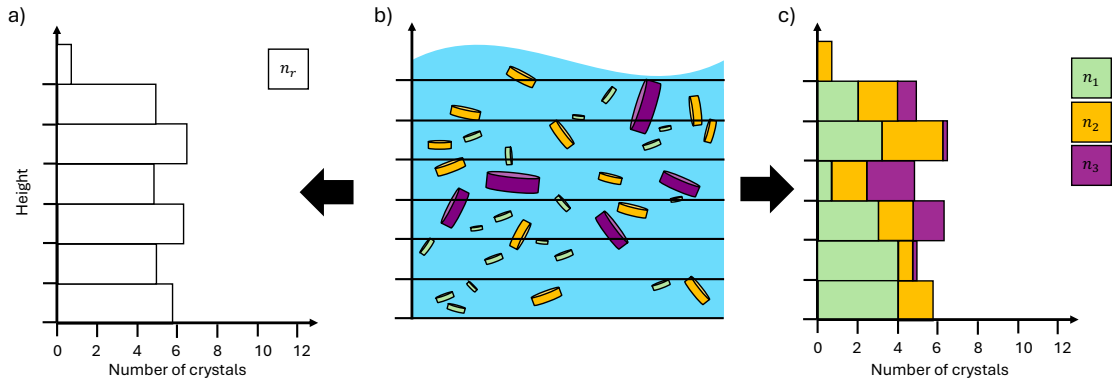

Figure 2.2: To demonstrate the difference between single-size-class and multiple-size-class frazil models we split a frazil ice population (panel b) into crystals at different height levels within a water column. a) Representation in a single-size-class frazil model, where a single mean crystal size is assumed and the number of crystals at each height level is calculated. c) Representation in a multiple-size-class frazil model, where the crystals are binned into N different size classes and the number of crystals of each size class at each height level is calculated. Here $N = 3$. A more complex single or multiple-size-class crystal model would discretise the grid in each spatial direction and calculate the number of crystals in each grid cell.

the difference between single and multiple-size-class frazil ice models versus an illustration of the true crystal population in a case when the crystal population density is calculated at certain heights. In the single-size-class model (panel a), the number of crystals at each height is calculated. In the multiple-size-class model (panel c) the crystals are binned into three separate size classes and the number of crystals is calculated in each size class at each height.

The spatial distribution of crystals changes due to advection, diffusion, nucleation, flocculation and gravitational rise. The mean size of crystals changes due to growth/melt, nucleation and flocculation. Single-size-class models should capture all of these processes. However, almost all single-size-class models ignore secondary nucleation and flocculation (Souillé et al., 2023). The exception is the model of Yang et al. (2023), where the number of crystals can change by secondary nucleation and flocculation, but these processes do not affect the mean crystal size.

The single-size-class models of Souillé et al. (2023) and Yang et al. (2023) can

be adapted to calculate the spatial distribution of frazil ice throughout the water column,

$$\frac{\partial n}{\partial t} + \mathbf{u} \cdot \nabla n - \nabla \cdot (\nu_c \nabla n) = \dot{N}_I + \dot{N}_T - \dot{N}_F - v_g \frac{\partial n}{\partial z}, \tag{2.1}$$

$$\frac{\mathrm{d}\overline{V}}{\mathrm{d}t} = \frac{Nu\, k_l (T_f - T) A_F}{\mathcal{L} \rho_I l}, \tag{2.2}$$

where n is the number of crystals per unit volume, $\dot{N}_F$ is the rate of flocculation, $\overline{V}$ is the mean crystal volume, $\mathcal{L}$ is the latent heat of solidification, ρ_I is density of ice, Nu is the crystal Nusselt number, k_l is the liquid thermal conductivity, T_f is the freezing temperature of ice, T is the fluid temperature, A_F is the area of the crystal that freezes, and l is a characteristic length scale for thermal diffusion. Choices for A_F and l are discussed in §2.3.1, $\dot{N}_I$ are discussed in §2.3.2, and $\dot{N}_T$ is discussed in §2.3.4.1, and $\dot{N}_F$ in §2.3.4.2. In this model, the spatial distribution of crystals changes due to advection, diffusion, nucleation, flocculation and gravitational rise. The mean size of crystals changes due to growth/melt.

All multiple-size-class frazil ice models are very similar in their basic form. We shall use the mixed layer model of Svensson and Omstedt (1994) as an example, but modify some of the coefficients to account for modifications from later publications and keep advection and diffusion for ease of later comparison. Crystals are divided into N size classes, with $i = 1$ being the smallest size class and $i = N$ being the largest. The size class $i = 1$ is chosen to have a radius corresponding to the survival radius (the radius below which the crystals melt (Lal et al., 1969)). The number of

crystals per unit volume n_i in each size class changes according to,

$$\frac{\partial n_i}{\partial t} + \underbrace{\mathbf{u}\cdot\nabla n_i}_{(1)} - \underbrace{\nabla\cdot(\nu_c\nabla n_i)}_{(2)} =$$

$$\begin{cases} -\underbrace{\Gamma_i n_i}_{(3a)} + \underbrace{\dot{N}_I}_{(4ai)} + \underbrace{\sum_{j=2}^{N}\alpha_{ji}n_j}_{(4aii)} - \underbrace{f_i n_i}_{(5a)} - \underbrace{v_{i,g}\frac{\partial n_i}{\partial z}}_{(6)}, & i=1, \\ -\underbrace{\Gamma_i n_i}_{(3a)} + \underbrace{\Gamma_{i-1}n_{i-1}}_{(3b)} - \underbrace{\beta_{i1}n_i}_{(4b)} - \underbrace{f_i n_i}_{(5a)} + \underbrace{F_{i-1}n_{i-1}}_{(5a)} - \underbrace{v_{i,g}\frac{\partial n_i}{\partial z}}_{(6)}, & 2\le i\le N-1, \\ +\underbrace{\Gamma_{i-1}n_{i-1}}_{(3b)} - \underbrace{\beta_{i1}n_i}_{(4b)} + \underbrace{F_{i-1}n_{i-1}}_{(5a)} - \underbrace{v_{i,g}\frac{\partial n_i}{\partial z}}_{(6)}, & i=N. \end{cases} \tag{2.3}$$

As in (1.1), the terms labelled (1) and (2) correspond to advection and diffusion. The terms (3a) and (3b) respectively describe growth out of and into size class i, with $-\Gamma_i$ corresponding to rate at which crystals growth out of size class i and $+\Gamma_{i-1}$ corresponding to the rate at which crystals grow into size class i from the size class below. The terms (4ai) and (4aii) are the primary and secondary nucleation rates of crystals into size class 1 and (4b) is the corresponding removal of crystals in the larger size classes, with β_{i1} corresponding to the rate of removal of crystals of size class i by secondary nucleation and α_{ji} corresponding to the rate of addition of crystals into size class 1 by secondary nucleation of crystals in size class i. The terms (5a) and (5b) describe flocculation of crystals out of and into size class i where it is assumed that only crystals of the size class below can flocculate into size class i. The rate of flocculation of crystals out of size class i is given by f_i and the rate of flocculations into size class i due to crystals flocculating in the size class below is given by F_{i-1} The term (6) describes crystal rise with $v_{g,i}$ the buoyant rise velocity of crystal i.

We shall now discuss how the terms parametrising crystal growth, seeding, rise and collisions in (2.3) are obtained across a range of models.

2.3.1 Crystal growth (Γ_i)

Disk shaped frazil ice crystals have been observed to grow predominately in the radial direction, parallel to the basal plane (Daly, 1984; McFarlane et al., 2014; Schneck et al., 2019).

The growth rate of a frazil ice crystal can be derived using energy conservation,

$$\mathcal{L}\frac{\mathrm{d}m}{\mathrm{d}t} = Nu\, k_l(T_f - T)\frac{A_F}{l}, \tag{2.4}$$

where $\mathcal{L}$ is the latent heat of solidification, m is the mass of the crystal, Nu is the Nusselt number, k_l is the liquid thermal conductivity, T_f is the freezing temperature of ice, T is the fluid temperature, A_F is the area of the crystal that predominantly loses heat and l is a characteristic length scale. This assumes that there is a single scale for each of A_F and l, when in reality there could be different l for planar faces and narrow curved edges (see Rees Jones and Wells (2015)).

The choice of freezing area and characteristic lengthscale varies across models: see Rees Jones and Wells (2015) for discussion. Most models assume there is only radial growth, yielding, $A_F = 2\pi r w$. Some models (e.g. Svensson and Omstedt (1994)) assume that l is the disk thickness w and others (e.g. Heorton et al. (2017), Holland and Feltham (2005), Smedsrud (2002), Smedsrud and Jenkins (2004), and Souillé et al. (2020)) assume l is the disk radius r. A more complete treatment by Rees Jones and Wells (2015) allowing for heat loss from the planar disk faces and the curved faces gives $A_F/l = (2\pi r)/[0.9008 - 0.2634\log(w/2r)]$.

As noted by Jones and Wells (2018) the differences in A_F and l can all be expressed in terms of a function $f(w/[2r])$, with $A_F/l = 2\pi r f(w/[2r])$ in (2.4) and $f = 1$ corresponding to the assumption that growth is radial and the characteristic lengthscale is w.

The crystal growth rate can be related to (2.4) by discretising the growth term (see Jones and Wells, 2018) in (1.1),

$$\frac{\partial}{\partial r}(Gn_r) \approx \frac{n_i}{V_{i+1}-V_i}\frac{\mathrm{d}V_i}{\mathrm{d}t} - \frac{n_{i-1}}{V_i-V_{i-1}}\frac{\mathrm{d}V_{i-1}}{\mathrm{d}t}. \tag{2.5}$$

Equation (2.5) is valid provided $V_{i+1}-V_i \to V_i - V_{i-1}$ as $\Delta V_i \to 0$, where $\Delta V_i = V_{i+1} - V_i$ (Jones and Wells, 2018). Thus,

$$\Gamma_i = \frac{1}{V_{i+1}-V_i}\left(\frac{\mathrm{d}V_i}{\mathrm{d}t}\right) = \frac{1}{V_{i+1}-V_i}\left(\frac{2\pi N u\, k_l(T_f - T)}{\rho_I \mathcal{L}}\right) r_i f_i. \tag{2.6}$$

The possibility of a different rate for melting was introduced by Holland and Feltham (2005) such that crystal growth is discretised as,

$$\frac{\mathrm{d}n_{i,growth}}{\mathrm{d}t} = \begin{cases} -\Gamma_i n_i + \Gamma_{i-1} n_{i-1}, & T < T_f, \\ -\mathcal{M}_i n_i + \mathcal{M}_{i+1} n_{i+1}, & T > T_f, \end{cases} \tag{2.7}$$

where in a similar way to how Γ_i is calculated,

$$\mathcal{M}_i = \frac{1}{V_i - V_{i-1}}\left(\frac{dV_i}{dt}\right) = \frac{1}{V_i - V_{i-1}}\left(\frac{N u\, k_l(T_f - T)}{\rho_I \mathcal{L}}\right)\frac{(2\pi r_i^2 + 2\pi r_i w_i)}{l}. \tag{2.8}$$

It is assumed that the melting area is the entire surface area of the crystal and l is w_i or r_i depending on the choice of characteristic lengthscale.

2.3.2 Seeding ($\dot{N}_I$)

Most models initiate with a certain number and size distribution of frazil ice crystals and then assume all subsequent new crystals only form through secondary nucleation (fracture of existing crystals). The exception is the model of Hammar (1994) who introduces a constant seeding rate and Chen et al. (2024) who argue that subsequent ice nucleation should take place under certain weather conditions (rainfall, snowfall, and high winds) and suggest a power function form

$$\dot{N}_I = \frac{a|T|}{V} \times 10^{k_{seed}|T|}, \tag{2.9}$$

where, $a = 1\ \mathrm{K^{-1}\,s^{-1}}$, T is the water temperature in degrees Celsius and k_{seed} is a coefficient obtained by calibrating against the weather conditions.

2.3.3 Crystal rise ($v_{i,g}$)

There is larger variation in the choice of rise velocity across models. For a more complete review see McFarlane et al. (2014). Models are either completely based on experimental results, a combination of experimental results and theory, or just theory.

Theoretical/combined approach

A common theoretical approach is to calculate the rise velocity by balancing the drag force with buoyancy and then to obtain the drag coefficient either from experiment or theory. For an anisotropic particle, the drag force is not co-linear with the slip velocity (the relative velocity between the particle and the flow) in general and is given by (Challabotla et al., 2015)

$$[\mathbf{F}^d]_i = K_{ij}|\mathbf{u} - \mathbf{u}_p|^2 \frac{u_j - u_{p,j}}{|\mathbf{u} - \mathbf{u}_p|}, \tag{2.10}$$

where $[\mathbf{F}^d]_i$ is the i component of the drag force acting on the particle, K_{ij} is the resistance tensor and u_j and $u_{p,j}$ are j components of the fluid velocity $\mathbf{u}$ and particle velocity $\mathbf{u}_p$ respectively. Frazil ice models often simplify this by setting $K_{ij} = \beta I_{ij}$ where I_{ij} is the identity matrix and β accounts for the different choices of crystal area perpendicular to the relative flow. This yields

$$\mathbf{F}^d = \beta C_D \rho r_i^2 |\mathbf{u} - \mathbf{u}_p|^2 \frac{\mathbf{u} - \mathbf{u}_p}{|\mathbf{u} - \mathbf{u}_p|}, \tag{2.11}$$

where C_D is the crystal drag coefficient and ρ is the fluid density (Liu et al., 2024). Various approaches are used to find βC_D. A number of approaches consider the likely particle Reynolds number of frazil ice crystals,

$$Re_p = \frac{2r|\mathbf{u}_p - \mathbf{u}|}{\nu}, \tag{2.12}$$

as this can be related to C_D, where ν is the fluid viscosity. To estimate β, different models make certain assumptions about the orientation of frazil ice crystals relative to the slip velocity.

If the frazil crystals rise broadside on,

$$\beta C_D = \begin{cases} \frac{\alpha}{Re_p}, & Re_p \ll 1, \\ \frac{\pi C_D}{2}, & Re_p > 1. \end{cases} \tag{2.13}$$

Note that for low Re_p, $C_{D,i}$ is inversely proportional to Re_p meaning that the drag force is directly proportional to the relative velocity. Manohar (1936) gives $\alpha = 32$ and Daly (1984) gives $\alpha = 2/(25\pi)$. The differences in the two results for the drag coefficient for $Re_p \ll 1$ must come from the method used to obtain the drag force. Bessel functions are used by Manohar (1936) to obtain the drag force on a cylinder. The method to obtain the second equation is not discussed in Daly (1984).

In the case when $Re_p > 1$, various approaches are used to estimate C_D. The models of Holland and Feltham (2005), Souillé et al. (2020), and Yang et al. (2023) use the crystal drag coefficient empirically determined by Gosink and Osterkamp (1983),

$$\log C_D = 1.386 - 0.892 \log Re_p + 0.111 (\log Re_p)^2. \tag{2.14}$$

Here C_D, was obtained by measuring $\mathbf{u}_p$ when $\mathbf{u}$ is zero, assuming that buoyancy balances drag ($|\mathbf{u}_p| = v_g$) and that the crystals rise broadside on with $\beta = \pi/2$. In this limit (2.11) becomes

$$v_g^2 = \left(1 - \frac{\rho_I}{\rho}\right) \frac{2wg}{C_D}, \tag{2.15}$$

where g is the acceleration due to gravity and C_D can be obtained from measuring v_g and w. An alternative formula for the drag coefficient when the disks are rising broadside on with $Re_p > 1$ is suggested by Daly (1984) for r and ν measured in SI units,

$$C_D = \begin{cases} \frac{98.0 r^{0.405}}{Re_p^{0.6} \nu^{0.27}}, & Re_p < 1000 \\ 2, & Re_p \geq 1000. \end{cases} \tag{2.16}$$

Svensson and Omstedt (1994) and Wang and Doering (2005) approximated the discontinuous data of Daly (1984) as

$$v_g = 75.4 r^{6/5}. \tag{2.17}$$

If instead it is assumed that the frazil crystals rise with their axis perpendicular to the slip velocity (Liu et al., 2024; McFarlane et al., 2014),

$$\beta C_D = \begin{cases} \frac{64}{3Re_p}, & Re_p \ll 1, \\ \frac{3\pi w C_D}{8r}, & Re_p > 1. \end{cases} \tag{2.18}$$

which uses the scaling due to Manohar (1936) for $Re_p \ll 1$. To determine C_D for $Re_p > 1$, empirical results are used. Liu et al. (2024) use the drag coefficient for a sphere at high Re_p (Kolev, 2012),

$$C_D = \begin{cases} \frac{24}{Re_p}\left(1 + 0.15Re_p^{0.697}\right), & Re_p < 1000 \\ 0.44, & Re_p \geq 1000. \end{cases} \tag{2.19}$$

An alternative approach is to assume an infinitely thin vertically rising disk. McFarlane et al. (2014) used the equations for the drag exerted on a vertical disk, assuming a laminar boundary layer was formed on both sides of an infinitely thin disk, to calculate

$$\beta C_D = \frac{6.56}{Re_p^{1/2}}. \tag{2.20}$$

Using equations based on the measured terminal velocities for atmospheric particles, Morse and Richard (2009) suggest obtaining the frazil ice rise velocity using a power law. This method is used by Heorton et al. (2017) yielding

$$v_g = \begin{cases} 6.229 \times 10^{-3} r^{1.621} & r \leq 0.635\text{mm} \\ (-0.412r^2 + 8.138r - 2.024) \times 10^{-3}, & r > 0.635\text{mm}, \end{cases} \tag{2.21}$$

where r is measured in millimetres and the velocity is in metres per second.

Experimental approach

Other frazil ice models are entirely based on experimental data. For example, Chen et al. (2024) use the experimental results from Matousek (1992) yielding

$$v_g = \frac{1.31 \times 10^{-5} (2r)^{0.29} w^{0.61}}{\nu}. \tag{2.22}$$

where r, w and ν are measured in SI units. These results were obtained by measuring the rise velocity of discs made of polyethylene (which has the same density as ice)

with radii of 1, 2 and 2.75 mm and thicknesses ranging from $0.03 - 0.27$mm.

Mixed approach

Finally, Jones and Wells (2018) argue more complicated parametrisations do not fit that much better than a simple linear relationship, and use the relationship,

$$v_g = 16r, \tag{2.23}$$

with r in SI units, suggested by McFarlane et al. (2014) from laboratory experimental data.

In order to obtain $v_{i,g}$, the rise velocity of crystals of size class i, r is replaced with r_i, w with w_i, and the mean particle velocity of crystals of size class i, $\langle \mathbf{u}_{p,i} \rangle$ is used to calculate the particle Reynolds number $Re_{p,i}$ of crystals of size class i.

The different choices of equation for the rise velocity mean that there is substantial variation in the rise velocity across models (see Fig. 4 of Souillé et al. (2023)). As the empirical data gives a large spread of velocities for each value of r, (see Fig.10 of McFarlane et al. (2014)), there is still little justification as to which equation for the rise velocity is preferable. However, choosing an equation used in a previous model allows ease of comparison across models.

2.3.4 Crystal collisions

We now discuss how secondary nucleation and flocculation are parametrised in frazil ice models. We shall reserve discussion on the weaknesses and strengths of these parametrisations until we have also reviewed how crystal collisions are modelled in other settings in §2.4.

2.3.4.1 Secondary nucleation (α_{ij} and β_{i1})

Models using the collision energy to determine the rate of secondary nucleation

According to Daly (1984), Mercier (1985), and Yang et al. (2023), the number of crystals produced of the first size class per collision should be a product of the number of nuclei produced per unit collision energy N_E, and the collision energy E_{coll}. The collision energy can be calculated by momentum and energy conservation (see (2.29)-(2.31) as an example), and is equal to the difference in kinetic energy of the particles before and after the collision, where it is assumed that some energy is lost in crystal fracture.

Considering crystals of size class j, the energy and frequency of collisions with other crystals will vary depending on the size, velocity and concentration of the other size classes. The coefficient α_{ji} in (2.3) corresponds to the rate of production of crystals of size class i due to collisions with a single crystal of size class j. Mercier (1985) and Daly (1984) calculate α_{ji}, by summing over all the interactions of crystals of size class j with crystals of other size classes,

$$\alpha_{ji} = \sum_{k=1}^{N} f_{coll,jk} E_{coll,jk} N_E. \tag{2.24}$$

$f_{coll,jk}$ is the collision frequency of a single crystal of size class j with crystals of size class k. The collision energy $E_{coll,jk}$ is now the mean collision energy of crystals of size class j and k. The total rate of production per unit volume $\mathcal{F}_{prod,ij}$ of crystals of size class i due to collisions with crystals of size class j is then,

$$\mathcal{F}_{prod,ij} = \alpha_{ji} n_j. \tag{2.25}$$

The single-size-class model of Yang et al. (2023) uses this approach to calculate the secondary nucleation rate, $\dot{N}_T$ in (2.1). For n crystals per unit volume of mean mass $\overline{m}$, mean radius $\overline{r}$, moving with mean velocity $\overline{u}$, they set

$$\dot{N}_T = f_{coll} E_{coll} N_E, \tag{2.26}$$

$$f_{coll} = \pi (2r)^2 \overline{u} n, \tag{2.27}$$

$$E_{coll} = \tau_{coll} \times 2 \times \frac{\overline{m u^2}}{2}, \tag{2.28}$$

where τ_{coll} is proportion of collisional energy transferred to the crystals and N_E is tuned to match experimental results. The collision frequency is equal to the average cylindrical volume swept out per unit second by a crystal of radius $2r$ moving with velocity $\overline{u}$ multiplied by the number of crystals per unit volume.

The only multiple-size-class model to consider the collision energy is the model of Hammar (1994). In this model it is assumed that collisions are inelastic such that after the collision the crystals will not be moving relative to each other and instead move with velocity $\mathbf{u}_{pi}$. The collision energy E_{coll} can be obtained by solving for momentum and energy conservation,

$$m_i\mathbf{u}_{pi} + m_j\mathbf{u}_{pj} = (m_i + m_j)\overline{\mathbf{u}}_{pij}, \tag{2.29}$$

$$\frac{1}{2}m_i|\mathbf{u}_{pi}|^2 + \frac{1}{2}m_j|\mathbf{u}_{pj}|^2 = \frac{1}{2}(m_i + m_j)|\overline{\mathbf{u}}_{pij}|^2 + E_{coll}, \tag{2.30}$$

$$E_{coll} = \frac{1}{2}\left(\frac{m_i m_j}{m_i + m_j}\right)(|\mathbf{u}_{pi} - \mathbf{u}_{pj}|)^2, \tag{2.31}$$

where m_i and $\mathbf{u}_{pi}$ is the mass and velocity of crystal i respectively.

In the model of Hammar (1994), the collision frequency between a single particle of size class i with n_j crystals per unit volume of size class j is calculated from the flux of particles into a sphere of surface area $r_i + r_j$ multiplied by the number density in size class j and the collision efficiency giving,

$$f_{coll,ij} = n_j \times \frac{1}{2} \times 4\pi(r_i + r_j)^2\langle|w_{ij,r}(r_i + r_j)|\rangle C_{eff}. \tag{2.32}$$

$w_{ij,r}(r_i + r_j)$ is radial component of the relative velocity between the two particles of size classes i and j separated by a distance $r_i + r_j$, $\langle\rangle$ is the mean and C_{eff} is the collision efficiency, defined as the fraction of particles that would have collided if particle-particle interactions were neglected (Daly, 1984).

The mean radial relative velocity $|w_{ij,r}(r_i + r_j)|$ is the sum of the mean radial relative velocity from turbulence $w_{ij,turb}$ and from buoyant differential rise $w_{ij,g}$.

The turbulent relative velocity is given by

$$w_{ij,turb} = \left(\frac{2}{\pi}\frac{\epsilon}{15\nu}\right)^{1/2}(r_i + r_j), \tag{2.33}$$

$$w_{ij,turb} = \left(\frac{\epsilon}{15\nu K_u^{1/2}}\right)^{1/2}(r_i + r_j), \tag{2.34}$$

depending on whether a normal (2.33) or lognormal (2.34) distribution is assumed for the fluid velocity distribution. K_u is the kurtosis of the velocity derivative. Derivations for $w_{ij,turb}$ can be found in (2.2.1) of Mercier (1985). To obtain an expression for $w_{ij,g}$ Hammar (1994) use the result of Findheisen (1939),

$$w_{ij,g} = \frac{0.2}{3}\left(\frac{4\pi}{3}\right)^{1/3}\frac{g}{\nu}\frac{|\rho_I - \rho|}{\rho}|r_i^2 - r_j^2|. \tag{2.35}$$

which determined crystal rise speeds from a balance of buoyancy and drag.

Models assuming one crystal is produced per collision

Many other models simplify the suggestion of Daly (1984), Mercier (1985), and Yang et al. (2023) and assume that one crystal of the smallest size class is produced per collision such that

$$\alpha_{ji} = \sum_{k=1}^{N} f_{coll,jk}. \tag{2.36}$$

These frazil ice models use a mean density in their collision calculation, instead of calculating a collision frequency that treats collisions between crystals of each size class separately. The collision frequency of crystals of size class j is obtained by calculating the volume swept by crystals of size class j per second, multiplied by the number of crystals per unit volume $\overline{n} = \sum_{i=1}^{N} n_i$. In most cases the velocity is assumed to be aligned perpendicular to the basal plane (i.e. along the axis of the cylindrical disk) such that the volume swept out in time Δt is the volume of a cylinder $\pi r_j^2 |\langle \mathbf{u}_{pj} \rangle| \Delta t$. Overall,

$$f_{coll,j} = \sum_{k=1}^{N} f_{coll,kj} = \pi r_j^2 |\langle \mathbf{u}_{pj} \rangle| \overline{n}. \tag{2.37}$$

Modifications to r

Heorton et al. (2017), Holland and Feltham (2005), Smedsrud (2002), and Smedsrud

and Jenkins (2004) suggest that, because the crystals can twist and turn in all directions as they move with the flow, a more appropriate choice of radius is the equivalent radius r_j^e (the radius of a sphere with the equivalent volume as the disk)

$$r_j^e = (3r_j^2 w_j/4)^{1/3}. \tag{2.38}$$

Modifications to $\overline{n}$

When comparing model outputs to experiments, the rate of secondary nucleation was found to be too high (Svensson and Omstedt, 1994). Thus, a limit is placed on $\overline{n}$ such that $\overline{n} = \min[n_{max}, \sum_i n_i]$. The limit describes the effect of unparametrised processes which limit the efficiency of the secondary nucleation process. For example if the concentration of frazil increases we might expect gravitational damping of the turbulence and hence a reduction in the collision frequency. This approach is used by many models (e.g. Holland and Feltham (2005), Jones and Wells (2018), Smedsrud (2002), Smedsrud and Jenkins (2004), Souillé et al. (2020), Svensson and Omstedt (1994), and Wang and Doering (2005)). Other models (e.g. Heorton et al. (2017)) suggest introducing a constant calibration parameter to limit the efficiency of the secondary nucleation process (see Radia (2014) for discussion). One purpose of the thesis is to find a more physically informed approach to reduce the collision rate.

Choice of $|\langle \mathbf{u}_{pj} \rangle|$

Methods to calculate the mean velocity $|\langle \mathbf{u}_{pj} \rangle|$ of crystals of size class j vary between authors. Most models assume that the relative velocity is a combination of the speed due to gravitational settling $v_{g,i}$ and the mean relative speed from turbulent motion $w_{j,turb}$. The models of Daly (1984) and Mercier (1985) assume the relative velocity due to gravitational settling and from turbulent motion can be superimposed linearly, $|\langle \mathbf{u}_{pj} \rangle| = v_{j,g} + v_{j,turb}$ whilst Heorton et al. (2017), Holland and Feltham (2005), Jones and Wells (2018), Smedsrud (2002), Smedsrud and Jenkins (2004), Souillé et al. (2020), Svensson and Omstedt (1994), Wang and Doering (2005), and Yang et al. (2023) sum the contribution of turbulence and gravitational settling

quadratically, $|\langle \mathbf{u}_{pj} \rangle| = (v_{j,g}^2 + v_{j,turb}^2)^{1/2}$. The linear assumption is preferred if the relative velocity due to gravitational settling and the relative velocity due to turbulence are close to co-linear. The quadratic assumption is preferred if this is not the case.

For a particle of size class j, all of Jones and Wells (2018), Souillé et al. (2020), Svensson and Omstedt (1994), Wang and Doering (2005), and Yang et al. (2023), assume

$$v_{j,turb} = \sqrt{\frac{4\epsilon}{15\nu}} r_j. \tag{2.39}$$

The expression for $v_{j,turb}$ comes from the calculation of the variance of the relative radial velocity, $\langle w_{j,r}^2 \rangle$, in a turbulent flow (Saffman and Turner, 1956).

In contrast Heorton et al. (2017), Holland and Feltham (2005), Smedsrud (2002), and Smedsrud and Jenkins (2004) use

$$v_{j,turb} = \left(\frac{3}{2d_i}\right)^{1/3} \sqrt{\frac{4\epsilon}{15\nu}} r_j. \tag{2.40}$$

The difference between the two models arises due to the choice of collision radius, where Jones and Wells (2018), Souillé et al. (2020), Svensson and Omstedt (1994), Wang and Doering (2005), and Yang et al. (2023) use the actual radius of the crystal and Heorton et al. (2017), Holland and Feltham (2005), Smedsrud (2002), and Smedsrud and Jenkins (2004) use the equivalent radius.

The settling velocity is equal to the terminal velocity of the particle. The choices for the settling velocity were outlined in §2.3.3.

Parametrisation of β_{i1}

The above discussion considered the parametrisation of α_{ij}. The rate of transition of nuclei out of size class i into size class 1 due to secondary nucleation, β_{i1}, can be

derived from α_{j1} using mass conservation. Let $dn_{i,nuc}/dt$ be the rate that crystals are transferred into or out of size class i by nucleation. Mass conservation yields

$$\beta_{i1} = \frac{V_1}{V_i}\alpha_{i1}. \tag{2.41}$$

Almost all models described in §2.3 use this parametrisation for β_{i1} with the exception being the model of Svensson and Omstedt (1994), who let $\beta_{i1} = \alpha_{i1}$ and therefore do not conserve mass.

2.3.4.2 Flocculation (f_i and F_{i-1})

The process of flocculation is only included in a limited number of models (Chen et al., 2024; Hammar, 1994; Souillé et al., 2020; Svensson and Omstedt, 1994; Wang and Doering, 2005; Yang et al., 2023).

The model of Hammar (1994) assumes that ζ crystals of the smallest size class break off when a collision occurs between crystals of size classes i and j. The colliding crystals merge into a new crystal of volume $V_{new,ij} = V_i + V_j - \zeta V_1$. The rate of removal of crystals from size class i due to flocculation is,

$$f_i = \sum_{k=1}^{N} f_{coll,ik}. \tag{2.42}$$

It is assumed that the volume of the new crystal formed after collisions of crystals of size class i with crystals of size class 1 is always greater or equal to a crystal of size class $i+1$. The rate $\mathcal{F}_{floc,i}$ at which crystals are added to size class i per unit volume from flocculation is

$$\mathcal{F}_{floc,i} = \sum_{j=1}^{i}\sum_{k=1}^{i} f_{coll,jk} n_j V_{frac,ij}, \tag{2.43}$$

where

$$V_{frac,ij} = \begin{cases} \frac{V_{new,ij}-V_i}{V_{i+1}-V_i}, & V_{i-1} \le V_{new,ij} < V_i \\ \frac{V_{i+1}-V_{new,ij}}{V_{i+1}-V_i}, & V_i \le V_{new,ij} < V_{i+1} \\ \frac{V_{new,ij}}{V_N}, & i = N, V_{new,ij} > V_N, \\ 0, & \text{otherwise.} \end{cases} \tag{2.44}$$

Here, the new crystal is distributed between the two neighbouring size classes, with fraction $V_{frac,ij}$ being added to each size class. In the case when the flocculated

crystal is larger than the largest size class, it is completely added to the largest size class. $V_{frac,ij}$ is chosen to conserve volume.

The models of Souillé et al. (2020), Svensson and Omstedt (1994), and Wang and Doering (2005) assume that flocculation is more effective for larger crystals, with the flocculation rate increasing linearly with radius,

$$f_j = a_{floc}\frac{r_j}{r_1}, \tag{2.45}$$

$$F_j = \frac{V_j}{V_{j-1}} f_j, \tag{2.46}$$

where F_j can be obtained from f_j using mass conservation in a similar method to that outlined for β_{i1} and α_{i1}.

Chen et al. (2024) use experimental observations to suggest crystals of different sizes are likely to flocculate, and split particles into three different groups where flocculation can only occur when collisions are between groups of different sizes.

The single-size-class frazil ice model of Yang et al. (2023) applies the same logic that is used for secondary nucleation to determine a collision rate, and then introduces a critical velocity for flocculation V_s. Yang et al. argue that crystal collisions with a velocity higher than the adhesion velocity will bounce off each other, whilst crystals colliding with a velocity at or below the adhesion velocity will flocculate. In the single-size-class frazil ice model of Yang et al. (2023),

$$\dot{N}_F = n^2\pi(2\overline{r})^2\overline{u}\beta_{floc}, \tag{2.47}$$

$$\beta_{floc} = \begin{cases} 1, & \overline{u} \leq V_s \\ 0, & \text{otherwise} \end{cases} \tag{2.48}$$

which we can adapt to a multiple-size-class-frazil-ice model via,

$$f_j = \pi r_j^2 u_j \overline{n}\beta_{floc,j} = \alpha_{j1}\beta_{floc,j}, \tag{2.49}$$

$$F_j = \frac{V_j}{V_{j-1}} f_j. \tag{2.50}$$

where $\beta_{floc,j}$ is 1 when $\langle \mathbf{u}_{p,j} \rangle \leq V_s$ and 0 otherwise. The critical adhesion velocity is obtained by estimating the energy required to separate the crystals (see Yang et al. (2023) for details).

2.4 Crystal collision models in other settings

Having demonstrated the variety of approaches used to model crystal collision in §2.3.4. We now discuss how particle collisions are parametrised in other settings. In §2.5 we then use this to identify weaknesses of current frazil ice models.

Parametrising particle collisions is important for understanding a range of natural processes, from planetary formation in protoplanetary nebula (Champney et al., 1995) to rain formation in clouds (Ayala et al., 2008). Particle collisions are also important for industrial processes ranging from crystallization (Evans et al., 1974) to froth flotation (Schubert, 1999). Therefore, there is a range of theory to draw on to apply to frazil ice crystal collisions. For a fuller review of collision modelling in a range of contexts see Meyer and Deglon (2011).

In general parameterisations define the average collision rate $\langle \mathcal{N}_{ij} \rangle$ between particles of size class i and j as

$$\langle \mathcal{N}_{ij} \rangle = V^2 n_i n_j \Gamma_{ij} = V f_{coll,ij} n_i = V f_{coll,ji} n_j. \tag{2.51}$$

(Devenish et al., 2012), where Γ_{ij} is the collision kernel between particles of sizes i and j. As in §1.6, n_i is the average number of particles of size i per unit volume and V is the volume.

2.4.1 Collision Kernel

The collision kernel for single particles of size clases i and j can be formulated as the product of the encounter frequency $\mathcal{F}_{enc,ij}$ and the collision efficiency $C_{eff,ij}$,

$$\Gamma_{ij} = \mathcal{F}_{enc,ij} C_{eff,ij}. \tag{2.52}$$

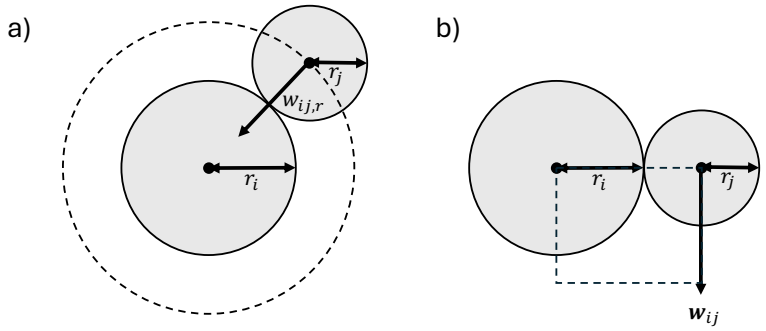

Figure 2.3: There are two different formulations to calculate the collision frequency. In the spherical formulation (panel a) the collision frequency is calculated from the frequency of particles entering a sphere of radius $r_i + r_j$. In the cylindrical formulation (panel b) the collision frequency is calculated from the frequency of particles entering a cylinder of radius $r_i + r_j$.

The collision efficiency is defined as the ratio of the number of particles that collide when particle-particle interactions are included to the number of particles that collide when particle-particle interactions are neglected (Daly, 1984). In other words the collision efficiency accounts for the reduction in the collision frequency due to hydrodynamic interactions. In the case when particle interactions do not affect collisions, the collision efficiency is unity.

We initially consider the simpler case of spherical particles with zero-inertia. The collision kernel can be defined in two formulations (Figure 2.3): the spherical formulation and the cylindrical formulation (Wang et al., 1998). Using the spherical formulation the collision kernel is obtained by calculating the volume influx of particles of radius r_j toward a particle of radius r_i, averaged over the collision surface S_c with area $4\pi(r_i + r_j)^2$ about the centre of the particle of radius r_i (i.e. the collision surface corresponds to the surface area of the sphere with radius equal to the sum of the particle radii). Defining the collision radius $r_{c,ij} = r_i + r_j$, and assuming only half the particles are travelling into the collision sphere,

$$\mathcal{F}_{enc,ij} = \frac{1}{V} \times \frac{1}{2} \times 4\pi r_{c,ij}^2 \langle |w_{ij,r}(r_{c,ij})| \rangle, \tag{2.53}$$

under the spherical formulation, where $w_{ij,r}(r_{c,ij}) = \mathbf{w}_{ij}(r_{c,ij}) \cdot \mathbf{r}_{c,ij}/r_{c,ij}$, $\mathbf{r}_{c,ij}$ is the separation vector and $\mathbf{w}_{ij}(r_{c,ij})$ is the relative velocity between the two particles

separated by a distance $r_{c,ij}$.

The cylindrical formulation instead calculates the volume influx of particles of radius r_j towards a particle of radius r_i averaged over the collision surface S_c with area $\pi(r_i + r_j)^2$ about the centre of a particle with radius r_i. Under the cylindrical approximation,

$$\mathcal{F}_{enc,ij} = \frac{\pi r_{c,ij}^2 \langle |\mathbf{w}_{ij}(r_{c,ij})| \rangle}{V}. \tag{2.54}$$

Unlike the spherical formulation, the cylindrical formulation assumes that the relative velocity $\mathbf{w}_{ij}$ in any instant is locally uniform over a spatial scale on the order of the collision radius $r_{c,ij}$, which is not necessarily the case for turbulent flow (Wang et al., 1998). Therefore, it is well-accepted that models based on a cylindrical formulation (as opposed to a spherical formulation) are erroneous for some flows (Meyer and Deglon, 2011). Both formulations produce the same results when calculating the collision kernel in an uncorrelated isotropic random velocity field or a uniform velocity field over the spatial scale of $r_{c,ij} = r_i + r_j$. For example, the latter occurs if the size of the particles is smaller than the Kolmogorov lengthscale (Wang et al., 1998).

Particles with finite inertia have a tendency to accumulate in areas of low vorticity due to the action of centrifugal forces and are thus distributed inhomogeneously in turbulent flow. This is known as the accumulation effect (Wang and Ayala, and Scott, and Wojciech, 2005). A radial distribution function $g(r_{c,ij})$ is added to the collision kernel to account for the accumulation effect. The radial distribution function is defined as the probability density of observing a particle pair at contact in the actual suspension, normalised by the corresponding value in a nominally uniform suspension (Devenish et al., 2012; Wang et al., 2000b),

$$g_{ij}(r_{c,ij}) = \frac{\langle n_i(r_i) n_j(r_i + r_{c,ij}) \rangle}{\langle n_i \rangle \langle n_j \rangle}. \tag{2.55}$$

where $n_i(r_i)$ is the number density of particles at location r_i and $\langle n_i \rangle$ is the spatially averaged number density of particles of radius r_i.

Overall, for spherical particles of finite inertia,

$$\Gamma_{ij} = \begin{cases} \frac{2\pi r_{c,ij}^2 \langle |w_{ij,r}(r_{c,ij})| \rangle g_{ij}(r_{c,ij}) C_{eff,ij}}{V}, & \text{spherical formulation,} \\ \frac{\pi r_{c,ij}^2 \langle |\mathbf{w}_{ij}(r_{c,ij})| \rangle g_{ij}(r_{c,ij}) C_{eff,ij}}{V}, & \text{cylindrical formulation.} \end{cases} \tag{2.56}$$

2.5 Comparison to frazil ice models

Having now given an overview in §2.4 of how crystal collisions are modelled in other settings and having giving an overview in §2.3.4 of how crystal collisions are modelled in frazil ice models, we now compare the approaches to model crystal collisions in other settings to what is currently done in frazil ice models. We identify weaknesses of the current approach used in frazil ice models. These weaknesses will be addressed in later chapters.

The collision models outlined in §2.4 all assume spherical particles, however frazil ice crystals are usually approximated as cylinders. In order to account for the approximate cylindrical shape of frazil ice crystals, models usually either set the contribution to the collision radius $r_{c,ij}$ from a single frazil ice crystal of size class i to be either the crystal radius r_i or the equivalent radius r_i^e (defined as the radius of a sphere with the same volume as the cylinder). Therefore, for cylindrical crystals we define $r_{c,ij} = r_{c,i} + r_{c,j}$ where $r_{c,i}$ is either r_i or r_i^e depending on the model.

Almost all of the frazil ice models described in §2.3.4 simplify (2.51) to,

$$\langle \mathcal{N}_{ij} \rangle = V^2 \langle n_i \rangle \overline{n} \Gamma_i. \tag{2.57}$$

With the exception of Hammar (1994), these models do not separately consider interactions between different size classes. The models summarised in §2.3.4 employ the cylindrical formulation to calculate the collision kernel, with

$$\Gamma_i = \frac{\pi r_{c,i}^2 \langle |\mathbf{w}_i(2r_{c,i})| \rangle}{V}, \tag{2.58}$$

where $\langle|\mathbf{w}_i(2r_{c,i})|\rangle = \langle|\mathbf{u}_{pj}(2r_{c,i})|\rangle$ in (2.37). The relative velocity is calculated assuming particles are separated by a distance $2r_{c,i}$, whilst the collision cylinder is of radius $r_{c,i}$. Therefore, these models assume that the collision frequency for each size class is calculated by modelling a crystal of the relevant size moving through a uniformly-distributed stationary cluster of point-like crystals, see Figure 2.4. This approach has several weaknesses which are detailed below in §2.5.1-§2.5.6.

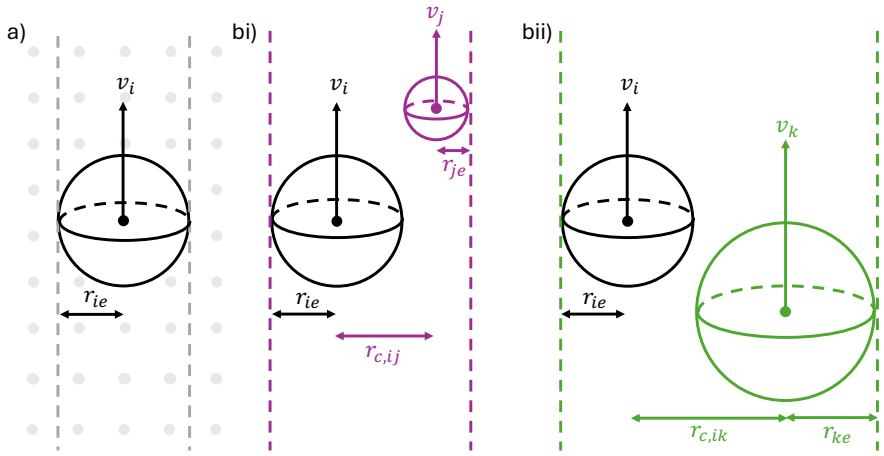

Figure 2.4: a) The collision frequency for each size class is calculated by modelling a crystal of the relevant size moving through a uniformly-distributed stationary cluster of point-like crystals. b) The collision radius should depend on the sizes of each of the colliding crystals and the size-class dependent relative velocity should be taken into account. bi) and bii) show how the collision radius changes with the crystal size.

2.5.1 Relative velocity and the collision radius should depend on both size classes

The first weakness is that the collision radius in frazil ice models is too small. Models let $r_{c,ij} = r_{c,i}$. The true collision radius involving collisions of crystals of radius r_i and r_j should be $r_{c,i} + r_{c,j}$. This approach underestimates the collision rate. In Chen et al. (2024), Jones and Wells (2018), Souillé et al. (2020), Svensson and Omstedt (1994), and Wang and Doering (2005) $r_{c,i} = r_i$, in Heorton et al. (2017), Holland and Feltham (2005), Smedsrud (2002), and Smedsrud and Jenkins (2004) $r_{c,i} = r_i^e$.

Further, this approach means that these frazil ice models ignore the fact that the relative rise velocity depends on the size of each interacting particle and the relative turbulent velocity depends on the particle separation. The relative velocity should depend on both interacting size classes, rather than just a single size class (i.e. $\mathbf{w}_{ij} \neq \mathbf{w}_i$), (see Figure 2.4). Additionally, there is an inconsistency in the choice of collision radius used to calculate the relative velocity ($2r_{c,i}$, see (2.58)) and to calculate the area swept out by the crystal ($r_{c,i}$).

2.5.2 Method to calculate the relative velocity

Common to all models is that the expression for $w_{i,turb}$ comes from the calculation for $\langle w_{turb,r}(2r_{c,ij})^2 \rangle$ in Saffman and Turner (1956). This is only strictly valid for particles with particle relaxation time τ_p less than the Kolmogorov timescale, τ_K and with particle radius r much less than the Kolmogorov lengthscale η_K. Frazil ice crystals can be on the order of millimetres in size, the same order of magnitude as the Kolmogorov lengthscale. Further, as $\langle |\mathbf{w}| \rangle$ is used in the cylindrical approximation it would be more appropriate to choose $w_{i,turb} = \langle |\mathbf{w}_{turb}(2r_{c,ij})| \rangle$ instead of taking the average radial velocity.

There is also uncertainty as to how to accurately obtain the relative velocity by combining the velocity due to turbulent fluctuations and the rise velocity (see §2.3.4).

2.5.3 Method to redistribute crystals between size classes

In all multiple-size class frazil ice models discussed in §2.3.4, where the volume of crystals in the smallest size class is greater than zero, it is assumed that every collision only changes the number of crystals in the colliding size classes and the smallest size class. However, consider the case when we have the volume difference between size classes is $V_i - V_{i-1} = V_1$. When a single crystal of size class 1 fractures from a crystal of size class i, the number of crystals in size class i should reduce by 1 and the number of crystals in size classes $i - 1$ and 1 should increase by 1.

In current models (see §2.3.4) the number of crystals in size class i would reduce by V_1/V_i and the number in size class $i-1$ would not change.

2.5.4 Choice of collision radius and inclusion of non-radial components of the relative velocity

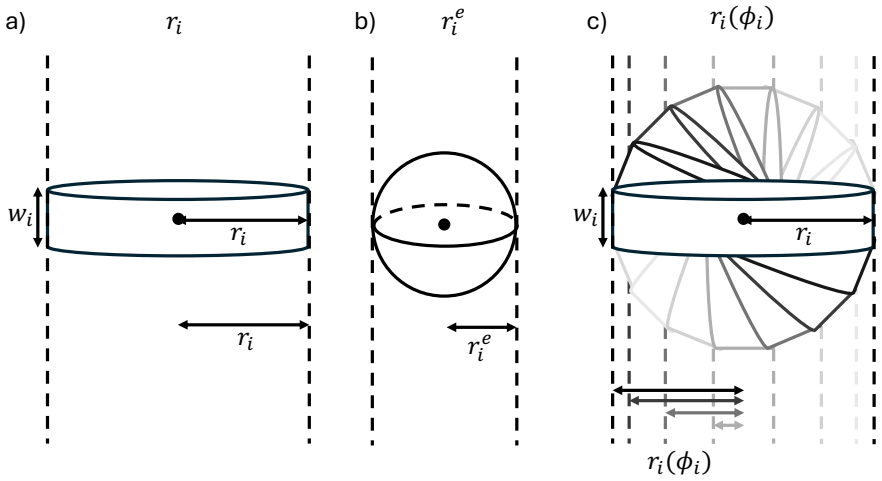

Figure 2.5: Different approaches to calculate the collision radius. Models assume either a) the collision radius is the sum of the radius r_i of each disk, b) the collision radius is the sum of the equivalent radius r_i^e of each of each disk, where the equivalent radius is the radius of a sphere that would give the same volume as the disk. A more accurate description would be c), where the collision radius depends on the orientation of the disks.

A further weakness comes from the fact that calculating the collision radius using either the equivalent radius or the actual radius of each crystal is still an approximation for the true radius (see Figure 2.5). A crystal can take any orientation as it rises through the fluid, so models should take into account how the collision radius depends on the relative orientation of each of the crystals. Additionally, all spherical particles of radius r_i entering a sphere of radius $r_i + r_j$, will collide with with a spherical particle of size r_j as long as the relative radial velocity is negative. However, for disk-like particles this will not necessarily be the case if the non-radial components dominate the motion.

2.5.5 Ignorance of particle interactions

Additionally, the models described in §2.3.4 assume a collision efficiency of unity, $C_{eff} = 1$, assuming particle interactions do not effect the collision rate. In reality

the presence of another particle is likely to alter the trajectory of an approaching particle due to the hydrodynamic forces between them, increasing or decreasing the likelihood of a collision. Hydrodynamic interactions have already been shown to be important in heterodispersed systems (Thomas et al., 1999) and for colliding cloud droplets (Wang and Ayala, and Scott, and Wojciech, 2005).

2.5.6 Assuming the particles are homogeneously distributed

The models described in §2.3.4 also assume the particles are homogeneously distributed and neglect the accumulation effect, setting the radial distribution function, $g_{ij} = 1$.

2.5.7 Summary

In this chapter we have introduced the existing observations that can be used to test numerical frazil ice models in §2.2 and the approaches to model frazil ice numerically in §2.3. We focussed our attention on crystal collisions and also outlined how crystal collisions are modelled elsewhere in the literature in §2.4. In §2.5 we then identified weaknesses in the current approach used to model frazil ice crystal collisions. These weaknesses will be addressed in subsequent chapters.

In §2.2 we noted that secondary nucleation and flocculation affect the size distribution and number of crystals and consequently change the heat and salt flux into the water because the solidification rate depends on the crystal size. Secondary nucleation depends on the turbulence intensity (see (2.39) and (2.40)). The observations of the crystal sizes, the crystal size distribution, and the water temperature can be used to test our model.

We also discussed the different numerical parametrisations of frazil ice processes. We showed that the methods used to parametrise secondary nucleation and flocculation vary substantially across models. This demonstrates the need for a better

understanding of secondary nucleation and flocculation.

Then we compared the approach used by frazil ice models to calculate the collision frequency, to the approach used to calculate the collision frequency in other settings. We identified several weaknesses of the current approach used in frazil ice models. These weaknesses are using the cylindrical formulation for the collision area instead of the spherical formulation, the assumptions required to calculate the mean relative velocity, the method to calculate the collision radius, the failure to consider non-radial components of the relative velocity, the neglect of the collision efficiency and the assumption that crystals are homogenously distributed. Therefore, this thesis derives a new parametrisation for the collision kernel of frazil ice crystals.

In §4 we derive a new expression for the relative velocity between crystals and allow the collision radius to include the size of each interacting size class. To do this we will adapt models for water droplet collisions in clouds (Ayala et al., 2008) and collisions of inertial particles (Chan et al., 2023; Yuu, 1984) to improve the parametrisation of the encounter frequency. In §5 we derive a parametrisation that allows the crystals to redistribute between multiple size classes when they collide. In §6 we let the collision radius depend on the orientation of each of the crystals and account for the non-radial components of the relative velocity. To obtain a collision efficiency, in §7 we first build physical insight by modelling the effect hydrodynamic interactions have on the trajectories and curvatures of two approaching plates with two dimensional flow. In §8 we then model the hydrodynamic interactions experienced by two approaching cylindrical disks. Finally, in §9 we implement our new parametrisation for crystal collisions into a mixed-layer frazil ice model. In each chapter we discuss the implications of each change by adding the change to a simplified frazil ice model.

"This is how you are to build it: the ark is to be 300 cubits long, 50 cubits wide and 30 cubits high."

— Genesis 6:15 NIV

3 Frazil ice models used in this thesis

Contents

3.1 Introduction

The remainder of this thesis will explore new treatments of frazil ice crystal interactions, that underpin many of the frazil ice models discussed in §2.3. This chapter introduces two simplified frazil ice models that will be used later in the thesis to illustrate the implications of the new treatment of crystal interactions. We first describe a mixed-layer frazil ice model with multiple size classes in §3.2 that we will use in §9 to test the effect of the combined changes we make to the parametrisation of secondary nucleation and flocculation. In §3.3 we then simplify the mixed-layer frazil ice model to create a frazil ice model with multiple size classes that only alters the crystal population by secondary nucleation. The latter

model will then be used in §4-§8 to assess the effect of each change we make to the parametrisation of crystal collisions, in a setting where crystal collisions are isolated. In §3.4 we discuss typical initial conditions used, and illustrate the behaviour of both the mixed-layer model and the simple model in §3.5.

3.2 Frazil ice model for a well mixed-layer

Following the discussion in §2, we describe a multiple-size-class frazil ice model that we will use in §9 to test the effect of changes to the parametrisation of crystal collisions. As mentioned in §2.2 we compare this model to the experimental data of McFarlane et al. (2015) and Schneck et al. (2019). In their experiments the turbulent kinetic energy dissipation rate ϵ was estimated to be between $2 \times 10^{-3}\mathrm{m}^2\mathrm{s}^{-3}$ and $3 \times 10^{-2}\mathrm{m}^2\mathrm{s}^{-3}$. We assume that the tank can be approximated as a well-mixed domain such that all physical quantities (temperature and crystal size distribution) are uniform over the tank and the turbulence is sufficient to overcome buoyant rise. A mixed-layer model can also be used to model frazil ice in the upper layer of a lake or the ocean (Jones and Wells, 2018). Under this assumption (2.3) becomes,

$$\frac{\partial n_i}{\partial t} = \begin{cases} -\Gamma_i n_i + \dot{N}_I + \sum_{j=2}^{N} \alpha_{ji} n_j - f_i n_i, & i = 1, \\ -\Gamma_i n_i + \Gamma_{i-1} n_{i-1} - \beta_{i1} n_i - f_i n_i + F_{i-1} n_{i-1}, & 2 \leq i \leq N-1, \\ +\Gamma_{i-1} n_{i-1} - \beta_{i1} n_i + F_{i-1} n_{i-1}, & i = N, \end{cases} \quad (3.1)$$

where as in (2.3), $-\Gamma_i$ corresponds to the growth rate out of size class i and Γ_{i-1} corresponds to the growth rate into size class i from the size class below, $\dot{N}_I$ is the primary and secondary nucleation rate of crystals into size class, α_{ji} is the rate at which crystals are added to size class 1 due to collisions involving size crystals of size class j, f_j is the rate at which crystals are removed from size class i by flocculation, β_{i1} is the rate at which crystals are removed from size class i by nucleation and F_{i-1} is the rate at which crystals are added to size class i by flocculation of crystals of size class $i-1$.

Variable	Symbol	Value/Equation	Units
Salinity expansion coefficient	β_S	7.86×10^{-4}	psu^{-1}
Temperature expansion coefficient	β_T	3.87×10^{-5}	$^o\text{C}^{-1}$
Latent heat of ice fusion	$\mathcal{L}$	3.35×10^5	J kg^{-1}
Reference density	ρ_0	1030	kg m^{-3}
Density of ice	ρ_I	920	kg m^{-3}
Density of water	ρ_w	(3.12)	kg m^{-3}
Specific heat capacity	c_w	3974	$\text{J kg}^{-1}\,^o\text{C}^{-1}$
Thermal conductivity	k_l	0.512	$\text{W m}^{-1}\,^o\text{C}^{-1}$
Nusselt number	Nu	1	
Reference salinity	S_0	34.5	psu
Reference temperature	T_0	-2	^{o}C
Freezing temperature	T_f	(3.3)	^{o}C
Kinematic viscosity	ν	1.95×10^{-6}	$\text{m}^2\,\text{s}^{-1}$

Table 3.1: Constants used in our frazil ice model. All values are the same as those used in Holland and Feltham (2005), but are listed here for ease of reference.

3.2.1 Method to parametrise crystal growth, seeding and collisions

We now discuss the choices to parametrise crystal growth, seeding, rise (which is used to calculate the collision frequency) and nucleation.

3.2.1.1 Crystal growth

In §2.3.1 we noted that the most complete parametrisation to date for crystal growth yields (Rees Jones and Wells, 2015)

$$\Gamma_i = \frac{1}{V_{i+1} - V_i}\left[\frac{2\pi Nu\, k_l(T_f - T)}{\rho_I \mathcal{L}}\right]\frac{r_i}{0.9008 - 0.2634\ln[w_i/(2r_i)]}. \tag{3.2}$$

Following Holland and Feltham (2005), we set

$$T_f = -0.0573S + 0.0832, \tag{3.3}$$

with the salinity S given in psu and the choices for Nu, k_l, ρ_I and $\mathcal{L}$ listed in Table 3.1.

3.2.1.2 Crystal seeding

We now discuss the choice for the primary nucleation rate (the crystal seeding rate). McFarlane et al. (2015) notes that additional seeding is likely to occur from

frost that forms in the cold room refrigeration system, but there is no method to calculate this seeding rate (McFarlane et al., 2015). Hence, for simplicity and in line with Holland and Feltham (2005), Svensson and Omstedt (1994), and Wang and Doering (2005) we set $\dot{N}_I = 0$ neglecting primary nucleation other than via the initial condition on n_i. When the concentration of frazil ice is large, secondary nucleation is likely to be the dominant source of nuclei (McFarlane et al., 2015) instead of seeding. Therefore, we initialise our simulation at the minimum observed temperature in the data of McFarlane et al. (2015) and Schneck et al. (2019), when the crystal concentration is already around one crystal per centimetre cubed and uncertainties due to the parametrisation of seeding are likely to be less significant.

3.2.1.3 Secondary nucleation and flocculation

To obtain an expression for secondary nucleation we combine (2.36) and (2.41),

$$V\alpha_{ji}n_j = \mathcal{F}_{coll,j}, \tag{3.4}$$

$$V\beta_{i1}n_i = \frac{V_1}{V_i}\mathcal{F}_{coll,i}. \tag{3.5}$$

where, $\mathcal{F}_{coll,i} = V\sum_{k=1}^{N} f_{coll,ik}n_i$ denotes the total collision frequency of crystals of size class i.

Improving parametrisations for flocculation and secondary nucleation will be the focus of this thesis. We will compare the improved parametrisations with the parametrisation for flocculation and secondary nucleation in Holland and Feltham (2005), where

$$\mathcal{F}_{coll,j} = V\pi(r_j^e)^2\overline{n}n_j\sqrt{v_{j,g}^2 + 4\epsilon/(15\nu)(r_j^e)^2}, \tag{3.6}$$

$$f_i = 0, \tag{3.7}$$

$$F_i = 0. \tag{3.8}$$

The choice for $v_{j,g}$ is discussed below.

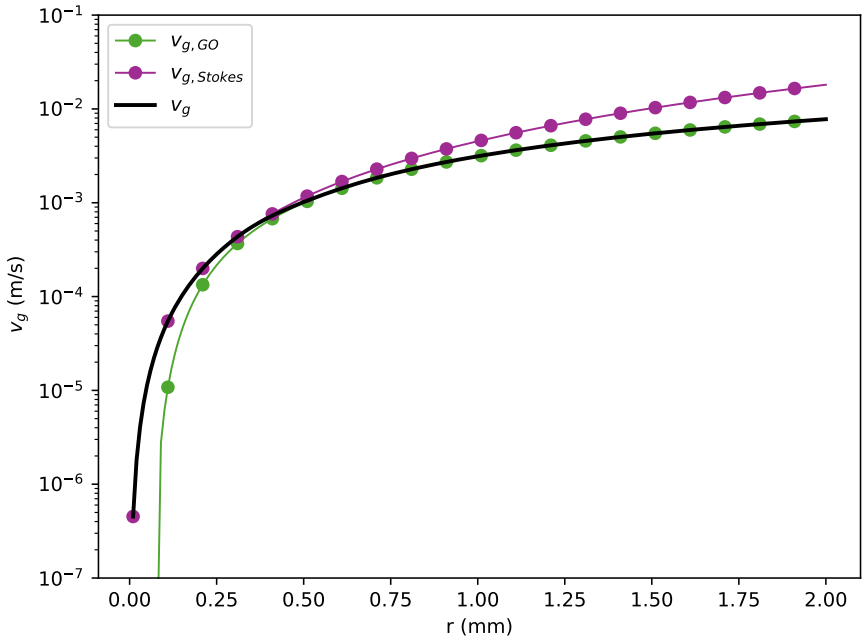

Figure 3.1: The rise velocity (black line) is calculated using a combination of the velocity obtained assuming Stokes flow (purple line) when $Re_p < 0.01$ and non-linear drag (green line) for $Re_p > 1$, with (3.9) used to switch between the two velocity profiles.

3.2.1.4 Crystal rise velocity

As there is no compelling reason to choose a particular parametrisation for the rise velocity, we use a slightly modified version of the rise velocity obtained by Holland and Feltham (2005) which allows us to compare our model to their mixed-layer model. In Holland and Feltham (2005), the rise velocity for each size class is calculated using an iterative approach to solve (2.15) using the crystal drag coefficient found by Gosink and Osterkamp (1983). For small crystals the resulting velocity leads to a particle Reynolds number much smaller than one. As the crystal drag coefficient in Gosink and Osterkamp (1983) is only found for $1 < Re_p < 100$, we use the Stokes flow solution, $\beta C_D = 32/Re_p$, found by Manohar (1936) to obtain the velocity for $Re_p < 0.01$. In line with Holland and Feltham (2005), to calculate Re_p, we set $\nu = 1.95 \times 10^{-6}$ m^2 s^{-1} and $\rho_I = 920$ kg m^{-3}. The solution obtained using the method in Holland and Feltham (2005) is denoted $v_{g,GO}$ and the velocity obtained assuming Stokes flow, $v_{g,Stokes}$. To transition between the two solutions we set $v_g = v_{g,GO} f[\ln(Re_p)] + v_{g,Stokes}\{1 - f[\ln(Re_p)]\}$

for $Re_p = 2rv_{g,GO}/\nu$, where the switching function,

$$f(x) = \begin{cases} 0, & x \leq x_{min}, \\ \frac{(x-x_{min})^2}{(x-x_{min})^2+(x_{max}-x)^2}, & x_{min} < x < x_{max}, \\ 1, & x \geq x_{max}, \end{cases} \tag{3.9}$$

with $x_{min} = \ln(0.1)$ and $x_{max} = \ln(1)$.

The smallest crystals ($r = 0.01$ mm) have a rise velocity of 4.5×10^{-7} m s^{-1} and the largest crystals ($r = 2$ mm) have a rise velocity of 7.8×10^{-3} m s^{-1}. The rise velocity is plotted in Figure 3.1. The transition between $v_{g,Stokes}$ and $v_{g,GO}$ occurs at $r \sim 0.4$ mm.

3.2.2 Heat flux

As the frazil ice crystals grow, they will introduce an additional heat flux into the water. The water temperature changes as,

$$\frac{dT}{dt} = \left.\frac{dT}{dt}\right|_{cooling} + \frac{\rho_I \mathcal{L}}{V \rho c_w} \frac{dV_{frazil}}{dt} \tag{3.10}$$

where $dT/dt|_{cooling}$ is the temperature change due to cooling from the atmosphere, V is the volume, c_w is the specific heat capacity listed in Table 3.1, and dV_{frazil}/dt is the growth rate of the frazil ice crystals. Using (2.4) we find,

$$\frac{dV_{frazil}}{dt} = \sum_{i=1}^{N} \frac{Nuk_l}{\rho_I \mathcal{L}} (T_f - T) 2\pi \left\{ \frac{N_i r_i}{0.9008 - 0.2634 \ln[w_i/(2r_i)]} \right\}. \tag{3.11}$$

where N_i is the number of crystals of size class i and as in §3.2.1.1 we have used the parametrisation for A_F/l suggested by Rees Jones and Wells (2015).

The density depends on the temperature T and salinity S of the water (Holland and Feltham, 2005),

$$\rho = \rho_0[1 + \beta_S(S - S_0) - \beta_T(T - T_0)] \tag{3.12}$$

with ρ_0, β_S, S_0, β_T and T_0 listed in Table 3.1. We shall test the mixed-layer model against the freshwater results of Schneck et al. (2019) and therefore there is no salt flux.

3.3 Simple frazil ice model

To isolate the effect of changes made to model of crystal collisions, we simplify the model in §3.2 so that the crystal size distribution is only modified by secondary nucleation, such that (3.1) becomes,

$$V\frac{\mathrm{d}n_i}{\mathrm{d}t} = \begin{cases} \sum_{j=2}^{N} \mathcal{F}_{coll,j}, & i = 1, \\ -\frac{V_1}{V_i}\mathcal{F}_{coll,i}, & 2 \leq i \leq N. \end{cases} \tag{3.13}$$

3.4 Initial conditions

In line with the model described in Holland and Feltham (2005), all the crystals have the same aspect ratio of $d = 50$, with crystals in the smallest size class having a radius of 0.01mm and crystals in the largest size class having a radius of 2mm.

One accurate model of crystal size redistribution by fracture treats the difference in volume between each size class as V_1, such that $V_n = 2\pi r_n^3/d = nV_1 = 2n\pi r_1^3/d$ and $r_n = n^{1/3}r_1$. For $0.01 \leq r_i \leq 2$ mm this would require 8×10^6 size classes, which would lead to impractical run times. Instead we initialise with 200 size classes. This allows us to capture the behaviour of the model under each change, whilst keeping the run time sensible. We choose three different initial conditions for the distribution of crystals. In the first case we follow the approach in Holland and Feltham (2005) and use a logarithmic spacing in radial space between size classes. The initial volume concentration of crystals in each size class is a uniform value of 0.0016. In the other cases we initialise with a uniform spacing in radial space between size classes. In one case we initialise with the same number of crystals in each size class and in the other case initialise with the same volume concentration of crystals in each size class.

The initial mean crystal radius changes depending on the choice of initial condition, as does the initial total number density of crystals. This means that the initial collision rate is likely to differ between models, with the rate being the highest when the crystals are logarithmically spaced as $\sum_i n_i$ is largest. The values

Model	Radial Spacing	Distribution	$\overline{r}$ (mm)	$\sum_i n_i$
1	linear	same number	1	6.4×10^6
2	linear	same concentration	0.014	7.8×10^{10}
3	logarithmic	same concentration	0.015	8.4×10^{11}

Table 3.2: Initial total number density of crystals $\sum_i n_i$ and mean crystal radius $\overline{r}$ in each of the different model setups. Crystals are either initialised with the same number of crystals in each size class in which case the distribution is 'same number' or the same concentration in which case the distribution is 'same concentration'.

for the initial mean radius and the initial number density $\sum_i n_i$ of crystals are given in Table 3.2. The mean radius is much smaller when the crystals are initialised with the same concentration in each size class.

Qualitatively we expect the changes to the collision kernel to have the same effect on the model behaviour, independently of how the radii bins are chosen. Therefore, choosing the different discretisation method for the radii, allows us to test the robustness of the model. Initiating with a linear radial spacing and uniform number of crystals allows easy physical interpretation of the changes.

When we use the simple model in §4-§8. In order to capture the effects on the behaviour in quiescent and turbulent flow we will let the kinetic energy dissipation rate ϵ vary between $10^{-8}\,\mathrm{m^2 s^{-3}}$ and $10^{-2}\ \mathrm{m^2 s^{-3}}$.

3.5 Example model result

We now illustrate the behaviour of the mixed-layer model described in §3.2 and the simple model described in §3.3. We initialise with the initial conditions described in §3.4. We use the turbulent kinetic energy dissipation rate, $\epsilon = 0.034\ \mathrm{m^2 s^{-3}}$, measured by McFarlane et al. (2015) for the tank also used by Schneck et al. (2019). We take the measured initial concentration when the temperature was a minimum in the zero salinity ($S = 0$) experiment of Schneck et al. (2019). This gives an initial supercooling of $-0.085\ ^o\mathrm{C}$, and 6.3×10^6 crystals per metre cubed with a mean radius of 0.66 millimetres. Schneck et al. (2019) reported a lognormal distribution

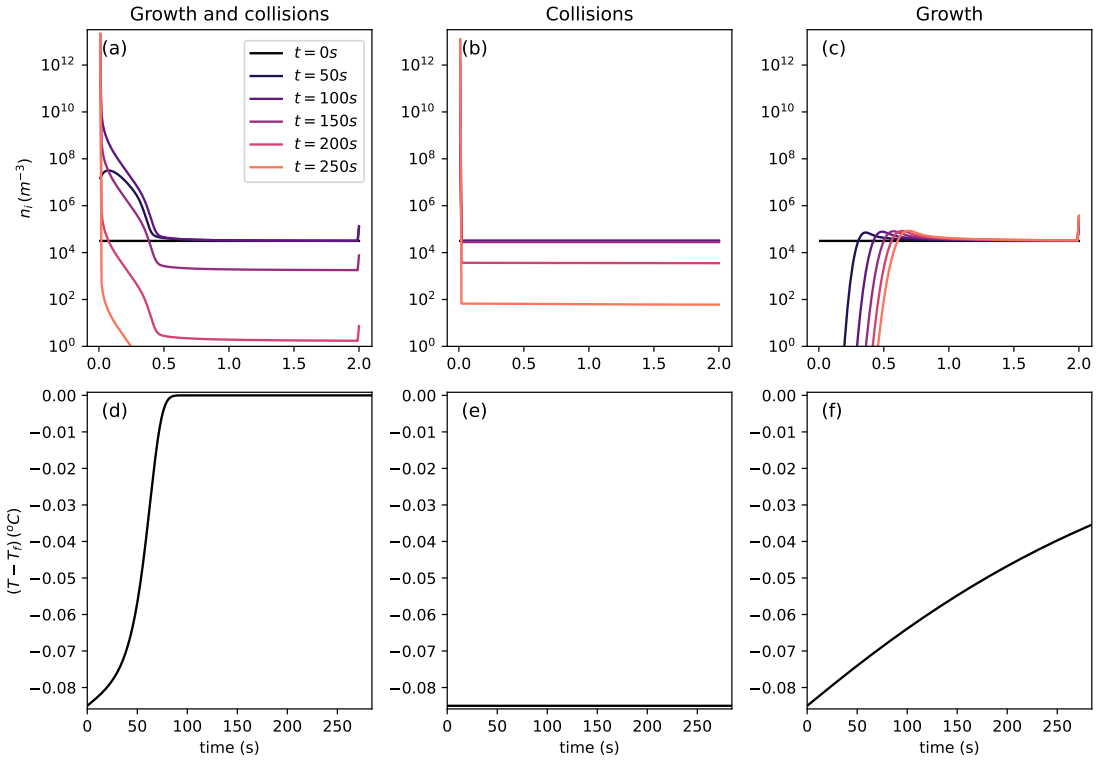

Figure 3.2: The change in crystal population and temperature for a frazil model run with the initial conditions described in §3.5 and §3.4. Panels a, b and c illustrate the change in number density in crystals of size class i with the coloured lines corresponding to number density of crystals in each size class at $t = [0, 50, 100, 150, 200, 250]$ s. Panels d, e and f are the change in temperature. In the first column (a and d) we use the full mixed-layer model described in §3.2. In the second column (b and e) we only allow the population to change by collisions and use the simple model described in §3.3. In the third column (c and f) we only allow the population to change by growth.

of crystals, but for simplicity and to clearly illustrate the behaviour of the model we choose to initialise with the radii linearly spaced and $N_i = 6.3 \times 10^6/N$ in each size class. This gives an initial mean radius of 1 mm, whilst the other initial conditions described in §3.4 have a much smaller mean radius. The number of size classes, N, is 200. Schneck et al. (2019) report an atmospheric cooling rate $dT/dt|_{cooling} \approx 2 \times 10^{-4}$ K s^{-1}. However, for simplicity, we set $dT/dt|_{cooling} = 0$ in this example.

We run three versions of the mixed-layer model. In the first version (panels a and d in Figure 3.2 and the solid lines in Figure 3.3) we use the full mixed-layer

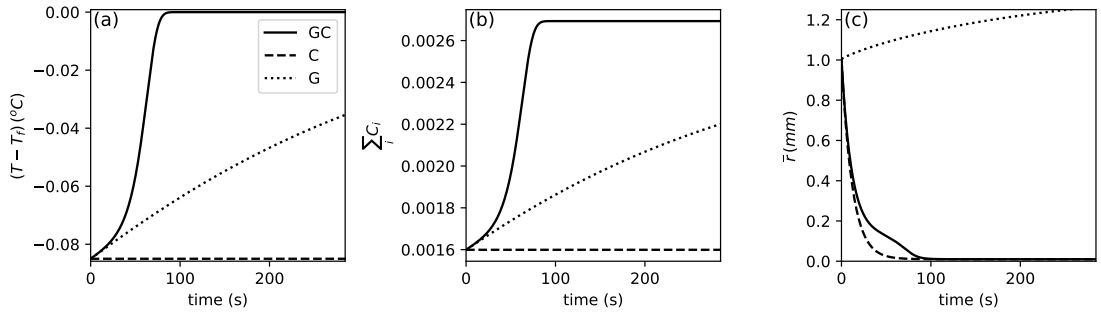

Figure 3.3: The change in temperature (panel a), total frazil ice concentration (panel b) and mean crystal radius (panel c) for frazil models run with the initial conditions described in §3.5 and §3.4. The solid lines are for data obtained using the full mixed-layer model described in §3.2 where growth and collisions (GC) are included. The dashed lines are for data obtained using the simple model described in §3.3 where the population only changes by collisions (C). The dotted lines are for data obtained using using the full mixed-layer model described in §3.2 but the population only changes by growth (G).

models where the crystal population evolves due to crystal growth and collisions. In the second version (panels b and e in Figure 3.2 and the dashed lines in Figure 3.3) we only allow the crystal population to evolve due to collisions (this is the same as using the simple model described in §3.3). In the third version (panels c and f in Figure 3.2 and the dotted lines in Figure 3.3) we only allow the crystal population to evolve due to crystal growth.

Figures 3.2 and 3.3 show that the models produce very different results, illustrating the importance of each of these processes. First, we note in Figure 3.2b that collisions act to decrease the number of crystals in all but the smallest size class (size class 1) such that the mean crystal radius approaches r_1, the radius of the crystals in size class 1 (see Figure 3.3c). In contrast, crystal growth acts to decrease the number of crystals in the smaller size classes (see Figure 3.2c). The total concentration trajectory Figure 3.3b follows the temperature Figure 3.3a because the temperature here is entirely controlled by latent heat release from ice growth. Therefore, collisions do not change the overall concentration of the frazil ice, whilst growth increases the concentration.

Figure 3.3c shows that the radius of the crystal population in the full mixed model mainly changes due to collisions (the solid line closely follows the dashed line). Once the supercooling is relieved the crystal population eventually becomes dominantly composed of crystals of the smallest size class as there is hardly any more growth into the larger size classes. There is a period of time between about 20 and 80 seconds where crystal growth acts to slow down the rate at which the number of crystals in size class one increases. Here, crystals grow to relieve the supercooling and the mean radius decreases at a slower rate than in the case with just collisions.

Comparing the temperature difference in Figure 3.3a we see that initially the supercooling is relived at similar rates when only growth is included and when the full mixed-layer model is used. The supercooling stays constant when growth is not included. When the full mixed-layer model is used, the supercooling approaches zero substantially faster than in the case when just growth is included (where it does not reach zero in the time plotted). This indicates significant interactions between crystal size redistribution and growth. In the experiment of Schneck et al. (2019) the supercooling was halved in approximately 110 seconds, about twice as slow as in the model run with the full mixed-layer model and twice as fast as in the model run only including growth. However, in our model we did not include cooling from the atmosphere or initialise with the correct crystal size distribution so we would not expect a perfect match with the experimental data. Comparing the mean crystal radius in Figure 3.3c we see that the mean radius increases when just growth is included, whilst the mean radius decreases when collisions occur. The decrease in radius due to collisions corresponds to a large number of crystals being produced, and therefore, the total surface area of frazil ice increasing. This increases the total growth rate of frazil ice leading to the temperature increasing faster when growth and collisions are included.

3.6 Overview

In this chapter we first in introduced a frazil ice model for a mixed-layer §3.2 where the frazil ice population changes due to growth and collisions. This model can be used to compare with the experimental results of McFarlane et al. (2015) and Schneck et al. (2019), and is also applicable to the upper, approximately well mixed, layer of a lake or the ocean. In §3.3 we then simplified the model to only include secondary nucleation. Both models use the parameters from the model of Holland and Feltham (2005) but also include a modification to the rise velocity to account for the particle Reynolds number being less than 1 when the crystals are small. There is uncertainly over the choice of method used to parametrise crystal rise and seeding (Souillé et al., 2023) and more future experimental observations is needed to reduce the uncertainty in these parametrisations. Due to computational limitations, we are also limited in the number of size classes we can use in our model. This means that some processes such as secondary nucleation carry discretisation error because the difference in volume between each size class is not equal to the crystal volume. In §3.5 we then demonstrated how the model behaves for conditions close to those in the freshwater experiment of Schneck et al. (2019) using a typical past parametrisation (Holland and Feltham, 2005) of secondary nucleation. Crystal growth increased the mean crystal size and relieved the supercooling. Crystal collisions enhanced the rate of temperature change when interacting with crystal growth and led to a decrease in the mean crystal size. In the following chapters we make improvements to the parametrisation of secondary nucleation. In §4-§8 these changes shall be implemented into the simple model to give us an understanding of the effect of each change before finally being implemented into the mixed-layer model in §9.

As I looked at the living creatures, I saw a wheel on the ground beside each creature with its four faces. This was the appearance and structure of the wheels: They sparkled like topaz, and all four looked alike. Each appeared to be made like a wheel intersecting a wheel. As they moved, they would go in any one of the four directions the creatures faced; the wheels did not change direction as the creatures went. Their rims were high and awesome, and all four rims were full of eyes all around.

— Ezekiel 1:15-18 NIV

4

Inclusion of differential size and a new expression to calculate the relative velocity

Contents

4.1 Introduction

Having introduced a simple frazil ice model to test the effects of our changes to how crystal collisions are parametrised, we now address the first of the concerns described in §2. Current frazil ice models do not correctly calculate the relative

velocity between crystals of different size classes. Further, when calculating the collision frequency of crystals of size class i, current frazil ice models assume that all crystals in the other size classes can be modelled as point-like particles.

In §4.2 we use the Maxey-Riley equation to derive an expression for the relative velocity between particles. In §4.3 we then allow both colliding size classes to contribute to the collision radius and particle separation. Finally, we obtain a new collision frequency, which neglects the assumption of point-like particles and gives an improved estimate for the particle relative velocities. We discuss the implications of the new model in §4.4.

We begin by deriving an expression for the relative velocity between particles of arbitrary size classes separated by a distance corresponding to their collision radius, $r_{c,ij}$.

4.2 Relative velocity

The relative velocity between two particles i and j at positions $\mathbf{r}_i$ and $\mathbf{r}_j$ is given by,

$$\mathbf{w}_{ij}(\mathbf{r}, t) = \mathbf{u}_{pi}(\mathbf{r}_i, t) - \mathbf{u}_{pj}(\mathbf{r}_j, t), \tag{4.1}$$

where $\mathbf{u}_{pi}$ is the velocity of particle i and $\mathbf{r} = \mathbf{r}_i - \mathbf{r}_j$. The relative radial velocity is given by,

$$w_{ij,r}(\mathbf{r}, t) = \mathbf{u}_{pi}(\mathbf{r}_i, t) \cdot \hat{\mathbf{r}} - \mathbf{u}_{pj}(\mathbf{r}_j, t) \cdot \hat{\mathbf{r}}, \tag{4.2}$$

where $\hat{\mathbf{r}} = \mathbf{r}/|\mathbf{r}|$. Therefore, to solve for the mean relative velocity between particles, we need to solve for the individual particle velocities.

4.2.1 Solution for the individual particle velocity

The equation of motion for a particle of density ρ_p (where for ice particles $\rho_p = \rho_I$) and volume V_p travelling with velocity $\mathbf{u}_p$ through a fluid with density ρ and velocity

u in the presence of other particles is given by (Poole et al., 2005),

$$\rho_p V_p \frac{\mathrm{d}\mathbf{u}_p}{\mathrm{d}t} = \mathbf{F}^g + \mathbf{F}^d + \mathbf{F}^i + \mathbf{F}^a + \mathbf{F}^B + \mathbf{F}^F + \mathbf{F}^\omega + \mathbf{F}^{LM} + \mathbf{F}^{PI}, \tag{4.3}$$

where the forces (**F** with superscripts) and the particle velocity depend on the position and time. The superscripts identify contributions to the force on the particle as follows: g is the force due to gravity; d is the viscous drag force; i is the inertial force due to the carrier fluid acceleration (or the gradient of the pressure and shear stress); a is the added mass force; B is the Basset (history) force which accounts for the additional drag force arising due to the development of a boundary layer or viscous flow during a transient acceleration of the particle (Poole et al., 2005); F is the Faxén correction to the viscous drag which accounts for the effects of non-uniform flow (Dolata and Zia, 2021); ω is the shear-induced lift force; LM is the Magnus lift force; PI is the force due to particle interactions. See Poole et al. (2005) for discussion of their origin.

In the limit when the particle Reynolds number is small,

$$\mathbf{F}^d = \frac{\rho V_p}{\tau_p}(\mathbf{u} - \mathbf{u}_p), \tag{4.4}$$

where τ_p is the particle relaxation time.

We can relate this to the expression for the drag force (2.11) in §2.3.3 by equating the two expressions for the drag force. Assuming $|\mathbf{u}_p| \approx v_g$ and $\mathbf{u} = 0$, such that $Re_p \approx 2rv_g/\nu$, we find,

$$\tau_p = \frac{2V_p}{r\nu}\frac{1}{\beta C_D Re_p} = \frac{v_g}{g}\left(1 - \frac{\rho_I}{\rho}\right)^{-1}. \tag{4.5}$$

where β and C_D were defined in §2.3.3, r is the crystal radius, g is the acceleration due to gravity, ν is the kinematic viscosity and v_g is the buoyant rise velocity.

Equation (4.3) can be simplified if the Kolmogorov lengthscale η_K of the fluid is larger than the size of the particle and if the ratio of the particle relaxation time to

the timescale τ_f of the fluid motion (defined as the Stokes number $St = \tau_p/\tau_f$) is small.

For conditions under which frazil ice forms, the Kolmogorov lengthscale of the fluid is roughly of order 10^{-3} m (Steinberg et al., 2021). This is approximately the lengthscale of the largest frazil ice crystals. Assuming τ_f is given by the Kolmogorov timescale, we estimate τ_p, using the combined rise velocity found in §3.4. Figure 4.1 plots the Stokes number, St for the range of expected values of the turbulent kinetic energy dissipation rate where frazil ice forms. When $St < 1$, the particle closely follows the fluid. When $St > 1$, the particle velocity lags the fluid velocity. For frazil ice, $St < 1$ in all cases (see Figure 4.1) and the maximum particle size is $\sim \eta_K$.

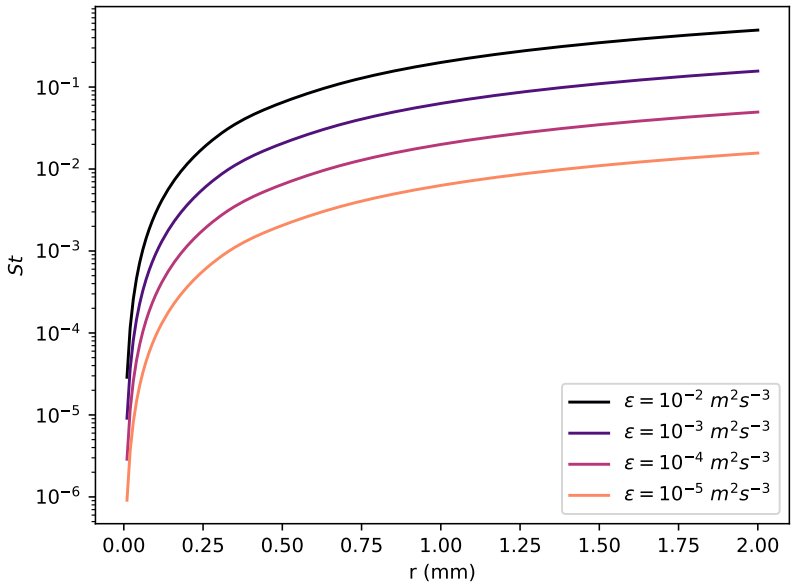

Figure 4.1: Stokes number for $\tau_f = \sqrt{\nu/\epsilon}$ and τ_p calculated using (4.5) with $d = 50$, and the combined rise velocity found in in §3.4.

In the limit when the particle is much smaller than the Kolmogorov lengthscale of the fluid $[r \ll (\nu^3/\epsilon)^{1/4}]$, the particle relaxation time τ_p is smaller than the timescale,

τ_f of the fluid motion (Eames and Gilbertson, 2004), and particle interactions are negligible, we can approximate (4.3) to

$$\rho_p V_p \frac{d\mathbf{u}_p}{dt} \approx \mathbf{F}^g + \mathbf{F}^d + \mathbf{F}^i + \mathbf{F}^a. \tag{4.6}$$

For frazil ice most frazil crystals satisfy this approximation except for the largest which are on the limit of the validity of this approximation. We therefore use (4.6) to make analytical headway into improving the parametrisation for the particle velocity. Dividing by the mass of the particle and including the expressions for the forces (Maxey and Riley, 1983) we obtain,

$$\frac{\mathrm{d}\mathbf{u}_p}{\mathrm{d}t} = -\left(1 - \frac{\rho}{\rho_p}\right) g\hat{\mathbf{z}} + \frac{\rho}{\rho_p}\frac{(\mathbf{u} - \mathbf{u}_p)}{\tau_p} + \frac{\rho}{\rho_p}\frac{\mathrm{D}\mathbf{u}}{\mathrm{D}t} + C_{add}\frac{\rho}{\rho_p}\left[\frac{\mathrm{D}\mathbf{u}}{\mathrm{D}t} - \frac{\mathrm{d}\mathbf{u}_p}{\mathrm{d}t}\right], \tag{4.7}$$

where C_{add} is the added mass coefficient and $D\mathbf{u}/Dt = \partial\mathbf{u}/\partial t + (\mathbf{u}\cdot\nabla)\mathbf{u}$.

We can rewrite (4.7) in the form,

$$\frac{\mathrm{d}\mathbf{u}_p}{\mathrm{d}t} = \frac{\mathbf{u} - \mathbf{u}_p}{\tau_p^*} + b_p^* g\hat{\mathbf{z}} + A_p\frac{\mathrm{D}\mathbf{u}}{\mathrm{D}t}. \tag{4.8}$$

where,

$$\tau_p^* = \tau_p\left(\frac{\rho_p}{\rho} + C_{add}\right), \qquad b_p^* = -\frac{\rho_p - \rho}{\rho_p + C_{add}\rho}, \quad A_p = \frac{\rho + \rho C_{add}}{\rho_p + \rho C_{add}}. \tag{4.9}$$

Integrating gives (Zaichik and Alipchenkov, 2010),

$$\mathbf{u}_p(\mathbf{r},t) = \frac{1}{\tau_p^*}\int_{-\infty}^{t}\left\{\mathbf{u}[\mathbf{r}(t'),t'] + \tau_p^* A_p\frac{\mathrm{D}\mathbf{u}[\mathbf{r}(t'),t']}{\mathrm{D}t}\right\}\exp\left[(t'-t)/\tau_p^*\right]dt' + \tau_p^* b_p^* g\hat{\mathbf{z}}, \tag{4.10}$$

which can be simplified by integrating the $\mathrm{D}\mathbf{u}/\mathrm{D}t$ term by parts to (Nguyen et al., 2016),

$$\mathbf{u}_p(\mathbf{r},t) = A_p\mathbf{u}(t) + \frac{(1-A_p)}{\tau_p^*}\int_{-\infty}^{t}\mathbf{u}(\mathbf{r}(t'),t')\exp\left[(t'-t)/\tau_p^*\right]dt' + \tau_p^* b_p^* g\hat{\mathbf{z}}, \tag{4.11}$$

giving an equation for the particle velocity. In §4.2.3 we use this expression to obtain an expression for the relative velocity of two frazil ice crystal separated by a distance $r_{c,ij}$. However, first we will discuss how the relative velocity currently used in frazil ice models can be obtained from (4.11). This emphasises the difference in our approach and the weakness of the current expression for the relative velocity.

4.2.2 Method used to obtain the relative velocity in previous frazil ice models

In §2.3.3 we noted that the relative velocity currently used in frazil models is a combination of the velocity due to gravitational settling v_g and the relative velocity from turbulent motion w_{turb}. In order to obtain the expression used for v_g and w_{turb} in frazil ice we take limits of (4.11), setting $\mathbf{u} = 0$ and $\tau_p^* b_p^* g = A_p = 0$ to obtain v_g and w_{turb} respectively. As was noted in §2.3.4 the relative velocity in frazil ice models is then obtained by linearly or quadratically combining the average component of the velocity due to buoyant rise and the component of the velocity due to turbulence. However, (4.7) allows us to solve for $\mathbf{u}_p$ simultaneously considering the component of the velocity due to buoyant rise and the component of the velocity due to turbulence, demonstrating one weakness of the current approach.

4.2.2.1 Expression for gravitational rise speed v_g

In quiescent flow ($\mathbf{u} = 0$), we obtain from (4.11) the gravitational rise velocity,

$$\mathbf{u}_p = \tau_p^* b_p^* g \hat{\mathbf{z}}. \tag{4.12}$$

For a crystal of size class i, the rise velocity is given by $v_{i,g} = \tau_{pi}^* b_p^* g$. The scaled particle relaxation timescale τ_{pi}^* for a crystal of size class i, can be found using the expressions for βC_D outlined in §2.3.3 for particles of size class i. Frazil ice models typically assume $w_{ij,g} = v_{i,g}$. However, as noted in (4.1) and (4.2), in the limit when $\mathbf{u} = 0$ the relative velocity should be the difference in rise velocity between two particles of size class i and j, $w_{ij,g} = |v_{i,g} - v_{j,g}|$, and not the rise velocity of a single particle.

4.2.2.2 Expression for w_{turb}

The expression for w_{turb} used in typical frazil ice models (Heorton et al., 2017; Holland and Feltham, 2005; Jones and Wells, 2018; Smedsrud, 2002; Smedsrud and Jenkins, 2004; Souillé et al., 2020; Svensson and Omstedt, 1994; Wang and Doering, 2005; Yang et al., 2023) can be obtained from (4.11) by assuming A_p (4.9) and

$\tau_p^* b_p^* g$ are negligible and $\tau_p^* \to 0$. However, for frazil ice, $\rho \sim \rho_I$, so the assumption of $A_p \ll 1$ is not valid which is a further weakness of frazil ice models.

Neglecting A_p and $\tau_p^* b_p^* g$, (4.11) reduces to,

$$\mathbf{u}_p(\mathbf{r}, t) = \frac{1}{\tau_p^*} \int_{-\infty}^{t} \mathbf{u}(x(t'), t') \exp\left[(t' - t)/\tau_p^*\right] dt'. \tag{4.13}$$

In order to obtain w_{turb}, typical (Heorton et al., 2017; Holland and Feltham, 2005; Jones and Wells, 2018; Smedsrud, 2002; Smedsrud and Jenkins, 2004; Souillé et al., 2020; Svensson and Omstedt, 1994; Wang and Doering, 2005; Yang et al., 2023) frazil ice models consider two particles separated by a distance $2r_{c,i}$, where $r_{c,i}$ is the contribution to the collision radius from a particle of size class i, and calculate the covariance of the particle velocities in the direction corresponding to their separation vector (the covariance of the longitudinal velocity component). This corresponds to the variance of the relative particle velocity at a distance equal to the collision radius if both particles are of the same size class, $r_{c,ii} = 2r_{c,i}$. We orientate our coordinate system such that the separation vector is in the $\hat{\mathbf{i}}$-direction, $\hat{\mathbf{r}} = \hat{\mathbf{i}}$, and denoting the $\hat{\mathbf{i}}$ component of the particle velocity as the radial component $u_{p,r}$, we calculate,

$$\langle u_{p,r}(\mathbf{x}) - u_{p,r}(\mathbf{x}+2\mathbf{r}_{c,i})\rangle^2 = \langle [u_{p,r}(\mathbf{x})]^2\rangle + \langle [(u_{p,r}(\mathbf{x}+2\mathbf{r}_{c,i})]^2\rangle - 2\langle u_{p,r}(\mathbf{x}) u_{p,r}(\mathbf{x}+2\mathbf{r}_{c,i})\rangle. \tag{4.14}$$

In the limit where $\tau_p^* \to 0$, (4.13) reduces to $\mathbf{u}_p = \mathbf{u}$ as the particle perfectly follows the flow. Therefore, we use the fluid velocity correlation assuming statistical homogeneity, $R_{lm}(\mathbf{r}) = \langle u_l(\mathbf{x}+\mathbf{r}) u_m(\mathbf{x})\rangle$, to work out the particle correlation. Here, u_l denotes the l-component of the fluid velocity. For the longitudinal particle velocity correlation,

$$\langle u_{p,r}(\mathbf{x}) - u_{p,r}(\mathbf{x}+2\mathbf{r})\rangle^2 = \langle [u_r(\mathbf{x})]^2\rangle + \langle [(u_r(\mathbf{x}+2\mathbf{r})]^2\rangle - 2\langle u_r(\mathbf{x}) u_r(\mathbf{x}+2\mathbf{r})\rangle, \tag{4.15}$$

$$= R_{11}(0) + R_{11}(0) - 2R_{11}(2r). \tag{4.16}$$

In the limit of small particles with radius much less than the Kolmogorov micro-scale, $R_{11}(r) = u'^2[1 - \epsilon r^2/(30\nu u'^2)]$ (Ayala et al., 2008) where $u'^2 = \langle \mathbf{u}^2 \rangle$ and ϵ is the

turbulent kinetic energy dissipation rate. Therefore,

$$w_{turb}^2 = \langle [w_r(2r)]^2 \rangle = \langle u_{p,r}(\mathbf{x}) - u_{p,r}(\mathbf{x}+2\mathbf{r}) \rangle^2 = \frac{4\epsilon r^2}{15\nu}, \tag{4.17}$$

which is the same result obtained by Saffman and Turner (1956). Therefore, for two crystals of size class i colliding, $w_{i,turb}^2 = 4\epsilon r_{c,i}^2/(15\nu)$.

4.2.2.3 Aside: the mean radial velocity

Finally, a further weakness of the current method used to obtain the relative velocity in frazil ice models is that frazil ice models use $\langle w_{turb,r}^2 \rangle$ to calculate the mean relative velocity due to turbulent fluctuations. As noted in §2.5, when using the cylindrical approximation, it would be more appropriate to use $\langle |\mathbf{w}_{turb}| \rangle$ instead of $\langle w_{turb,r}^2 \rangle$ to calculate the mean relative velocity due to turbulent fluctuations. Applying the same method as outlined in §4.2.2.2 but instead calculating $\langle |\mathbf{w}(r)| \rangle$ gives,

$$\langle |\mathbf{w}(r)| \rangle = \left(\sqrt{\frac{2}{\pi}} + \sqrt{\frac{\pi}{2}} \right) \sqrt{\frac{r^2}{15\nu}} = \left(\sqrt{\frac{2}{\pi}} + \sqrt{\frac{\pi}{2}} \right) \sqrt{\langle [w_r(r)]^2 \rangle}. \tag{4.18}$$

(see Wang et al. (1998)). Therefore, if the mean relative velocity was used instead of the radial relative velocity, then the relative velocity due to turbulence would be roughly twice as large.

4.2.3 Calculation for the relative velocity

Having noted the weaknesses in the current approach used to obtain the relative velocity in frazil ice models, we now calculate a new expression for the relative velocity. We use (4.7) to solve for $\mathbf{u}_p$ simultaneously considering the component of the velocity due to buoyant rise and the component of the velocity due to turbulence. Given the higher accuracy of the spherical approximation, we calculate $\langle |w_{ij,r}| \rangle$ instead of $\langle |\mathbf{w}_{ij}| \rangle$.

Ayala et al. (2008) calculated $\langle |w_{ij,r}| \rangle$ for water droplets in clouds by solving (4.7) for $A_p \ll 1$. As for frazil ice we cannot neglect A_p we adapt the approach of Ayala et al. (2008), and combine the method with the approaches of Yuu (1984) and

Chan et al. (2023) who calculated $|\mathbf{w}_{ij}|$ for $b_p^* = 0$. We first outline the argument of Ayala et al. (2008) and argue how it can be extended to the case of finite A_p. Then we adapt the approach of Yuu (1984) and Chan et al. (2023) to calculate $\langle|w_{ij,r}|\rangle$ for $b_p^* = 0$. Finally, we derive a new expression for $\langle|w_{ij,r}|\rangle$.

4.2.3.1 Solution for $\langle|w_r|\rangle$ neglecting fluid acceleration ($A_p = 0$).

Following Ayala et al. (2008), when $A_p = 0$ (valid for $\rho \ll \rho_p$) for a particle of size class i, (4.11) reduces to,

$$\mathbf{u}_{pi}(\mathbf{r}_i, t) = \frac{1}{\tau_{pi}^*} \int_{-\infty}^{t} \mathbf{u}(\mathbf{x}(t'), t') \exp\left((t' - t)/\tau_{pi}^*\right) dt' + \tau_{pi}^* b_p^* g \hat{\mathbf{z}}. \tag{4.19}$$

Using the definition of the relative radial velocity (4.2), and defining

$$h_{ij}(\theta) = (\tau_{pi}^* - \tau_{pj}^*) b_p^* g \hat{\mathbf{z}} \cdot \hat{\mathbf{r}} = (\tau_{pi}^* - \tau_{pj}^*) b_p^* g \cos\theta, \tag{4.20}$$

$$\zeta_{ij}(\mathbf{r}, \theta, t) = \hat{\mathbf{r}} \cdot [\mathbf{u}_{pi}(\mathbf{r}_i, t) - \mathbf{u}_{pj}(\mathbf{r}_j, t)] - h_{ij}(\theta), \tag{4.21}$$

where θ is the angle from the z axis. We find that the relative radial velocity between particles of size class i and j separated by a distance r is given by,

$$w_{ij,r}(r, \theta, t) = \zeta_{ij}(r, \theta, t) + h_{ij}(\theta), \tag{4.22}$$

such that the relative velocity is split into a fluctuating component (with mean zero over time) due to turbulent fluctuations and a mean component due to buoyancy. The function $\zeta(r, \theta, t)$ can depend on θ due to the coupled impact of turbulent fluctuations and gravity on the motion of particles.

The mean absolute radial velocity at a specific angle is given by,

$$\langle|w_{ij,r}(r, \theta)|\rangle = \int_{-\infty}^{\infty} |w_{ij,r}(r, \theta)| P_{w_{ij,r}}(r, \theta) dw_{ij,r}, \tag{4.23}$$

(where we have also averaged over space and time assuming the system is homogenous and stationary). $P_{w_{ij,r}}(r, \theta)$ is the probability of the relative velocity at an angle θ and separation r being $w_{ij,r}(r, \theta)$ at a given instant in time.

It is common in collision models (e.g. Ayala et al. (2008), Dodin and Elperin (2002), Varaksin (2019), Wang et al. (2000b), and Zaichik et al. (2005)) to assume ζ_{ij} is normally distributed with standard deviation $\sigma_{ij}(r,\theta)$ such that the probability distribution $P_{w_{ij,r}}(r,\theta)$ can be written as,

$$P_{w_{ij,r}}(r,\theta) = \frac{1}{\sqrt{2\pi}\sigma_{ij}(r,\theta)} \exp\left(-\frac{[w_{ij,r}(r,\theta) - h_{ij}(\theta)]^2}{2\sigma_{ij}(r,\theta)^2}\right). \tag{4.24}$$

Integrating (4.23) gives,

$$\langle|w_{ij,r}(r,\theta)|\rangle = \sqrt{\frac{2}{\pi}}\sigma_{ij}(r,\theta)\exp\left[-\frac{h_{ij}(\theta)^2}{2\sigma_{ij}(r,\theta)^2}\right] + h_{ij}(\theta)\mathrm{Erf}\left[\frac{h_{ij}(\theta)}{\sqrt{2}\sigma_{ij}(r,\theta)}\right]. \tag{4.25}$$

To find the mean relative radial velocity we take the average integral over the surface of the collision sphere assuming a uniform distribution of pair density (Ayala et al., 2008),

$$\langle|w_{ij,r}(r)|\rangle = \frac{1}{2}\int_0^\pi \langle|w_{ij,r}(r,\theta)|\rangle \sin\theta d\theta = \int_0^{\pi/2} \langle|w_{ij,r}(r,\theta)|\rangle \sin\theta d\theta, \tag{4.26}$$

where we have used $|w_r(\pi-\theta)| = |w_r(\theta)|$ to obtain the second equation.

To obtain an expression for $\sigma_{ij}(r,\theta)$, we assume that the standard derivation of the relative velocity is independent of the angle between the separation vector and the z-axis, $\sigma_{ij}(r,\theta) = \sigma_{ij}(r)$ (valid when turbulence dominates buoyancy (Zaichik and Alipchenkov, 2003)). Under this assumption we integrate (4.26) using (4.25) for $\langle|w_{ij,r}(r,\theta)|\rangle$ to obtain the result of Dodin and Elperin (2002) neglecting fluid acceleration,

$$\langle|w_{ij,r}(r)|\rangle = \sqrt{\frac{2}{\pi}}\sigma_{ij}(r)\Bigg\{\frac{1}{2}\exp\left[-\frac{w_{ij,g}^2}{2\sigma_{ij}(r)^2}\right] + \frac{\sqrt{\pi}}{2}\left(\frac{w_{ij,g}}{\sqrt{2}\sigma_{ij}(r)} + \frac{\sigma_{ij}(r)}{\sqrt{2}w_{ij,g}}\right)\mathrm{Erf}\left[\frac{w_{ij,g}}{\sqrt{2}\sigma_{ij}(r)}\right]\Bigg\}, \tag{4.27}$$

where we have defined $w_{ij,g} = (\tau_{pi}^* - \tau_{pj}^*)b_p^* g$.

4.2.3.2 Inclusion of fluid acceleration

If we now include fluid acceleration, $A_p \neq 0$, we can still use the approach of Ayala et al. (2008), outlined in §4.2.3.1. We again split the relative radial velocity into a fluctuating component and a mean component and assume that the fluctuating component is normally distributed with standard deviation $\sigma_{ij}(r,\theta)$. Therefore, $\langle w_{ij,r}(r,\theta)\rangle$ is still described with (4.27) but the statistics of $\sigma_{ij}(r)$ are changed as A_p is no longer negligible.

We now calculate $\sigma_{ij}(r)$ when $A_p \neq 0$. Following the assumption used in collision models that the relative velocities follow a Gaussian distribution, $\sigma_{ij}(r)^2 = \langle w_{ij,r}(r)^2\rangle$, we solve (4.8), setting $b_p^* = 0$ to obtain an expression for $\langle w_{ij,r}(r)^2\rangle$. This is consistent with our assumption that in order for $\sigma_{ij}(\theta) = \sigma_{ij}$ turbulence must dominate. We adapt the approach of Ngo-Cong et al. (2018) and Yuu (1984) and Chan et al. (2023) who calculated $|\mathbf{w}_{ij}|$ for $b_p^* = 0$ in (4.8).

4.2.3.3 Calculation of σ_{ij}

Remembering we are assuming that the relative velocities follow a Gaussian distribution, $\sigma_{ij}(r)^2 = \langle w_{ij,r}(r)^2\rangle$ and choosing $\hat{\mathbf{r}} = \hat{\mathbf{i}}$, we want to calculate the standard deviation of the fluctuating velocity when the particles are separated by a distance $r_{c,ij} = r_{c,i} + r_{c,j}$,

$$\sigma_{ij}(r_{c,ij})^2 = \langle[\mathbf{u}_{pi}(\mathbf{r}_{c,i})\cdot\hat{\mathbf{r}} - \mathbf{u}_{pj}(\mathbf{r}_{c,j})\cdot\hat{\mathbf{r}}]^2\rangle = \langle[u_{pi,x}(\mathbf{r}_{c,i}) - u_{pj,x}(\mathbf{r}_{c,j})]^2\rangle, \qquad (4.28)$$

where $u_{pi,l}$ is the $l-$component of the velocity of particle i.

To calculate σ_{ij} we first calculate the velocity correlation of two ghost particles (particles which do not feel the presence of another particle and are thus able to overlap in space) located at the same point and then relate this to their velocity correlation when the particle centre of masses are separated by a distance $r_{c,ij}$.

In homogenous turbulence, two ghost particles with neutral density ($b_p^* = 0$) and size class i located at the same point have radial velocity correlation given by (see Appendix B)

$$\langle u_{pi,x}(\mathbf{x})^2 \rangle = \mathcal{A}_i \langle u_x^2 \rangle. \tag{4.29}$$

If one particle is of size class i and the other is of size class j, the radial velocity correlation is given by (see Appendix B)

$$\langle u_{pi,x}(\mathbf{x}) u_{pj,x}(\mathbf{x}) \rangle = \mathcal{B}_{ij} \langle u_x^2 \rangle, \tag{4.30}$$

where, as in the previous sections, u_x is the fluid velocity in the $x-$direction and $\mathcal{A}_i$ and $\mathcal{B}_{ij}$ are given by (B.3) and (B.4).

To relate the radial component of the velocity correlation of two ghost particles when they are located at the same point to their velocity correlation when the distance between their centre of masses is $r_{c,ij} = r_{c,i} + r_{c,j}$ we follow Yuu (1984) and Ngo-Cong et al. (2018) and use a Taylor series setting,

$$u_{pi,r}(\mathbf{r}_{c,i}) = u_{pi,r}(\mathbf{0}) \pm r_{c,i} \frac{\partial u_{pi,r}(\mathbf{0})}{\partial r}, \tag{4.31}$$

$$u_{pj,r}(\mathbf{r}_{c,j}) = u_{pj,r}(\mathbf{0}) \mp r_{c,j} \frac{\partial u_{pj,r}(\mathbf{0})}{\partial r}. \tag{4.32}$$

where, as the choice of $\mathbf{x}$ is arbitrary, we have chosen $\mathbf{x} = \mathbf{0}$. The $\pm$ corresponds to setting $\hat{\mathbf{r}} = \pm(\mathbf{r}_{c,i} - \mathbf{r}_{c,j})/|\mathbf{r}_{c,i} - \mathbf{r}_{c,j}|$.

The real variance is the arithmetic average of two cases expressed by the plus/minus sign in (4.31) and (4.32). Substituting in (4.31) and (4.32) to (4.28), taking the arithmetic average and letting the $u_{pi,x} = u_{pi,x}(\mathbf{0})$ and $u_{pj,x} = u_{pj,x}(\mathbf{0})$ we find,

$$\sigma_{ij}(r_{c,ij})^2 = \langle u_{pi,x}^2 \rangle + \langle u_{pj,x}^2 \rangle - 2\langle (u_{pi,x} u_{pj,x}) \rangle + \left\langle \left(r_{c,i} \frac{\partial u_{pi,x}}{\partial x} \right)^2 \right\rangle + \left\langle \left(r_{c,i} \frac{\partial u_{pj,x}}{\partial x} \right)^2 \right\rangle + 2 \left\langle \left(r_{c,i} r_{c,j} \frac{\partial u_{pi,x}}{\partial x} \frac{\partial u_{pj,x}}{\partial x} \right) \right\rangle. \tag{4.33}$$

When the turbulence field is homogeneous (Yuu, 1984) ((Monin et al., 2007) for derivation),

$$\left\langle \frac{\partial u_{pi,x}}{\partial x} \right\rangle = \frac{\partial}{\partial x} \left\langle u_{pi,x} \right\rangle, \tag{4.34}$$

$$\left\langle \left(\frac{\partial u_{pi,x}}{\partial x} \right)^2 \right\rangle = \frac{\partial^2}{\partial x^2} \left\langle u_{pi,x}^2 \right\rangle, \tag{4.35}$$

$$\left\langle \left(\frac{\partial u_{pi,x}}{\partial x} \right) \left(\frac{\partial u_{pj,x}}{\partial x} \right) \right\rangle = \frac{\partial^2}{\partial x^2} \left\langle u_{pi,x} u_{pj,x} \right\rangle, \tag{4.36}$$

such that,

$$\sigma_{ij}(r_{c,ij})^2 = \langle u_{pi,x}^2 \rangle + \langle u_{pj,x}^2 \rangle - 2\langle (u_{pi,x} u_{pj,x}) \rangle + \frac{\partial}{\partial x^2} \left(r_{c,i}^2 \langle u_{pi,x}^2 \rangle + r_{c,j}^2 \langle u_{pj,x}^2 \rangle + 2 r_{c,i} r_{c,j} \langle u_{pi,x} u_{pj,x} \rangle \right). \tag{4.37}$$

Substituting in (4.29) and (4.30),

$$\sigma_{ij}(r_{c,ij})^2 = (\mathcal{A}_i + \mathcal{A}_j - 2\mathcal{B}_{ij}) \langle u_x^2 \rangle + (\mathcal{A}_i r_{c,i}^2 + \mathcal{A}_j r_{c,j}^2 + 2\mathcal{B}_{ij} r_{c,i} r_{c,j}) \left\langle \left(\frac{\partial u_x}{\partial x} \right)^2 \right\rangle. \tag{4.38}$$

From Taylor (1935),

$$\left\langle \left(\frac{\partial u_x}{\partial x} \right)^2 \right\rangle = \frac{\epsilon}{15\nu}, \tag{4.39}$$

And assuming isotropic turbulence, $\langle u_x^2 \rangle = \langle u^2 \rangle / 3 = u'^2/3$,

$$\sigma_{ij}(r_{c,ij})^2 = (\mathcal{A}_i + \mathcal{A}_j - 2\mathcal{B}_{ij}) \frac{u'^2}{3} + (\mathcal{A}_i r_{c,i}^2 + \mathcal{A}_j r_{c,j}^2 + 2\mathcal{B}_{ij} r_{c,i} r_{c,j}) \left(\frac{\epsilon}{15\nu} \right). \tag{4.40}$$

For $\tau_p^* \to 0$ (the assumption used in frazil ice models), $\mathcal{A}_i, \mathcal{B}_{ij} \to 1$ because $\mathbf{u}_p \to \mathbf{u}$ and

$$\sigma_{ij}^2(r_{c,ij}) \to \frac{\epsilon}{15\nu} (r_{c,i} + r_{c,j})^2. \tag{4.41}$$

4.2.3.4 Final expression for $\langle |w_r| \rangle$

We obtain a final expression for the mean relative velocity $\langle |w_r| \rangle$ from (4.27) using (4.40) to specify $\sigma_{ij}(r_{c,ij})$ and with,

$$w_{ij,g} = b_p^* g(\tau_{pi}^* - \tau_{pj}^*). \tag{4.42}$$

with $\mathcal{A}_i$ and $\mathcal{B}_{ij}$ given by (B.3) and (B.4) and derived in Appendix B. In cases where u' is known the full expression for σ_{ij} can be used in the model. In the cases where u' is unknown the expression for σ_{ij} (4.41) in the limit when $\tau_{pi}^* \to 0$ can be used instead. In the limit of $w_{ij,g} \gg \sigma_{ij}, \langle|w_{ij,r}|\rangle \to w_{ij,g}/2$. In the limit of $w_{ij,g} \ll \sigma_{ij}, \langle|w_{ij,r}|\rangle \to \sigma_{ij}\sqrt{2/\pi}$.

4.3 Derivation for the encounter frequency

As was noted in §2.5, the encounter frequency, $\mathcal{F}_{enc,ij}$, currently used in frazil ice models is obtained using the cylindrical formulation with

$$\mathcal{F}_{enc,ij} = \frac{\pi r_{c,ij}^2 \sqrt{w_{ij,g}^2 + \sigma_{ij}^2}}{V} \tag{4.43}$$

and $r_{c,ij} = r_{c,i}$, $w_{ij,g} = v_{i,g}$ and $\sigma_{ij} = \sigma(2r_{c,i})$ because the particles in size classes other than i are assumed to be stationary and point-like when calculating collisions with crystals of size class i. We refer to this model as the 'old cylindrical, point-like formulation' or 'CP' for short.

However, in §4.2.2.3 we noted that, because the volume swept out in the cylindrical formulation is given by $\langle|\mathbf{w}|\rangle$ instead of $\langle|w_r|\rangle$, it would be more appropriate to use the statistics of $|\mathbf{w}|$ to obtain the relative velocity such that we use (4.18) for $|\mathbf{w}|_{turb}$. Equation (4.43) becomes

$$\mathcal{F}_{enc,ij} = \frac{\pi r_{c,ij}^2 \sqrt{w_{ij,g}^2 + \sigma_{ij}^2 \left(\frac{(\pi+2)^2}{2\pi}\right)}}{V}, \tag{4.44}$$

with $r_{c,ij} = r_{c,i}$, $w_{ij,g} = v_{i,g}$ and $\sigma_{ij} = \sigma_{ij}(2r_{c,i})$ unchanged. We refer to this model as the 'new cylindrical, point-like formulation' or 'nCP' for short.

Even though this approach ensures the consistency of the expression for the relative velocity due to turbulent fluctuations and the cylindrical geometry used to obtain the encounter frequency, an even more accurate approach (see §2.4.1) would be to obtain the encounter frequency using the spherical approximation which

avoids the assumption used in cylindrical formulation that the relative velocity in any instant is locally uniform over a spatial scale on the order of the collision radius. In this case we use the equations derived in §4.2.3.4 to obtain the relative velocity and substituting into the expression (2.53) for the encounter frequency we find,

$$\mathcal{F}_{enc,ij} = \frac{2\pi r_{c,ij}^2 \sqrt{\frac{2}{\pi}} \sigma_{ij}}{V} \left[\frac{1}{2} \exp\left(-\frac{w_{ij,g}^2}{2\sigma_{ij}^2} \right) + \frac{\sqrt{\pi}}{2} \left(\frac{w_{ij,g}}{\sqrt{2}\sigma_{ij}} + \frac{\sigma_{ij}}{\sqrt{2} w_{ij,g}} \right) \mathrm{Erf}\left(\frac{w_{ij,g}}{\sqrt{2}\sigma_{ij}} \right) \right], \tag{4.45}$$

$$= \frac{2\pi r_{c,ij}^2 \langle |w_{ij,r}| \rangle}{V}, \tag{4.46}$$

again with $r_{c,ij} = r_{c,i}$, $w_{ij,g} = v_{i,g}$ and $\sigma_{ij} = \sigma_{ij}(2r_{c,i})$ unchanged. We refer to this model as the 'new spherical, point-like formulation' or 'SP' for short.

A further improvement is made if we no longer assume that the other crystals are point-like, and include their relative rise velocities and let both crystals contribute to the collision radius. In this case we let $r_{c,ij} = r_{c,i} + r_{c,j}$, $w_{ij,g} = |v_{i,g} - v_{j,g}|$ and $\sigma_{ij} = \sigma(r_{c,ij})$ in (4.43)-(4.46) and the formulations are termed 'CD', 'nCD' and 'SD' respectively. A summary of the different acronyms and the formulations they correspond to is given in Table 4.1.

Name	Acronym	$\mathcal{F}_{coll,i}$	$\mathcal{F}_{enc,ij}$	$r_{c,ij}$	$w_{ij,g}$	σ_{ij}
old cylindrical, point-like	CP	(4.52)	(4.43)	$r_{c,i}$	$v_{i,g}$	$\sigma(2r_{c,i})$
new cylindrical, point-like	nCP	(4.52)	(4.44)	$r_{c,i}$	$v_{i,g}$	$\sigma(2r_{c,i})$
new spherical, point-like	SP	(4.52)	(4.46)	$r_{c,i}$	$v_{i,g}$	$\sigma(2r_{c,i})$
old cylindrical, differential size	CD	(4.53)	(4.43)	$r_{c,i} + r_{c,j}$	$\lvert v_{i,g} - v_{j,g} \rvert$	$\sigma(r_{c,ij})$
new cylindrical, differential size	nCD	(4.53)	(4.44)	$r_{c,i} + r_{c,j}$	$\lvert v_{i,g} - v_{j,g} \rvert$	$\sigma(r_{c,ij})$
new spherical, differential size	SD	(4.53)	(4.46)	$r_{c,i} + r_{c,j}$	$\lvert v_{i,g} - v_{j,g} \rvert$	$\sigma(r_{c,ij})$

Table 4.1: The acronyms for the different formulations used to calculate the collision frequency suggested in this chapter, together with the equations used to obtain the collision and encounter frequency.

4.3.1 Comparison of the different formulations

Figure 4.2 compares the different formulations defined in (4.43)-(4.46). We plot the scaled encounter frequency $\mathcal{F}_{enc,ij}/(r_{c,ij}^2 \sigma_{ij})$ as a function of $w_{ij,g}/\sigma_{ij}$ such that the result is independent on whether the crystals are assumed to be point-like or not.

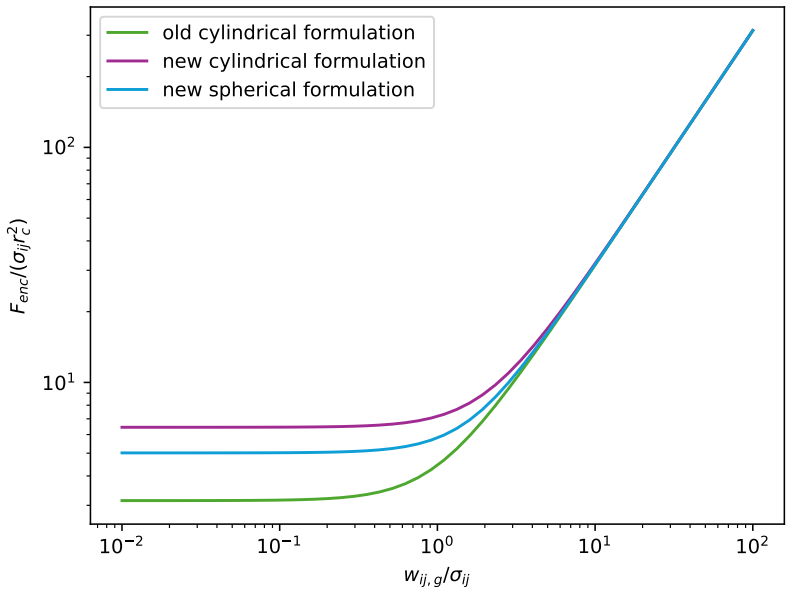

Figure 4.2: Comparison of the encounter frequency obtained using (4.43)-(4.46).

All the formulations give the same encounter frequency when buoyancy dominates, $w_{ij,g} \gg \sigma_{ij}$. However, in the limit $w_{ij,g} \ll \sigma_{ij}$ when turbulence becomes significant, the encounter frequency differs between the models with the new cylindrical formulation giving the highest encounter frequency by a factor of two compared to the old cylindrical formulation and the new spherical formulation increasing the encounter frequency by a factor of 1.6 compared with the old cylindrical formulation. This is due to different assumptions the models make about the relative velocity statistics of the flow, with the spherical formulation not relying on the relative velocity in any direction being locally uniform over a spatial scale on the order of the collision radius.

For the data considered in this thesis there is no estimate of u' available so we will use (4.41) to obtain σ_{ij}. If estimates of u' are available (4.40) is preferable. We use the rise velocities used in our simple model defined in §3 such that $w_{ij} = |v_{i,g} - v_{j,g}|$.

Figure 4.3 shows the encounter frequency obtained with the new model (4.46) (left column) and the encounter frequency currently used in frazil ice models (4.43)

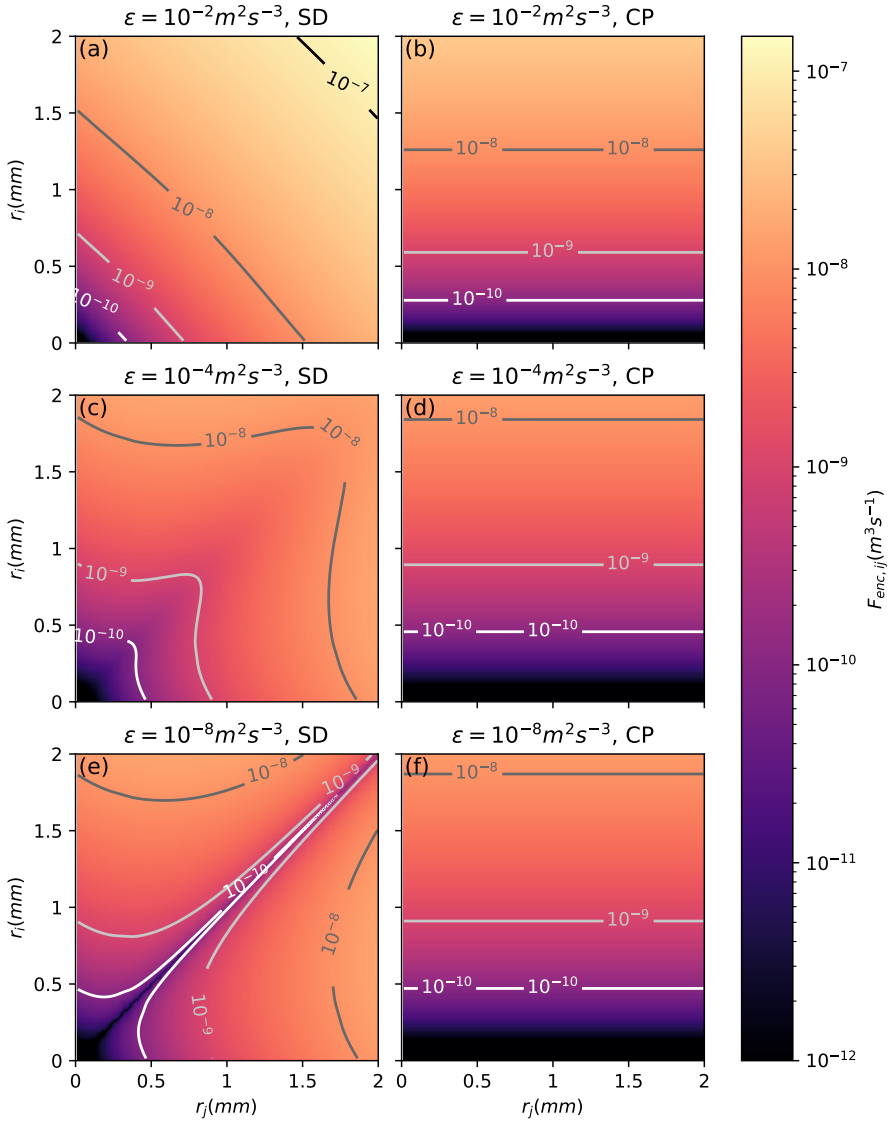

Figure 4.3: Comparison of the encounter frequency obtained with the new model (4.46) (left column) to the encounter frequency currently used in frazil ice models (4.43) (right column) for $\epsilon = (10^{-2}, 10^{-4}, 10^{-8})\mathrm{m}^2\mathrm{s}^{-3}$. The calculation for the rise velocity discussed in §3.4.

(right column) for $\epsilon = (10^{-2}, 10^{-4}, 10^{-8})\mathrm{m}^2\mathrm{s}^{-3}$. Using the new spherical formulation $\mathcal{F}_{enc,ij} = \mathcal{F}_{enc,ji}$, whilst in the old model $\mathcal{F}_{enc,ij} = \mathcal{F}_{enc,i}$, meaning that the encounter frequency does not depend on r_j. The effect of increasing turbulence is seen clearly in panels (a), (c) and (e). In more turbulent flow the relative velocity increases with the separation between the crystals so the contours are approximately along lines of constant $r_i + r_j$ for $\epsilon = 0.01\mathrm{m}^2\mathrm{s}^{-3}$. In almost quiescent flow, the relative velocity is proportional to the difference in rise velocities between the crystals. This

means that the relative velocity is close to zero when the crystals are the same size so the contours follow lines of constant $r_i = r_j$ for large but similar values of r_i and r_j.

In the limits where the relative velocity is dominated by the velocity due to turbulence or by the velocity due to buoyant rise we can find approximate expressions for the encounter frequency.

For $\epsilon = 0.02$ m^{2}s^{-3} the relative velocity in all cases is dominated by the velocity due to turbulence ($\sigma_{ij} \gg w_{ij}$). In the old CP formulation, combining (4.41) and (4.43) we obtain,

$$\mathcal{F}_{enc,ij} \approx \frac{2\pi r_{c,i}^3 \sqrt{\frac{\epsilon}{15\nu}}}{V}. \tag{4.47}$$

When allowing for differential crystal size (CD formulation), combining (4.41) and (4.43) we obtain,

$$\mathcal{F}_{enc,ij} \approx \frac{\pi (r_{c,i} + r_{c,j})^3}{V} \sqrt{\frac{\epsilon}{15\nu}}. \tag{4.48}$$

In the new spherical formulation (SD formulation), combining (4.41) and (4.46) we obtain,

$$\mathcal{F}_{enc,ij} \approx \frac{\sqrt{\frac{2}{\pi}} 2\pi (r_{c,i} + r_{c,j})^3}{V} \sqrt{\frac{\epsilon}{15\nu}}. \tag{4.49}$$

Therefore, in the turbulent case, for large values of r_i and r_j the encounter frequency is higher when considering differential crystal sizes, as the collision radius and relative velocity is higher. The encounter frequency when considering differential crystal size is lower for small values of r_j as the increase in collision radius under the SD and CD formulations does not overcome the decrease in relative velocity as the separation between the crystals is now $(r_{c,i} + r_{c,j})$ instead of $2r_{c,i}$. From (4.48) and (4.49), the collision frequency for crystals of size classes i and j is 1.6 times higher under the SD compared to the CD formulation.

For $\epsilon = 10^{-8}$ m^{2}s^{-3}, the relative velocity in all cases is dominated by the velocity due to buoyancy ($\sigma_{ij} \ll w_{ij}$). In the old model using (4.43) we obtain,

$$\mathcal{F}_{enc,ij} \approx \frac{\pi r_{c,i}^2 v_{i,g}}{V}. \tag{4.50}$$

In the SD formulation using (4.46) we instead obtain,

$$\mathcal{F}_{enc,ij} \approx \frac{\pi (r_{c,i} + r_{c,j})^2 |v_{i,g} - v_{j,g}|}{V}. \tag{4.51}$$

In the quiescent case, the encounter frequency is higher under the new spherical formulation than in the old model for cases where the difference in size between the colliding crystals is large and their relative velocity is large. In cases where the crystals are a similar size the collision frequency is smaller than in the old model as the relative velocity is smaller.

4.4 Implementation into the simple frazil ice model

We have suggested two improvements to current frazil ice models. The first is a new expression for the relative velocity in the spherical approximation and the second is no longer treating the other size classes involved in a collision as stationary point-like particles. We now implement these changes into the model described in §3.

Under the old parameterisation,

$$\mathcal{F}_{coll,i} = V^2 \mathcal{F}_{enc,ik} \overline{n} n_i. \tag{4.52}$$

with $\mathcal{F}_{enc,ik}$ given by (4.43). In order to compare across models we here set $\overline{n} = \sum_i n_i$.

In our new parametrisation which involves separately modelling collisions between crystals of each size class using the spherical formulation,

$$\mathcal{F}_{coll,i} = V^2 \sum_{k=1}^{N} \mathcal{F}_{enc,ik} n_k n_i \tag{4.53}$$

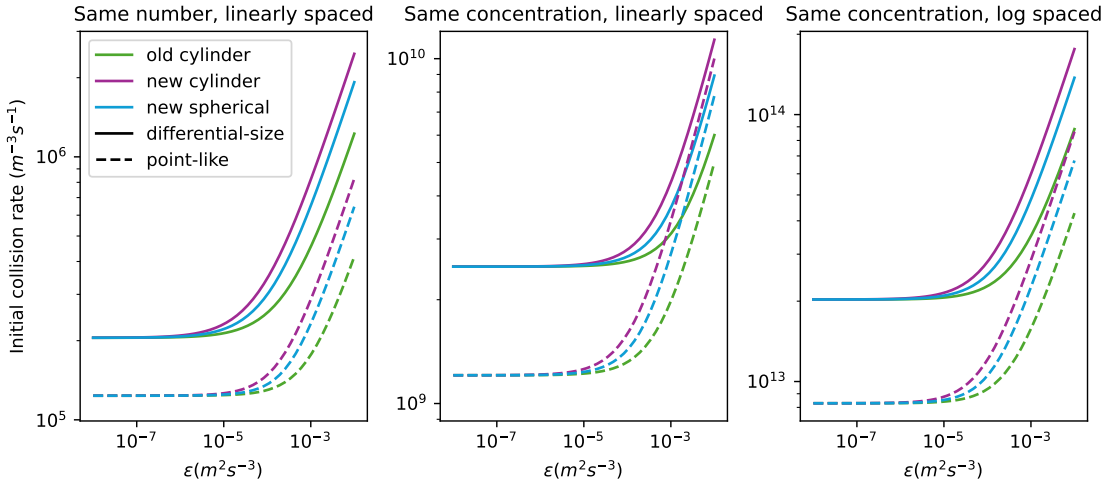

Figure 4.4: Initial collision rate for the three different initial conditions given in the panel title and described in §3. The crystal population is either initialised with the same number or the same concentration of crystals in each size class. The crystal radii increases either linearly or logarithmically with the index of the size class. Dashed lines are using the point-like assumption (CP, nCP and SP formulations) and solid lines are using the differential size assumption (CD, nCD and SD formulations). Different colours correspond to the collision rate given by the old cylindrical, new cylindrical and new spherical formulations (see (4.43)-(4.46)).

with $\mathcal{F}_{enc,ik}$ given by (4.46). We have assumed that when two crystals collide, dendrites are broken off both of them so two crystals of the smallest size class are produced.

4.4.1 Effect of using the different encounter frequency formulations on the initial collision rate

Figure 4.4 shows the initial collision rate for each of the different model setups. Comparing the initial collision rate under the point-like approximation (dashed lines) to our suggestion of including differential size in the collision parameterisation (solid lines), we see that the initial collision rate is faster in all model setups as long as the method to calculate the relative velocity is the same between models. This is because the collision rate of smaller particles with larger particles is substantially faster when considering differential crystal size, compared to the point-like approximation. Comparing the different methods to calculate the initial relative velocity (4.43)-

(4.46) (coloured lines), we see that the old cylindrical method consistently gives a lower collision rate for large ϵ, followed by the new spherical method and then the new cylindrical method.

As the cylindrical and spherical formulations give the same encounter frequency in quiescent flow, the initial collision rate in quiescent flow depends only on whether differential-size is included. In turbulent flow, $\sigma_{ij} \gg w_{ij}$ and $\mathcal{F}_{enc,ij} \propto \sigma_{ij}$ in each of the formulations. The increase in collision rate for each of the methods can thus be understood by comparing $\mathcal{F}_{enc,ij}/\sigma_{ij}$ for the three different formulations.

4.4.2 Effect of using the different encounter frequency formulations on the collision rate as $n_1 \to \overline{n}$.

As all the frazil ice crystal collisions are assumed to break-off crystal fragments of size class 1, $n_1 \to \overline{n}$ as $t \to \infty$ and we can predict the effect of using each of the different encounter frequency formulations on the collision rate when $n_1 \sim \overline{n}$.

In the turbulent case, $\sigma_{ij} \gg w_{ij,g}$. In the limit when $t \to \infty$, because $n_1 \to \overline{n}$ we find:

i) using the old CP model ((4.47) coupled with (4.52)),

$$\mathcal{F}_{coll,i} \approx 2\pi r_{c,i}^3 V \sqrt{\frac{\epsilon}{15\nu}} n_1 n_i \tag{4.54}$$

ii) when allowing for differential crystal size using (4.48) coupled with (4.53) and the old cylindrical formulation (CD) to get the relative velocity,

$$\mathcal{F}_{coll,i} \approx \pi (r_{c,i} + r_{c,1})^3 V \sqrt{\frac{\epsilon}{15\nu}} n_1 n_i \approx \pi r_{c,i}^3 V \sqrt{\frac{\epsilon}{15\nu}} n_1 n_i \text{ for } i \gg 1. \tag{4.55}$$

iii) when when allowing for differential crystal size and using the new spherical formulation to get the relative velocity (SD) (4.49) with (4.53),

$$\mathcal{F}_{coll,ij} \approx \sqrt{\frac{2}{\pi}} 2\pi V (r_{c,i} + r_{c,j})^3 \sqrt{\frac{\epsilon}{15\nu}} n_1 n_i \approx \sqrt{\frac{2}{\pi}} 2\pi V r_{c,i}^3 \sqrt{\frac{\epsilon}{15\nu}} n_1 n_i \text{ for } i \gg 1. \tag{4.56}$$

Therefore, at later times we predict that including differential crystal size will lead to a slower collision rate than that predicted with the point-like assumption. For

the larger size classes, $r_i \gg r_1$, including differential crystal size and the spherical formulation, will give a higher collision rate than that obtained using differential crystal size and the old cylindrical model but still a slower rate than that obtained when assuming the crystals are point-like.

In the quiescent case, $\sigma_{ij} \ll w_{ij,g}$. In the limit when $t \to \infty$, we find:
i) using the old model (CP, nCP, SP)

$$\mathcal{F}_{coll,i} \approx V\pi r_{c,i}^2 w_{i,g} n_1 n_i. \tag{4.57}$$

ii) in the case when we account for differential crystal size (CD, nCD, SD),

$$\mathcal{F}_{coll,i} \approx V\pi(r_{c,i} + r_{c,1})^2 |w_{i,g} - w_{1,g}| n_1 n_i \approx V\pi r_{c,i}^2 w_{i,g} n_1 n_i \text{ for } i \gg 1, \tag{4.58}$$

and as we noted before, the old cylindrical, new cylindrical and new spherical models all give the same collision rate in the quiescent case. Therefore, we predict that at later times, the collision rate will be the same for all models.

4.4.3 Results

In the discussion below we show results for the frazil ice model initialised with the same number of crystals in each size class. The same qualitative results are obtained for each of the different initial setups discussed in §3 and a quantitative comparison is shown in Figure 4.8.

4.4.3.1 Effect of including differential crystal size in turbulent flow

We first consider the limit of high-turbulence ($\epsilon = 0.01\text{m}^2\text{s}^{-3}$) and compare the CP and CD formulations. Figure 4.5 shows the effect of including differential crystal size on the collision rate. In this figure the collision rate using the old CP formulation (dashed lines) is compared to the collision rate using the CD formulation where differential crystal size is used to calculate the collision radius (solid lines).

We see that the number crystals in each of the size classes decreases at a very similar rate in the CP formulation (the dashed lines are almost on top of each other

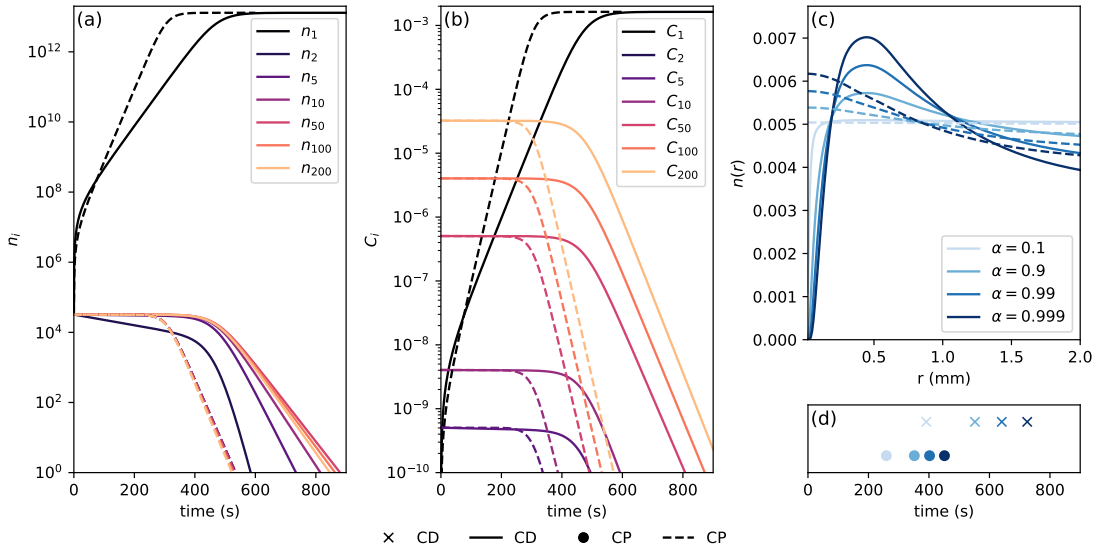

Figure 4.5: The change as a function of time in (a) the number density of crystals in each size class, (b) the concentration of crystals in each size class for $\epsilon = 10^{-2}$ m^{2}s^{-3}. Panel (c) is the normalised number of crystals in size classes 2-200 ($n(r_i) = n_i / \sum_{i=2}^{200} n_i$ and $n_2 = 0.02$ mm) when $n_1 = \alpha\overline{n}$ and represents how the crystals are distributed within the size classes. Panel (d) is the time taken for n_1 to reach $\alpha\overline{n}$. The dashed lines and circular markers are for data obtained using the CP formulation. The solid lines and cross markers are for data obtained using the CD formulation. See Table 4.1 for a description of each of the formulations. We initialize with the same number of crystals in each size class.

in panel a). In the CD formulation the number of crystals in size class two initially decreases at a faster rate than the crystals of size class two in the CP formulation (as expected from the discussion in §4.3.1). This is due to the increase in the collision radius when the smaller size classes collide with the larger size classes under the CD formulation. Further, in comparing the distribution of crystals in each of the size classes (panel c), there are relatively fewer crystals in the smallest size classes for the same value of n_1 in each of the formulations, demonstrating that crystals are lost faster in the smaller size classes when differential size is included.

The collision rate is initially slower in the old model (the dashed line increases more slowly than the solid line for r = 0.01 mm), as expected from the discussion in §4.3.1, but soon the collision rate using the CP formulation becomes faster than the collision rate using CD formulation due to the factor of two difference between (4.54) and (4.55).

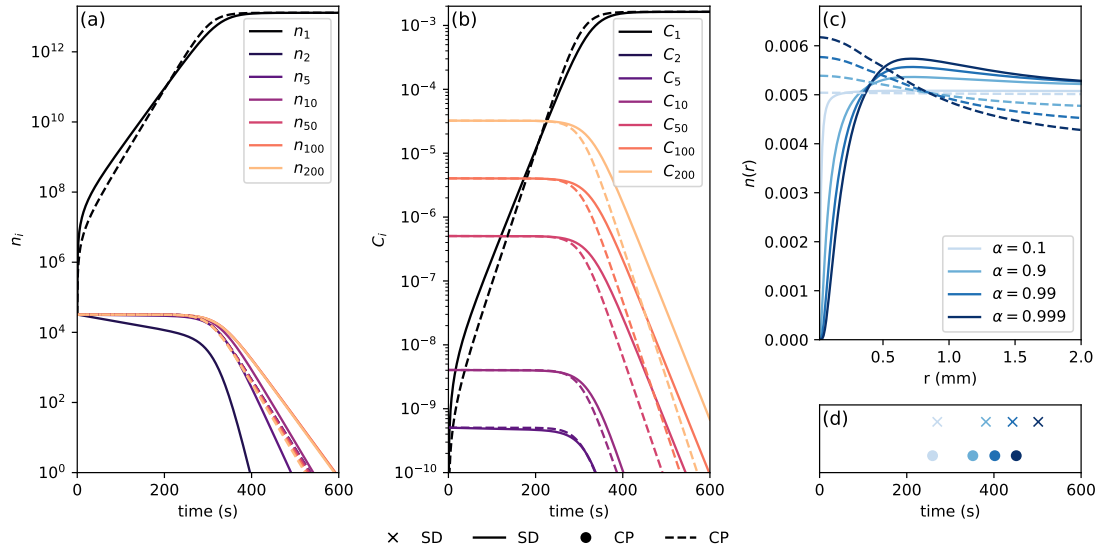

Figure 4.6: Comparison of crystal number evolution between spherical, differential size (SD) formulation and old cylindrical point-like (CP) formulation. Same as Figure 4.5 but solid lines and cross markers are for data obtained using the SD formulation. (See Table 4.1 for a description of each of the formulations.)

4.4.3.2 Effect of choosing the spherical or cylindrical formulation in turbulent flow

Figure 4.6 compares the effect of using the new spherical approximation (4.46) and (4.53) instead of the old cylindrical formulation (4.43) and (4.52). The solid lines now show the collision rate calculated using the SD formulation, whilst the dashed lines are still the old CP formulation. The collision rate under the SD formulation is now similar to the collision rate in the old CP model (the crosses in panel (d) are now much closer to the circles) but the crystal size distribution is very different, reflecting the fact that smaller crystals collide at a higher rate in the new model.

4.4.3.3 Quiescent flow ($\epsilon = 10^{-8}$ m^{2}s^{-3})

Figure 4.7 shows how the numerical models behave in the limit of weak-turbulence ($w_{ij,g} \gg \sigma_{ij}$). In line with the discussion in §4.3.1 we see that the collision rate of the smaller crystals is higher when considering differential crystal size than for point particles (the solid lines for $r_i = (0.02, 0.01, 0.1)$ decrease faster with time in Figure 4.7a than the dashed line and the crystal population distribution contains relatively more crystals in the smaller size classes for the CP formulation than the

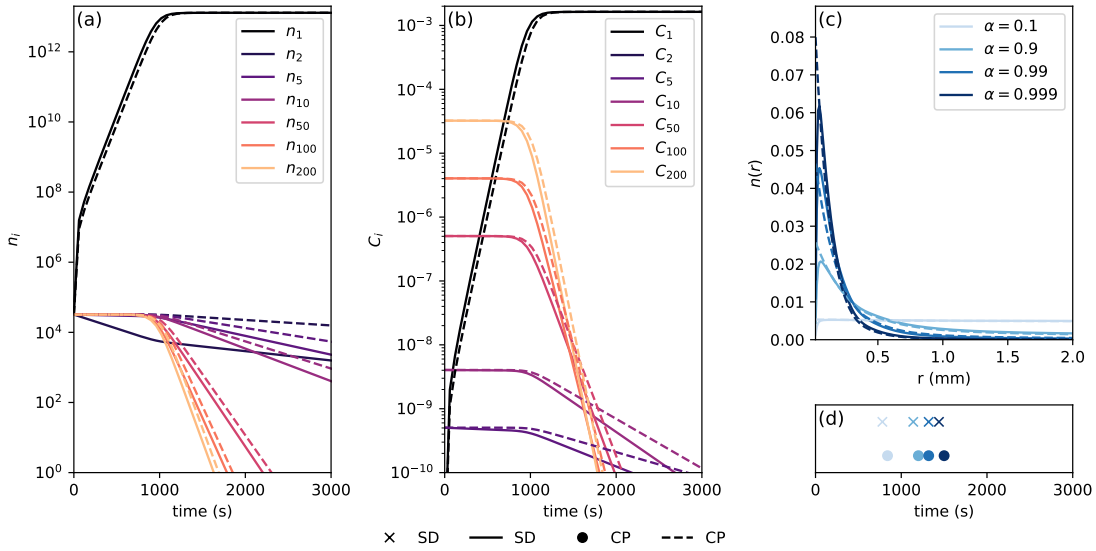

Figure 4.7: Comparison of crystal number evolution between spherical, differential size (SD) formulation and old cylindrical point-like (CP) formulation. Same as Figure 4.6 but with $\epsilon = 10^{-8}\mathrm{m}^2\mathrm{s}^{-3}$.

CD formulation at the same value of α. The collision rate of the larger particles is similar in both models as $n_1 \to \overline{n}$ in line with the reasons discussed in §4.4.2.

4.4.3.4 Comparison across a wider range of initial conditions

In the preceding discussion we only compared the CP and SD formulations for $\epsilon = 10^{-2}\mathrm{m}^2\mathrm{s}^{-3}$ and $\epsilon = 10^{-8}\mathrm{m}^2\mathrm{s}^{-3}$. We also only used the model where we initialise with the same number of crystals in linearly distributed size classes. We now compare the CP and SD formulations for $\epsilon = (10^{-8}, 10^{-5}, 10^{-4}, 10^{-3}, 10^{-2})$ $\mathrm{m}^2\mathrm{s}^{-3}$, as for the intermediate values of ϵ the relative velocity is a combination of the velocity due to turbulence and buoyancy. We also compare across the three different model initial conditions discussed in §3.

We compare the times taken (panels a, c, e of Figure 4.8) for n_1 to reach $\alpha\overline{n}$ and the mean radii (panels b, d, f of Figure 4.8) of crystals in size classes 2-N under the two different formulations. In each of the rows we initialise with one of the three different setups discussed in §3. In panels (a)-(d) the radii are linearly binned and we initialise with the same number of crystals (panels a and b) or the same concentration (panels c and d) of crystals in each of the size classes. In panels (e)-(f)

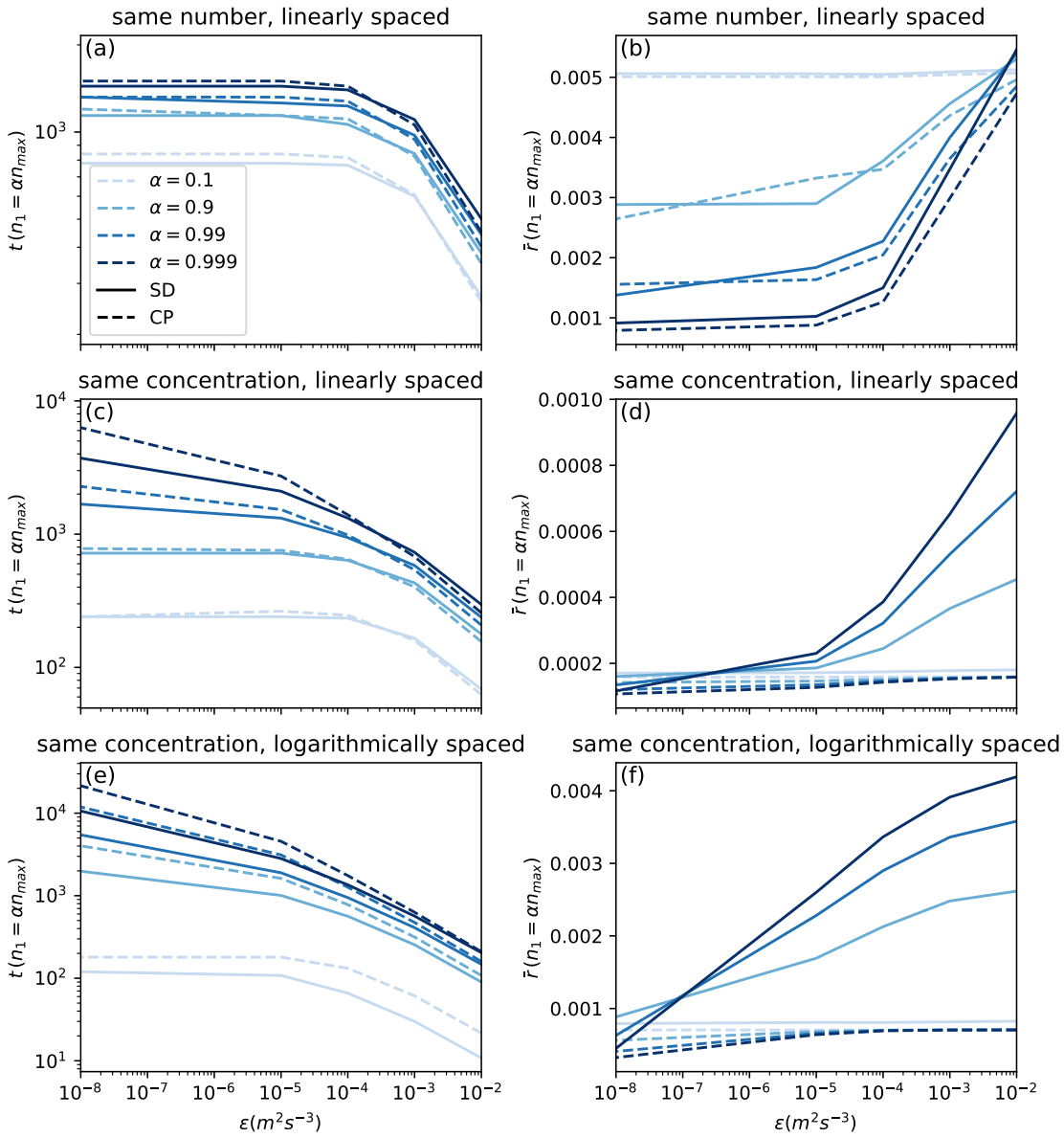

Figure 4.8: Panels a, c, e are the time taken for n_1 to reach $\alpha\overline{n}$ as a function of the turbulent dissipation rate ϵ. Panels b, d, f are the normalised mean radii of crystals in size classes 2-N as a function of ϵ, calculated as $\bar{r} = \sum_{i=2}^{N} r_i n_i / \sum_{i=2}^{N} n_i$ under the CP and SD formulations. In each of the rows we initialise with one of the three different setups discussed in §3. In panels (a)-(d) the radii are linearly binned and we initialise with the same number of crystals (panels a and b) or the same concentration (panels c and d) of crystals in each of the size classes. In panels (e)-(f) the radii are logarithmically binned and we initialise with the same concentration of crystals in each of the size classes.

the radii are logarithmically binned and we initialise with the same concentration of crystals in each of the size classes.

The collision rate increases with ϵ. The collision rate using the SD formulation is consistently faster than that using the CP formulation when the flow is more quiescent ($\epsilon < 10^{-4}\mathrm{m}^2\mathrm{s}^{-3}$) across all model setups (left column). When the flow is more turbulent ($\epsilon > 10^{-4}\mathrm{m}^2\mathrm{s}^{-3}$), the collision rate at larger values of α is slower under the SD formulation than under the CP formulation. This is because the CP approximation gives a higher collision rate when collisions are mostly with crystals of size class 1. The exception comes for the case when we initialise with logarithmically spaced crystals. In this case, there are initially much larger numbers of crystals in the smaller size classes than in the other models, so when α is close to one, most of the crystals remaining are very close in size to the crystals in size class 1. Therefore, for n_1 to increase large numbers of collisions are required involving crystals of the smaller size classes. However, under the SD formulation the crystal population is less strongly dominated by crystals in the smallest size classes when α is close to one ($\overline{r}$ is larger). This means that when n_1 is close to $\overline{n}$, collisions still occur between crystals of the larger size classes and crystals of the smaller size classes, so the collision rate is higher.

For small values of α the mean radius is sensitive to the initial crystal distribution, meaning that the mean radius is initially much smaller when the crystals are initialised with the same concentration in each size class (see Table 3.2 for the initial values of $\overline{r}$). The mean radius is consistently higher with the SD formulation as the collision rate of crystals of the smaller size classes increases, leaving relatively more crystals in the larger size classes at the same value of α. For all cases the mean radius also increases with the turbulence. This is because the ratio of the collision rate of larger particles with particles of size class 1 to the collision rate of smaller particles with particles of size class 1 is higher in the quiescent case than in the turbulent case (see §B.2). Hence, the particle distribution shifts more to the smaller size classes

in the quiescent case. This can also be seen by comparing Figure 4.6c and Figure 4.7c.

The increase in the mean radius with ϵ is more substantial in the SD formulation than the CP formulation when we initialise with the same concentration of crystals in each size bin. This is because there are initially substantially more crystals in the smaller size classes. Therefore, in the quiescent case, very few crystals remain in the larger size classes at large values of α, whilst in the turbulent case there are still crystals remaining in the larger size classes because the change in collision rate increases less with radius.

The heat flux from each crystal is proportional to the crystal radius. Therefore, the total heat flux depends on the total number of crystals and how the crystals are distributed among the size classes. The SD formulation changes the collision rate and the radial distribution of the crystals, increasing the relative number of crystals in the larger size classes. Therefore, changing to the SD formulation will likely alter the heat flux and the subsequent effect frazil ice crystals have on the water column when included in a full frazil ice model. We postpone consideration of these changes to the energy balance until §9, where we use a complete frazil ice model which also accounts for other improvements to parametrising collisions from §5-§8.

4.5 Conclusions

In this chapter we have derived a new expression for the encounter frequency. Previous models have often assumed that the particles outside of the colliding size class are stationary and point-like. We call this the CP formulation. Instead, we separately considered the interactions between each of the crystal size classes, and allowed the radius and velocity of each size class to contribute to the collision radius. We have also obtained a new expression (4.27) for the relative radial velocity of the particles by combining the approaches of Ayala et al. (2008) and Yuu (1984) and Chan et al. (2023). In the case when both the turbulent kinetic energy and the dissipation rate ϵ of the fluid flow is known, then (4.40) should be used to calculate

σ_{ij}. Otherwise (4.41) can be used instead if only ϵ is known, as explained here in a simple model. Overall, we obtain a new expression (4.46) for the encounter frequency which we term the spherical differential size (SD) formulation and a subsequent expression (4.53) for the collision frequency.

Although, the SD formulation is an improvement to the previous CP formulation, there are still some weaknesses of this model. Firstly, we have used an approximation to the Maxey-Riley equation to solve for the particle velocity. This approximation holds for small frazil ice crystals but is less accurate for larger crystals with a radius similar to the Kolmogorov length scale of the flow. Therefore, for these crystals, the forces that were assumed negligible in deriving (4.27) might have some effect. Secondly, in line with other collision models the formulation assumes that the distribution of the relative velocities is Gaussian, which may not always be the case (Mercier, 1985; Rani et al., 2014). In some settings the relative velocities have instead been observed to be log-normally distributed (Mercier, 1985). It would be interesting to see how an encounter frequency would change if it was instead derived assuming that the relative velocities are log-normally distributed. Finally, to be used to its full potential the model relies on knowing the turbulent kinetic energy and the dissipation rate ϵ of the fluid flow, which is not always known.

We have implemented these changes into the simple frazil ice model detailed in §3. When the effects of differential size are included, the collision rate of crystals in the smallest size classes increases due to the increase in collision radius and relative velocity when they interact with crystals of larger sizes. This means that the mean radius of the crystal population model is higher when including differential crystal size then when using the point-like assumption. The collision rate increases with the turbulent dissipation rate because the relative velocity increases. Turbulence starts to be significant when $\epsilon > 10^{-5}$ $\mathrm{m^2 s^{-3}}$. Initially the SD formulation gives a higher collision rate across all model runs than the CP formulation. When most of the crystals are in size class 1 the collision rate is almost the same under both the SD

and the CP models for quiescent flow ($\epsilon = 10^{-8}\mathrm{m}^2\mathrm{s}^{-3}$). As the turbulence increases the collision rate is slower under the SD formulation than the CP formulation as the separation radius used to calculate the relative velocity is smaller. There is also considerable sensitivity to the initial crystal population distribution and how the size classes are binned.

Using the SD formulation changes both the collision frequency and the distribution of crystals among the size classes and hence will impact the heat flux and the resultant properties of the water column when implemented into a full frazil ice model. Before doing this we consider further improvements to the parametrisation of crystal collisions.

"And no one pours new wine into old wineskins. Otherwise, the new wine will burst the skins; the wine will run out and the wineskins will be ruined. No, new wine must be poured into new wineskins. And no one after drinking old wine wants the new, for they say, 'The old is better.'"

—Luke 5:37-39 NIV

5 Redistribution

Contents

5.1 Introduction

Having derived a new expression for the collision frequency in §4, we now address the second of the weaknesses outlined in §2.5.3. As was noted in §2.5.3, to correctly redistribute the crystals after a collision, there should be change in the number of crystals in intermediate size classes, in the smallest size class and in the colliding size classes. Currently only the number of crystals in the colliding size classes and the smallest size class changes. In this chapter we implement a method to more accurately redistribute the crystals using the recommended SD formulation described in §4. The method is derived in §5.2 and the results of implementing redistribution is given in §5.3.

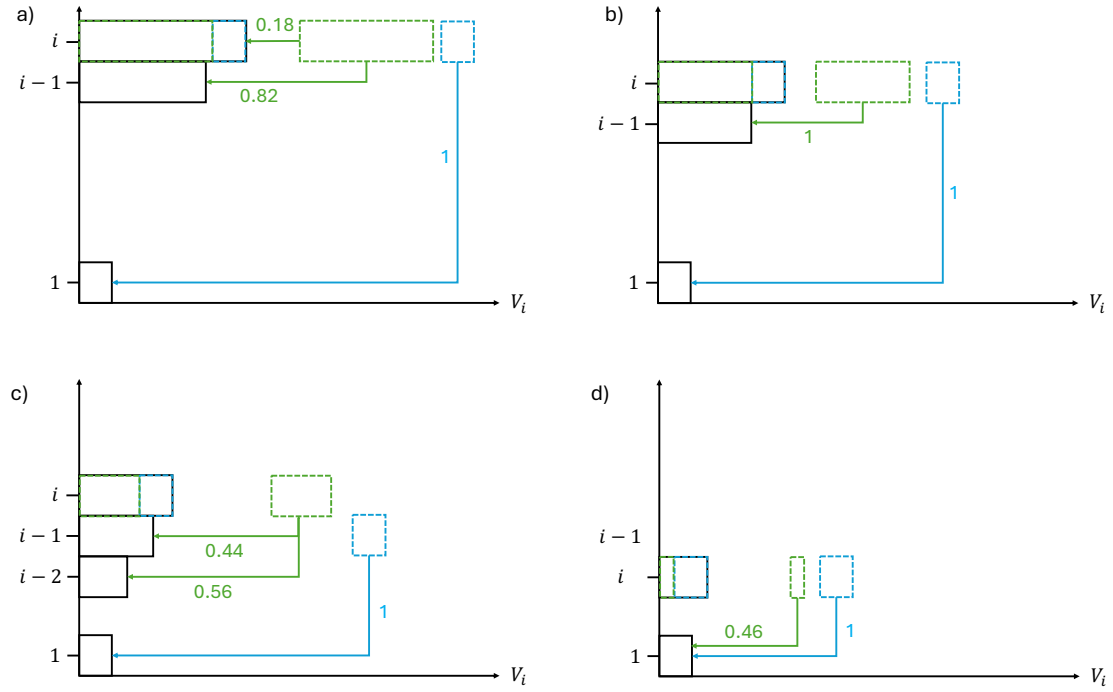

Figure 5.1: Four different ways a fractured crystal from size class i can redistribute into different size classes. Here $V_{rem} = V_1$. The number of crystals added to each size class is shown above the corresponding arrow. Panel (a) the volume of the larger fractured crystal fragment is added to the size classes with volumes sandwiching the size of the fractured crystal. The larger size class in the sandwich is size class i. Panel (b) the volume of the larger fractured crystal fragment is equal to the volume of crystals in a smaller size class so the number of crystals in the smaller size class increases by 1 and the number of crystals in size class i decreases by 1. Panel (c) the volume of the larger fractured crystal is added to the size classes with volumes sandwiching the size of the fractured crystal. The larger size class in the sandwich is smaller than i so the number of crystals in size class i decreases by 1. Panel (d) the volume of the crystal fragments are less than or equal to V_1 so all the volume of the fractured crystal is added to size class 1 and the number of crystals in size class i decreases by 1.

5.2 Method to redistribute

We consider the case when a volume V_{rem} of ice is removed from a crystal of size class i such that the crystal now has volume $V_{crystal} = V_i - V_{rem}$. There are four different ways that the fractured crystal could redistribute into the different size classes, which are illustrated in Figure 5.1. In Figure 5.1 we assume $V_{rem} = V_1$, so each crystal fracture always results in the number of crystals in size class 1 increasing by 1 and then the remaining volume of ice is divided according to the discussion below.

If there exists a size class $i-\alpha$ with crystals of volume $V_{crystal}$ (panel b), then the number of crystals in size class $i-\alpha$ should increase by 1, the number of crystals in size class i should decrease by 1.

If there is no size class with crystals of volume $V_{crystal}$, then the fractured crystal will distribute as a fractional increase in the number of crystals in size class $i-\alpha$ and $i-\beta$ (panels a and c). Crystals in size class $i-\alpha$ have volume $V_{i-\alpha}$ which satisfies $V_{i-\alpha} < V_{crystal}$, $V_k < V_{i-\alpha}\,\forall\, k < i$ (i.e. size class $i-\alpha$ is the largest class with crystals smaller than $V_{crystal}$). Crystals in size class $i-\beta$ have volume $V_{i-\beta}$ which satisfies $V_{i-\beta} > V_{crystal}$, $V_k > V_{i-\beta}\,\forall\, k > i$ (i.e. the smallest size class $i-\beta$ with crystal size larger than $V_{crystal}$ but closer in size to $V_{crystal}$ than crystals in any other size class that have a volume larger than $V_{crystal}$). If the volume removed is very small or the volumes are very different, then $\beta = 0$ (panel a).

It is possible to reduce the spacing between size classes sufficiently such that $V_{crystal} < V_1$ for some fracture events. In this case we assume that all the crystals become crystals of size class 1 (panel d).

We now set out the transition rules for each cases, choosing a scheme that enforces mass conservation. We define $V_{rem} = \zeta V_1$. Firstly, we derive a new expression for the rate at which crystals are removed from size class i and added to size class 1 when $V_{crystal} \leq V_1$ (panel d in Figure 5.1). The relevant size classes are i and 1. The total volume of crystals in these size classes before and after the collision are

$$V_{before} = N_1 V_1 + N_i V_i, \tag{5.1}$$

$$V_{after} = N_1' V_1 + (N_i - 1) V_i, \tag{5.2}$$

where N_i is the number of crystals in size class i. Setting, $N_1' = N_1 + \Delta N_1$ and applying mass conservation we find,

$$\Delta N_1 = \frac{V_i}{V_1}. \tag{5.3}$$

Secondly, we derive a new expression for the rate at which crystals are removed from size class i when $\beta = 0$ and $V_{crystal} \geq V_{i-\alpha}$ (panel a in Figure 5.1). We let the number of crystals in size class i before the collision be n_i and the number after the collision be n_i'. The total volume of ice in size classes 1, i and $i - \alpha$ before and after the collision is given by,

$$V_{before} = N_1 V_1 + N_{i-\alpha} V_{i-\alpha} + N_i V_i, \tag{5.4}$$

$$V_{after} = N_1' V_1 + N_{i-\alpha}' V_{i-\alpha} + N_i' V_i. \tag{5.5}$$

In the case when $V_{rem} = V_i - V_{i-\alpha}$, $N_i' - N_i = -1$ and $N_{i-\alpha}' - N_{i-\alpha} = +1$. In the case when $V_{rem} = 0$, $N_i' - N_i = 0$ and $N_{i-\alpha}' - N_{i-\alpha} = 0$. Thus, we choose an interpolation between these end member cases,

$$N_{i-\alpha}' - N_{i-\alpha} = \frac{V_{rem}}{V_i - V_{i-\alpha}}. \tag{5.6}$$

Using $V_{before} = V_{after}$ and noting that $N_1' = N_1 + \zeta$ as $V_{rem} = \zeta V_1$. we solve for N_i',

$$N_i' - N_i = -\frac{V_{rem}}{V_i - V_{i-\alpha}}, \tag{5.7}$$

Thirdly, we derive a new expression for the rate at which crystals are removed from size class i when $\beta \neq 0$ and $V_{crystal} \geq V_{i-\alpha}$ (panel c in Figure 5.1). The total volume of ice in size classes 1, i and $i - \alpha$ before and after the collision is given by,

$$V_{before} = N_1 V_1 + N_{i-\alpha} V_{i-\alpha} + N_{i-\beta} V_{i-\beta} + N_i V_i, \tag{5.8}$$

$$V_{after} = (N_1 + \zeta) V_1 + N_{i-\alpha}' V_{i-\alpha} + N_{i-\beta}' V_{i-\beta} + (N_i - 1) V_i. \tag{5.9}$$

As $V_{crystal} = V_i - \zeta V_1$ and $V_{before} = V_{after}$ we find,

$$V_{crystal} = (N_{i-\alpha}' - N_{i-\alpha}) V_{i-\alpha} + (N_{i-\beta}' - N_{i-\beta}) V_{i-\beta}. \tag{5.10}$$

In the case when $V_{crystal} = V_{i-\alpha}$, $N_{i-\beta}' = N_{i-\beta} = 0$ and $N_{i-\alpha}' - N_{i-\alpha} = +1$. In the case when $V_{crystal} = V_{i-\beta}$, $N_{i-\beta}' - N_{i-\beta} = 1$ and $N_{i-\alpha}' - N_{i-\alpha} = 0$. Interpolating between these end numbers we choose,

$$N_{i-\alpha}' - N_{i-\alpha} = \frac{V_{i-\beta} - V_{crystal}}{V_{i-\beta} - V_{i-\alpha}} = \frac{V_{i-\beta} - V_i + V_{rem}}{V_{i-\beta} - V_{i-\alpha}}. \tag{5.11}$$

and substituting in (5.10),

$$N'_{i-\beta} - N_{i-\beta} = \frac{V_{crystal} - V_{i-\alpha}}{V_{i-\beta} - V_{i-\alpha}} = \frac{V_i - V_{rem} - V_{i-\alpha}}{V_{i-\beta} - V_{i-\alpha}}. \tag{5.12}$$

In the case when $\beta = 0$, substituting in (5.6) and (5.7) to (5.5) and (5.11) and (5.12) to (5.9), whilst setting $n_{i-\beta} = 0$ to avoid double counting, we find that (5.5) and (5.9) are equivalent.

For each size class i undergoing a collision, we define α_i and β_i as the values of α and β for size class i. We define size class k_{min} as the largest size class k which satisfies, $V_k - V_{rem} \leq V_1$ (i.e. size class k_{min} is the largest size class which, during a collision, fractures into a crystal smaller than size class 1). Maintaining the assumption that $V_{rem} = \zeta V_1$ and using (5.3), (5.6), (5.7), (5.11) and (5.12). Our simple frazil model becomes,

$$V\frac{dn_{i,nuc}}{dt} = \begin{cases} -\left\{\mathcal{H}(\beta_i) + [1 - \mathcal{H}(\beta_i)]\left(\frac{\zeta V_1}{V_i - V_{i-\alpha_i}}\right)\right\}\mathcal{F}_{coll,i}, & i = N, \\ -\left\{\mathcal{H}(\beta_i) + [1 - \mathcal{H}(\beta_i)]\left(\frac{\zeta V_1}{V_i - V_{i-\alpha_i}}\right)\right\}\mathcal{F}_{coll,i} + \dots & 1 < i < N, \\ \quad \sum_{k=k_{min}}^{N}\left[\left(\frac{V_{k-\beta_k} - V_k + \zeta V_1}{V_{k-\beta_k} - V_{k-\alpha_k}}\right)\delta(k - \alpha_k - i) + \dots\right. \\ \quad \left.\left(\frac{V_k - \zeta V_1 - V_{k-\alpha_k}}{V_{k-\beta_k} - V_{k-\alpha_k}}\right)\delta(k - \beta_k - i)\right]\mathcal{F}_{coll,k} \\ \zeta \sum_{i=2}^{N}\mathcal{F}_{coll,i} + & i = 1 \\ \quad \sum_{k=k_{min}}^{N}\left(\frac{V_{k-\beta_k} - V_k + \zeta V_1}{V_{k-\beta_k} - V_{k-\alpha_k}}\right)\delta(k - \alpha_k - 1) + \\ \quad \sum_{k=2}^{k_{min}-1}\frac{V_k - \zeta V_1}{V_1}\mathcal{F}_{coll,k}, \end{cases} \tag{5.13}$$

where

$$\mathcal{H}(\beta) = \begin{cases} 1, & \beta > 0, \\ 0, & \beta = 0. \end{cases} \tag{5.14}$$

In the limit when we break off one crystal of size class 1 per collision, $\zeta = 1$ and the difference in volume between size classes is large, $V_i - V_{i-\alpha} \gg V_{i-\alpha}$ we recover the equations used to parametrise secondary nucleation in Heorton et al. (2017), Holland and Feltham (2005), Jones and Wells (2018), Radia (2014), Smedsrud

(2002), Smedsrud and Jenkins (2004), Souillé et al. (2020), and Wang and Doering (2005).

In the limit when $V_i - V_{i-1} = \zeta V_1$,

$$V\frac{dn_{i,nuc}}{dt} = \begin{cases} -\mathcal{F}_{coll,i}, & i = N, \\ -\mathcal{F}_{coll,i} + \mathcal{F}_{coll,i+1}, & 1 < i < N, \\ \zeta \sum_{i=2}^{N} \mathcal{F}_{coll,i} + \mathcal{F}_{coll,i+1}, & i = 1. \end{cases} \tag{5.15}$$

5.3 Results

We now implement (5.13) into the simple frazil model defined in §3. We continue to use the spherical differential size (SD) formulation defined in §4 for the crystal collision rates and keep all other parameters and initial conditions the same, apart from now using (5.13) to distribute the particles after a collision. We define models which use the SD formulation and allow redistribution, the spherical, differential size redistribution model or SDR for short. Results are shown for an initial setup where the number of crystals in each of the size classes is initially uniform and the increase in radius between size classes is linear. Qualitatively the results are the same for the different initial conditions and discretisations. A summary of the net effects on the collision frequency and mean radius for each of the initial models is discussed in §5.4.

Figure 5.2 and Figure 5.3 show the effect of redistribution on the simple frazil model, for cases initialised with the same number of crystals in each size class and the size classes linearly binned in radial space. In both cases the mean radius decreases faster when we allow redistribution (in panel c $n(r)$ shifts to the left with increasing α for the cases when redistribution is included) and we see a cascading effect where the number of particles in the larger size classes asymptote to zero and the number of crystals in the size classes below subsequently increases. For a given n_1 the total number of crystals is higher when redistribution occurs than without redistribution. To understand this consider the limit when the gap between size classes is equal to V_1, $\zeta = 1$, so that one additional crystal fragment is produced per

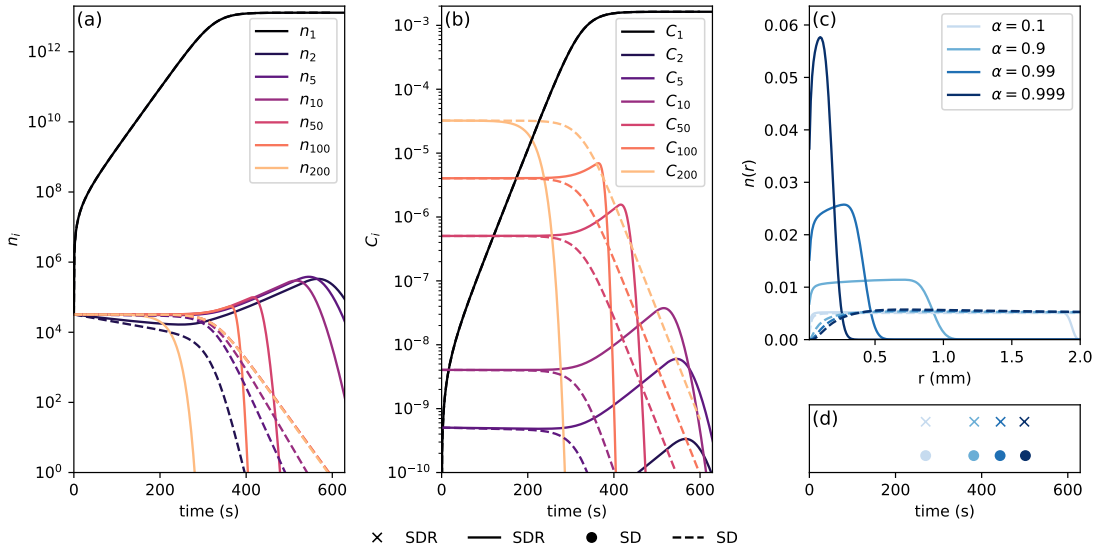

Figure 5.2: The change over time of (a) the number density of crystals in each size class, (b) the concentration of crystals in each size class for $\epsilon = 10^{-2}$ m^{2}s^{-3}. The n_1 and C_1 dashed lines overlap with the solid n_1 and C_1 lines. Panel (c) shows is the normalised number of crystals in size classes 2-200 ($n(r_i) = n_i / \sum_{i=2}^{200} n_i$ and $n_2 = 0.02$ mm) when $n_1 = \alpha\overline{n}$ and indicates how the crystals are distributed within the size classes. Panel (d) is the time taken for n_1 to reach $\alpha\overline{n}$. The dashed lines and circular markers are for data obtained using the spherical, differential size (SD) formulation. The solid lines and cross markers are for data obtained using the spherical, differential size redistribution (SDR) formulation. We initialise with the same number of crystals in each size class.

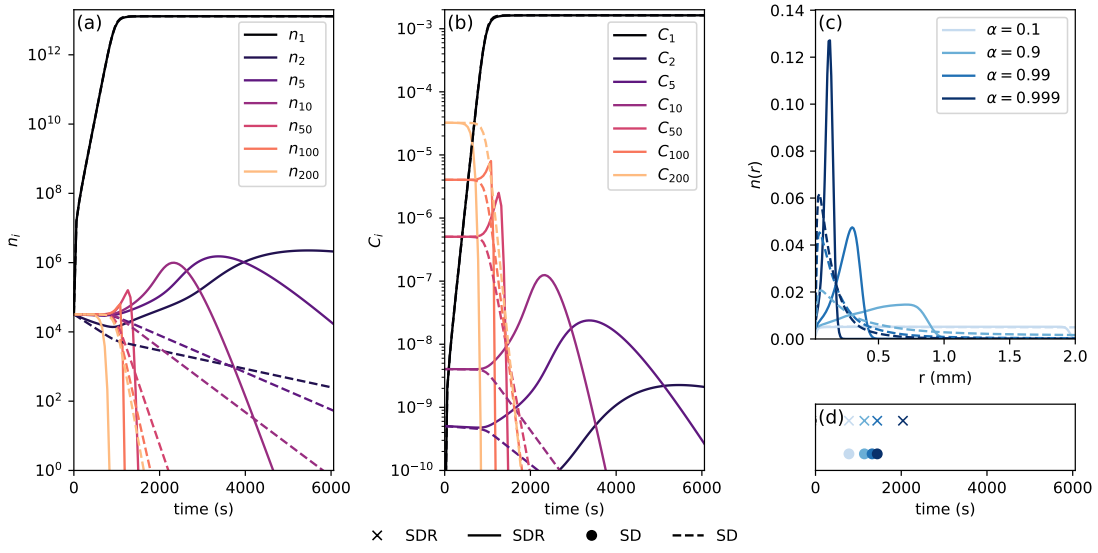

Figure 5.3: Same as Figure 5.2 but with lower turbulent dissipation rate, $\epsilon = 10^{-8}$m^{2}s^{-3} so that differential gravitational rise of crystals plays a more significant role. The n_1 and C_1 dashed lines overlap with the solid n_1 and C_1 lines.

collision. Without redistribution we would produce $(1 - V_1/V_i)$ additional crystals per collision.

In the turbulent case (Figure 5.2) the total collision rate remains unchanged despite the change in the shape of the size distribution (the equivalently coloured crosses and circles are at the same time in panel d). This is due to two competing effects. Firstly, the number of crystals for the same value of n_1 is higher in the SDR case due to redistribution than in the SD case, and hence there are more crystals to collide with, which increases the collision frequency. Secondly, the number of crystals in the smaller size classes is relatively higher in the SDR case. These crystals have a smaller collision radius and relative velocity so the collision frequency decreases. These two effects seem to cancel out and the resultant net collision frequency is unchanged.

In the quiescent case (Figure 5.3) the collision rate decreases when redistribution is added. In this case the relative velocity is due to the difference in the rise velocity and not proportional to the collision radius as was the case for $\epsilon = 0.02$ m^{2}s^{-3}. The rise velocity is very small when the crystals are all small. This means that the increase in the number of crystals is insufficient to counter the decrease in the encounter frequency and the collision rate decreases.

5.4 Comparison across a wider range of initial conditions

In the preceding discussion we only compared the CP and SD formulations for $\epsilon = 10^{-2}$m^{2}s^{-3} and $\epsilon = 10^{-8}$m^{2}s^{-3}. We also only used the model where we initialise with the same number of crystals in linearly distributed size classes. We now compare the SD and SDR formulations for $\epsilon = (10^{-8}, 10^{-5}, 10^{-4}, 10^{-3}, 10^{-2})$ m^{2}s^{-3}, as for the intermediate values of ϵ the relative velocity is a combination of the velocity due to turbulence and buoyancy. We also compare across the three different

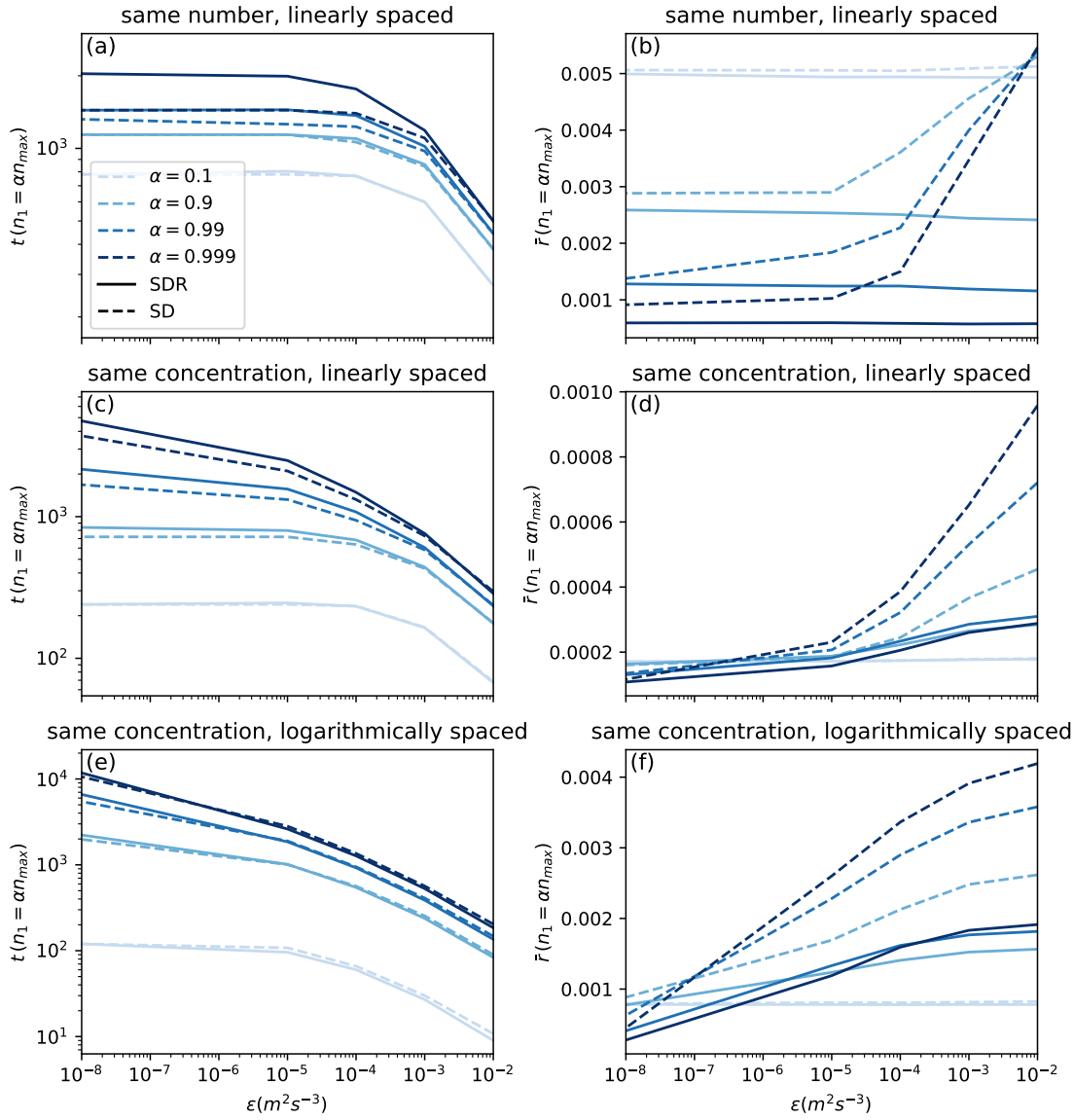

Figure 5.4: Sensitivity of evolutions timescale and mean radii to the turbulent dissipation rate ϵ for different model configurations. Panels a, c, e are the time for n_1 to reach $\alpha\overline{n}$ for different α shown by the line colour, and the formulation shown by the line type. Panels b, d, f are the corresponding normalised mean radii of crystals in size classes 2-N, calculated as $\bar{r} = \sum_{i=2}^{N} r_i n_i / \sum_{i=2}^{N} n_i$ under the SD and SDR formulations for collision and redistribution. In each of the rows we initialise with one of the three different setups discussed in §3. In panels (a)-(d) the radii are linearly binned and we initialise with the same number of crystals (panels a and b) or the same concentration (panels c and d) of crystals in each of the size classes. In panels (e)-(f) the radii are logarithmically binned and we initialise with the same concentration of crystals in each of the size classes.

model initial conditions discussed in §3.

We compare the times taken (panels a, c, e of Figure 5.4) for n_1 to reach $\alpha\overline{n}$ and the mean radii at this time (panels b, d, f of Figure 5.4) of crystals in size classes 2-N under the two different formulations. In each of the rows we initialise with one of the three different setups discussed in §3. In panels (a)-(d) the radii are linearly binned and we initialise with the same number of crystals (panels a and b) or the same concentration (panels c and d) of crystals in each of the size classes. In panels (e)-(f) the radii are logarithmically binned and we initialise with the same concentration of crystals in each of the size classes.

Panels (a, c, e), show that for $\alpha \geq 0.9$, redistribution decreases the collision rate for small values of ϵ and there is little change in the collision rate for larger values of ϵ. There is a smaller decrease in the collision rate for small values of ϵ is smaller when we initialise with the same concentration of crystals in each size class, because we are already initialising with more crystals in the smaller size classes and the effect of redistribution shifting the crystal population to be dominantly composed of crystals in the smaller size cases makes less of a difference.

Panels (b, d, f) show that, in all cases, redistribution decreases the mean radius of the crystals. For a given value of n_1, the mean radius with redistribution is almost independent of ϵ in the case when we initiate with the same number of crystals in each size class. However, Figure 5.2 and Figure 5.3 shows that the crystal population distribution $n(r)$ is shaped differently with few crystals of the smallest size classes remaining at $\alpha = 0.999$ when $\epsilon = 10^{-8}\mathrm{m}^2\mathrm{s}^{-3}$. This leads to $n(r)$ being narrower at $\epsilon = 10^{-8}\mathrm{m}^2\mathrm{s}^{-3}$ than at $\epsilon = 10^{-2}\mathrm{m}^2\mathrm{s}^{-3}$. The reason for faster removal of the crystals of smaller size classes in the more quiescent case is due to the velocity difference as discussed in §4.4.3.4.

When the crystals are instead initialised with the same concentration of crystals in each size class the mean radius increases with ϵ. In these cases there are initially substantially more crystals in the smaller size classes than in the larger size classes. The reason why the mean radius increases slightly with ϵ when we initialise with the same concentration of crystals in each size class is discussed in §4.4.3.4 but redistribution here makes the effect less pronounced, as crystals cascade down from the larger size classes.

5.5 Conclusion

In this chapter we have introduced a method to more accurately redistribute a fractured crystal into the surrounding size classes. The crystal fractures into ζ crystals of size class 1 and the remaining volume of the fractured crystal is redistributed in the two neighbouring size classes above and below the fragment size. In the case when the fractured crystal is the size of a smaller size class, the fractured crystal is put into that size class. In the case when the fractured crystal is smaller than the smallest size class, the fractured crystal are put into the smallest size class. The resulting equation (5.13) to redistribute the crystals is implemented into the simple frazil model described in §3. In all cases redistribution acted to decrease the mean radius of the crystal population due to the cascading effect of adding crystals to the smaller size classes. For a given value of n_1, adding in redistribution increased the number of crystals. For smaller values of ϵ, the collision frequency decreased with the SDR formulation compared to the SD formulation because the maximum possible difference in relative velocity decreased faster than in the case when redistribution was not included due to the larger crystals being removed faster. For larger values of ϵ, the change in collision frequency was small due to the competing effects of increasing the number of crystals and decreasing the mean crystal size.

Although this method does more accurately model the volume changes within the crystal population model, it is limited by the model setup. In order to accurately

redistribute the crystals, the size classes must have volume $V_k = kV_1$ such that $V_k - V_{k-1} = V_1$. This would require too many size classes for the population model to run on reasonable timescales. Further, there is uncertainly surrounding the choice of V_1 and whether crystal fracture should always only fracture off crystals of the smallest size classes.

Using the spherical, differential size redistribution formulation changes both the collision frequency and the distribution of crystals among the size classes. It is likely to change the heat flux and the resultant properties of the water column when implemented into a full frazil ice model which depends on the number of crystals and the crystal sizes. Before doing this, we shall enact further improvements to the parametrisation of crystal collisions.

"He has inscribed a circle on the face of the waters at the boundary between light and darkness."

— Job 26:10 ESV

6 Variable crystal orientation

Contents

6.1 Introduction

Having addressed in §4-§5 the first three weaknesses of the current method used in frazil ice models to parametrise crystal collisions we now move on to the next weakness outlined in §2.5. We noted that frazil ice models incorrectly assume that the collision radius $r_{c,i}$ when considering crystal collisions involving size class i is equal to the crystal radius r_i or the equivalent radius r_i^e depending on the model (see §2.3.4) for details. As was addressed in §4, both crystals should contribute to the collision radius, $r_{c,ij} = r_{c,i} + r_{c,j}$ in collisions between crystals of size class i and

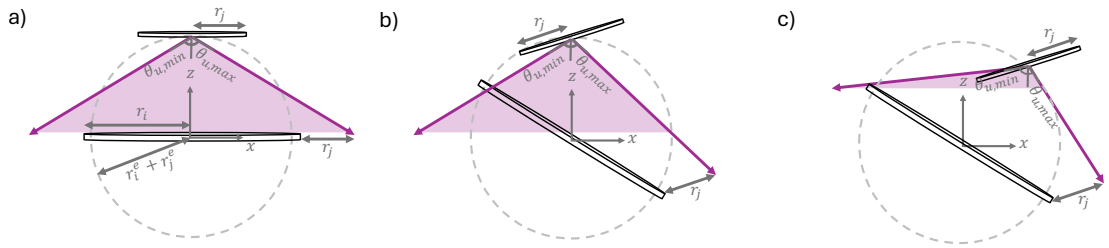

Figure 6.1: a) In the instantaneous rest frame of the bottom crystal consider two crystals approaching with centres-of-mass separation $r_i^e + r_j^e$. The top crystal will collide with the bottom crystal if the orientation of the relative velocity vector, defined to have angle θ_u to the $-z$-axis, and ϕ_u to the x-axis within the x-y plane, is between a range of angles. For clarity, in this sketch, we allow the crystals to only rotate in the $x-z$ plane and their centre of masses lie along the line $y = 0$ with $-\pi \leq \phi_u \leq \pi$. Collisions occur for $\theta_{u,min} \leq \theta_u \leq \theta_{u,max}$. Panel a shows $\theta_{u,min}$ and $\theta_{u,max}$ for the symmetric system, where the axis of each of the crystals is along the z axis and $|\theta_{u,min}| = |\theta_{u,max}|$. b) $\theta_{u,min}$ and $\theta_{u,max}$ change as the orientation of the crystals change and $|\theta_{u,min}| \neq |\theta_{u,max}|$. c) $\theta_{u,min}$ and $\theta_{u,max}$ also depend on the position of each of the crystals.

size class j, rather than just a single crystal of size class i. In the previous chapters (§4 and §5), we calculated the collision frequency for spherical crystals assuming that all crystals within a sphere of radius $r_e^i + r_j^e$ and with a negative relative radial velocity collide. However, for two cylinders at a distance $r_i^e + r_j^e$, collisions are only possible when the velocity vector has certain orientations (panel a in Figure 6.1). The relative velocity has angle θ_u to the $-z$-axis and ϕ_u to the x-axis within the x-y plane. The range of angles over which collisions are possible depend on the orientation (panel b in Figure 6.1) and initial position (panel c in Figure 6.1) of each of the crystals.

In this chapter we calculate two new expressions for the encounter frequency including the effects of variable crystal and velocity orientation. In §6.2 we first define the angles used to describe the orientation of the crystals. In §6.3 we calculate an expression for the encounter frequency which takes into account the relative velocity of the crystals and their orientation. As certain orientations of the crystals and the relative velocity vector are more probable than others, in §6.3 we then discuss different options for the probability distribution functions (PDFs) of the cylinder orientation and relative velocity. In §6.5 these PDFs are combined with the method

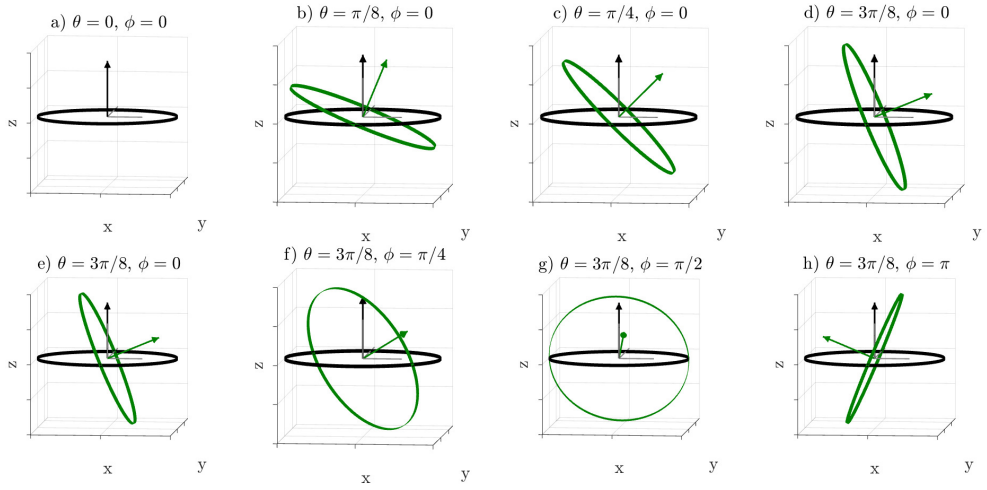

Figure 6.2: The orientation of a cylinder changes as the cylinder is rotated by an angle θ from the $z-$axis and ϕ about the $z-$axis in spherical polar coordinates. In panels a - d, the cylinder is initially orientated with its axis vertical ($\theta = \phi = 0$). θ is increased from 0 in panel a to $3\pi/8$ in panel d. In panels e - h, $\theta = 3\pi/8$ and ϕ is increased from 0 to π.

in §6.3 to obtain a new expression for the encounter frequency. We discuss how this expression for the encounter frequency compares to the expression used in §5 in §6.7.

6.2 Cylinder orientation

We begin by defining the crystal orientation angles needed to calculate the collision criteria. We can describe the orientation of a cylinder using the angles θ and ϕ in spherical polar co-ordinates where θ is the angle the axis of the cylinder makes with the $z-$axis and ϕ is the angle the axis of the cylinder makes with the $x-$axis in the x-y plane. Figure 6.2 shows how the axis of the cylinder changes as θ and ϕ are increased. There is a symmetry the area swept out by the cylinder being identical when the axis of the cylinder makes an angle θ or an angle $\pi - \theta$ with the z-axis. Therefore, all relevant cylinder orientation are met by varying θ between 0 and $\pi/2$, and ϕ between 0 and 2π.

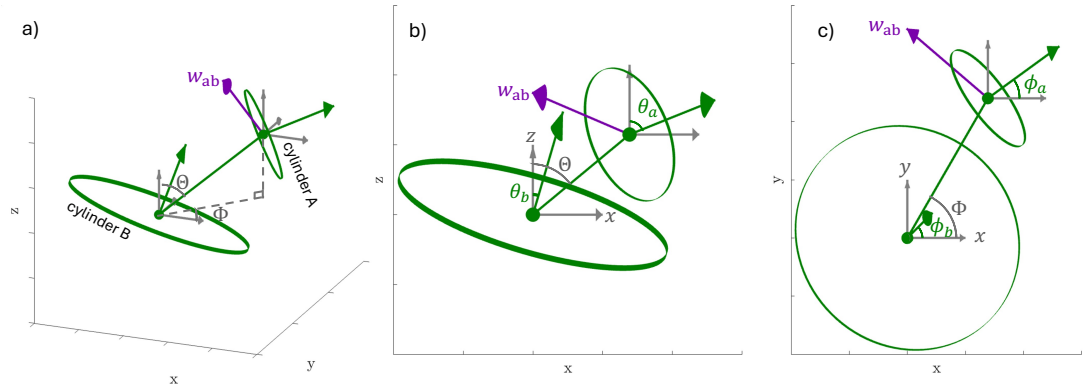

Figure 6.3: a) We consider two cylinders, A and B approaching. We work in the rest from of cylinder B such that cylinder A has velocity $\mathbf{w}_{ab}$ and the x, y, z directions are externally imposed rather than being measured relative to the disk. The centre of mass of cylinder B is at (0, 0, 0) and the centre of mass of cylinder A is at $(r_{max} \sin\Theta\cos\Phi, r_{max}\sin\Theta\sin\Phi, r_{max}\cos\Theta)$ where Θ and Φ are the respective polar and azimuthal angles in spherical polar co-ordinates with respect to the Cartesian axes. b) cylinders A and B are at respective angles θ_a and θ_b to the z-axis. c) cylinders A and B have respective azimuthal angles ϕ_a and ϕ_b to the z-axis. Panels a-c are the same initial setup but viewed in different planes.

6.3 Collision criteria

We now derive a new expression for the encounter frequency that accounts for the variable orientation and direction of the relative velocity of the cylinders. In the special case of two cylinders of sizes classes i and j with relative velocity $\mathbf{w}_{ij} = w_{ij}\hat{\mathbf{z}}$, the maximum possible separation between the centre of masses whilst the cylinders are in contact is given by $r_{max,ij} = \sqrt{r_i^2 + (w_i/2)^2} + \sqrt{r_j^2 + (w_j/2)^2}$.

We denote the cylinder of size class i as cylinder A and the cylinder of size class j as cylinder B. We consider these two cylinders approaching with the setup shown in Figure 6.3. Cylinder A has orientation $\theta = \theta_a$ and $\phi = \phi_a$ and cylinder B has orientation $\theta = \theta_b$ and $\phi = \phi_b$ where the angles are measured with respect to the lab frame. The centre of mass of cylinders A and B is at $\mathbf{x}_a$, $\mathbf{x}_b$, respectively, and we set $\mathbf{x}_b = 0$ and $\mathbf{x}_a = (r_{max,ab}\sin\Theta\cos\Phi, r_{max,ab}\sin\Theta\sin\Phi, r_{max,ab}\cos\Theta)$ where Θ is the polar angle with respect to the Cartesian z axis, and Φ is the azimuthal angle relative to the x-axis (so that the y axis has $\Phi = \pi/2$). In the Cartesian coordinate system, cylinders A and B move with velocity $\mathbf{u}_{pa} = (u_{pa,x}, u_{pa,y}, u_{pa,z})$,

$\mathbf{u}_{pb} = (u_{pb,x}, u_{pb,y}, u_{pb,z})$. We work in the rest frame of cylinder B such that cylinder A has velocity $\mathbf{w}_{ab} = \mathbf{u}_{pa} - \mathbf{u}_{pb} = (w_{ab,x}, w_{ab,y}, w_{ab,z})$. We assume that the background flow between the disks is uniform. We assume that the orientation of the cylinders stays constant as they approach each other. In reality, for turbulent flow below the Kolmogorov lengthscale the relative velocity should vary linearly with distance (Pope, 2000) and the orientations of the cylinders might change. However, for simplicity and ease of comparison with the hydrodynamic case introduced in §7 we assume changes in orientation are negligible. A collision will occur if the surface of the cylinders come into contact.

The relative velocities in the spherical coordinate system are related to the relative velocities in the lab frame by

$$w_{ab,r} = w_{ab,x} \sin\theta_u \cos\phi_u + w_{ab,y} \sin\theta_u \sin\phi_u - w_{ab,z} \cos\theta_u, \tag{6.1}$$

$$w_{ab,\Theta} = -w_{ab,x} \cos\theta_u \cos\phi_u - w_{ab,y} \cos\theta_u \sin\phi_u - w_{ab,z} \sin\theta_u, \tag{6.2}$$

$$w_{ab,\Phi} = -w_{ab,x} \sin\phi_u + w_{ab,y} \cos\phi_u. \tag{6.3}$$

where θ_u and ϕ_u are the angles in spherical polar co-ordinates describing the orientation of $\mathbf{w}_{ab}$ relative to the $-z$ and x axes respectively.

Assuming that the probability of the centre of mass of cylinder A being located at angle Φ to cylinder B is uniform then the collision probability should be independent of Φ. We hence define a collision kernel,

$$\mathcal{K}_{coll,ab} = \mathcal{K}_{coll,ab}(\Theta, \phi_a, \theta_a, \phi_b, \theta_b, w_{ab,r}, w_{ab,\theta}, w_{ab,\Phi}) \tag{6.4}$$

where $\mathcal{K}_{coll,ab} = 0$ when there is no collision and $\mathcal{K}_{coll,ab} = 1$ when there is a collision. Using the collision kernel, in the spherical approximation the encounter

frequency is now given by

$$\mathcal{F}_{enc,ab} = \frac{2\pi r_{max,ab}^2}{V} \int_{-\infty}^{\infty} \mathrm{d}w_{ab,r} \int_{-\infty}^{\infty} \mathrm{d}w_{ab,\Theta} \int_{-\infty}^{\infty} \mathrm{d}w_{ab,\Phi} \times \int_0^{\pi/2} \mathrm{d}\theta_b \int_0^{2\pi} \mathrm{d}\phi_b \int_0^{\pi/2} \mathrm{d}\theta_a \int_0^{2\pi} \mathrm{d}\phi_a \int_0^{\pi} \sin\Theta \, \mathrm{d}\Theta \times \mathcal{K}_{coll,ab}(\Theta, \phi_a, \theta_a, \phi_b, \theta_b, w_{ab,r}, w_{ab,\Theta}, w_{ab,\Phi}) |w_{ab,r}| \times \rho(\phi_a)\rho(\theta_a)\rho(\phi_b)\rho(\theta_b)\rho(w_{ab,r})\rho(w_{ab,\Theta})\rho(w_{ab,\Phi}). \quad (6.5)$$

where $\rho(x)$ is the probability distribution function (PDF) of variable x. Assuming $\mathcal{K}_{coll,ab} = 1$ for all values of $\Theta, \phi_a, \theta_a, \phi_b, \theta_b, w_{ab,\Theta}, w_{ab,\Phi}$ and $w_{ab,r} < 0$ and $\mathcal{K}_{coll,ab} = 0$ for all values of $\Theta, \phi_a, \theta_a, \phi_b, \theta_b, w_{ab,\Theta}, w_{ab,\Phi}$ and $w_{ab,r} \geq 0$, and that $\int_0^{\infty} \rho(w_{ab,r}) \mathrm{d}w_{ab,r} = 1/2$ we obtain,

$$\mathcal{F}_{enc} = \frac{2\pi r_{max,ab}^2 \langle |w_{ab,r}| \rangle}{V} \quad (6.6)$$

which is the same expression (4.46) that was previously used to obtain the encounter frequency when $r_{max,ab} = r_{c,ab}$.

In the limit of quiescent flow, the velocity of each of the cylinders is parallel which means the collision rate is the same under the cylindrical or spherical approximation because $\mathbf{w}_{ab} = w_{ab,g}\hat{z} = w_{ab,g}(\cos\Theta\hat{\mathbf{R}} - \sin\Theta\hat{\mathbf{\Theta}})$. In this limit a collision will occur if the projected area of the cylinders in the $x - y$ plane overlaps and the faster rising cylinder is below the slower rising cylinder. The expression for the collision kernel becomes,

$$\mathcal{F}_{enc,ab} = \frac{2\pi r_{max,ab}^2}{V} \int_0^{\pi/2} \mathrm{d}\theta_b \int_0^{2\pi} \mathrm{d}\phi_b \int_0^{\pi/2} \mathrm{d}\theta_a \int_0^{2\pi} \mathrm{d}\phi_a \int_0^{\pi} \sin\Theta |w_{ab,g} \cos\Theta| \mathrm{d}\Theta \times \mathcal{K}_{coll}(\Theta, \phi_a, \theta_a, \phi_b, \theta_b)\rho(\phi_a)\rho(\theta_a)\rho(\phi_b)\rho(\theta_b). \quad (6.7)$$

If $\mathcal{K}_{coll,ab} = 1$ when the disks have a negative radial velocity ($\mathcal{K}_{coll,ab} = 1$ for all values of $\phi_a, \theta_a, \phi_b, \theta_b$ and $\pi/2 \leq \Theta \leq \pi$) and $\mathcal{K}_{coll,ab} = 0$ when the disks have a positive radial velocity ($\mathcal{K}_{coll,ab} = 0$ for all values of $\phi_a, \theta_a, \phi_b, \theta_b$ and $0 \leq \Theta < \pi/2$) we obtain,

$$\mathcal{F}_{enc,ab} = \frac{\pi r_{max,ab}^2 |w_{g,ab}|}{V} \quad (6.8)$$

which is again the same expression (2.58) previously used to obtain the encounter frequency in the quiescent limit when $r_{max,ab} = r_{c,ab}$.

Calculating $\mathcal{F}_{enc,ab}$ requires knowledge of the PDFs of $\phi_a, \theta_a, \phi_b, \theta_b, w_{ab,r}, w_{ab,\Theta}, w_{ab,\Phi}$. In the discussion below we suggest potential choices for these PDFs.

6.4 Choices for probability distributions

6.4.1 Choices for orientation probability

Understanding how anisotropic particles behave in turbulence is a complex process (see review by Voth and Soldati, 2017). In quiescent flow, it has been shown that the falling style of disk-shaped particles can be classified into six different regimes based on their rise velocity and their inertia (Auguste et al., 2013). Disks rising slowly with small inertia move with the axis of the disk parallel to the velocity (they rise broadside on). As the rise velocity and inertia increases the disks tend to tumble. Using the results from Auguste et al. (2013), where the region boundaries are based on the dimensionless inertia ratio I^* and Archimedes number Ar of the disks we can find where frazil ice crystals would fit on the regime diagram. For frazil ice of constant aspect ratio, $I^* = \pi\rho_I[1+4/(3d)]/(64d\rho)$ and $Ar = \sqrt{3/8}v_g r/\nu$. Substituting the values for the aspect ratio d, density of ice ρ_I, density of water ρ, rise velocity v_g, crystal radius r and kinematic viscosity ν used in §3 we find that for frazil ice in water $I^* \sim 10^{-3}$ and $Ar < 10$. This means that in quiescent flow, frazil ice crystals would lie in the steady velocity regime, where they rise with their axis parallel to the velocity.

As the flow gets more turbulent, the orientation of the disks gets more random as they align with the principle axis of the strain rate matrix (Roy et al., 2018) which is along different directions in different parts of the flow. This was observed in the experimental results of Tinklenberg et al. (2024) and the numerical results of Challabotla et al. (2015) and Anand et al. (2020).

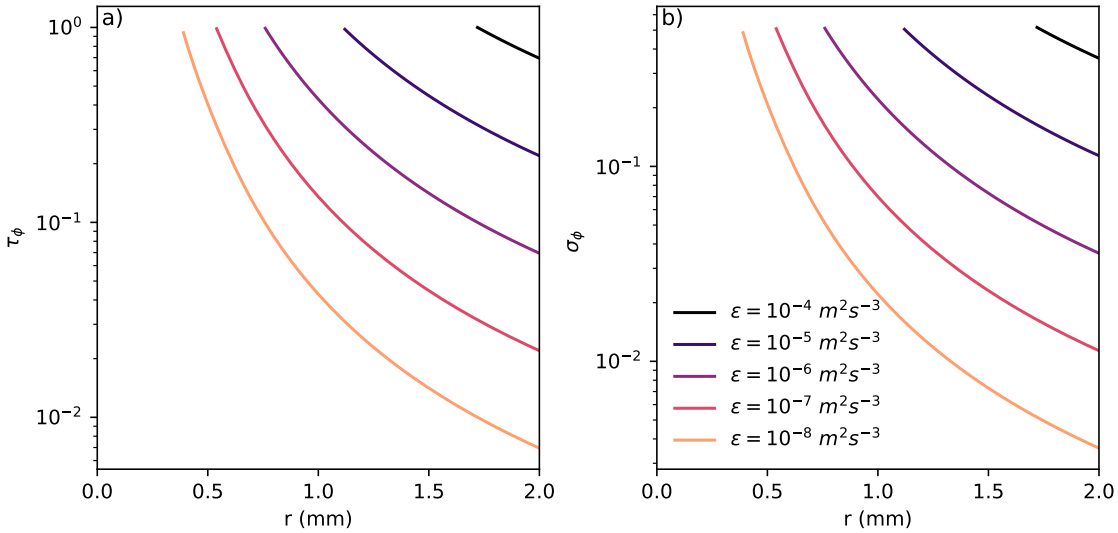

Figure 6.4: Panel a) τ_ϕ as a function of r for different ϵ. Only values of ϵ and r where $\tau_\phi \leq 1$ are plotted. Crystals orientation are close to the horizontal when $\tau_\phi < 1$ (see Gustavsson et al., 2021) which requires larger r at small ϵ. b) the standard deviation of the angle that the crystal axis makes with the vertical for the values of ϵ and r where $\tau_\phi < 1$.

To determine when turbulent effects become significant Gustavsson et al. (2021) performed a scale analysis on the equations of motion for small disks with $r \ll \eta_K$ falling in the Stokes regime. They found that the axes of the disks are randomly distributed when the rotation of the disk due to turbulence is faster than the rotation due to settling. This occurs when the Stokes number is small and the velocity due to rise is much smaller than the velocity due to turbulence. Following Gustavsson et al. (2021), we denote the relative ratio of timescales for turbulence and settling as $\tau_\phi = 3(v_K/v_g)^2$, where $v_K = (\nu\epsilon)^{1/4}$ is the Kolmogorov velocity scale. When $\tau_\phi \gg 1$, the orientation of the disks is random. When $\tau_\phi < 1$, the crystal is oriented close to the horizontal as its orientation is mainly due to buoyant rise. Using the values for v_g and ν defined in §3 we calculate τ_ϕ. Panel a of Figure 6.4 plots the values of ϵ and r where $\tau_\phi < 1$ (at $\tau_\phi = 1$ the crystals are approximately randomly orientated). Crystals with radii less than 0.5 mm have $\tau_\phi < 1$ for $\epsilon \geq 10^{-8}$ m^2 s^{-3}. Crystals with larger radii are predicted to have a high probability of having an orientation close to the horizontal in more quiescent conditions, with the orientation becoming more random as the turbulence increases. For $\epsilon > 10^{-4}$ m^2 s^{-3} any crystal with $r < 1.7$

mm is approximately randomly orientated.

When $\tau_\phi < 1$, the standard deviation of the crystal orientation, σ_ϕ, from the horizontal depends on the rate at which the crystal orientation changes due to the local velocity gradients, the time it takes for the crystal to cross an eddy, and the time taken for the flow to respond to other inertial effects. Gustavsson et al. (2021) estimated how σ_ϕ changes with the timescale for each of these processes. Calculating the different timescales in table 2 of Gustavsson et al. (2021) we find that when $\tau_\phi < 1$, frazil ice crystals are in regime 2 of the phase space in Gustavsson et al. (2021). In this regime, the standard deviation of the particle orientation is given by $\sigma_\phi \sim 1.54(\nu\epsilon)^{1/2}/v_g^2$. Panel b of Figure 6.4 plots the standard deviation of the particle orientations when $\tau_\phi < 1$.

However, the true orientation of frazil ice crystals is made more complicated because larger crystals have at least one dimension larger than the Kolmogorov scale. This means that crystals interact with the non-linear variation of the velocity field, and the point-particle models used to get the previous results are no longer accurate (Voth and Soldati, 2017). Furthermore, the particle Reynolds number of larger crystals is greater than one, suggesting that the Stokes flow assumption is not valid. However, the experimental results of Tinklenberg et al. (2024) suggest that disks with diameters larger than the Kolmogorov scale, falling with particle Reynolds numbers greater than one follow a similar qualitative trend, with the axis starting parallel to the vertical for low ϵ and then becoming more randomly orientated as the turbulence increases.

All of these results apply to dilute particle suspensions. Hamid et al. (2024) ran simulations for suspensions of disk-shaped particles with volume fractions increasing to 0.1. As the volume fraction occupied by the particles increased, the orientation of the particles shifted from being dominantly horizontal when the volume fraction was 0.0003 to dominantly vertical when the volume fraction was greater than 0.001.

At intermediate volume fractions the distribution was more random.

Given there is still much uncertainty about the particle orientations, we suggest two parametrisations for the orientations of the crystals to explore in this thesis. In the first parametrisation the orientations are uniformly distributed in any direction with $\rho(\theta_a) = \rho(\theta_b) = 2/\pi$, for $0 \leq \theta_a, \theta_b \leq \pi/2$. In the second parametrisation the orientation is sharply peaked around the axis of the crystal being vertical, which we approximate by $\rho(\theta_a) = \rho(\theta_b) = \delta(\theta_a) = \delta(\theta_b)$. In both cases we assume a uniform distribution for $\rho(\phi_a)$ and $\rho(\rho_b)$.

6.4.2 Choices for velocity probability

Following the approach outlined in §4.2.3.1, and the assumption used in many collision models (Zaichik and Alipchenkov, 2003) that each component of the particle velocity correlation can be modelled as Gaussian, for particles separated by a distance $r_{max,ab}$ we find

$$\rho(w_{ab,r}) = \frac{1}{\sqrt{2\pi}\sigma_{abR}} \exp\left[\frac{-(w_{ab,r} - w_{ab,g}\cos\Theta)^2}{2\sigma_{abR}^2}\right], \tag{6.9}$$

$$\rho(w_{ab,\Theta}) = \frac{1}{\sqrt{2\pi}\sigma_{ab\Theta}} \exp\left[\frac{-(w_{ab,\Theta} + w_{ab,g}\sin\Theta)^2}{2\sigma_{ab\Theta}^2}\right], \tag{6.10}$$

$$\rho(w_{ab,\Phi}) = \frac{1}{\sqrt{4\pi}\sigma_{ab\Phi}} \exp\left[\frac{-w_{ab,\Phi}^2}{2\sigma_{ab\Phi}^2}\right]. \tag{6.11}$$

In the limit when the scaled particle relaxation timescale $\tau_p^* \to 0$, which is the limit we have used to derive this model, $\sigma_{ab\Theta} = \sigma_{ab\Phi} = \sqrt{2}\sigma_{abR}$, with $\sigma_{abR} = \sigma_{abR}(r_{max,ab})$ given by (4.41) (see Pope, 2000). When $\sigma_{ab} \ll w_{ab,g}$ the PDFs of $w_{ab,r}$ and $w_{ab,\Theta}$ are very sharply peaked about $w_{ab,g}\cos\Theta$ and $-w_{ab,g}\sin\Theta$ respectively.

6.5 Numerical method to calculate the encounter frequency

Having obtained an expression (6.5) for the encounter frequency that accounts for the non radial velocity components and variable orientation of the crystals and having found choices for the PDFs needed to calculate $\mathcal{F}_{enc,ab}$ we now calculate

$\mathcal{F}_{enc,ab}$ for frazil ice crystals. The value of $\epsilon^{1/2} r_{max,ab}$ can change by several orders of magnitude which means that finding the encounter frequency using (6.5) requires evaluating the collision kernel $\mathcal{K}$ over a large range of velocities. However, when the crystal orientations and velocities do not change as they approach (which is the case considered here), the probability of a collision depends only on the direction of the relative velocity. Therefore, instead of testing if a collision occurs for all possible values of $w_{ab,r}$, $w_{ab,\Theta}$, $w_{ab,\Phi}$, we instead calculate the range of θ_u and ϕ_u over which a collision occurs. We initialise two cylinders at separation $r_{max,ab}$, orientation θ_a, θ_b, ϕ_a, ϕ_b and with the velocity vector orientated at angle θ_u, ϕ_u. We then let the cylinders to move towards each other. A collision occurs if the cylinder surfaces make contact during the simulation and does not occur if the surfaces do not make contact. We do this for a discrete set of angles and relative sizes, with $\Theta = [0, 5, 15, \ldots, 75, 85, 86, 87, 88, 89]^o$, $\theta_a = [0, 5, 15, \ldots, 75, 85, 90]^o$, $\theta_b = [0, 5, 15, \ldots, 75, 85, 90]^o$, $\phi_a = [5, 15, \ldots, 345, 355]^o$, $\phi_b = [5, 15, \ldots, 345, 355]^o$ and when $\max\{r_i/r_j, r_j/r_i\} = [1, 4/3, 2, 5, 10, 200]$. The result is two 6D matrixes at each r_i/r_j ratio in $\phi_u, \Theta, \theta_a, \theta_b, \phi_a, \phi_b$ space with one matrix containing the maximum value of θ_u required for a collision at $\phi_u = [0, 1, 2, \ldots, 359, 360]^o$ and the other containing the minimum value of θ_u required for a collision.

In Figure 6.5a), we plot the range of θ_u and ϕ_u over which a collision occurs for for $r_i = r_j$, $\Theta = 35^o$, $\theta_a = 35^o$, $\theta_b = 65^o$, $\phi_a = 55^o$, $\phi_b = 155^o$. The collision boundary is initially determined to within 0.5^o accuracy for $\phi_u = [-180, -175, -170, \ldots, 180]^o$ (white circles) and then interpolated (white line) to find the collision boundary at 1^o intervals in ϕ_u. In panels b-f of Figure 6.5 we show how this collision boundary changes when $\theta_a, \theta_b, \phi_a, \phi_b$ and Θ each increase and decrease by 10^o with the other values being kept constant. We then linearly interpolate over the full matrix of gridded values of θ_u to find the collision boundary for $\Theta, \theta_a, \theta_b$ spaced by 1^o and ϕ_a, ϕ_b spaced by 10^o. The wider spacing in ϕ_i is chosen to speed up the calculation and because the collision boundary was observed to vary less with ϕ_i than with θ_i

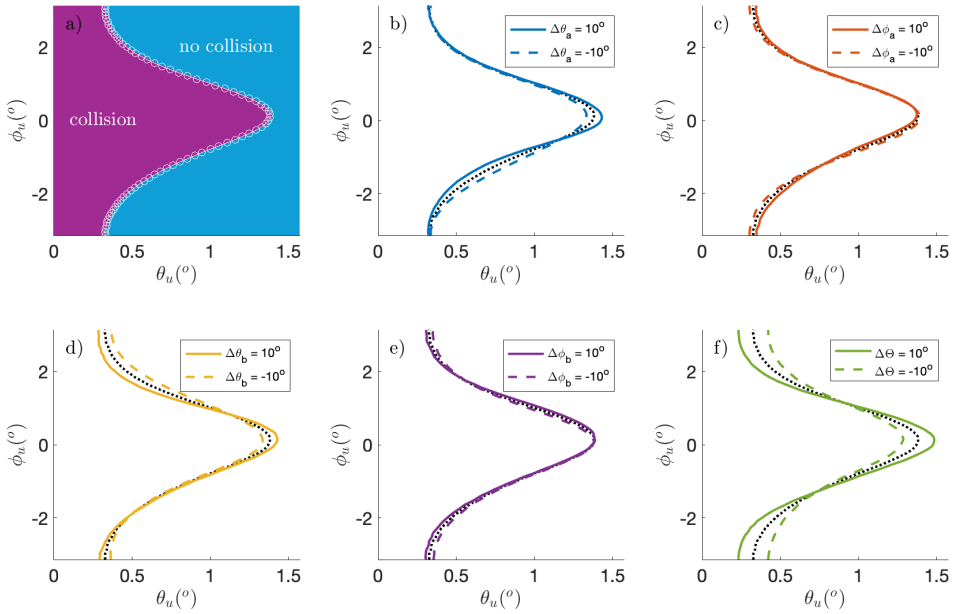

Figure 6.5: a) the collision boundary for $r_i = r_j$, $\Theta = 35^o$, $\theta_a = 35^o$, $\theta_b = 65^o$, $\phi_a = 55^o$, $\phi_b = 155^o$. The collision boundary is found to within 1/2 a degree for $\phi_u = [-180, -175, -170, \ldots, 180]^o$ (white circles) and then interpolated (white line) to find the collision boundary at 1 degree intervals. The new collision boundary when b) θ_a, c) θ_b, d) ϕ_a, e) ϕ_b, f) Θ each increase (solid lines) and decrease (dashed lines) by 10^o with all the other values staying constant. The dotted black line is the original collision boundary

and Θ.

We use (6.9)-(6.11) to obtain the joint probability distribution $\rho(\theta_u, \phi_u)$ at each value of $w_{ab,R}$ for selected values of $\max\{r_i/r_j, r_j/r_i\} = [1, 1.01, 1.1, 1.33, 2, 5, 10, 100]$. The encounter frequency is then given by,

$$\mathcal{F}_{enc,ab} = \frac{2\pi r_{max,ab}^2}{V} \int_{-\infty}^{\infty} \mathrm{d}w_{ab,r} \int_0^{\pi/2} \mathrm{d}\theta_b \int_0^{2\pi} \mathrm{d}\phi_b \int_0^{\pi/2} \mathrm{d}\theta_a \times \int_0^{2\pi} \mathrm{d}\phi_a \int_0^{\pi} \sin\Theta \, \mathrm{d}\Theta \int_{-\pi}^{\pi} d\phi_u \int_{\theta_{u,min}(\phi_u,\Theta,\phi_a,\theta_a,\phi_b,\theta_b)}^{\theta_{u,max}(\phi_u,\Theta,\phi_a,\theta_a,\phi_b,\theta_b)} \mathrm{d}\theta_u \times |w_{ab,r}| \rho(\phi_a)\rho(\theta_a)\rho(\phi_b)\rho(\theta_b)\rho(w_{ab,r})\rho(\theta_u, \phi_u | w_{ab,r}). \quad (6.12)$$

Comparing to (6.5), the collision kernel is now accounted for by the introduction of the integration limits on the θ_u integral.

6.6 Results for the encounter frequencies

We shall now compare our new expression for the encounter frequency (6.12) to the expression (4.46) which was used to calculate the encounter frequency in §5. In this chapter we have introduced two changes to method to calculate the encounter frequency. Firstly, we have altered the collision radius of the sphere, choosing all disks to have the same aspect ratio d such that $r_{c,ij} = r_{max,ij} = (r_i+r_j)(1+1/d^2)^{1/2}$ instead of $r_{c,ij} = r_i^e = r_j^e$ which was used in §5. Secondly, we have introduced a collision kernel that depends on the crystal orientation and the non-radial components of the relative velocity. To isolate the effects of these two changes we write (6.12) as

$$\mathcal{F}_{enc,ij} = \frac{2\pi(r_i^e + r_j^e)^2\langle|w_{ij,r}(r_i^e + r_j^e)|\rangle\mathcal{R}(r_{c,ij})\mathcal{W}(r_{c,ij})\mathcal{T}_{ij}}{V}, \tag{6.13}$$

where $\mathcal{R}(r_{c,ij}) = r_{c,ij}^2/(r_i^e + r_j^e)^2$, $\mathcal{W}(r_{c,ij}) = \langle|w_{ij,r}(r_{c,ij})|\rangle/\langle|w_{ij,r}(r_i^e + r_j^e)|\rangle$ and

$$\begin{aligned}\mathcal{T}_{ij} = \frac{1}{\langle|w_{ij,r}(r_{c,ij})|\rangle}\int_{-\infty}^{\infty}\mathrm{d}w_{ij,r}\int_0^{\pi/2}\mathrm{d}\theta_j\int_0^{2\pi}\mathrm{d}\phi_j\int_0^{\pi/2}\mathrm{d}\theta_i\times \\ \int_0^{2\pi}\mathrm{d}\phi_i\int_0^{\pi}\sin\Theta\,\mathrm{d}\Theta\int_{-\pi}^{\pi}d\phi_u\int_{\theta_{u,min}(\phi_u,\Theta,\phi_i,\theta_i,\phi_j,\theta_j)}^{\theta_{u,max}(\phi_u,\Theta,\phi_i,\theta_i,\phi_j,\theta_j)}\mathrm{d}\theta_u\times \\ |w_{ij,r}|\rho(\phi_i)\rho(\theta_i)\rho(\phi_j)\rho(\theta_j)\rho(w_{ij,r})\rho(\theta_u,\phi_u|w_{ij,r})).\end{aligned} \tag{6.14}$$

$\mathcal{R}(r_{c,ij})$ and $\mathcal{W}_{ij}(r_{c,ij})$ respectively account for the modification to the area of the collision sphere and the mean radial velocity when the collision radius changes. $\mathcal{T}_{ij}$ accounts for a reduction to the collision rate due to the non-radial velocity components and variable orientation being considered.

In §6.4.1 we outlined two choices of $\rho(\theta_i)$ for $i = a, b$ leading to two options for the encounter frequency when non-radial velocity components are included. We denote the encounter frequency when the disks are parallel, $\rho(\theta_i) = \delta(\theta_i)$ as $\mathcal{F}_{enc,ij}^0$ and the encounter frequency when the disks are randomly oriented, $\rho(\theta_i) = 2/\pi$ as $\mathcal{F}_{enc,ij}^A$. For completeness, we also calculate the encounter frequency for $r_{c,ij} = r_i+r_j$ and $\mathcal{T}_{ij} = 1$ as Jones and Wells (2018), Souillé et al. (2020), Svensson and Omstedt (1994), Wang and Doering (2005), and Yang et al. (2023) choose this method to calculate the collision radius and it will be interesting compare how the encounter

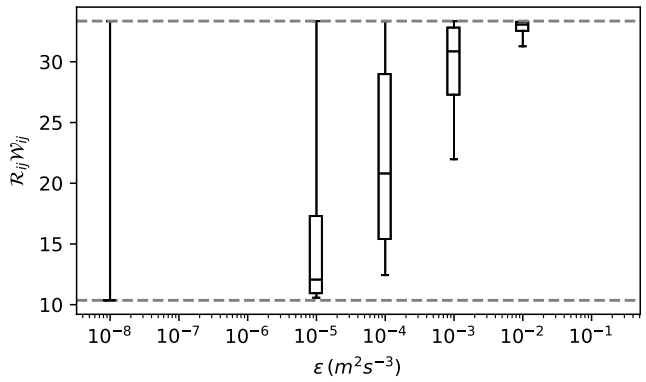

Figure 6.6: Box plots showing the distribution of $\mathcal{W}_{ij}(r_{c,ij})\mathcal{R}_{ij}(r_{c,ij})$ for $r_{c,ij} = r_i + r_j$ and $r_{max,ij}$ and $0.01\,\text{mm} \leq r_i, r_j \leq 2\,\text{mm}$ as a function of ϵ. Due to the small aspect ratio of the disks, box plots are indistinguishable and lie on top of each other for $r_{c,ij} = r_i + r_j$ and $r_{c,ij} = r_{max,ij}$. The whiskers of the plot correspond to the range of $\mathcal{W}_{ij}(r_{c,ij})\mathcal{R}_{ij}(r_{c,ij})$. The box plots at $\epsilon = 10^{-8}$ m^{2}s^{-3} have a very small interquartile range shown as a single line close to $\mathcal{R}_{ij}\mathcal{W}_{ij} = 10$. The dashed lines are the minimum $[(2d/3)^{2/3}]$ and maximum $[(1 + 1/d^2)^{3/2}(2d/3)]$ value of $\mathcal{W}_{ij}(r_{c,ij})\mathcal{R}_{ij}(r_{c,ij})$.

frequency changes across all documented choices of $r_{c,ij}$. We denote the encounter frequency calculated with this method as $\mathcal{F}^r_{enc,ij}$ and the encounter frequency setting $r_{c,ij} = r^e_i + r^e_j$ as $\mathcal{F}_{enc,ij}$.

We first illustrate how changing the collision radius is likely to alter the encounter frequency. We calculate $\mathcal{W}_{ij}\mathcal{R}_{ij}$ for $0.01\,\text{mm} \leq r_i, r_j \leq 2\,\text{mm}$ for $r_{c,ij} = r_i + r_j$ and $r_{c,ij} = r_{max,ij}$. Figure 6.6 shows box plots of the range of values for $\mathcal{W}_{ij}\mathcal{R}_{ij}$ for $\epsilon = [10^{-8}, 10^{-5}, 10^{-4}, 10^{-3}, 10^{-2}]$ m^{2}s^{-3}. As $d = 50$, $r_{max,ij} \approx r_i + r_j$ so the box plots for both choices of $r_{c,ij}$ are indistinguishable. The value of $\mathcal{W}_{ij}\mathcal{R}_{ij}$ is close to $\mathcal{R}^2_{ij} = (2d/3)^{2/3}$ for $r_{c,ij} = r_i + r_j$ for almost all values of $r_{c,ij}$ for $\epsilon = 10^{-8}$ m^{2}s^3 as the relative velocity is dominated by the buoyant rise velocity to $\langle|w_{r,ij}|\rangle$ is independent of the collision radius. The exception is when the crystals are very close to or exactly the same size and in this case the relative velocity is dominated by the turbulent component. As ϵ increases, $\mathcal{W}_{ij}\mathcal{R}_{ij}$ approaches $\mathcal{R}^3_{ij} = (1 + 1/d^2)^{3/2}(2d/3)$ for $r_{c,ij} = r_{max,ij}$ as the turbulent component becomes the dominant contribution to the rise velocity and the turbulent relative velocity $\propto \mathcal{R}(r_{c,ij})$. Therefore, from the ranges shown in Figure 6.6 we expect the increase in collision radius for $r_{c,ij} = r_i + r_j$

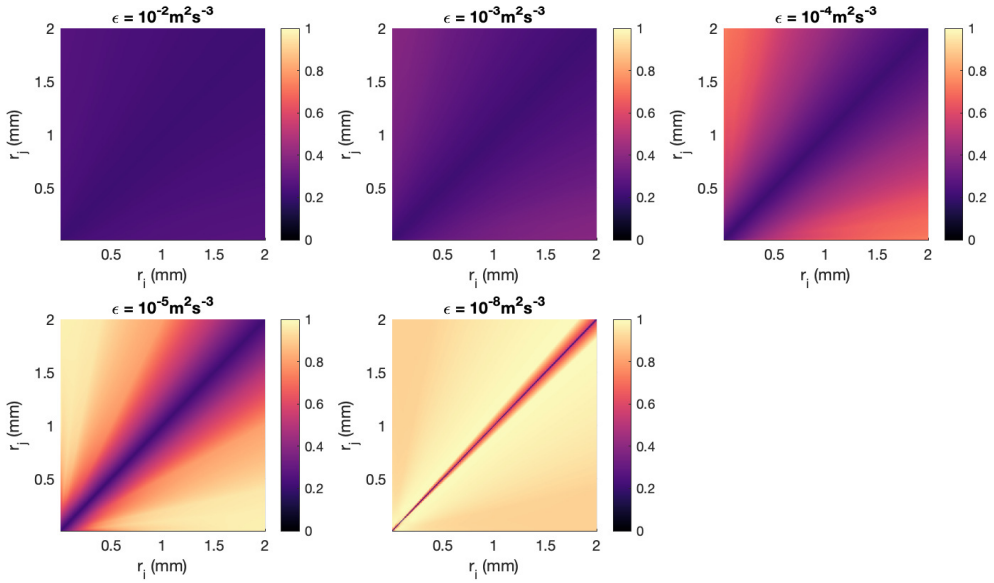

Figure 6.7: $\mathcal{T}_{ij}$ for $\epsilon = [10^{-8}, 10^{-5}, 10^{-4}, 10^{-3}, 10^{-2}]$ m^{2}s^{-3} calculated assuming $\rho(\theta_i) = \delta(\theta_i)$ for $i = a, b$.

and $r_{max,ij}$ to make the collision rate between 10 and 33 times faster with the increase in collision rate being higher at larger values of ϵ.

Next, we calculate $\mathcal{T}_{ij}$ for the two choices of $\rho(\theta_i)$ listed in §6.4.1. Figure 6.7 shows $\mathcal{T}_{ij}$ for $\epsilon = [10^{-8}, 10^{-5}, 10^{-4}, 10^{-3}, 10^{-2}]$ m^{2}s^{-3} and $\rho(\theta_i) = \delta(\theta_i)$. When the flow is very turbulent, the velocity vector is randomly orientated so the probability of a collision is lower and therefore, $\mathcal{T}_{ij}$ is smallest at the highest value of ϵ plotted, $\epsilon = 0.02$ m^{2}s^{-3}. As the flow becomes more quiescent there is a higher probability of the velocity vector being vertical. For $\theta_i = 0$ the crystals will always collide when the velocity is vertical and the smaller crystal is below the larger crystal and hence $\mathcal{T}_{ij}$ increases. The maximum value of $\mathcal{T}_{ij}$ is 0.27 at $\epsilon = 0.01$m^{2}s^{-3} and 0.99 at at $\epsilon = 10^{-8}$m^{2}s^{-3}. When $r_i = r_j$, there is no velocity due to buoyant rise so $\mathcal{T}_{ij}$ is small even at small values of ϵ explaining the narrow strip at $\epsilon = 10^{-8}$ m^{2}s^{-3}.

Figure 6.8 shows $\mathcal{T}_{ij}$ for $\epsilon = [10^{-8}, 10^{-5}, 10^{-4}, 10^{-3}, 10^{-2}]$ m^{2}s^{-3} and $\rho(\theta_i) = 2/\pi$. As was the case for $\rho(\theta_i) = \delta(\theta_i)$, $\mathcal{T}_{ij}$ is smallest at the highest value of ϵ. This is again because the velocity is more randomly orientated. The maximum value of $\mathcal{T}_{ij}$

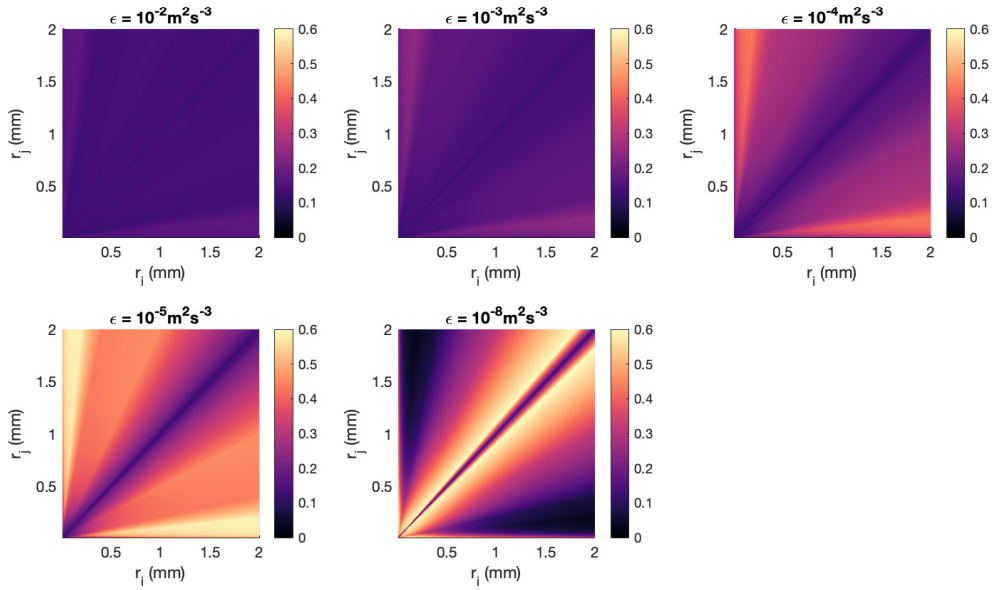

Figure 6.8: $\mathcal{T}_{ij}$ for $\epsilon = [10^{-8}, 10^{-5}, 10^{-4}, 10^{-3}, 10^{-2}]$ m^{2}s^{-3} calculated assuming $\rho(\theta_i) = 2/\pi$ for $i = a, b$.

at $\epsilon = 0.01$ m^{2}s^{-3} is 0.17 which is lower than the value for $\rho(\theta_i) = \delta(\theta_i)$. This reflects the additional decrease in the number of collisions due to the crystals rotating. The maximum value of $\mathcal{T}_{ij} = 0.6$ is found when $\epsilon = 10^{-8}$ m^{2}s^{-3}. Examining $\theta_{u,min}(\phi_u, \Theta, \phi_a, \theta_a, \phi_b, \theta_b)$ and $\theta_{u,max}(\phi_u, \Theta, \phi_a, \theta_a, \phi_b, \theta_b)$ we find that there is a greater range of $\theta_{u,min}$ and $\theta_{u,max}$ over which collisions are possible for larger values of r_i/r_j. However, the highest number of collisions for $\Theta > 0$ occurs at θ_u close to but not equal to 0. This means that there is a trade off between the increase in r_i/r_j increasing the range of θ_u over which collisions are possible and hence increasing $\mathcal{T}_{ij}$ and the increase in r_i/r_j meaning that the velocity has a higher probability of being orientated at $\theta_u = 0$ and hence decreasing $\mathcal{T}_{ij}$. This explains why T_{ij} switches from increasing with increasing r_i/r_j for $\epsilon = 10^{-5}$ m^{2}s^{-3} to decreasing with increasing r_i/r_j for $\epsilon = 10^{-8}$ m^{2}s^{-3}.

6.7 Effect of the new encounter frequency

To compare the difference that changing the parametrisation for the encounter frequency makes to the crystal population, we run simulations for each of the

parametrisations for the encounter frequency. We initialise using the model described in §3 where the number of crystals in each size class is initially constant and the size classes are linearly spaced in radial space. For each simulation we calculate the times τ taken for n_1 to reach $\alpha\overline{n}$ for $\alpha = [0.001, 0.01, 0.1, 0.9, 0.99, 0.999]$ and the mean radius $\overline{r}$ of crystals in size classes 2-200, $\overline{r} = \sum_{i=2}^{N} n_i r_i / \sum_{i=2}^{N} n_i$ for $\epsilon = [10^{-8}, 10^{-5}, 10^{-4}, 10^{-3}, 10^{-2}]$ m^{2}s^{-3}. We then take the ratio of τ and $\overline{r}$ calculated using each of the different parametrisations for the encounter frequency, to the values of τ and $\overline{r}$ calculated using $\mathcal{F}_{enc,ij}$ (where we set the collision radius as $r_e^e + r_j^e$). For each of the calculations we use the spherical differential size formulation, detailed in §5.

The ratios are shown in Figure 6.9. Panel a, for all cases the timescale over which collisions take place increases compared to the timescale for $\mathcal{F}_{enc,ij}$ with $r_{c,ij} = r_i^e + r_j^e$. The increase is most significant for $\mathcal{F}^r_{enc,ij}$. For $\mathcal{F}^r_{enc,ij}$ (calculated using $r_{c,ij} = r_i + r_j$ and setting $\mathcal{T}_{ij} = 1$) the collisions are between $(2d/3)^{2/3}$ and $2d/3$ times faster compared with the collision rate calculated using $\mathcal{F}_{enc,ij}$ with $r_{c,ij} = r_i^e + r_j^e$. For $\mathcal{F}^r_{enc,ij}$ the ratio of the collision times for $\mathcal{F}^r_{enc,ij}$ and $\mathcal{F}_{enc,ij}$ increases with ϵ. This is due to $\langle |w_{ij,r}| \rangle$ becoming increasingly dominated by the contribution of turbulence, leading to the relative velocity becoming increasingly proportional to $r_{c,ij}$ and hence $\mathcal{W}_{ij}$ approaching $r_i + r_j/(r_i^e + r_j^e)$. For more quiescent conditions $\mathcal{W}_{ij} \sim 1$. For $\mathcal{F}^0_{enc,ij}$ (calculated using $r_{c,ij} = r_{max,ij}$ and calculating $\mathcal{T}_{ij}$ with $\rho(\theta_i) = \delta(\theta_i)$ for $i = a, b$) the increase to the collision rate compared to the collision rate for $\mathcal{F}_{enc,ij}$ is similar for all values of ϵ with the increase being slightly larger for the more quiescent flow. This is because the increase in $\mathcal{W}_{ij}$ with increasing ϵ is overcome by the decrease in $\mathcal{T}_{ij}$ with increasing ϵ and hence the ratio of the increase to the collision timescale decreases with increasing ϵ. For $\mathcal{F}^A_{enc,ij}$ (calculated using $r_{c,ij} = r_{max,ij}$ and calculating $\mathcal{T}_{ij}$ with $\rho(\theta_i) = 2/\pi$ for $i = a, b$) the increase to the collision rate compared to the collision rate for $\mathcal{F}_{enc,ij}$ has a less clear trend with ϵ. This is because of the difference in $\mathcal{T}_{ij}$ for $\rho(\theta_i) = \delta(\theta_i)$ and $\rho(\theta_i) = 2/\pi$.

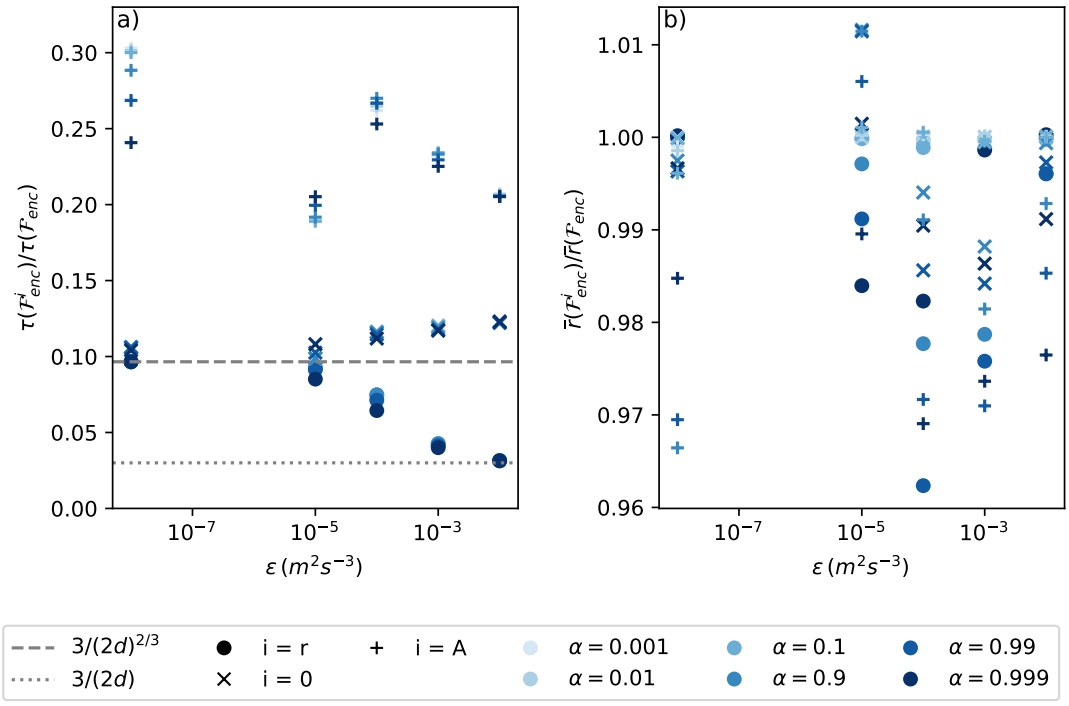

Figure 6.9: Effect of using the different parametrisations for the encounter frequency. a) the ratio of the time for n_1 to reach $\alpha\overline{n}$ using $\mathcal{F}^i_{enc,ij}$ divided by the time for n_1 to reach $\alpha\overline{n}$ using $\mathcal{F}_{enc,ij}$, plotted as a function of ϵ. The circles are the ratio for $i = r$ (where $r_{c,ij} = r_i + r_j$ and $\mathcal{T}_{ij} = 1$), the crosses are the ratio for $i = 0$ (where $r_{c,ij} = r_{max,ij}$ and $\mathcal{T}_{ij}$ is calculated assuming $\rho(\theta_i) = \delta(\theta_i)$ for $i = a, b$) and the plusses are the ratio for $i = A$ (where $r_{c,ij} = r_{max,ij}$ and $\mathcal{T}_{ij}$ is calculated assuming $\rho(\theta_i) = 2/\pi$ for $i = a, b$). The values of α are colour coded according to the legend. The dashed lines are the maximum and minimum values of $\mathcal{R}_{ij}\mathcal{W}_{ij}$. b) the ratio of the mean radius of crystals in size classes 2-200 at the corresponding values of α (using the same colours).

Panel b shows there is little change in the mean radius (the ratios are all very close to 1) when we change the parametrisation for the encounter frequency, suggesting that the dominant change is for the timescale over which the collisions occur.

6.8 Conclusion

In this chapter we have addressed the fourth weakness discussed in §2.5, the fact that variable orientation and non-radial velocity components should be considered when calculating the collision radius and the encounter frequency. To address this weakness we first derived a new expression (6.5) for the encounter frequency which includes a collision kernel $\mathcal{K}$ which takes a value of 1 or 0 depending on whether a

collision occurs or does not occur for the initial condition considered. We showed that the previous expression (4.46) for the encounter frequency can be retrieved by setting the collision kernel $\mathcal{K} = 1$ when $w_{ij,r} < 0$ and $\mathcal{K} = 0$ when $w_{ij,r} \geq 0$. The collision kernel depends on the probability distributions for the orientation of the frazil ice crystals and the probability distributions for the relative velocity. We discussed choices for the probability distributions in §6.4 and chose Gaussian distributions for the components of the relative velocity, uniform distributions for $\rho(\phi_i)$ where ϕ_i is the angle the axis of crystal i makes with the $x-$axis in the $x - y$ plane in the lab frame and either $\rho(\theta_i) = \delta(\theta_i)$ corresponding to all crystals being horizontal or $\rho(\theta_i) = 2/\pi$ corresponding to the crystal axis having a random orientation with respect to the z-axis. Then in §6.5 we calculated the range of possible orientations of the velocity vector for a collision to occur for two disks initially separated by $r_{c,ij} = r_{max,ij} = \sqrt{r_i^2 + (w_i/2)^2} + \sqrt{r_j^2 + (w_j/2)^2}$. We chose this radius as it is the maximum distance possible separation between the centre of masses whilst the crystals are in contact. Finally, in §6.7 we examined the effect of our changes on the encounter frequency. We found that the changes had little effect on the way the number of crystals in each size class evolved with time as the mean crystal radius for the same number of crystals in the smallest size class did not change much with the parametrisation for the encounter frequency. Changing the encounter frequency did increase the overall collision rate in comparison to the model discussed in §5. The collision rate was between 3 and 10 times faster with the increase depending on the turbulent kinetic energy dissipation rate and the choice of $\rho(\theta_i)$ with setting $\rho(\theta_i) = \delta(\theta_i)$ leading to a greater increase in the collision rate than setting $\rho(\theta_i) = 2/\pi$ and the increase being greatest for $\epsilon = 10^{-2}$ m^{2}s^{-3}.

However, there are some weaknesses with the outlined approach. Firstly, as was explained in §6.4.1 there is no experimental or theoretical result for the probability distribution of the crystal orientations for frazil ice crystals. This means there is uncertainty in the correct choice to make for $\rho(\theta_i)$. In this chapter we chose $\rho(\theta_i) = \delta(\theta_i)$ and $\rho(\theta_i) = 2/\pi$. The different choices led to a different collision

rate when the encounter frequencies were inputted into the simple frazil ice model. For $\epsilon = 0.02$ m^{2}s^{-3} the collision rate was approximately 3 times higher when $\rho(\theta_i) = \delta(\theta_i)$ was used to calculate the encounter frequency than when $\rho(\theta_i) = 2/\pi$ was used. Therefore, more work is needed to characterise $\rho(\theta_i)$. Secondly, these calculations are accurate for perfectly cylindrical frazil ice crystals of constant aspect ratio, $d = 50$. Although it reasonable to approximate frazil ice crystals as cylinders (McFarlane et al., 2015), some frazil ice crystals can also have dendritic, hexagonal or irregular shapes (Schneck et al., 2019) for which cases the calculation is less valid. Further, aspect ratios ranging from 5 to 100 have been observed (Souillé et al., 2023). Therefore, it would be interesting to see how the encounter frequency changes with different choices of the aspect ratio.

"Raise your staff and stretch out your hand over the sea to divide the water so that the Israelites can go through the sea on dry ground."

— Exodus 14:16 NIV

7

2D Collision Efficiency

Contents

7.1 Introduction

We now address the next of the problems highlighted in §2.5.5: ignorance of particle interactions when calculating frazil crystal collision rates. Up until now we have assumed that all collisions are ballistic, i.e. that the relative velocity does not deviate from its initial value as the particles approach. This is the equivalent to assuming the collision efficiency, which was defined in §2.4.1 as the ratio of the number of particles that collide when particle-particle interactions are included to the number of particles that collide when particle-particle interactions are neglected, is unity. However, in order to collide, frazil ice crystals have to squeeze out or freeze the fluid between them. These hydrodynamic interactions create additional forces and torques on each crystal that are not currently considered in frazil ice models. Hydrodynamic interactions will likely alter the crystal trajectory and thus affect the collision efficiency. In the following two chapters we calculate the effect of hydrodynamic interactions and derive a new collision efficiency.

7.2 Lubrication approximation

In order to understand what happens when the disks come together, we model the flow of fluid out from between two surfaces. We consider the case where the size of the surfaces is much greater than the gap between the surfaces. In this limit we can relate the pressure p between the disks to the velocity at which the disks approach each other using the lubrication approximation (Reynolds, 1886),

$$\frac{\partial p}{\partial x_i} = \eta \frac{\partial^2 u_i}{\partial z^2}, \tag{7.1}$$

where u_i is the fluid velocity in the i direction and η is the dynamic viscosity. (A derivation of the lubrication approximation is given in appendix C). Using the pressure and velocity we can calculate the forces and torques on each of the disks.

7.2.1 Validity of the lubrication approximation for the disks coming together

Before using the lubrication approximation we justify its validity for modelling frazil ice crystal collisions. We assume that the flow is incompressible. For the lubrication approximation to be valid we require that,

- $H \ll L$, where h and L are characteristic lengthscales in the vertical and horizontal directions respectively.
- $Re\, h^2/L^2 \ll 1$, where $Re = \rho U L/\eta$ is the Reynolds number. This condition also typically ensures laminar flow.

The first assumption that $H^2/L^2 \ll 1$ becomes slightly less valid for larger tilt angles between the upper and lower disks. However, Cawthorn and Balmforth (2010) compared the results from the lubrication approximation for a wedge approaching a plane to the numerical solution for the Stokes flow and found close agreement for small ($\alpha = \pi/12$) tilt angles of the wedge. For larger tilt angles ($\alpha = \pi/3$), the calculated force showed the incorrect dependence on gap thickness but agreed within an order of magnitude. As we are only aiming to get a rough approximation for the force we will use the lubrication approximation throughout. We next derive the pressure and thus the forces and torques between the disks.

7.3 Simplified case of two approaching plates

To gain physical insight we begin by considering the simplified case of hydrodynamic interactions of two approaching rectangular plates in two dimensions before moving on to consider a three-dimensional disk-like geometry in §8. We neglect freezing of the crystals. This work builds on the results of Moy et al. (2017) who solved for the squeeze flow between two angled surfaces which are not allowed to translate, Cawthorn and Balmforth (2010) who applied lubrication theory to a falling wedge, and Wilkinson et al. (2023) who considered the dynamics of a single freely moving solid plate approaching an infinite plate at an angle. Previous work (Cawthorn and

Balmforth, 2010; Wilkinson et al., 2023) showed that finite-time contact is possible under certain conditions. Elastic deformation of a sheet in the presence of a thin fluid film above a rigid substrate has received significant attention (e.g. Audoly, 2011; Hewitt et al., 2015; Hosoi and Mahadevan, 2004; Wagner and Vella, 2011). Building on this, we here obtain the conditions under which finite-time contact is possible when a second freely moving plate is included, as well as quantifying small amplitude elastic deformation in order to determine the conditions for fracture.

After setting up the problem and deriving the forces and torques on the plates in §7.4, we state the equations of motion for the plates in §7.5. In §7.6 we derive an expression for the stresses on the plates and the corresponding curvature induced by elastic bending. Results are shown in §7.7. In §7.7.1 the different plate trajectories are discussed, along with an estimate of the critical velocity required for a collision to occur in this two-dimensional geometry. In §7.7.2 an approximation for the maximum curvature and corresponding stress in each plate is obtained. We apply the results to frazil ice crystals in §7.7.3 and summarise our findings in §7.8.

7.4 Setup and derivation of the forces and torques

7.4.1 Setup

We begin by obtaining the equations of motion, pressure, forces and torques experienced by two approaching plates A and B. We model the two dimensional flow and the motion of the plates moving in the $x' - z'$ plane, as shown in Figure 7.1.

Plates A and B have respective lengths L_a and L_b, thicknesses D_a and D_b, and masses per unit width m_a and m_b. For this two-dimensional problem, the fluid flow is only in the x'-z' plane. We consider a system where $L_a \leq L_b$ but note that results can be obtained for the case $L_b < L_a$ by symmetry arguments. As shown in Figure 7.1, the top plate A has centre of mass (x'_a, z'_a) and moves with local velocity $\mathbf{u}_a = (u'_{ax}, u'_{az})$. Likewise, the bottom plate B has centre of mass (x'_b, z'_b) and moves with local velocity $\mathbf{u}_b = (u'_{bx}, u'_{bz})$. The velocity of the fluid between the

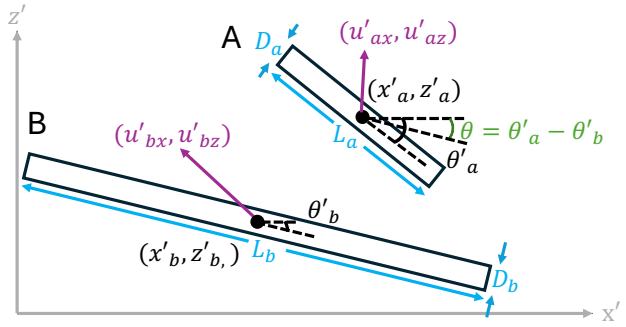

Figure 7.1: Plate geometries in the laboratory frame S'. Two plates approach in the x'-z' plane, with normal vector $\hat{\mathbf{y}}$ into the page so that angles increase in the clockwise-direction. The top plate A has centre of mass (x'_a, z'_a) and moves with local velocity (u'_{ax}, u'_{az}). Likewise, the bottom plate, B, has centre of mass (x'_b, z'_b) and moves with local velocity (u'_{bx}, u'_{bz}). Plates A and B are at an angle θ'_a, θ'_b to the $x'-$axis respectively. The relative angle between the plates $\theta = \theta'_a - \theta'_b$.

plates is (u'_x, u'_z). We initially assume that the plates remain planar, before later considering small amplitude bending to understand the conditions for fracture. The plates are allowed to translate and rotate in response to the hydrodynamic stresses. We can split the velocity of the plates into a translational component, denoted with superscript ^{t} and a rotational component, such that the velocity at location $\mathbf{r}$ on plate $i = a, b$ is given by $\mathbf{u}'_i = \mathbf{u}'^{t}_i + \omega'_i \hat{\mathbf{y}}' \times (\mathbf{r}' - \mathbf{r}'_i)$, where ω'_i is the angular velocity about the centre of mass, $\mathbf{r}_i = (x'_a, z'_a)$. In the derivation and figures below we assume the thicknesses of the plates D_a, D_b is much smaller than their length, so that they can be treated as infinitely thin from the point of view of the fluid flow.

7.4.2 Rotated reference frame

The forces and torques on the plates depend on the fluid pressure and viscous shear stress. To simplify the algebra, we calculate the pressure in a reference frame S in which the bottom plate is instantaneously horizontal ($\theta_b = 0$); (note that frame S is not a rest frame of plate B, with the two plates in S maintaining angular velocities $\omega_a = \omega'_a$, $\omega_b = \omega'_b$, along with translational motion). In general $\theta = \theta'_a - \theta'_b$ can be positive or negative. In the derivation below we illustrate the method for the case where $\theta < 0$ and assume plates A and B completely overlap, as shown in Figure 7.2. The more complex case of incomplete overlap is covered in section D.2, and the

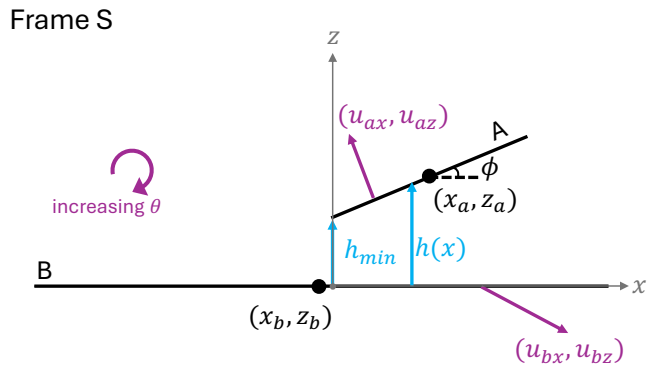

Figure 7.2: We calculate the pressure and resulting forces and torques in reference frame S, in which the bottom plate is instantaneously horizontal. The distance h between the plates, measured perpendicular to plate B, depends on x and $\phi = -\theta$, with minimum perpendicular distance, h_{min}.

case with $\theta > 0$ is detailed in section D.3.

As in Figure 7.2 we define the acute angle $\phi = -\theta$. We set $x = 0$ at the left-hand edge of plate A, which has position $z = h(x,t)$ and we set $z = 0$ as the instantaneous location of plate B, and write $h(x,t) = h_{min}(t) + x\tan[\phi(t)]$. The coordinates x, z in frame S are related to coordinates x', z' in the lab frame S' by

$$x = \cos\theta'_b(x'-x'_a) - \sin\theta'_b(z'-z'_a) + L_a\cos(\theta'_a-\theta'_b)/2, \quad z = \sin\theta'_b(x'-x'_b) + \cos\theta'_b(z'-z'_b). \tag{7.2a, b}$$

Neglecting the thickness of the plates, the decomposition of the plate velocity into rotating and a translating parts, yields

$$\begin{pmatrix} u_{ax} \\ u_{az} \end{pmatrix} = \begin{pmatrix} u^t_{ax} \\ u^t_{az} \end{pmatrix} + \omega_a \begin{pmatrix} h(x,t) - z_a \\ x_a - x \end{pmatrix}, \tag{7.3}$$

$$\begin{pmatrix} u_{bx} \\ u_{bz} \end{pmatrix} = \begin{pmatrix} u^t_{bx} \\ u^t_{bz} \end{pmatrix} + \omega_b \begin{pmatrix} -z_b \\ x_b - x \end{pmatrix}. \tag{7.4}$$

The velocities and angular velocities for plate i in frame S' are related to those in frame S by

$$\begin{pmatrix} u^{t'}_{ix} \\ u^{t'}_{iz} \end{pmatrix} = \begin{pmatrix} \cos\theta'_b & \sin\theta'_b \\ -\sin\theta'_b & \cos\theta'_b \end{pmatrix} \begin{pmatrix} u^t_{ix} \\ u^t_{iz} \end{pmatrix}, \qquad \omega'_i = \omega_i. \tag{7.5}$$

7.4.3 Fluid flow

When the relative angle, $\theta = \theta_a - \theta_b$ is small and the minimum distance between the plates, h_{min}, is small compared to L_a and L_b, we can use the lubrication approximation (§7.2) to model the hydrodynamic forces on the plates.

By conservation of mass for incompressible flow the change in local height h between the two plates is related to the volume flux q_x of fluid in the $x-$direction by

$$\frac{\partial h}{\partial t} = -\frac{\partial q_x}{\partial x}, \qquad q_x = \int_0^h u_x \, \mathrm{d}z. \tag{7.6a, b}$$

The x-component of (7.1) is

$$\frac{\partial p}{\partial x} = \eta \frac{\partial^2 u_x}{\partial z^2}. \tag{7.7}$$

Integrating and applying the no slip boundary conditions $u_x = u_{bx}$ at $z = 0$ and $u_x = u_{ax}$ at $z = h$ gives

$$u_x = -z\frac{(h-z)}{2\eta}\frac{\partial p}{\partial x} + u_{bx}\frac{(h-z)}{h} + \frac{u_{ax}z}{h}. \tag{7.8}$$

The local rate of change of the height $\partial h/\partial t$ only depends on the horizontal velocity u_{ax} of the top plate A and the relative vertical velocity, $u_{az} - u_{bz}$, of the two plates,

$$\frac{\partial h}{\partial t} = u_{az} - u_{bz} - u_{ax}\frac{\partial h}{\partial x} \tag{7.9}$$

(see Figure 7.2). Combining (7.3), (7.4), (7.6), (7.8) and (7.9) we obtain a governing equation for the pressure,

$$\frac{\partial}{\partial x}\left(h^3(x)\frac{\partial p(x)}{\partial x}\right) = 12\eta\left[(u^t_{az} - u^t_{bz}) - (\omega_a - \omega_b)x + \omega_a x_a - \omega_b x_b - \frac{1}{2}\left(u^t_{ax} - u^t_{bx} - \omega_a z_a + \omega_b z_b\right)\frac{\partial h}{\partial x}\right]. \tag{7.10}$$

For the lubrication assumption to hold, ϕ must be small, so $\partial h/\partial x = \tan\phi \approx \phi$ and $\cos\phi \approx 1$. Assuming negligible plate sheet thickness, we also have, $x_a \approx L_a/2$, $z_a \approx h_{min} + L_a\phi/2$ and $z_b = 0$. The boundary conditions on (7.10) are $p(0) = p(L_a) = 0$ because the pressure is negligible in all regions that are not directly between the two plates.

7.4.3.1 Non dimensionalisation and solution for the pressure

We define dimensionless variables with a tilde,

$$\tilde{x} = x/L_a, \quad \tilde{h}_{min} = h_{min}/L_a, \quad \tilde{t} = t/T, \quad \tilde{\omega} = T\omega,$$

$$\tilde{z} = z/L_a, \quad \tilde{\mathbf{u}} = \mathbf{u}/(L_a/T), \quad \tilde{p} = \frac{p}{12\eta/T}, \tag{7.11a-g}$$

where $T = m_a/(12\eta)$ is the viscous damping timescale of crystal motion, and define

$$\Omega = \tilde{\omega}_a - \tilde{\omega}_b, \tag{7.12}$$

$$V = (\tilde{u}^t_{az} - \tilde{u}^t_{bz}) + \tilde{\omega}_a\tilde{x}_a - \tilde{\omega}_b\tilde{x}_b - \frac{\phi}{2}\left(\tilde{u}^t_{ax} - \tilde{u}^t_{bx} - \tilde{\omega}_a\tilde{z}_a\right). \tag{7.13}$$

Equation (7.10) becomes,

$$\frac{\partial}{\partial\tilde{x}}\left[(\tilde{h}_{min} + \tilde{x}\phi)^3\frac{\partial\tilde{p}}{\partial\tilde{x}}\right] = -\Omega\tilde{x} + V, \tag{7.14}$$

subject to the conditions $\tilde{p}(0) = \tilde{p}(1) = 0$. Noting that this equation is linear in $\tilde{p}$, we can split the solution for the pressure into two components $\tilde{p} = \Omega\tilde{p}_\Omega + V\tilde{p}_V$. This allows us to assess the contribution of each component later. The components satisfy,

$$\frac{\partial}{\partial\tilde{x}}\left[(\tilde{h}_{min} + \tilde{x}\phi)^3\frac{\partial\tilde{p}_\Omega}{\partial\tilde{x}}\right] = -\tilde{x}, \qquad \frac{\partial}{\partial\tilde{x}}\left[(\tilde{h}_{min} + \tilde{x}\phi)^3\frac{\partial\tilde{p}_V}{\partial\tilde{x}}\right] = 1. \tag{7.15a, b}$$

Solving each equation we obtain,

$$\tilde{p}_V(\tilde{x}) = \frac{\tilde{x}(\tilde{x}-1)}{(2\tilde{h}_{min} + \phi)(\tilde{h}_{min} + \phi\tilde{x})^2}, \tag{7.16}$$

$$\begin{aligned}\tilde{p}_\Omega(\tilde{x}) = \frac{1}{2\phi^3(2\tilde{h}_{min} + \phi)(h_{min} + \phi\tilde{x})^2}\Big[&2\phi^2\tilde{h}_{min}(\tilde{x}-1)\tilde{x} + \dots \\ &- \tilde{h}^2_{min}(\tilde{x}-1)(2\tilde{h}_{min} + \phi + \phi\tilde{x})\ln\tilde{h}_{min} + \dots \\ &+ \tilde{x}(\tilde{h}_{min} + \phi)^2(2\tilde{h}_{min} + \phi\tilde{x})\ln(\tilde{h}_{min} + \phi) + \dots \\ &- (2\tilde{h}_{min} + \phi)(\tilde{h}_{min} + \phi\tilde{x})^2\ln(\tilde{h}_{min} + \phi\tilde{x})\Big],\end{aligned} \tag{7.17}$$

where we have individually imposed $\tilde{p}_V(0) = \tilde{p}_V(1) = \tilde{p}_\Omega(0) = \tilde{p}_\Omega(1)$.

7.4.4 Forces and torques

Having obtained an expression for the pressure between the plates, we now calculate the forces and torques on each plate in frame S before translating the forces and torques to the lab frame S' where the equations of motion are more straightforward.

Consistent with the approximations of lubrication theory (Reynolds, 1886), the stresses $\mathbf{T}_i$ on the plates have dominant contributions from the pressure p and the viscous shear stress $\eta \partial u_x/\partial z$, given by

$$T_{ax} \approx -p\frac{\partial h}{\partial x} - \eta \frac{\partial u_x}{\partial z}\bigg|_{z=h}, \qquad T_{az} \approx p, \tag{7.18}$$

$$T_{bx} \approx \eta \frac{\partial u_x}{\partial z}\bigg|_{z=0}, \qquad T_{bz} \approx -p. \tag{7.19}$$

To calculate the force per unit width $\mathbf{F}_i$ on each of the plates ($i = A, B$) we integrate the stress vector over the length of each plate. We initially assume A entirely overlaps with B, and the force is dominated by stresses in the thin gap between the plates, with the stress approximated as zero in the region where the plates do not overlap. This yields

$$\mathbf{F}_a = \int_0^{L_a} \mathbf{T}_a \,\mathrm{d}x, \qquad \mathbf{F}_b = \int_0^{L_a} \mathbf{T}_b \,\mathrm{d}x. \tag{7.20a, b}$$

Using (7.3), (7.4) and (7.8) to calculate $\partial u_x/\partial z$ at $z = 0$ and $z = h$, and combining with (7.18) and (7.20), we obtain an expression for the force per unit width on plate A,

$$F_{ax} = -\int_0^{L_a} \left[p\frac{\partial h}{\partial x} + \frac{h}{2}\frac{\partial p}{\partial x} + \eta(u^t_{ax} - u^t_{bx} - \omega_a z_a)\frac{1}{h} + \eta\omega_a \right] \mathrm{d}x, \qquad F_{az} = \int_0^{L_a} p \,\mathrm{d}x. \tag{7.21a, b}$$

Integrating the term involving $\partial p/\partial x$ by parts, letting $\partial h/\partial x = \phi$ and knowing that the pressure is zero at the boundaries,

$$F_{ax} = -\int_0^{L_a} \left[\frac{p\phi}{2} + \eta(u^t_{ax} - u^t_{bx} - \omega_a z_a)\frac{1}{h} + \eta\omega_a \right] \mathrm{d}x, \qquad F_{az} = \int_0^{L_a} p \,\mathrm{d}x. \tag{7.22a, b}$$

A similar calculation for plate B shows $\mathbf{F}_a = -\mathbf{F}_b$, as expected for low Reynolds number flow in a lubrication film.

The torque per unit width τ on each plate is given by

$$\tau_i = \int (\mathbf{r} - \mathbf{r}_i) \times \mathbf{T}_i \, \mathrm{d}x. \tag{7.23}$$

Under the lubrication approximation, the leading order contributions are

$$\tau_a \approx -\hat{\mathbf{y}} \int_0^{L_a} (x - x_a) p \, \mathrm{d}x, \qquad \tau_b \approx \hat{\mathbf{y}} \int_0^{L_a} (x - x_b) p \, \mathrm{d}x. \tag{7.24a, b}$$

Applying the non-dimensionalisation from §7.4.3.1, and expressing the dimensionless forces $\tilde{F}$ and torques $\tilde{\tau}$ in terms of the dimensionless variables $\tilde{p}, \tilde{u}^t_{ax}, \tilde{u}^t_{bx}, \tilde{\omega}_a, \tilde{z}_a$ (see section D.1), we obtain $F = (12\eta L_a/T)\tilde{F}$ and $\tau = (12\eta L_a^2/T)\tilde{\tau}$.

The forces $\mathbf{F}$ and torques τ calculated in frame S are related to the forces $\mathbf{F}'$ and torques τ' in frame S' via a rotation about the $\hat{\mathbf{y}}$ axis,

$$\begin{pmatrix} F'_x \\ F'_z \end{pmatrix} = \begin{pmatrix} \cos\theta'_b & \sin\theta'_b \\ -\sin\theta'_b & \cos\theta'_b \end{pmatrix} \begin{pmatrix} F_x \\ F_z \end{pmatrix}, \qquad \tau' = \tau. \tag{7.25a, b}$$

7.4.5 Additional cases

The calculation above is valid for $\theta < 0$ and the plates completely overlapping. When plates A and B no longer completely overlap, we define $\tilde{x}_1$ and $\tilde{x}_2$ as the respective minimum and maximum value of $\tilde{x}$ where overlap occurs, which replace the location of the boundary conditions and the integral limits in that case. In frame S, $\tilde{x}_1$ and $\tilde{x}_2$ are given by

$$\tilde{x}_1 = \max[0, \tilde{x}_b - 1/(2\gamma)], \qquad \tilde{x}_2 = \min[1, \tilde{x}_b + 1/(2\gamma)], \tag{7.26a, b}$$

where $\gamma = L_a/L_b$. We solve for cases with partial overlap in section D.2, and we solve for $\theta > 0$ in section D.3.

7.5 Plate Motion

The motion of the plates is modelled using the forces and torques from (7.25). We state the equations of motion below, then discuss the possible end results of a simulation.

7.5.1 Equations of motion

The equations of motion for plate i, rotating about its centre of mass with moment of inertia per unit width $m_i L_i^2/12$ for plates of negligible thickness, are given by

$$\frac{\mathrm{d}^2\vec{x}_i'}{\mathrm{d}t^2} = \frac{\vec{F}_i}{m_i}, \qquad \frac{\mathrm{d}^2\theta_i'}{\mathrm{d}t^2} = \frac{12\tau_i'}{m_i L_i^2}, \tag{7.27a, b}$$

Employing the non-dimensionalisation in §7.4.3.1 and §7.4.4, we obtain the dimensionless equations of motion for the plates,

$$\frac{\mathrm{d}^2}{\mathrm{d}\tilde{t}^2}\begin{pmatrix}\tilde{x}_a' \\ \tilde{z}_a' \\ \theta_a'\end{pmatrix} = \begin{pmatrix}\tilde{F}_{ax}' \\ \tilde{F}_{az}' \\ 12\tilde{\tau}_a'\end{pmatrix}, \qquad \frac{\mathrm{d}^2}{\mathrm{d}\tilde{t}^2}\begin{pmatrix}\tilde{x}_b' \\ \tilde{z}_b' \\ \theta_b'\end{pmatrix} = \frac{m_a}{m_b}\begin{pmatrix}\tilde{F}_{bx}' \\ \tilde{F}_{bz}' \\ 12\gamma^2\tilde{\tau}_b'\end{pmatrix}. \tag{7.28a, b}$$

We solve the equations of motion numerically using the Python programming language with an explicit Runge-Kutta method of order 5(4) (Dormand and Prince, 1980).

7.5.2 Initial conditions

We consider three geometries, with $\gamma = L_a/L_b = 1,\ 1/2,\ 10^{-5}$, chosen to capture three distinct cases for the relative acceleration experienced by the top and bottom plates. When $\gamma = 1$ both plates have equal and opposite accelerations, whereas when $\gamma = 10^{-5}$ the bottom plate has negligible acceleration. We also assume that the plates have equal densities and thicknesses so that $m_a/m_b = \gamma$. The equations of motion in (7.28) require 12 initial conditions. We focus here on varying the initial angle and relative velocity, setting $\theta_a' = \theta_{in}$ and $\tilde{u}_{az}^{t'} = \tilde{v}_{in}$ at $\tilde{t} = 0$. We set the initial minimum separation $\tilde{h}_{min} = \tilde{h}_{in} = 1$ at $\tilde{t} = 0$, so that $\tilde{z}_a' = 1 + |\theta_{in}|/2$ and the plates have dimensional initial separation L_a. We set all the other values $\tilde{x}_a', \tilde{x}_b', \tilde{z}_b', \tilde{u}_{ax}^{t'}, \tilde{u}_{bx}^{t'}, \tilde{u}_{bz}^{t'}, \tilde{\omega}_a', \tilde{\omega}_b', \tilde{\theta}_b'$ to 0 at $\tilde{t} = 0$. The lubrication

approximation does not strictly hold with $\tilde{h}_{min}$ of order 1, but the forces are generally small so do not significantly affect the motion until smaller values of $\tilde{h}_{min}$ are reached. Furthermore, we only consider results where the final minimum distance is much less than 1. We consider the range $0 \leq \theta_{in} \leq 7^o$ and $-1000 \leq \tilde{v}_{in} \leq -0.01$. For frazil ice crystals we expect $\tilde{v}_{in} \geq -10$ so this captures the expected range of velocities for frazil ice crystals.

7.5.3 End criteria

We end the simulation if one of the following conditions is reached: i) the plates no longer overlap at all, ii) the plates collide, iii) the modulus of the angle between the plates exceeds 20^o (motivated by the breakdown of the lubrication approximation for large angles), iv) the plates start to move away from each another. The end criteria are therefore,

i) No overlap

$$|\tilde{x}_a - \tilde{x}_b| > (1/\gamma + 1)/2. \tag{7.29}$$

ii) Collision

$$\tilde{h}_{min} = \begin{cases} \tilde{z}_a + \theta(\tilde{x}_a - \tilde{x}_1) \leq 10^{-6}, & \theta < 0, \\ \tilde{z}_a - \theta(\tilde{x}_2 - \tilde{x}_a) \leq 10^{-6}, & \theta > 0, \end{cases} \tag{7.30}$$

where expressions for $\tilde{x}_1$ and $\tilde{x}_2$, in (7.26) account for the different limits in the case when there is incomplete overlap. The threshold on $\tilde{h}_{min}$ for collision is set to 10^{-6} because once the simulation reaches this point, we found that there was negligible change in the collision velocities when we instead use smaller values down to $\tilde{h}_{min} = 10^{-13}$.

iii) Large angles

$$|\theta| > 20^o. \tag{7.31}$$

iv) Threshold for moving away from each other

We calculate this threshold using the velocities of the ends ($\tilde{x} = 0, 1$ in frame

S) of plate A, relative to the velocity of the points on plate B directly below the ends of A. We define

$$\tilde{u}_{z,RHS} = \tilde{u}^t_{za} - \tilde{u}^t_{zb} - \frac{\omega_a - \omega_b}{2} - \omega_b(\tilde{x}_a - \tilde{x}_b), \qquad \tilde{u}_{z,LHS} = \tilde{u}^t_{za} - \tilde{u}^t_{zb} + \frac{\omega_a - \omega_b}{2} - \omega_b(\tilde{x}_a - \tilde{x}_b). \tag{7.32a, b}$$

If $\tilde{u}_{z,RHS}$ and $\tilde{u}_{z,LHS}$ are both positive then the crystals are moving apart.

7.6 Elastic beam deflection

The pressure arising from the lubrication flow can cause the plates to bend if they deform elastically. Figure 7.3 schematically illustrates the pressure and the resulting deformation. If the bending stresses are sufficiently large, the plates may snap via bending-induced fracture. We determine the stresses on the plates using the dynamic beam equation (Bokhari et al., 2012) for the deflection w_i,

$$\frac{\partial^2 w_i}{\partial t^2} + \frac{EI_i}{\rho D_i}\frac{\partial^4 w_i}{\partial x^4} = \frac{p(x,t)}{\rho D_i} \tag{7.33}$$

where ρ is the density of the beam, E is the elastic modulus and I_i is the second moment of area in the y-z plane per unit width ($I_i = \int z^2 dz = D_i^3/12$ for beams with a rectangular cross section). We assume that the beam is sufficiently stiff and elastic deformation is sufficiently small that its impact on the fluid flow can be neglected, and hence we can use $p(x,t)$ from the calculation with planar plates and gap thickness $h(x,t)$ from §7.4.

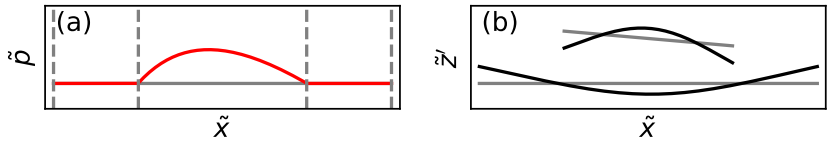

Figure 7.3: Computing (a) illustrative pressure distribution along plate B (red line) with the dashed grey lines showing the edges of plates A and B. (b) Corresponding separation of two plates (grey lines), and the corresponding elastic deflection (black lines) due to the pressure on each plate. The pressure has been scaled and the deflection has been exaggerated for clearer visualisation.

We assume the dimensionless deflection, w_i/L_a, can be described by a translating part $\tilde{z}_i$ and a rotating part $\tilde{\theta}_i(\tilde{x}-\tilde{x}_i)$ (as described in §7.4), plus a small bending deflection,

$$\frac{w_i}{L_a} = \pm[\tilde{z}_i(\tilde{t}) - \tilde{\theta}_i(\tilde{t})(\tilde{x}-\tilde{x}_i)] + \tilde{w}_i(\tilde{x},\tilde{t})\frac{L_a^4\rho D_i}{T^2 E I_i}, \tag{7.34}$$

where $\tilde{w}_i$ is a scaled bending deflection and $i \in \{a,b\}$. The sign of the term in the square brackets is positive if $i=a$ and negative if $i=b$. With the deflection being in the $+\hat{z}$ direction when $\tilde{w}_i$ is positive.

Employing the non-dimensionalisation from §7.4.3.1 and substituting in I_i we obtain an equation for the dimensionless small bending deflection, $\tilde{w}_i$,

$$\frac{12^3\eta^2 L_a^2}{E\rho D_a^2 D_i^2}\frac{\partial^2\tilde{w}_i}{\partial\tilde{t}^2} + \frac{\partial^4\tilde{w}_i}{\partial\tilde{x}^4} = \frac{D_a}{D_i}\tilde{p} \pm \left[-\frac{\partial^2\tilde{z}_i}{\partial\tilde{t}^2} + (\tilde{x}-\tilde{x}_i)\frac{\partial^2\tilde{\theta}_i}{\partial\tilde{t}^2}\right]. \tag{7.35}$$

In section D.4 we show that the derivatives of $\tilde{z}_i(\tilde{t})$ and $\tilde{\theta}_i(\tilde{t})$ are equivalent to those of $\tilde{z}_i(\tilde{t})$ and $\tilde{\theta}_i(\tilde{t})$ defined in §7.4.4 for $\tilde{z}_b' = \tilde{\theta}_b' = 0$.

We consider the limit of a stiff beam for which $12^3 L_a^2\eta^2/(E\rho D_a^2 D_i^2) \ll 1$. For example, for frazil ice, typical values are $L_a \sim 10^{-3}$ m, $\eta \sim 10^{-3}\,\mathrm{kgm^{-1}s^{-1}}$, $E \sim 10^9$ Pa, $D_b, D_a \sim 10^{-4}$ m, $\rho \sim 10^3\,\mathrm{kgm^{-3}}$, so $12^3 L_a^3\eta^2/(E\rho D_a^2 D_i^2) \sim 10^{-7} \ll 1$. We therefore ignore the first term and have,

$$\frac{\partial^4\tilde{w}_i}{\partial\tilde{x}^4} = \frac{D_a}{D_i}\tilde{p} \pm \left[-\frac{\mathrm{d}^2\tilde{z}_i}{\mathrm{d}\tilde{t}^2} - (\tilde{x}-\tilde{x}_i)\frac{\mathrm{d}^2\tilde{\theta}_i}{\mathrm{d}\tilde{t}^2}\right]. \tag{7.36}$$

This approximation considers the quasi-steady response, neglecting transient propagation of elastic waves.

7.6.1 Boundary conditions

The ends of the beams are free and hence there is no shear force or bending moment on the ends of the beam. We work in a rescaled coordinate system detailed in

section D.2 such that edge of plate A is at $\tilde{x} = 0$ and $\tilde{x} = 1$. Following Pradhan and Chakraverty (2019), for plate A,

$$\left.\frac{\partial^2 \tilde{w}_a}{\partial \tilde{x}^2}\right|_{\tilde{x}=0} = \left.\frac{\partial^2 \tilde{w}_a}{\partial \tilde{x}^2}\right|_{\tilde{x}=1} = 0, \qquad \left.\frac{\partial^3 \tilde{w}_a}{\partial \tilde{x}^3}\right|_{\tilde{x}=0} = \left.\frac{\partial^3 \tilde{w}_a}{\partial \tilde{x}^3}\right|_{\tilde{x}=1} = 0. \tag{7.37a, b}$$

For plate B with ends at $\tilde{x} = M, P$,

$$\left.\frac{\partial^2 \tilde{w}_b}{\partial \tilde{x}^2}\right|_{\tilde{x}=M} = \left.\frac{\partial^2 \tilde{w}_b}{\partial \tilde{x}^2}\right|_{\tilde{x}=P} = 0, \qquad \left.\frac{\partial^3 \tilde{w}_b}{\partial \tilde{x}^3}\right|_{\tilde{x}=M} = \left.\frac{\partial^3 \tilde{w}_b}{\partial \tilde{x}^3}\right|_{\tilde{x}=P} = 0. \tag{7.38a, b}$$

7.6.2 Calculation of the curvature and stress

The curvature $\kappa_i = \partial^2 w_i / \partial x^2$ is related to the dimensionless curvature $\tilde{\kappa}_i = \partial^2 \tilde{w}_i / \partial \tilde{x}^2$ by

$$\kappa_i = \frac{\rho D_i L_a^3}{E I_i T^2} \tilde{\kappa}_i = \frac{12^3 L_a \eta^2}{E \rho D_i^2 D_a^2} \tilde{\kappa}_i. \tag{7.39}$$

The maximum tensile and compressive stress σ_{tens} and σ_{comp} occur at the top and bottom of the beam, and are given by (see Gere and Goodno, 2009)

$$\sigma_{tens} = \sigma_{comp} = \frac{E D_i}{2} \left|\kappa_{max}\right| = \frac{864 L_a \eta^2}{\rho D_i D_a^2} \left|\tilde{\kappa}_{max}\right|. \tag{7.40}$$

To determine whether the plates experience sufficient stress to fracture, we calculate the curvature of the plates and then compare the stress (7.40) to the fracture toughness of the material. Note that (7.40) implies that the fracture criteria is independent of the elastic modulus: whilst softer plates have larger amplitude deformation, the corresponding elastic stress is controlled by the underlying amplitude of the hydrodynamic load.

We now describe how the dimensionless curvature $\tilde{\kappa}_i$ is found. Exploiting the linearity of the equations, and recalling the decomposition $\tilde{p}(\tilde{x}, t) = \Omega \tilde{p}_\Omega + V \tilde{p}_V$, we solve (7.36), (7.37), (7.38) for $\ddot{\tilde{z}}_i$, $\ddot{\tilde{\theta}}_i$ and the V and Ω components of $\tilde{w}_i$ and hence find $\tilde{\kappa}_i$. Here, $\tilde{p}_V$ is given by (7.16) and $\tilde{p}_\Omega$ is given by (7.17) for $0 < \tilde{x} < 1$, with $\tilde{p}_V = \tilde{p}_\Omega = 0$ outside of that range. We decompose

$$\tilde{\kappa}_i = \frac{D_a}{D_i} \left(V \tilde{\kappa}_{i,V} + \Omega \tilde{\kappa}_{i,\Omega}\right), \tag{7.41}$$

where the factor D_a/D_a is included to match the coefficient in front of $\tilde{p}$ in (7.36).

The solutions for the curvature calculation were found using Mathematica and are lengthy so not written here. However, it is useful to consider the approximations for $\tilde{h}_{min}/\theta \to 0$,

$$\tilde{\kappa}_{a,V} = \frac{1}{\theta^3}\left[(2\tilde{x} - 5\tilde{x}^2 + 3\tilde{x}^3 - \tilde{x}\ln\tilde{x}) + (\tilde{x} - 2\tilde{x}^2 + \tilde{x}^3)\ln\left(\frac{\tilde{h}_{min}}{\theta}\right) + \mathcal{O}\left(\frac{\tilde{h}_{min}}{\theta}\right)\right], \tag{7.42}$$

$$\tilde{\kappa}_{a,\Omega} = \frac{1}{\theta^3}\left[\frac{\tilde{x} - 1 - \ln\tilde{x}}{4} + \mathcal{O}\left(\frac{\tilde{h}_{min}}{\theta}\right)\right], \tag{7.43}$$

$$\tilde{\kappa}_{b,V} = \frac{(P-\tilde{x})}{6\theta^3(M-P)\left(M(3P+2)-P^2\right)}\Bigg\{M^2(3\tilde{x}+2) - 2M\left(P\tilde{x}+P+\tilde{x}^2\right) + 4P^2 - 2(5P+4)\tilde{x}^2 + P(11P+4)\tilde{x} + 2\ln\left(\frac{\tilde{h}_{min}}{\theta}\right)\Bigg[M^2(3\tilde{x}+2) - 2M\left(P\tilde{x}+P+\tilde{x}^2\right) + P^2 - (P+2)\tilde{x}^2 + P(2P+1)\tilde{x}\Bigg]\Bigg\} + \mathcal{O}\left(\frac{\tilde{h}_{min}}{\theta}\right), \tag{7.44}$$

$$\tilde{\kappa}_{b,\Omega} = -\frac{(P-\tilde{x})}{24\theta^3(M-P)\left[P^2 - M(3P+2)\right]}\Bigg(21M^2\tilde{x} + 14M^2 - 14MP\tilde{x} - 14MP - 14M\tilde{x}^2 + 5P^2\tilde{x} + 4P^2 + 2P\tilde{x}^2 + 4P\tilde{x} - 8\tilde{x}^2\Bigg) + \mathcal{O}\left(\frac{\tilde{h}_{min}}{\theta}\right). \tag{7.45}$$

Solutions for the opposite limit of $\theta \to 0$ are given in §D.5. Due to the $\ln(\tilde{h}_{min}/\theta)$ terms in (7.42) and (7.44), the curvature will become infinite in the limit $h_{min} \to 0$ whenever $V \neq 0$. Hence, the stresses diverge and will cause fracture whenever the disks make a direct contact. We see below that fracture is also possible without contact for a certain range of initial velocities.

7.7 Results

7.7.1 Trajectories and collision criteria

Example solutions are shown in Figure 7.4 and we begin be making a few general observations about their behaviour. The hydrodynamic force acts to reduce the

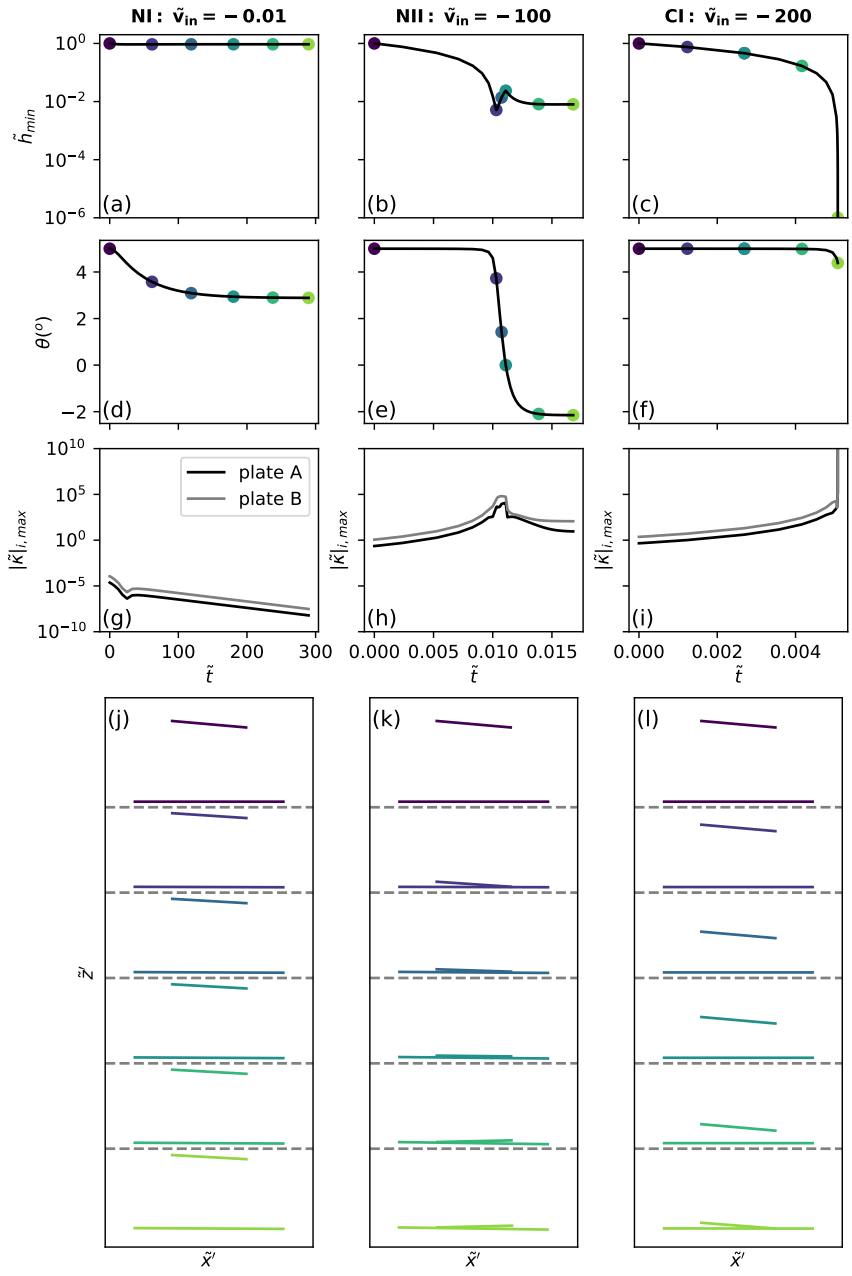

Figure 7.4: Motion of the two plates, starting with $\tilde{h}_{min} = 1$, relative angle $\theta_{in} = 5^o$, and initial relative velocity $\tilde{v}_{in} \in -\{0.01, 100, 200\}$ from left to right. All the other initial conditions are 0. The bottom plate is twice as long as the top plate ($\gamma = 1/2$). The category of motions is noted in the title for each column. Panels (a)-(c) show the minimum distance between the plates over time. Panels (d)-(f) show the evolution of the relative angle. Panels (g)-(i) show maximum curvature as a function of time. Panels (j)-(l) show some snapshots of the motion at the times indicated by the corresponding colour coded dots in (a)-(f). The snapshots are shifted evenly in $\tilde{z}$ and separated by a grey dashed line to make visualisation easier. Time increases from top to bottom. A collision occurs for $\tilde{v}_{in} = -200$ in the bottom snapshot in panel (l). In all cases the relative angle initially decreases and plate A translates to the right.

relative vertical speed of the plates, and can act to prevent a collision (left and centre columns) when a simple 'ballistic' trajectory given the initial conditions would have predicted it. However, for sufficiently large initial velocities, the hydrodynamic force is insufficient to prevent a collision (right column). The pressure increases with decreasing gap thickness, and varies assymetrically, with higher pressure near the narrower end of the gap. Hence, it produces a torque on both plates that reduces the relative angle. In some cases the relative angle passes through zero. Finally, as we initialize with $0 \leq \theta \leq 7^o$, plate A always translates in the positive x direction. This is because initially F_{ax} in (7.22) is dominated by the pressure integral, leading to $F_{ax} > 0$ for the initial slope of the plate we have chosen. For some of the model runs the relative angle θ becomes greater than 20^o, our chosen cut-off angle, and we choose to end the simulation because the lubrication approximation becomes invalid for large angles.

We categorise four different types of outcome:

- Category NI: no collision and no sign change in θ,
- Category NII: no collision and sign change in θ,
- Category CI: collision and no sign change in θ,
- Category CII: collision and sign change in θ.

In all simulations considered here only categories NI, NII and CI are found to be possible. To illustrate the three different observed categories we plot the motion for $\gamma = 1/2$, $\theta_{in} = 5^o$ and $\tilde{v}_{in} = [-0.01, -100, -200]$ in Figure 7.4. The angle θ changes due to both plates A and B rotating, with plate B rotating less because it has a higher inertia than plate A for $\gamma = 1/2$. In case NI, the relative velocity is sufficiently small that the hydrodynamic force slows the plates down before the torque is sufficient for the relative angle to pass through zero. In case NII a sign change in the angle occurs, $\tilde{h}_{min}$ passes through a local minima and the curvature passes through a local maxima. It is complex to explain the time

dependence of the curvature. Broadly the curvature increases with increasing Ω and $|V|$ and decreasing $\tilde{h}_{min}$ and $|\theta|$, with the curvature becoming infinite when $\tilde{h}_{min} = 0$. Therefore, we see a local maximum in the curvature close to $\theta = 0$, in places where θ is rapidly changing and Ω is large because $\tilde{h}_{min}$ is small. In case NI, $\tilde{h}_{min}$ remains of order 1 and the curvature simply decreases as the relative velocity between the plates and hence $|V|$ decreases.

Figure 7.5 shows the category of the motion between the plates as a function of the initial relative velocity and initial angle for $\gamma = 10^{-5}$, 1/2 and 1, corresponding to different relative sizes of the plates. Category NI only occurs for smaller initial velocities than the range shown here, for which $\tilde{h}_{min}$ remains relatively large throughout. Therefore, the only observed categories of motion are NII and CI. The boundary between NII and CI is dependent on γ. This is due to the fact that the relative angle decreases much more when plate B is shorter, has smaller inertia and so rotates more and the resistive lubrication force increases.

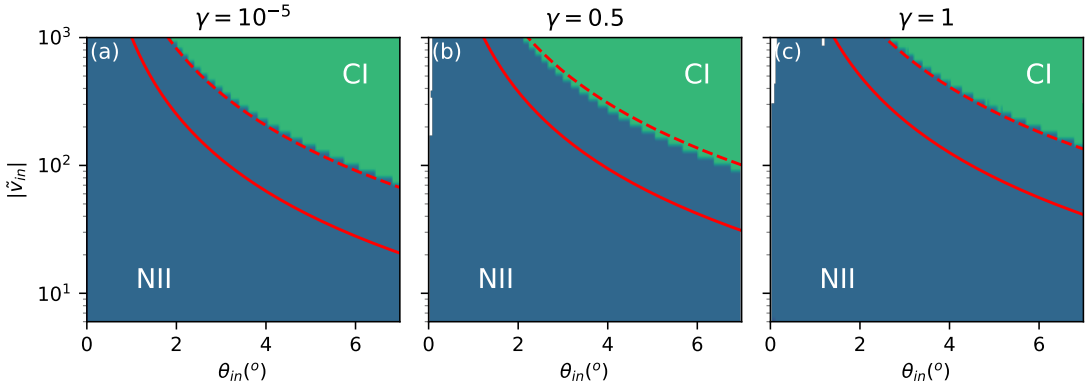

Figure 7.5: Category of the motion of the two plates with (a) very different sizes ($\gamma = L_a/L_b = 10^{-5}$), (b) somewhat different sizes ($\gamma = 1/2$) or (c) the same size ($\gamma = 1$). The plates are initialised with relative angle θ_{in}, $\tilde{h}_{min} = 1$, $\tilde{u}^t_{az} = \tilde{v}_{in} < 0$ and all the other initial conditions being 0. Category NII designates no collision and a sign change in θ. Category CI designates a collision, without a sign change in θ. Case NI designates no collision and no sign change in θ occurs for smaller values of $|\tilde{v}_{in}|$ than are shown in the figure, for which the plates remain comparatively further apart. The solid red line is the predicted collision boundary assuming no rotation using (7.51). The dashed red line is the alternative collision boundary using (7.52).

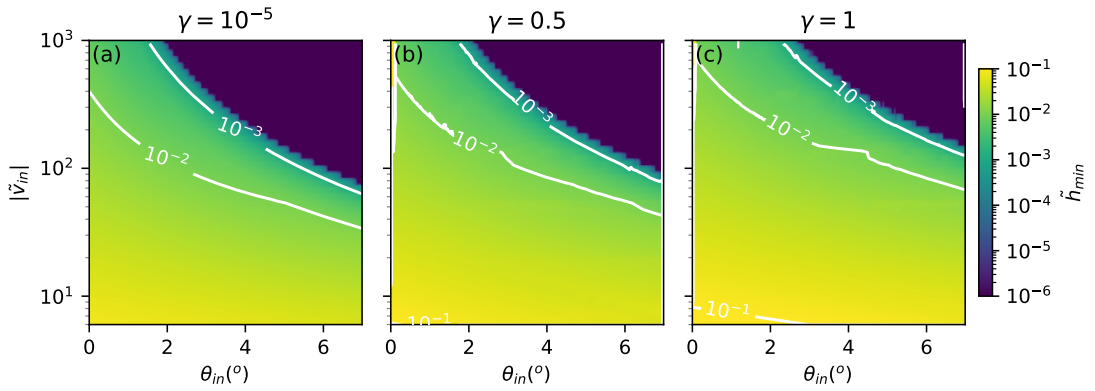

Figure 7.6: Minimum distance between the two plates for different ratios of plate sizes $\gamma = L_a/L_b$: (a) $\gamma = 10^{-5}$, (b) $\gamma = 0.5$, (c) $\gamma = 1$. The plates are initiated with angle θ_{in}, $\tilde{h}_{min} = 1$, $\tilde{u}^t_{az} = \tilde{v}_{in}$ and all the other initial conditions being 0. The white contours are lines of constant h_{min}, and the dark purple shaded region corresponds to the collision criteria being reached.

Figure 7.6 shows the minimum distance between the plates during the simulation. The region of phase space above the collision boundary grows as the length of the bottom plate increases, allowing collisions for smaller values of θ_{in} and $|\tilde{v}_{in}|$.

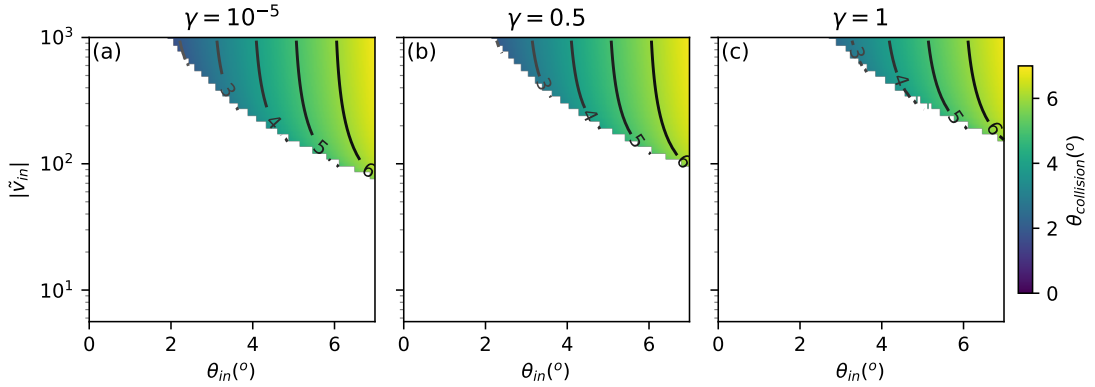

Figure 7.7: Collision angle between the two plates for different ratios of plate sizes $\gamma = L_a/L_b$: (a) $\gamma = 10^{-5}$, (b) $\gamma = 0.5$, (c) $\gamma = 1$. The plates are initiated with angle θ_{in}, $\tilde{h}_{min} = 1$, $\tilde{u}^t_{az} = \tilde{v}_{in}$ and all the other initial conditions being 0. The regions shaded in white are where a collision does not occur. The contour lines are lines of constant $\theta_{collision}$.

Further evidence of the cause for the changes to the collision boundary with γ is illustrated in Figure 7.7, which shows the angle $\theta_{collision}$ between the two plates at the point when they collide. The collision angle decreases with increasing γ

(the curvature of the contours increases with γ) for plates initialised with the same value of $\tilde{v}_{in}$ and θ_{in} but for a larger value of γ. The region shaded white is where a collision does not occur. The contours of constant θ indicate that the change in θ is relatively modest when the collision angle is positive, and remains far from $\theta = 0$. This suggests the potential approximate the position of the collision boundary by solving (7.28) assuming θ is constant, as described below.

7.7.1.1 Collision boundary

Initially, the horizontal forces are much weaker than the vertical forces ($|F_x| \sim |\theta F_z|$ in (7.22)) when u_{ax}, u_{bx} and ω_a are small. Hence we assume that the plates fully overlap and only translate in the $z-$direction with negligible rotation ($u_{ax} = u_{bx} = \omega_a = \omega_b = 0$). Combining the equations of motion (7.28) for the two plates by noting $\tilde{F}_{bz} = -\tilde{F}_{az}$, and using $\tilde{h}_{min} = \tilde{z}_a - \tilde{z}_b - |\theta|/2$ with θ constant, we have

$$\frac{d^2\tilde{h}_{min}}{d\tilde{t}^2} = \tilde{F}_{az}\left(1 + \frac{m_a}{m_b}\right). \tag{7.46}$$

Setting $\tilde{p} = V\tilde{p}_V = (\mathrm{d}\tilde{h}_{min}/\mathrm{d}\tilde{t})\tilde{p}_V$ from the simplification of (7.13) and using the expression for F_{az} in (7.22) along with the non-dimensionalisation defined in §7.4.4, we find,

$$\frac{d^2\tilde{h}_{min}}{d\tilde{t}^2} = \left(1 + \frac{m_a}{m_b}\right)\frac{\mathrm{d}\tilde{h}_{min}}{\mathrm{d}\tilde{t}}\frac{1}{|\theta|^3}\left[\ln\left(\frac{\tilde{h}_{min}}{\tilde{h}_{min} + |\theta|}\right) + \frac{2|\theta|}{2\tilde{h}_{min} + |\theta|}\right], \tag{7.47}$$

where we have used the integral result (D.6) from appendix D.1. When $\theta > 0$, we find

$$\frac{\mathrm{d}^2\tilde{h}}{\mathrm{d}\tilde{t}^2} = \frac{\mathrm{d}\tilde{h}}{\mathrm{d}\tilde{t}}\frac{1}{\theta^3}\left(1 + \frac{m_a}{m_b}\right)\left[\ln\left(\frac{\tilde{h}}{\tilde{h} + \theta}\right) + \frac{2\theta}{2\tilde{h} + \theta}\right]. \tag{7.48}$$

where we have set $\tilde{h} = \tilde{h}_{min}$ for brevity.

$$\frac{\mathrm{d}\tilde{h}}{\mathrm{d}\tilde{t}} - \tilde{v}_{in} = \frac{1}{\theta^3}\left(1 + \frac{m_a}{m_b}\right)[f(\tilde{h}, \theta) - f(\tilde{h}_{in}, \theta)], \tag{7.49}$$

where $\tilde{v}_{in}$ is the initial relative velocity of the plates, $\tilde{h}_{in}$ is the initial value of $\tilde{h}$ and

$$f(\tilde{h}, \theta) = -\tilde{h}\ln\left(1 + \frac{\theta}{\tilde{h}}\right) + \theta\left[\ln\left(2 + \frac{\theta}{\tilde{h}}\right) - \ln\left(1 + \frac{\theta}{\tilde{h}}\right)\right] \tag{7.50}$$

In order to collide we require $\mathrm{d}\tilde{h}/\mathrm{d}\tilde{t} < 0$ at $\tilde{h} = 0$. As $\tilde{h} \to 0$ we find $\mathrm{d}\tilde{h}/\mathrm{d}\tilde{t} \to \tilde{v}_{in} - (1 + m_a/m_b)f(\tilde{h}_{in}, \theta)/\theta^3$. Further, for sufficiently small initial values of $\theta/\tilde{h}_{in}$,

$f(\tilde{h}_{in}, \theta) \approx \theta(\ln 2 - 1)$. Therefore, the collision boundary without rotation or translation is approximately at,

$$|\tilde{v}_{in}| = \left(1 + \frac{m_a}{m_b}\right) \frac{1 - \ln 2}{\theta^2}. \tag{7.51}$$

Figure 7.5 compares the predicted collision boundary from (7.51) in red with the actual boundary between category NII (shaded in blue) and category CI (shaded in green). Although the analytical collision boundary differs from the true boundary by a factor of around $3|\tilde{v}_{in}|$, the shape of the curve does seem to match the true boundary relatively well. The potential sources of disagreement between the numerical and approximate collision boundary seem to arise from the small changes in θ and the horizontal translation of the plates, meaning that $\tilde{\omega}$ and $\tilde{u}_x^t$ are no longer negligible as the plates approach collision. Informed by the structure of (7.51) but with a modified numerical prefactor, the red dashed line in Figure 7.5 shows an alternative expression,

$$|\tilde{v}_{in}| = \left(1 + \frac{m_a}{m_b}\right) \frac{1}{\theta^2}, \tag{7.52}$$

which provides a reasonable fit to the true boundary.

7.7.2 Stress and curvature

Recall that the maximum stress at any instant is proportional to the maximum curvature $|\kappa_i|_{max}$. We therefore consider the maximum curvatures of plates A and B over all time and space that is induced by elastic bending as calculated in §7.6. We calculate the curvatures for $\gamma = 10^{-5}$ as in this case we do not have to consider the scenarios when the plates do not fully overlap. Figure 7.8 shows that the maximum curvature increases with increasing relative velocity $\tilde{v}_{in}$, but has much weaker dependence on θ_{in} (the contours are approximately aligned with the θ_{in}-axis). The exception comes in the case where a collision occurs where, as noted in §7.6.2, the curvature becomes infinite (white areas). We find that the maximum curvature occurs close to the centre of each plate. The curvature increases with

increasing $|\tilde{v}_{in}|$, as the pressure difference across the plate increases with $|\tilde{v}_{in}|$. The maximum curvature of plate B is much larger than the maximum curvature of plate A. The difference is evaluated in §7.7.2.1.

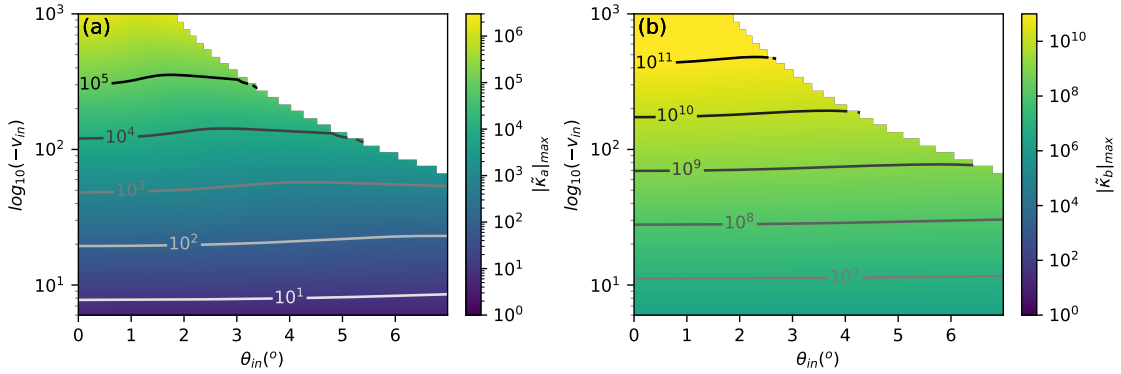

Figure 7.8: Maximum dimensionless curvature for the plates with initial velocity $\tilde{v}_{in}$ and initial angle θ_{in}. We set $D_a = D_b$ and $\gamma = L_a/L_b = 10^{-5}$. The white region corresponds to simulations which ended in a collision, leading to an infinite curvature. The contours are lines of constant dimensionless curvature. a) the maximum curvature of plate A. b) the maximum curvature of plate B.

7.7.2.1 Analytical approximation for maximum curvature in the case when the plates do not collide

Figure 7.8 shows that the maximum curvature is largely independent of θ_{in}. We therefore obtain an approximation for the maximum curvature by considering the case when $\theta_{in} = 0$ and $\tilde{x}_a = \tilde{x}_b$ throughout the motion. In that case $\Omega = 0$, $V = \tilde{u}^t_{az} - \tilde{u}^t_{bz}$ and $\tilde{h} = \tilde{h}_{min}$ throughout, and we find (see §D.5) that the maximum curvature at any instant occurs at the midpoint of plates A and B and is given by,

$$|\tilde{\kappa}_i|_{max} = \left| \frac{D_a V}{384 D_i \tilde{h}^3} \left(\frac{4L_i}{L_a} - 3 \right) \right|, \tag{7.53}$$

for $i = a, b$. If the plates have the same thickness, $D_a = D_b$, then $|\tilde{\kappa}_b|_{max} > |\tilde{\kappa}_a|_{max}$ for $L_b > L_a$ so the larger plate will break first. Equation (7.53) shows that $|\tilde{\kappa}_b|_{max} \gg |\tilde{\kappa}_a|_{max}$ for $\gamma = 10^{-5}$, consistent with Figure 7.8. The curvature increases with increasing V and decreasing $\tilde{h}$ due to enhanced lubrication pressure.

To see how (7.53) evolves through time we first relate V to $\tilde{h}$, noting that $V = \tilde{u}^t_{az} - \tilde{u}^t_{bz} = d\tilde{h}/d\tilde{t}$. We use (7.28) to relate the forces at zero angle to the

translational velocity. If $\theta_{in} = 0$ and $\tilde{x}_a = \tilde{x}_b$, then $\tilde{\omega}_a = \tilde{\omega}_b = 0$ for all time. Therefore, $\tilde{p} = V\tilde{p}_V$ and $-\tilde{F}_{bz} = \tilde{F}_{az} = V\int_0^1 \tilde{p}_V d\tilde{x} = -V/(12\tilde{h}^3)$ from (D.11), so the equations of motion give

$$\frac{\mathrm{d}V}{\mathrm{d}\tilde{t}} = -\left(1 + \frac{m_a}{m_b}\right)\frac{V}{12\tilde{h}^3}. \tag{7.54}$$

Solving with the initial condition $V(0) = \tilde{v}_{in}, \tilde{h}(0) = \tilde{h}_{in}$, we obtain

$$V = \tilde{v}_{in} + \frac{1}{24}\left(1 + \frac{m_a}{m_b}\right)\left(\frac{1}{\tilde{h}^2} - \frac{1}{\tilde{h}_{in}^2}\right). \tag{7.55}$$

Substituting (7.55) into (7.53) we find an expression for the predicted maximum curvature $\tilde{\kappa}_i|_{pred}$ in terms of $\tilde{h}$,

$$|\tilde{\kappa}_i|_{pred} = \left|\frac{D_a}{384 D_i \tilde{h}^3}\left(\frac{4L_i}{L_a} - 3\right)\left[\tilde{v}_{in} + \frac{1}{24}\left(1 + \frac{m_a}{m_b}\right)\left(\frac{1}{\tilde{h}^2} - \frac{1}{\tilde{h}_{in}^2}\right)\right]\right|. \tag{7.56}$$

Initially the magnitude of the curvature increases as the gap thickness $\tilde{h}$ decreases, and there is increasing resistance to squeezing out the fluid between the plates. However, the resulting deceleration eventually leads to a reduction in pressure between the plates and the curvature decreases with further decreasing $\tilde{h}$. As the maximum stress is proportional to the maximum curvature from (7.40), these physical effects also impact the variation of the stress.

We find the value of $\tilde{h}$ where the curvature is largest by maximising (7.56) over values of $\tilde{h}$ where $d\tilde{h}/d\tilde{t} < 0$, such that,

$$\tilde{h} \geq \left(\frac{1}{\tilde{h}_{in}^2} - \frac{24\tilde{v}_{in}}{1 + \frac{m_a}{m_b}}\right)^{-1/2}. \tag{7.57}$$

In this case we find that $|\tilde{\kappa}|_{max}$ is largest at its local maximum over time, which is found at

$$\tilde{h} = \tilde{h}_{max} = \tilde{h}_{in}\sqrt{\frac{5(1 + m_a/m_b)}{3(1 + m_a/m_b - 24\tilde{h}_{in}^2\tilde{v}_{in})}}. \tag{7.58}$$

and the curvature then has magnitude,

$$|\tilde{\kappa}_i|_{max} = \left|\frac{\sqrt{15}}{192000}\frac{D_a}{D_i}\left(\frac{4L_i}{L_a} - 3\right)\frac{(1 + m_a/m_b - 24\tilde{h}_{in}^2\tilde{v}_{in})^{5/2}}{\tilde{h}_{in}^5(1 + m_a/m_b)^{3/2}}\right|. \tag{7.59}$$

For the maximum curvature to be at $\tilde{h}_{max}$ we also require $\tilde{h}_{max} \leq \tilde{h}_{in}$, which requires,

$$\tilde{v}_{in} \leq -\frac{1}{36\tilde{h}_{in}^2}\left(1+\frac{m_a}{m_b}\right) = v_{crit}. \tag{7.60}$$

In the cases where $\tilde{h}_{max} > \tilde{h}_{in}$ the maxima immediately occurs when $\tilde{h} = \tilde{h}_{in}$, although the lubrication approximation is less valid in such cases anyway. Overall,

$$|\tilde{\kappa}_i|_{max} \approx \begin{cases} \left|\frac{D_a}{D_i}\frac{\sqrt{15}}{192000}\left(\frac{4L_i}{L_a}-3\right)\frac{(1+m_a/m_b-24\tilde{h}_{in}^2\tilde{v}_{in})^{5/2}}{\tilde{h}_{in}^5(1+m_a/m_b)^{3/2}}\right|, & \tilde{v}_{in} \leq v_{crit}, \\ \left|\frac{D_a}{D_i}\frac{1}{384}\left(\frac{4L_i}{L_a}-3\right)\frac{\tilde{v}_{in}}{\tilde{h}_{in}^3}\right|, & \tilde{v}_{in} > v_{crit}. \end{cases} \tag{7.61}$$

Figure 7.9 compares the maximum curvature obtained for each angle to the analytical estimate from (7.61). The ratio of the numerical maxima to the analytical maxima is less than 1.6 in all cases for $0 \leq \theta_{in} \leq 7^o$.

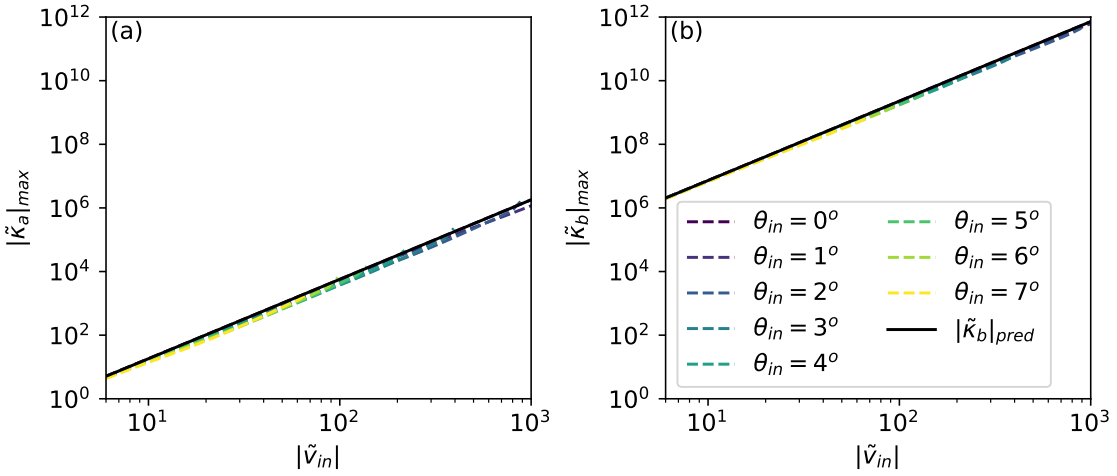

Figure 7.9: a) Maximum curvature for plate A, $|\tilde{\kappa}_a|_{max}$ for $\gamma = 10^{-5}$ as a function of the initial velocity $\tilde{v}_{in}$. Each of the coloured lines corresponds to a different value of θ_{in} and the black line is the analytical estimate from (7.61). b) Maximum curvature for plate B, $|\tilde{\kappa}_b|_{max}$ for $\gamma = 10^{-5}$ as a function of the initial velocity $\tilde{v}_{in}$. Results where a collision occurred are not plotted.

We can relate the expression for the maximum dimensionless curvature to the true curvature and stresses using (7.39) and (7.40). Combining (7.40), (7.61) and letting $\tilde{h}_{in} = 1$ (as used in the simulations), the maximum tensile and compressive stress in plate i is given by,

$$\sigma_{max} = \frac{9L_a\eta^2}{4\rho D_i^2 D_a}\left(\frac{4L_i}{L_a}-3\right)\begin{cases} \frac{\sqrt{15}}{500}\frac{1}{(1+m_a/m_b)^{3/2}}\left(1+\frac{m_a}{m_b}-24\tilde{v}_{in}\right)^{5/2}, & \tilde{v}_{in} \leq -\left[\frac{1+(m_a/m_b)}{36}\right], \\ -\tilde{v}_{in}, & \tilde{v}_{in} > -\left[\frac{1+(m_a/m_b)}{36}\right]. \end{cases} \tag{7.62}$$

Recalling that the true initial relative vertical velocity v_{in} is related to the dimensionless vertical velocity $\tilde{v}_{in}$ by $v_{in} = 12\eta\tilde{v}_{in}/(\rho D_a)$, we can rearrange (7.62) to find the minimum $|v_{in}|$ required to cause the plates to fracture at a given fracture stress σ_{max},

$$v_{in} = \frac{12\eta}{\rho D_a}\begin{cases} -\frac{\sigma_{max}}{\alpha}, & \sigma_{max} \leq \frac{\alpha}{36}\left(1+\frac{m_a}{m_b}\right), \\ \frac{1}{24}\left[\left(1+\frac{m_a}{m_b}\right) - \left(\frac{\sigma_{max}}{\alpha\beta}\right)^{2/5}\right], & \sigma_{max} > \frac{\alpha}{36}\left(1+\frac{m_a}{m_b}\right). \end{cases} \tag{7.63}$$

Here $\alpha = (4L_i/L_a - 3)\,9L_a\eta^2/(4\rho D_i^2 D_a)$ and $\beta = \sqrt{15}(1+m_a/m_b)^{-3/2}/500$.

7.7.3 Application to frazil ice

We now apply our results for the collision criteria and fracture criteria to frazil ice. We use both the numerical collision boundary and the collision boundary given by (7.52) as well as the analytical fracture boundary (7.63) to calculate whether frazil ice crystals are likely to collide and/or fracture under the likely conditions found in polynyas. Our results apply for crystals approaching close to parallel and, although the crystals are often disk-shaped (Schneck et al., 2019), we apply the 2D results with L_i given by the crystal diameter. The weakness of these assumptions is discussed in §7.8.

The maximum tensile strength σ_{max} of a single ice crystal is $\sim$ 1-10 MPa (Schulson and Duval, 2009). The thickness of a crystal D_i is related to the crystal radius, r_i and aspect ratio d by $D_i = 2r_i/d$ and $r_i \sim r_i/2$. We choose a lower bound of $\sigma_{max} = 1$ MPa (Schulson and Duval, 2009) and $\rho_I = 920\,\mathrm{kgm}^{-3}$ (Svensson and Omstedt, 1998), $\eta = 1.9\times10^{-3}\,\mathrm{kg\,m^{-1}\,s^{-1}}$ (ITTC, 2011). In line with Souillé et al. (2023) we choose $5 \leq d \leq 100$, $0.002 \leq r_b \leq 10$ mm and $10^{-5} \leq r_a/r_b \leq 1$, which are the maximum possible range that these values are observed to take across a compilation of various experiments. The maximum expected velocities of the crystals within a polynya are $\sim 0.1\,\mathrm{ms}^{-1}$ (Herman et al., 2020).

We first calculate the velocity required for a collision. The approximation (7.52) for the collision boundary predicts that the minimum dimensionless relative speed for a collision at small relative angles $(0 < \theta_{in} < 7)^o$ is $|\tilde{v}_{in}| = 67$. Recalling that

the dimensionless velocity $\tilde{v}_{in}$ is related to the velocity v_{in} by $v_{in} = 12\eta\tilde{v}_{in}/(\rho D_a)$. This means that we require $D_a > 1$cm for $|v_{in}| < 0.1$ m/s which clearly violates the assumption of a thin plate used in the model and the plate thickness is much larger than observed thicknesses of frazil ice crystals (Souillé et al., 2023). If instead of using the analytical expression for a collision, we use the numerical collision boundary, we find that the minimum dimensionless relative velocity to cause a collision is $\tilde{v}_{in} = [-77, -98, -156]$ for the case when $\gamma = L_a/L_b = [10^{-5}, 1/2, 1]$, respectively and $\theta \leq 7^o$. This suggests that collisions of frazil ice crystals for typical oceanographic conditions are unlikely. For higher values of θ_{in}, (7.52) suggests that the required initial relative velocity may be small enough for a collision of these crystals to occur with the criteria varying $\propto \theta_{in}^{-2}$. However, further work is required to test whether this result derived using the lubrication approximation is still valid at larger angles.

Next, using (7.63), we calculate the minimum initial speed required for fracture in the case when a collision does not occur. Varying L_a, L_b and d across the full range of parameter values, we find that the minimum initial speed required for the crystals to fracture is > 1 m/s. This is an order of magnitude faster than the likely maximum speed of crystals in polynyas (but may be possible close to the mechanical stirrers used in laboratory experiments), suggesting that crystals are unlikely to fracture without making contact. However, further work is required to test the validity of (7.63) for plates of similar length.

This suggests that, when crystals approach close to parallel at typical oceanographic velocities, secondary nucleation by crystals snapping can only occur for similarly sized crystals in typical polynya conditions with thicknesses of at least 1cm, which means the crystals will be $\mathcal{O}(10\,\text{cm})$ in diameter. If a large number of crystals are to be produced in a short period of time this would either need (i) significant numbers of collisions of large crystals carried at the faster speeds, (ii) smaller scale dendrite snapping, or potentially (iii) approach at a steeper angle than

considered here. The second of these would support the current implicit hypothesis that secondary nucleation occurs when small dendritic structures are broken off from the crystal surface (Svensson and Omstedt, 1994). However, further work is required to rule out the third option as we need to understand the conditions for crystals snapping at larger relative angles.

7.8 Conclusions

In this chapter we have considered how hydrodynamic interactions alter the trajectory of two thin stiff elastic plates approaching with small relative angle. Using the thin-film approximation and Euler-Bernoulli beam theory, we have calculated the criteria for two thin and stiff elastic plates to collide and/or fracture when moving through a viscous fluid in two spatial dimensions. We initialised simulations with plates at relative angles $0 \leq \theta_{in} \leq 7^o$ and dimensionless relative vertical velocity $10^{-4} \leq |\tilde{v}_{in}| \leq 10^3$. The critical velocity for collision increases with the viscosity of the fluid and decreases with the density and thickness of the smaller plate, the initial relative angle between the plates and the ratio of the mass of the smaller plate to the mass of the larger plate. An approximation for the critical velocity is given by (7.52).

In cases when a collision does not occur, we found an analytical approximation (7.62) for the maximum stress on each plate. The maximum stress increases with initial relative speed. The condition, (7.62) can also be used to obtain the minimum initial speed which causes the plates to fracture (7.63) without collision. We also showed that in cases where a collision occurs the stress diverges so that the plates always fracture. These results could be relevant to fracture criteria in industrial crystallisers or mechanically stirred systems with large velocities.

We applied this collision and fracture criteria to frazil ice. The results show that for typical polynya conditions, with initial relative velocities of ~ 0.1 m/s fracture is unlikely for disks of typical size approaching close to parallel. The velocities required to fracture, when the disks approach close to parallel, in the case when

the crystals do not collide are at least an order of magnitude higher than the likely speeds of crystals in polynyas. This might tentatively support the current implicit hypothesis that secondary nucleation occurs by small dendrites breaking off from crystals (Svensson and Omstedt, 1994) rather than by complete crystal snapping. However, the lubrication calculations suggest that the critical velocities reduce significantly ($\propto \theta^{-2}$) with increasing relative angle of the plates. More work is therefore needed to rule out collision and fracture at steeper angles of approach where the lubrication approximation breaks down.

This chapter has also focused on the collision of thin plate-like crystals. Frazil ice crystals are observed to mostly have thin-circular disk-like geometries (Schneck et al., 2019), requiring consideration of the third dimension. The fluid flux between two approaching circular disks will be different to the one-dimensional flux in the rectangular case, and hence the restive lubrication force is likely to be different. Plate theory (Mittelstedt, 2023) would have to be used instead of beam-theory to model the deflection of disk-shaped crystals. Further, we found that collisions become more likely when the initial relative angle between the plates is greater, but for large angles the lubrication approximation breaks down. Hence, the next chapter explores the case when the initial relative angle is larger and accounts for the full three-dimensional disk geometry.

"Then Moses stretched out his hand over the sea, and all that night the Lord drove the sea back with a strong east wind and turned it into dry land. The waters were divided, 22 and the Israelites went through the sea on dry ground, with a wall of water on their right and on their left."

— Exodus 14:21-22 NIV

8 3D Collision Efficiency

Contents

8.1 Introduction

In §7 we calculated the effect of two-dimensional hydrodynamic interactions on two approaching plates. We found that the relative velocity needed for these plates to collide is high relative to the likely velocities of frazil ice crystals in polynyas. However, we noted that this calculation gives only an approximate result as in reality frazil ice crystals are often disk-shaped (Daly, 1984) and would generate

three-dimensional patterns of flow.

Therefore, in this chapter we adapt the calculation described in §7 to apply to disk-shaped objects and eventually obtain an expression for the collision efficiency introduced in §2.4.1. After describing the initial setup in §8.2, we follow the same approach of first in §8.3 using the lubrication approximation to calculate the forces and torques on each disk. Then in §8.4 we define the equations of motion, initial conditions and the end criteria for the simulations. In §8.5.1 we compare the results of the full 3D calculation to the results found in §7 for the 2D case. Finally, in §8.5.2 we calculate a collision efficiency.

8.2 Setup

As in §6 we consider collisions of disk A with disk B. In §6.2 we defined two angles to describe the orientation of a disk in the laboratory frame. Following the notation in §7, we denote angles measured in the lab frame with a prime. Therefore, following the definitions in §6.2, θ_i' is the angle the axis of disk i makes with the z'-axis and ϕ_i', is the angle the axis of disk i makes with the $x'-$axis in the x'-y' plane. In this chapter we assume that both disks A and B are orientated with the same angle $\phi_a' = \phi_b'$, chosen as $\phi_a' = \phi_b' = 0$ so that the geometry is symmetric in y'. This removes a degree of freedom from our problem and makes it far less computationally expensive. However, it does mean that we do not fully capture all possible orientations.

Letting the initial setup be symmetric in y', we use a similar geometry to the 2D case (see Figure 8.1). We use the setup shown in Figure 8.1 where the top disk is labelled A with centre of mass (x_a', z_a') and moves with local velocity (u_{ax}', u_{az}') in the x'-z' plane. Likewise, the bottom disk, labelled B has centre of mass (x_b', z_b') and moves with local velocity (u_{bx}', u_{bz}') in the $x - z$ plane. The velocity of the fluid in between the disks is (u_x', u_z'). We define θ_a' and θ_b' as the respective angles between the x'-axis and the basal planes of disks A and B. Disks A and B have

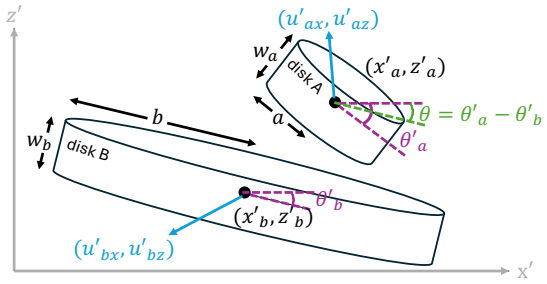

Figure 8.1: Frame S'. We consider two disks moving only in the $xz-$plane. The top disk is labelled A with centre of mass (x'_a, z'_a) and moves with local velocity (u'_{ax}, u'_{az}). Likewise, the bottom disk, labelled B has centre of mass (x'_b, z'_b) and moves with local velocity (u'_{bx}, u'_{bz}). The relative angle between the disks $\theta = \theta'_a - \theta'_b$. The radii and widths of disks A and B are a, w_a and b, w_b respectively.

respective radii a, b and widths w_a, w_b. The aspect ratios d_a, d_b of the disks A and B are given by, $d_a = 2a/w_a$, $d_b = 2b/w_b$.

8.3 Derivation of the forces and torques

8.3.1 Rotated reference frame

Following the same method for the 2D case (see §7.4.2), we first obtain the pressure and calculate the forces and torques on the disks. As for the 2D case, the pressure is independent of the coordinate system, so to simplify the algebra we choose to calculate the pressure in the reference frame where the bottom disk is instantaneously horizontal (frame S).

Figure 8.2 shows the possible orientations of disk A for $0 \leq \theta_a \leq 2\pi$. The configuration is cyclic for $\theta_a \mapsto \theta_a + n\pi$, where n is an integer. There are two different possible orientations. The first case is for $0 + n\pi \leq \theta_a \leq \pi/2 + n\pi$ where n is an integer and corresponds to case A and case C in Figure 8.2. In this setup the flat face is to the left of the minimum point. The second case is for $\pi/2 + n\pi < \theta_a < n\pi$ where n is an integer (case B and case D in Figure 8.2). In this setup the lower planar face is to the right of the minimum point. As in the 2D case, in the derivation below we illustrate the method by solving for the second case when $n\pi - \pi/2 < \theta < n\pi$ and for disks A and B completely overlapping . The case

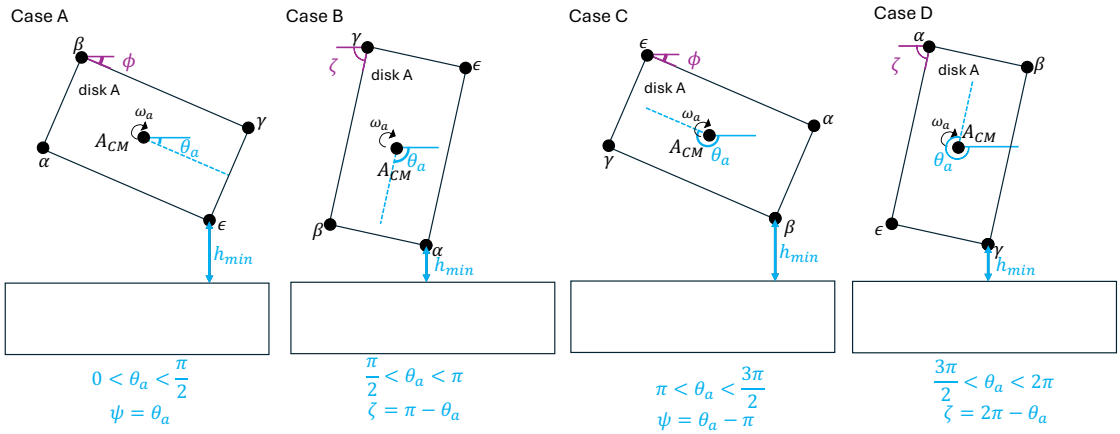

Figure 8.2: The minimum distance and location of the lowest point of disk A both change as disk A rotates by an angle θ_a, where $\theta_a = \theta'_a - \theta'_b$. We plot the orientations of disk A in frame S (where disk B is instantaneously horizontal). Comparing case A and C, and case B and D, the setup looks the same for $\theta_a \mapsto n\pi + \theta_a$ where n is an integer, with the only difference being that the location changes on the disk where the lowest point is found (point ϵ in case A, point α in case B, point β in case C and point γ in case D). We define angles ϕ and ζ as the acute angle between the planar face of disk A and the x-axis. Where ζ is used when the height of the planar face above disk B decreases with x and ϕ is used when the height of the planar face above disk B increases with x.

of $n\pi \leq \theta \leq \pi/2 + n\pi$ is solved for in §E.2 and the more complex case of incomplete overlap is solved for in §E.3.

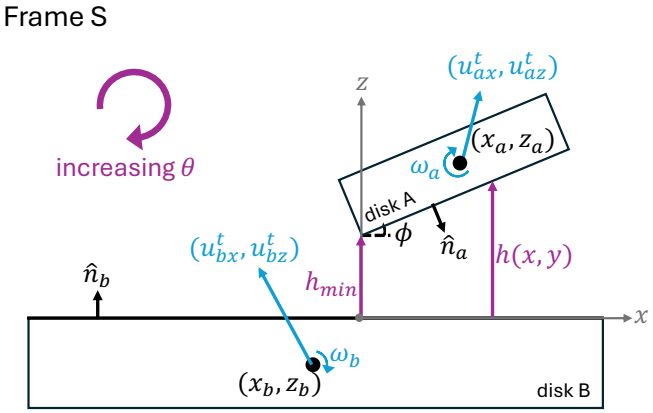

Figure 8.3: We calculate the pressure and resulting forces and torques in reference frame S in which the bottom plate is horizontal. We set $\phi = -\theta$. The perpendicular distance $h(x)$ between the plates depends on x and ϕ, with the minimum perpendicular distance given by h_{min}.

Figure 8.3 shows frame S, the inertial reference frame where disk B is instanta-

neously horizontal. Like in §7.4.2 we set ϕ to be the acute angle between the x-axis and the lower planar face of disk A (see Figure 8.2). For $-\pi/2 < \theta < 0$, $\phi = -\theta$, we set $x = 0$ to be at the minimum distance between the disks and locate the top of the bottom disk to be along $z = 0$. Defining the coordinates x', z' in the lab frame S', the coordinates x, z in frame S are related to the coordinates in frame S' by

$$x = \cos\theta'_b(x' - x'_a) - \sin\theta'_b(z' - z'_a) + a\cos\phi - \frac{w_a}{2}\sin\phi, \tag{8.1}$$

$$z = \sin\theta'_b(x' - x'_b) + \cos\theta'_b(z' - z'_b) - \frac{w_b}{2}, \tag{8.2}$$

such that in frame S in the region where disk A overlaps with disk B,

$$h(x,y) = \begin{cases} h_{min} - x\cot\phi + \frac{a \pm (a^2 - y^2)^{1/2}}{\sin\phi}, & x < 0 \\ h_{min} + x\tan\phi, & x \geq 0. \end{cases} \tag{8.3}$$

Derivations for the expressions for $h(x,y)$ can be found in §E.1. The differences between (8.1)-(8.3) in the 2D case and (7.2) in §7.4.2 arise from the cylindrical geometry where the thickness of the crystal is no longer neglected and both faces must be taken into account.

8.3.2 Fluid flux and pressure

Similarly to the 2D case, mass conservation implies that the change in distance h between two objects will be equal to the divergence of the fluid flux $\mathbf{q}$ spreading out from the two objects,

$$\frac{\partial h}{\partial t} + \nabla \cdot \mathbf{q} = 0. \tag{8.4}$$

where, as in the 2D case, we have again neglected freezing, a justification for this is given in §E.4. Using the same method as in the 2D case, and noting that $q_y = \int_0^h u_y \, \mathrm{d}z$, and $u_{by} = u_{ay} = 0$ we can derive an expression for the flux in the $x-$ and $y-$ directions. The equation for $\partial h/\partial t$ is the same as (7.9). We combine the solution to (8.4) with (7.9) to obtain an expression for the pressure,

$$\frac{\partial}{\partial x}\left(h^3(x,y)\frac{\partial p(x,y)}{\partial x}\right) + \frac{\partial}{\partial y}\left(h^3(x,y)\frac{\partial p(x,y)}{\partial y}\right) = 12\eta\left[(u_{az} - u_{bz}) - u_{ax}\frac{\partial h}{\partial x} + \frac{1}{2}\frac{\partial (u_{ax} + u_{bx})h}{\partial x}\right]. \tag{8.5}$$

Like in the 2D case we split the velocity of each crystal into a translational and rotational component $\dot{\mathbf{r}} = \mathbf{u^t} + \omega \times (\mathbf{r} - \mathbf{r}_{CM})$ (c.f. (7.3) and (7.4)), where the rotation is about the centre of mass. The equation to obtain the translational and rotational velocities in frame S, (7.5) is the same as that used in the 2D case.

8.3.2.1 Coordinate system

In Frame S, $z_b = -w_b/2$ and the planar surface of the bottom disk is parallel to the z-axis (Figure 8.3), such that the expression for the pressure becomes,

$$\frac{\partial}{\partial x}\left(h^3(x,y)\frac{\partial p(x,y)}{\partial x}\right) + \frac{\partial}{\partial y}\left(h^3(x,y)\frac{\partial p(x,y)}{\partial y}\right) = 12\eta\Bigg[(u^t_{az} - u^t_{bz}) - (\omega_a - \omega_b)x + \omega_a x_a - \omega_b x_b - \frac{1}{2}\left(u^t_{ax} - u^t_{bx} - \omega_a z_a - \frac{\omega_b w_b}{2}\right)\frac{\partial h}{\partial x}\Bigg]. \quad (8.6)$$

The edges of the smaller disk are at (see §E.1) $x = [a \pm (a - y^2)^{1/2}]\cos\phi)$ and $x = -w_a \sin\phi + [a \pm (a - y^2)^{1/2}]\cos\phi$.

We assume that the pressure difference in the region where the disks do not overlap. If the surface of A is completely on top of the surface of B the boundary condition is given by,

$$p(x = [a + (a^2 - y^2)^{1/2}]\cos\phi) = 0, \quad (8.7)$$

$$p(x = -w_a \sin\phi + [a - (a^2 - y^2)^{1/2}]\cos\phi) = 0. \quad (8.8)$$

In the scenario when the surface of A is not completely on top of the surface of B, the pressure difference is zero at the boundary of disk B.

8.3.2.2 Non dimensionalisation and solution for the pressure

We use the same non-dimensionalisation as in in the 2D case (see §7.4.3.1) but set $L_a = a$ and we include an additional scaling, $y = a\tilde{y}$. We set,

$$\Omega = \tilde{\omega}_a - \tilde{\omega}_b, \quad (8.9)$$

$$V = (\tilde{u}^t_{az} - \tilde{u}^t_{bz}) + \tilde{\omega}_a\tilde{x}_a - \tilde{\omega}_b\tilde{x}_b, \quad (8.10)$$

$$U = \frac{1}{2}\left(\tilde{u}^t_{ax} - \tilde{u}^t_{bx} - \tilde{\omega}_a\tilde{z}_a - \frac{\tilde{\omega}_b\tilde{w}_b}{2}\right), \quad (8.11)$$

such that (8.6) becomes,

$$\frac{\partial}{\partial\tilde{x}}\left(\tilde{h}^3(\tilde{x},\tilde{y})\frac{\partial\tilde{p}(\tilde{x},\tilde{y})}{\partial\tilde{x}}\right)+\frac{\partial}{\partial\tilde{y}}\left(\tilde{h}^3(\tilde{x},\tilde{y})\frac{\partial\tilde{p}(\tilde{x},\tilde{y})}{\partial\tilde{y}}\right) = -\Omega\tilde{x}+V-U\frac{\partial\tilde{h}}{\partial\tilde{x}}. \quad (8.12)$$

Compared to the expressions for Ω and V in §7.4.3.1, note that the previous expression for V (7.13) has been split into V and U because $\partial\tilde{h}/\partial\tilde{x}$ varies on each face.

As in §7.4.3.1, this equation is linear in $\tilde{p}$. Hence we split the pressure into three components $\tilde{p}=V\tilde{p}_V+U\tilde{p}_U+\Omega\tilde{p}_\Omega$, and individually impose the boundary condition that each component of the pressure is zero at the points where the disks no longer overlap. The components satisfy,

$$\frac{\partial}{\partial\tilde{x}}\left(\tilde{h}^3(\tilde{x},\tilde{y})\frac{\partial\tilde{p}_\Omega(\tilde{x},\tilde{y})}{\partial\tilde{x}}\right)+\frac{\partial}{\partial\tilde{y}}\left(\tilde{h}^3(\tilde{x},\tilde{y})\frac{\partial\tilde{p}_\Omega(\tilde{x},\tilde{y})}{\partial\tilde{y}}\right)=-\tilde{x}, \quad (8.13)$$

$$\frac{\partial}{\partial\tilde{x}}\left(\tilde{h}^3(\tilde{x},\tilde{y})\frac{\partial\tilde{p}_V(\tilde{x},\tilde{y})}{\partial\tilde{x}}\right)+\frac{\partial}{\partial\tilde{y}}\left(\tilde{h}^3(\tilde{x},\tilde{y})\frac{\partial\tilde{p}_V(\tilde{x},\tilde{y})}{\partial\tilde{y}}\right)=1, \quad (8.14)$$

$$\frac{\partial}{\partial\tilde{x}}\left(\tilde{h}^3(\tilde{x},\tilde{y})\frac{\partial\tilde{p}_U(\tilde{x},\tilde{y})}{\partial\tilde{x}}\right)+\frac{\partial}{\partial\tilde{y}}\left(\tilde{h}^3(\tilde{x},\tilde{y})\frac{\partial\tilde{p}_U(\tilde{x},\tilde{y})}{\partial\tilde{y}}\right)=-\frac{\partial\tilde{h}}{\partial\tilde{x}}. \quad (8.15)$$

We solve numerically for $\tilde{p}_\Omega$, $\tilde{p}_V$ and $\tilde{p}_U$ for $10^{-6}\leq\tilde{h}_{min}\leq10^4$, $0\leq\phi\leq\pi/2$, $-(b-a)\leq\tilde{x}_a-\tilde{x}_b\leq b-a$ using a finite difference scheme. We initially set $\tilde{h}_{min}=10^4$ and use 501×501 grid points to solve (8.13)-(8.15) for the components of the pressure. As $\tilde{h}_{min}$ decreases to 10^{-6} we increase the grid resolution about the location where $\tilde{h}(\tilde{x},\tilde{y})=\tilde{h}_{min}$. Full details can be found in §E.5.

Figure 8.4 shows $\tilde{p}_V$ for $\phi=\pi/4$. The maximum pressure increases by 12 orders of magnitude from $\tilde{h}_{min}=10^2$ to $\tilde{h}_{min}=10^{-6}$. The pressure distribution becomes increasingly sharply peaked and the location of the maximum pressure shifts from being close to the centre of disk A to being close to $\tilde{x},\tilde{y}=0$, the location of the lowest point of disk A. Hence, when the V terms dominate and $\tilde{h}_{min}$ is small we expect the hydrodynamic stresses to be highly localised near the lower edge of disk A.

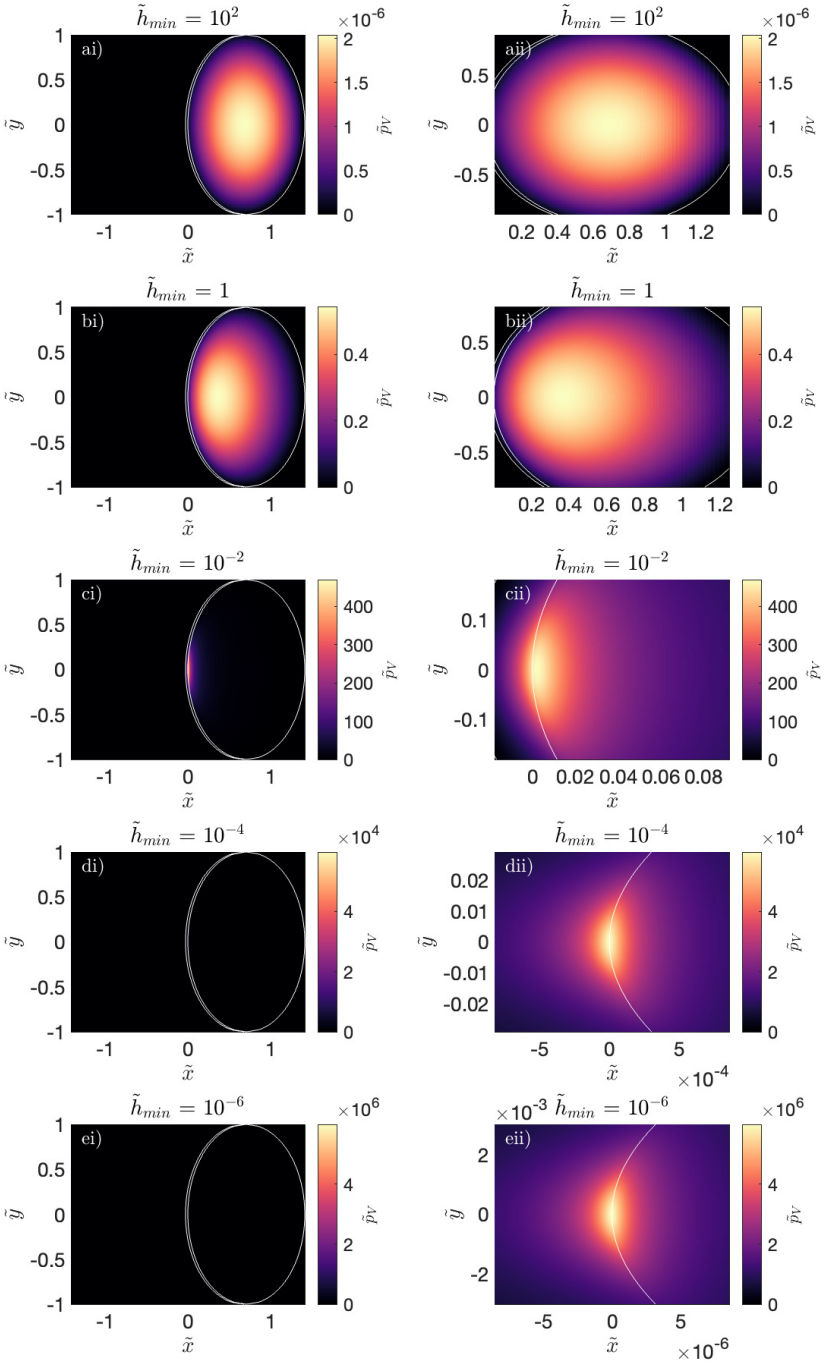

Figure 8.4: The pressure $\tilde{p}_V$ calculated for $\phi = \pi/4$ for $\tilde{h}_{min}$ decreasing from 10^2 in the top row to 10^{-6} in the bottom row. Panels ai, bi, ci, di and ei show the full pressure distribution. Panels aii, bii, cii, dii and eii show the pressure distribution zoomed close to its maximum, such that the pressure only reduces by about a factor of 5 from its maximum value in the panel. The white lines are the edges of disk A.

8.3.3 Forces and torques

Having obtained an expression for the pressure between the disks, we can calculate the forces and torques on each disk. The forces and torques are obtained by the same method as detailed in §7 but the integral is over the surface S_a of the smaller disk rather than along a line when evaluating per unit length (7.22) and (7.24) in §7 become,

$$-\mathbf{F}_b = \mathbf{F}_a \approx \begin{pmatrix} -\iint\limits_{S_a} \left[\frac{p}{2}\frac{\partial h}{\partial x} + \eta(u^t_{ax} - u^t_{bx} - \omega_a z_a - \omega_b w_b/2)\frac{1}{h} + \eta\omega_a\right] dxdy \\ 0 \\ F \end{pmatrix}, \quad (8.16)$$

$$\tau_a \approx -\hat{\mathbf{y}}\left[\iint\limits_{S_a} xpdxdy - x_a F\right], \quad (8.17)$$

$$\tau_b \approx \hat{\mathbf{y}}\left[\iint\limits_{S_a} xpdxdy - x_b F\right], \quad (8.18)$$

where $F = \iint_{S_a} p\mathrm{d}x\mathrm{d}y$ and again we have employed integration by parts for the terms involving $p\partial h/\partial x$ and set the pressure to be zero in the non-overlapping region.

The result (7.25) relates the forces and torques between frames S' and S, valid also here in 3D as well as in the previous 2D case.

Applying the non-dimensionalisation from in §7.4.3.1 and §8.3.2.2, we express the dimensionless forces $\tilde{F}$ and torques $\tilde{\tau}$ in terms of the dimensionless variables $\tilde{p}, \tilde{u}^t_{ax}, \tilde{u}^t_{bx}, \tilde{\omega}_a, \tilde{z}_a$. We obtain $F = (12\eta a^2/T)\tilde{F}$ and $\tau = (12\eta a^3/T)\tilde{\tau}$. We then integrate the pressure to find the forces and torques. The numerical method to solve for the forces and torques is discussed in §E.6.

Figure 8.5 shows $|\iint \tilde{p}_V \mathrm{d}\tilde{x}\mathrm{d}\tilde{y}|$ as a function of ϕ. Initially $F = V\iint \tilde{p}_V \mathrm{d}\tilde{x}\mathrm{d}\tilde{y}$, so this plot gives insight into the initial expected behaviour of the disks. For small $\tilde{h}_{min}$, the resistive force is several orders of magnitude higher when the disks are close to parallel or close to perpendicular. Therefore, this plot suggest that collisions may be possible at much lower speeds when the disks are far from them being parallel

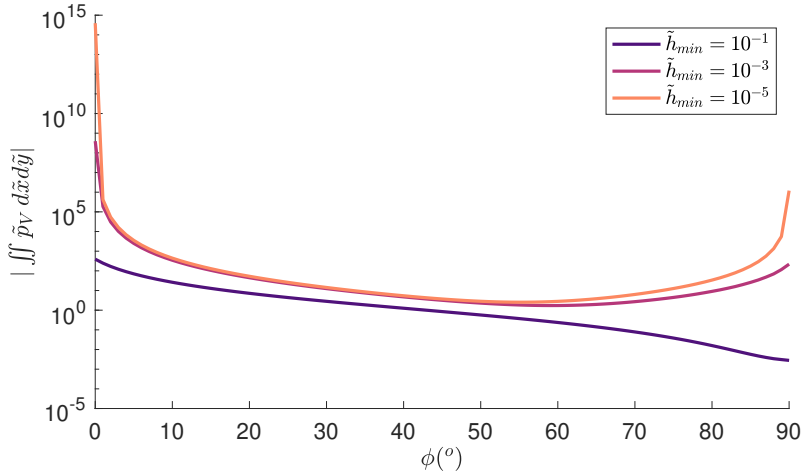

Figure 8.5: $|\iint \tilde{p}_V \mathrm{d}\tilde{x}\mathrm{d}\tilde{y}|$ as a function of ϕ for $\tilde{h}_{min} = 10^{-1}$, 10^{-3} and 10^{-5}, indicated by the different coloured lines.

or perpendicular. The minimum value is not at $\phi = 45^o$ reflecting the asymmetry of the disk configuration. Plots of the other components can be found in §E.6.

8.4 Disk motion

8.4.1 Equations of motion

Defining a rotation axis about the centre of mass of each of the disks, disks A and B have moments of inertia

$$I_a = \frac{1}{4} m_a a^2 \left(1 + \frac{4}{3d^2}\right), \quad I_b = \frac{1}{4} m_b b^2 \left(1 + \frac{4}{3d^2}\right), \tag{8.19a, b}$$

respectively. For disk i with mass m_i, moment of inertia I_i, centre of mass coordinates $\mathbf{x}'_i = (x'_i, y'_i, z'_i)$, translational velocity, $\mathbf{u}_i^{t'} = (u_{ix}^{t'}, 0, u_{iz}^{t'})$ angular velocity ω'_i and at an angle θ'_i to the horizontal in the lab frame, the equations of motion are given by,

$$\frac{d^2\mathbf{x}'_i}{dt^2} = \frac{\mathbf{F}'_i}{m_i}, \quad \frac{d^2\theta'_i}{dt^2} = \frac{\tau'_i}{I_i}. \tag{8.20}$$

Employing the non-dimensionalisation in §7.4.3.1 and §8.3.2.2, and letting $\gamma = a/b$ and $\lambda = [1 + 4/(3d^2)]^{-1}$, we obtain the dimensionless equations of motion for the disks,

$$\frac{\mathrm{d}^2}{\mathrm{d}\tilde{t}^2} \begin{pmatrix} \tilde{x}'_a \\ \tilde{z}'_a \\ \theta'_a \end{pmatrix} = \begin{pmatrix} \tilde{F}'_{ax} \\ \tilde{F}'_{az} \\ 4\lambda\tilde{\tau}'_a \end{pmatrix}, \qquad \frac{\mathrm{d}^2}{\mathrm{d}\tilde{t}^2} \begin{pmatrix} \tilde{x}'_b \\ \tilde{z}'_b \\ \theta'_b \end{pmatrix} = \frac{m_a}{m_b} \begin{pmatrix} \tilde{F}'_{bx} \\ \tilde{F}'_{bz} \\ 4\lambda\gamma^2\tilde{\tau}'_b \end{pmatrix}. \tag{8.21}$$

We solve the equations of motion using the Matlab programming language and the ode15s solver which is a variable-step, variable-order solver based on numerical differentiation formulas of orders 1 to 5 (Champney et al., 1995). We set the relative and absolute tolerances to 10^{-5} for each of the variables.

8.4.2 Initial conditions

A sketch showing the initial setup can be found in Figure E.5 in §E.7. In order to run simulations for all possible geometries we require $0 \leq \Theta \leq \pi/2$, $-\pi/2 \leq \theta'_a < \pi/2$, $-\pi/2 \leq \theta'_b < \pi/2$, where Θ is the angle between the line connecting the centre of masses of disks B and A and the z' axis (see Figure 6.3). As the disk geometry is symmetric after a rotation of $\theta \mapsto \theta + \pi$ (see Figure 8.2) θ'_a and θ'_b only vary by π. However, note that by symmetry arguments we can achieve all possible geometries by instead choosing $0 \leq \Theta \leq \pi/2$, $-\pi/2 \leq \theta'_a < \pi/2$, $\theta'_b = 0$. Defining the original values of Θ, θ'_a and θ'_b as Θ^L, θ'^L_a and θ'^L_b and the smaller range as Θ, θ'_a and θ'_b, in §E.7 we show how this smaller range of Θ and θ'_b can still achieve all possible geometries and how they are related to Θ^L, θ'^L_a and θ'^L_b.

As in §6 we initialise each simulation with the centre of mass of the disks a dimensionless distance $\tilde{r}_{max,ab} = \sqrt{1 + [w_a/(2a)]^2} + \sqrt{(b/a)^2 + [w_b/(2a)]^2}$ apart; this is the maximum distance possible separation between the centre of masses whilst the cylinders are in contact. For large values of b/a this means that $\tilde{h}_{min} \gg 1$. However, as the lubricating force does not have a noticeable effect until $\tilde{h}_{min} \ll 1$, these simulations still give useful results. We run simulations for $b/a = [1, 4/3, 2, 5, 10, 100]$.

We define the relative velocity $\tilde{\mathbf{w}}_{ab} = \tilde{\mathbf{u}}'^t_a - \tilde{\mathbf{u}}'^t_b$. To determine the range of initial velocities to use in the simulations we note that the dimensionless velocity is related to the velocity by $\tilde{\mathbf{w}}_{ab} = \mathbf{w}_{ab}/[6\eta d/(\pi\rho_I a)]$. In §6.4 we stated expressions for the PDFs of $\rho(w_{ab,r})$ (6.9), $\rho(w_{ab,\Theta})$ (6.10). Noting that, $w_{ab,x} = w_{ab,r}\sin\Theta + w_{ab,\Theta}\cos\Theta$ and $w_{ab,z} = w_{ab,r}\cos\Theta - w_{ab,\Theta}\sin\Theta$ we can use the PDFs of $\rho(w_r)$, $\rho(w_\Theta)$ to obtain

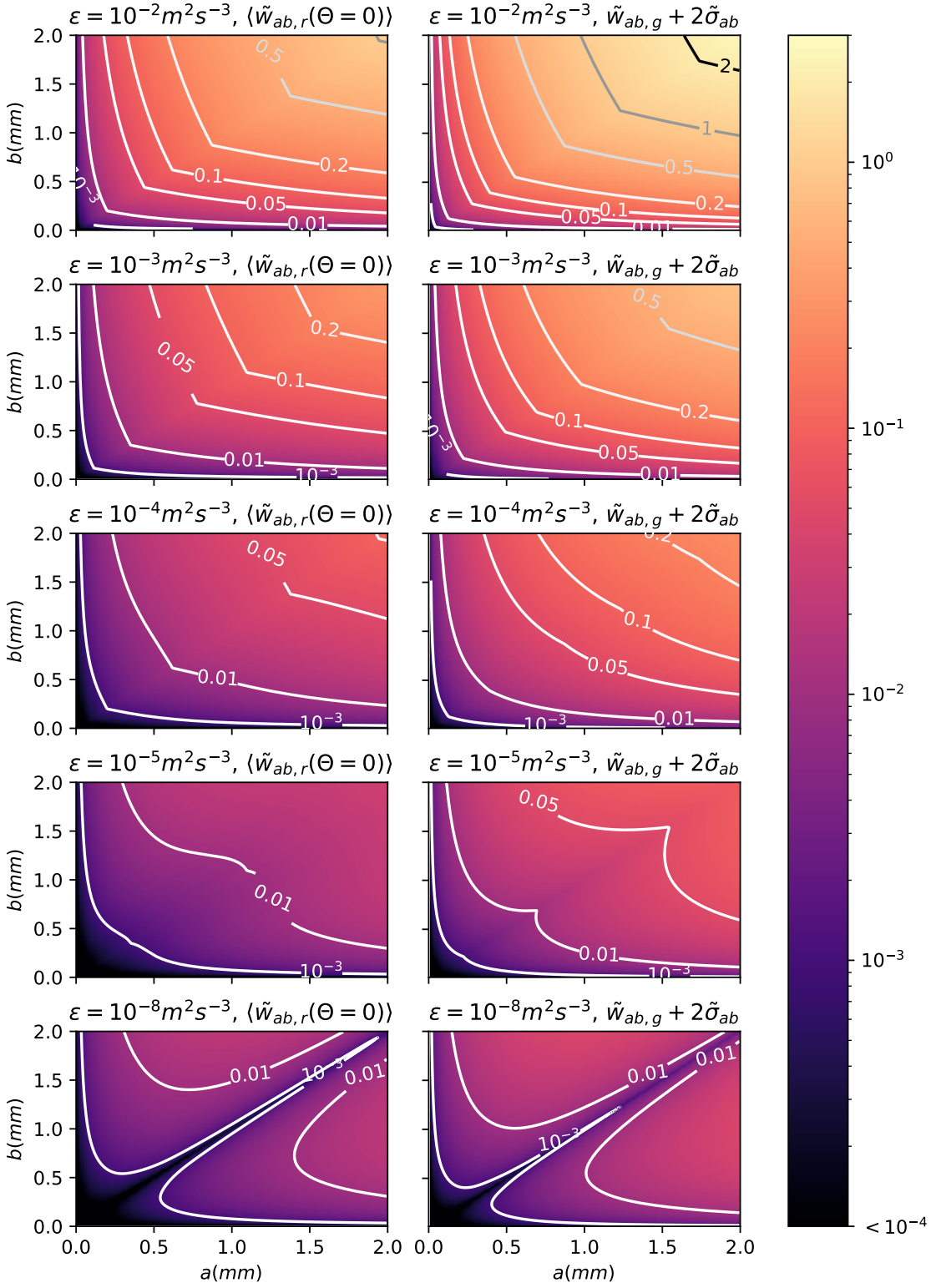

Figure 8.6: Using the PDFs for $w_{r,ab}$ and $w_{\Theta,ab}$ we estimate a range for $\tilde{\mathbf{w}}_{ab}$. The left hand column plots the scaled mean radial relative velocity at $\Theta = 0$, $\langle \tilde{w}_{r,ab} \rangle$ at $\Theta = 0$ for $0\,\text{mm} \leq a, b \leq 2\,\text{mm}$. The right hand column plots, $\tilde{w}_{ab,g} + 2\tilde{\sigma}_{ab} = [w_{ab,g} + 2\sigma(r_{max,ab})]/[6\eta d/(\pi \rho_I \min\{a, b\})]$ for $0\,\text{mm} \leq a, b \leq 2\,\text{mm}$ which is the location of the location of the 95^{th} percentile of $\tilde{w}_{r,ab}$ for $\Theta = 0$. The turbulent kinetic energy dissipation rate ϵ decreases from top to bottom.

a range of $|\tilde{\mathbf{w}}_{ab}|$ to use for our simulations. The right hand column of Figure 8.6 plots $\tilde{w}_{ab,g} + 2\tilde{\sigma}_{ab} = [w_{ab,g} + 2\sigma(r_{max,ab})]/[6\eta d/(\pi\rho_I \min\{a,b\})]$ where, using (4.41), $\sigma(r_{max,ab}) = \sqrt{\epsilon/(15\nu)}r_{max,ab}$. The probability of $|\tilde{\mathbf{w}}_{ab}|$ being less than this value is roughly 0.95. Therefore, we choose to run simulations for $10^{-4} \leq |\tilde{\mathbf{w}}_{ab}| \leq 10$. We also plot $\langle \tilde{w}_{r,ab} \rangle$ at $\Theta = 0$. The value of $\langle \tilde{w}_{r,ab} \rangle$ at $\Theta = 0$ and the value of $\tilde{w}_{ab,g} + 2\tilde{\sigma}_{ab}$ both increase with turbulent kinetic energy dissipation rate ϵ, suggesting that larger relative velocities become more likely with increasing turbulence. For $\epsilon \geq 10^{-4}$ m^{2}s^{-3} the dimensionless relative velocity increases with increasing a and b. For $\epsilon < 10^{-4}$ m^{2}s^{-3} the dimensionless relative velocity increases with increasing with a and b and $a \neq b$.

8.4.3 End Criteria

In §7.5.3 we defined four possible end criteria for a simulation. i) no overlap, ii) collision, iii) large angles, iv) the disks move away. The same criteria can be used to decide whether a collision occurred in the 3D case. In some cases the lubrication approximation means that the disks take an infinite length of time to make contact. In order to avoid numerical difficulties due to this we add in an additional timeout criteria to stop simulations once $t \geq 100\tilde{h}_{min}/|\tilde{\mathbf{w}}_{ab}|$.

We have calculated the forces and torques for all angles. The lubrication approximation is less accurate at larger angles, but with expected errors of less than an order or magnitude (Cawthorn and Balmforth, 2010). We therefore choose to remove the large angle criteria as an end point for a simulation, and instead replace it with a criteria when the dominant contribution to the lubricating force is likely to come from the curved face of disk B, instead of the planar face of disk B. The criteria for no overlap, collision and moving away also change because of the finite thickness of the disks. The end criteria in the 2D case are therefore as follows:

i) no overlap

The disks no longer overlap if the outermost $x-$locations of the edges of the top disk are outside of the base of the bottom disk, e.g. in case a) of Figure 8.2 point α or γ is outside the edge of disk B. In Table 8.1 we specify the conditions for the disks not to overlap.

θ_a	No overlap LHS	No overlap RHS
$0 \leq \theta_a < \pi/2$	$x_\gamma(\theta_a) < x_b - b$	$x_b + b < x_\alpha(\theta_a)$
$\pi/2 \leq \theta_a < \pi$	$x_\epsilon(\theta_a) < x_b - b$	$x_b + b < x_\beta(\theta_a)$
$\pi \leq \theta_a < 3\pi/2$	$x_\alpha(\theta_a) < x_b - b$	$x_b + b < x_\gamma(\theta_a)$
$3\pi/2 \leq \theta_a < 2\pi$	$x_\beta(\theta_a) < x_b - b$	$x_b + b < x_\epsilon(\theta_a)$

Table 8.1: Criteria for the disks no longer to overlap for $0 < \theta_a \leq 2\pi$. For larger and smaller values of theta the relation is cyclic due to the 2π rotational symmetry. See Figure 8.2 for the locations of points α, β, ϵ and γ, which have corresponding x coordinates x_i for $i \in \{\alpha, \beta, \epsilon, \gamma\}$.

ii) collision

$$\tilde{h}_{min} \leq 10^{-8}, \tag{8.22}$$

where $\tilde{h}_{min}$ is given by (E.8) for $n\pi - \pi/2 < \theta < n\pi$ and (E.7) for $n\pi \leq \theta \leq \pi/2 + n\pi$. The threshold on h_{min} for collision is set to 10^{-8} because once the simulation reaches this point, we found that there was negligible change in the relative velocities when we instead use smaller values down to $\tilde{h}_{min} = 10^{-13}$.

iii) curved surface more relevant

If the z-coordinate of the lowest point of disk A is lower than the upper surface of disk B and the minimum distance parallel to the planar surface of disk B between the surface of disk A and the curved surface of disk B (D_c in Figure 8.7) is shorter than the minimum distance perpendicular to the planar surface of disk B between the surface of disk A and the planar upper surface of disk B (D_p in Figure 8.7) then the dominant contribution to the pressure should come from the interaction between disk A and the curved surface of disk B (as is the case in Figure 8.7a, b). This occurs when the centre of mass of disk A is to the left of disk B and $\zeta < \pi/4$ or

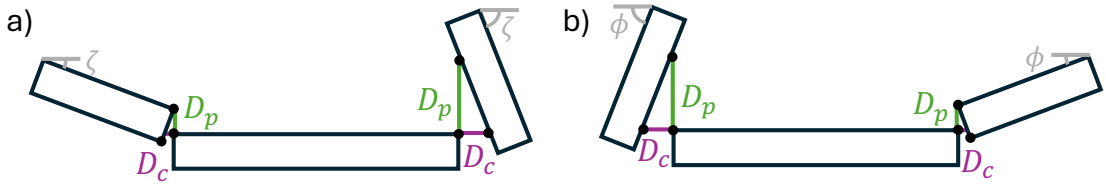

Figure 8.7: Cases where the minimum distance parallel to the planar surface of disk B between the surface of disk A and the curved surface of disk B (D_c) is shorter than the minimum distance perpendicular to the planar surface of disk B between the surface of disk A and the planar upper surface of disk B (D_p). This occurs when the lowest point of disk A is below the upper surface of disk B and when a) the centre of mass of disk A is to the left (right) of disk B and $\zeta < \pi/4\,(\zeta > \pi/4)$ or b the centre of mass of disk A is to the left (right) of disk B and $\phi > \pi/4\,(\phi < \pi/4)$). D_p and D_c are marked with the green and purple lines respectively.

$\phi > \pi/4$ or when the centre of mass of disk A is to the right of disk B and $\zeta > \pi/4$ or $\phi < \pi/4$. We have not calculated the pressure for this case so we do not include simulations which reach this criteria.

iv) the disks move away

For the disks to be moving away from each other, the relative velocity of the disks in frame S must be in the $\hat{\mathbf{z}}$ direction. This is not equivalent to saying that the translational velocity of the disks is in the $\hat{\mathbf{z}}$ direction, as the disks could still be rotating towards each other. The relative vertical velocity between point p on the surface of disk A and point l on the surface of disk B is given by $w_{ab,z}(x_p, x_l) = u_{za}(x = x_p) - u_{zb}(x = x_l) = u^t_{za} - u^t_{zb} - \omega_a(x_p - x_a) + \omega_b(x_l - x_b)$, where x_p corresponds to the x-location of the point p and x_l corresponds to the x-location of the point l. Letting $x_p = x_l$ such that we compare the relative velocity of the surfaces at the same value of x, we require all of,

- $w_{ab,z}(x_\alpha, x_\alpha) = u^t_{za} - u^t_{zb} - (\omega_a - \omega_b)(x_a + w_a/2\cos\theta_a - a\sin\theta_a) + \omega_a x_a - \omega_b x_b > 0,$
- $w_{ab,z}(x_\beta, x_\beta) = u^t_{za} - u^t_{zb} - (\omega_a - \omega_b)(x_a - w_a/2\cos\theta_a - a\sin\theta_a) + \omega_a x_a - \omega_b x_b > 0,$
- $w_{ab,z}(x_\gamma, x_\gamma) = u^t_{za} - u^t_{zb} - (\omega_a - \omega_b)(x_a - w_a/2\cos\theta_a + a\sin\theta_a) + \omega_a x_a - \omega_b x_b > 0,$
- $w_{ab,z}(x_\gamma, x_\gamma) = u^t_{za} - u^t_{zb} - (\omega_a - \omega_b)(x_a + w_a/2\cos\theta_a + a\sin\theta_a) + \omega_a x_a - \omega_b x_b > 0,$

to be true.

8.5 Results

8.5.1 Comparison to the 2D case

Before calculating a collision efficiency we compare the results when $\tilde{\mathbf{w}}_{ab} = \tilde{w}_{ab}\hat{\mathbf{z}}$ and $\Theta = 0$ to the results obtained in §7 for the 2D case.

8.5.1.1 Trajectories

In §7 we noted that there were three possible categories of trajectory for the crystals:

- Category NI: no collision and no sign change in θ,
- Category NII: no collision and sign change in θ,
- Category CI: collision and sign change in θ.

We now see how this compares in the 3D case. We first calculate the trajectories for $b/a = 2$ and compare them to the trajectories in Figure 7.4. In §7 the dimensionless velocity is given by $\tilde{\mathbf{v}} = \mathbf{v}(\rho_I D_a)/(12\eta)$, whilst in this chapter the dimensionless velocity is given by $\tilde{\mathbf{w}}_{ab} = \mathbf{w}_{ab}(\rho_I a\pi)/(6\eta d)$ and $a/d = 2D_a$. Therefore, to compare the results for the same dimensionless velocities we let $\tilde{\mathbf{w}}_{ab} = \pi\tilde{\mathbf{v}}$.

We initialise each simulation with $\tilde{\mathbf{w}}_{ab} = \tilde{w}_{ab}\hat{\mathbf{z}}$ and $\Theta = 0$. Figure 8.8 shows the trajectories for $|\tilde{\mathbf{w}}_{ab}| = [0.01, 60, 100, 200]\pi$, where the case $|\tilde{\mathbf{w}}_{ab}|$ is added to illustrate regime NII. The same three categories of motion exist as were observed in the 2D case but the trajectories are slightly changed. A collision now occurs for $|\tilde{\mathbf{w}}_{ab}| = 100\pi$, whilst a collision did not occur at the equivalent value in the 2D case. In the cases of $|\tilde{\mathbf{w}}_{ab}| = 0.01\pi$ and $|\tilde{\mathbf{w}}_{ab}| = 200\pi$ the category of motion did not change but the amount of rotation is more significant for $|\tilde{\mathbf{w}}_{ab}| = 0.01\pi$ and less significant for $|\tilde{\mathbf{w}}_{ab}| = 200\pi$. This may be due to the change in the equations of motion with $m_a/m_b = a^3/b^3$ in the 3D case and m_a/m_b assumed to be equal to a/b in the 2D case meaning that the forces and torques experiences by the disks and plates are

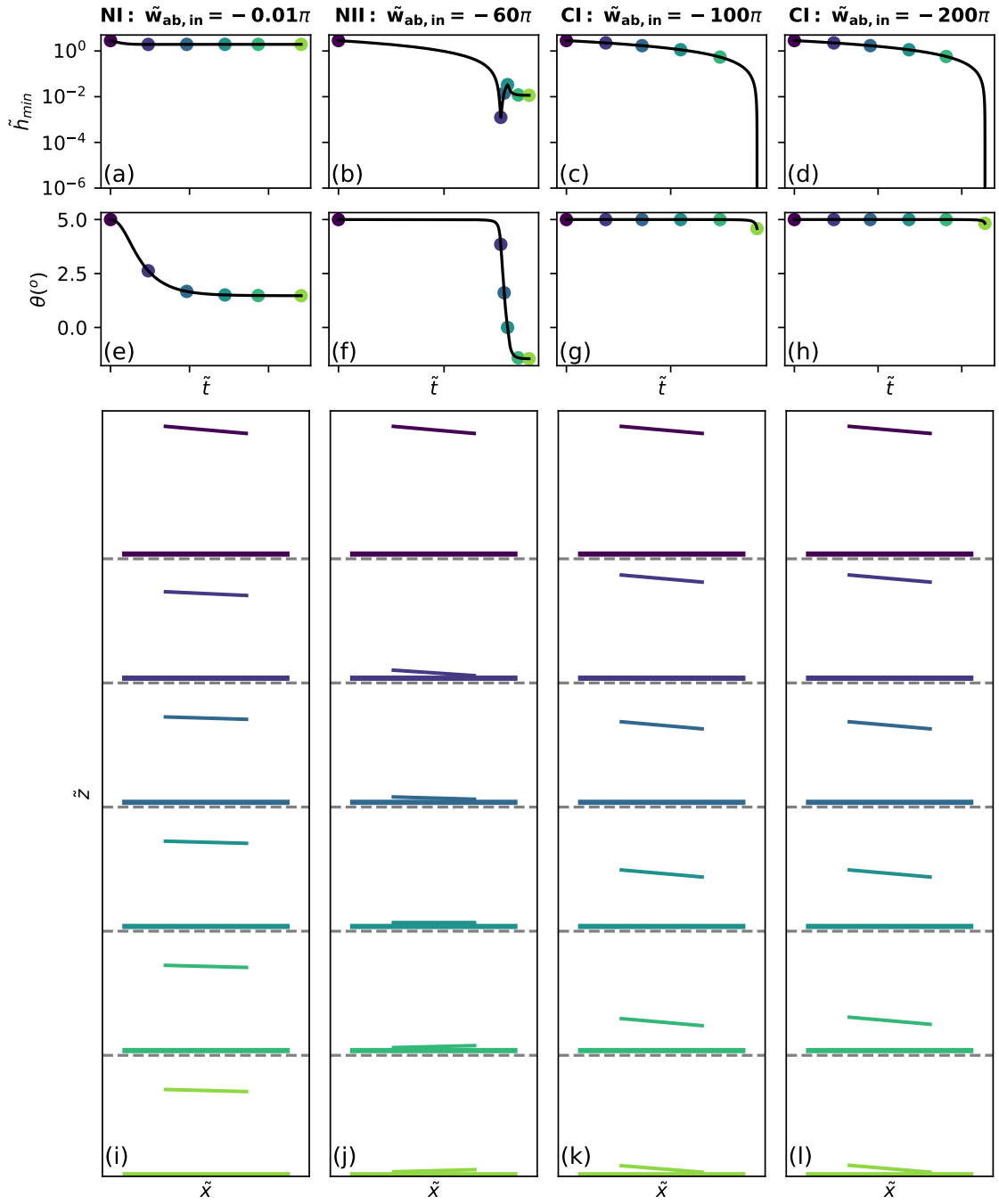

Figure 8.8: Motion of the two disks, starting with $\Theta = 0$ such that $\tilde{x}_a = \tilde{x}_b$, $r_{c,ab} = r_{max,ab}$, relative angle $\theta_{in} = 5^o$, and initial relative velocity $\tilde{\mathbf{w}}_{ab,in} \in -\{0.01, 70, 100, 200\}\pi\hat{\mathbf{z}}$ from left to right. All the other initial conditions are 0. The bottom disk is twice as long as the top disk ($a/b = 1/2$). The category of motion is noted in the title for each column. Panels (a)-(d) show the minimum distance between the plates over time. Panels (e)-(h) show the evolution of the relative angle. Panels (i)-(l) show some snapshots of the motion at the times indicated by the corresponding colour coded dots in (a)-(h). The snapshots are shifted evenly in $\tilde{z}$ and separated by a grey dashed line to make visualisation easier. Time increases from top to bottom. A collision occurs for $\tilde{\mathbf{w}}_{ab,in} = -100\pi$ and -200π in the bottom snapshot in panels k and l. In all cases the relative angle initially decreases and plate A initially translates to the right.

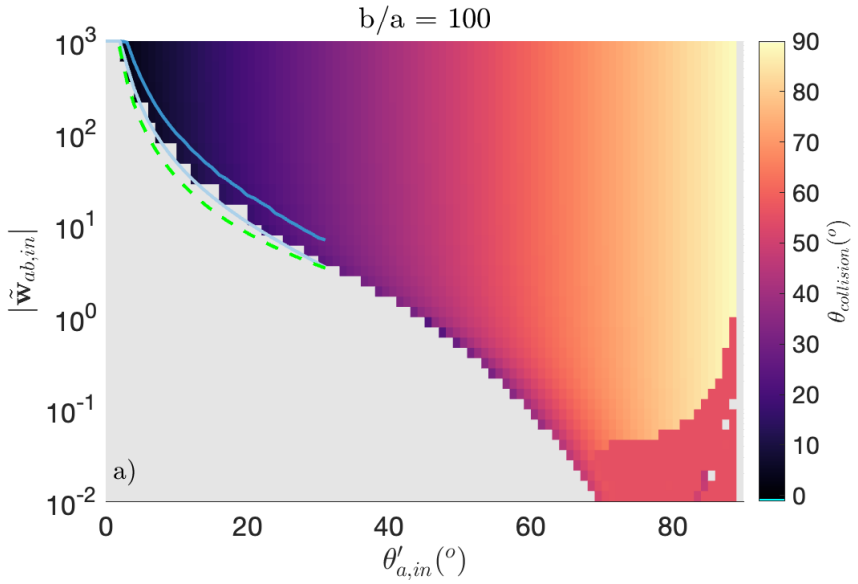

Figure 8.9: The collision angle $\theta_{collision} = \theta'_a - \theta'_b$ for disks initialised at angle $\theta'_{a,in}$ and relative velocity $\tilde{\mathbf{w}}_{ab,in} = |\tilde{\mathbf{w}}_{ab,in}|\hat{\mathbf{z}}$ with ratio $b/a = 100$. The light blue line is the collision boundary calculated using interval bisection for $\theta'_{a,in} \leq 30^o$ (for comparison to the small angle case in §7) and $b/a = 100$. The darker blue line is the collision boundary calculated using interval bisection for $b/a = 1$. The dashed green line is the predicted collision boundary using (7.52).

different. Further, the moment of inertia is different for the plates and disks. The trajectory for $|\tilde{\mathbf{w}}_{ab}| = 60\pi$ is in category NII with θ changing sign but no collision, demonstrating that all three categories of motion are still observed in the 3D case.

8.5.1.2 Collision angle

As we are particularly interested in the dynamics when a collision occurs, we also compare the collision angle and collision boundary in the 3D case to the 2D case. Again, we initialise simulations with $\tilde{\mathbf{w}}_{ab} = \tilde{w}_{ab}\hat{\mathbf{z}}$ and $\Theta = 0$. We use the expression (7.52) that we found to approximate the collision boundary well in §7 and test how successfully it can be used in the 3D case.

We first examine the collision angle and the collision boundary for $b/a = 100$. Figure 8.9 shows the collision angle $\theta_{collision} = \theta'_a - \theta'_b$. The collision angle changes with the initial value of θ'_a, which we term $\theta'_{a,in}$ and the initial relative velocity $|\tilde{\mathbf{w}}_{ab}|$. Collisions are now possible at much lower speeds with steeper angles. A collision

does not occur in the regions shaded grey. Similar to the 2D case, higher initial relative velocities are required to cause a collision for smaller values of $\theta'_{a,in}$. This is because it is harder to squeeze fluid out and cause a collision when the disks are close to parallel. No collisions occur when the disks are initially perpendicular or parallel as in this case finite time contact is not possible, because the force diverges two rapidly as the gap thickness tends to zero. As was the case in §7, the relative angle does not change significantly as the disks approach and collide for cases when the initial value of θ'_a is small. This means that the assumptions used to derive the equation for the collision boundary (7.52) used in §7 remain valid, other than changes in the disk geometry. We find that (7.52) estimates a velocity threshold for collision which is a maximum of 1.53 times smaller than the numerically determined velocity threshold calculated using interval bisection for $\theta'_{a,in} \leq 30^o$. Above this value the 3D disk geometry starts to become more important and the error increases. By comparing the light blue line to the darker blue line which show the collision boundary for $b/a = 1$ and $b/a = 100$ respectively, we see that somewhat higher velocities are required to cause a collision when the disks are a similar size and have smaller relative angle. This is the same trend as in §7.

There is a region $70^o \lesssim \theta'_{a,in} \leq 90^o$ where the collision angle changes significantly between two values of $|\tilde{\mathbf{w}}_{ab,in}|$. Figure 8.10 plots the trajectory for two initial velocities close to the transition region. In all cases the disks are initialised with $\theta'_a = 85^o$, $\Theta = 0$, $\theta'_b = 0$ and $\tilde{\mathbf{w}}_{ab,in} = |\tilde{\mathbf{w}}_{ab,in}|\hat{\mathbf{z}}$. In Figure 8.10a very little rotation occurs, with the difference between the relative angle between the disks when they collide $\theta_{collision}$ and the original angle, $\theta'_{a,in}$ equal to 0.1^o. In Figure 8.10b significant rotation occurs, $\theta_{collision} - \theta'_{a,in} = 29.5^o$. We also test if changing the ratio of the disk sizes alters the trajectory in the case where significant rotation occurs. Figure 8.10c plots the trajectory for $b/a = 2$. In this case the disks rotate by a larger angle of 37.5^o, due the smaller inertia of the bottom disk for $b/a = 2$, than for $b/a = 100$ changing the trajectory. The disks start rotating by a significant amount when

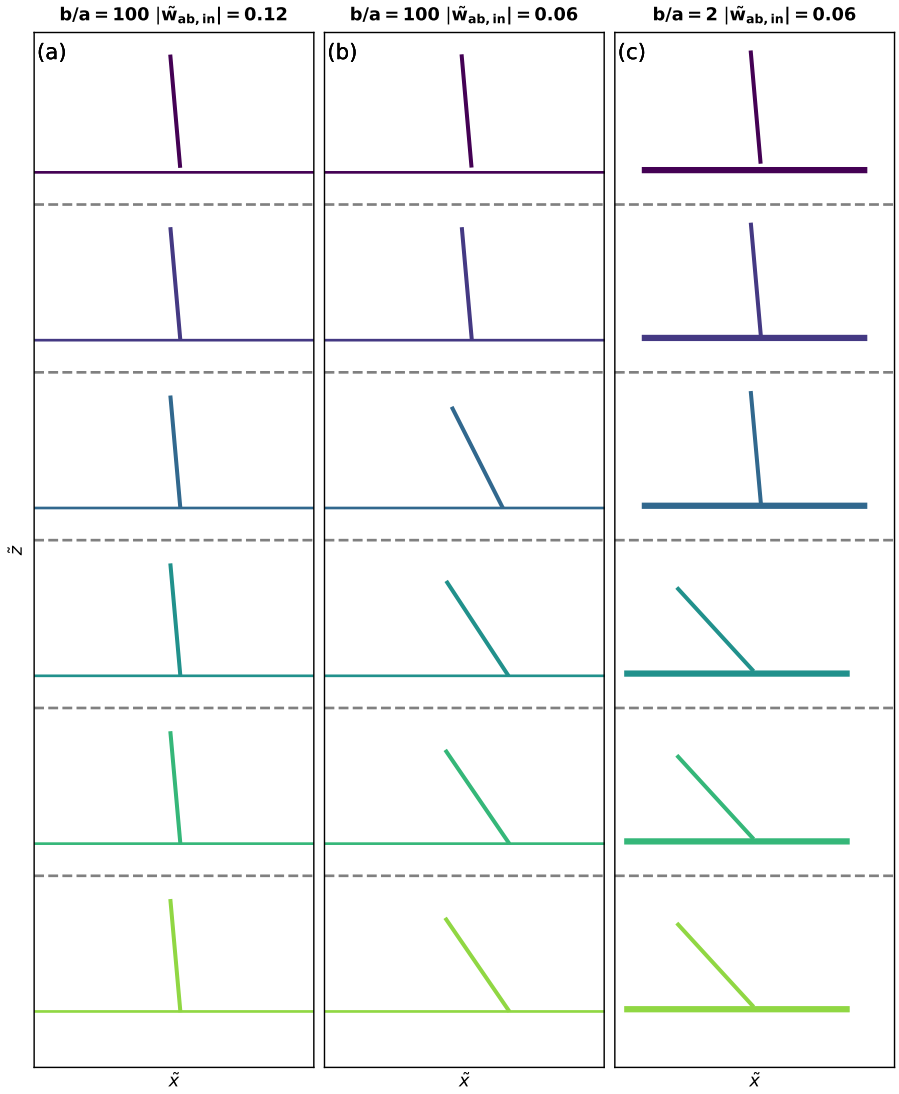

Figure 8.10: Trajectories for disks initialised at angle $\theta'_{a,in} = 85^o$ with $\Theta = 0$, $\theta'_b = 0$. The ratio of the radii of the disks along with their initial relative velocity is given in the title of the panel. From top to bottom the position of the disk is plotted for $\tilde{h}_{min} = [10^{-1}, 10^{-2}, 10^{-3}, 10^{-4}, 10^{-5}]$ and the collision position. Only the top surface of disk B is plotted in panels a and b.

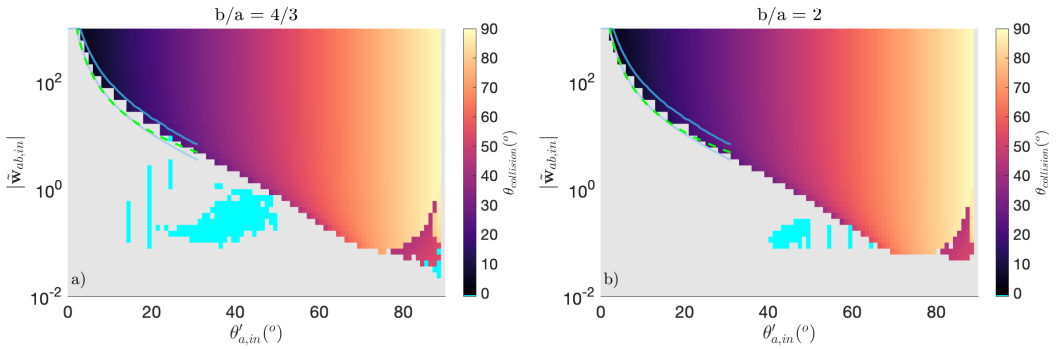

Figure 8.11: The collision angle $\theta_{collision} = \theta'_a - \theta'_b$ for disks initialised at angle $\theta'_{a,in}$ and relative velocity $\tilde{\mathbf{w}}_{ab,in} = |\tilde{\mathbf{w}}_{ab,in}|\hat{\mathbf{z}}$ with ratio a) $b/a = 4/3$, b) $b/a = 2$. The light blue line is the collision boundary calculated using interval bisection for $b/a = 100$ and the darker blue line is the collision boundary calculated using interval bisection for $b/a = 1$. The dashed green line is the predicted collision boundary using (7.52).The cyan patches are where the solver was unable to meet the integration tolerances.

$\tilde{h}_{min} < 0.01$.

Figure 8.11 shows the collision angle and the collision boundary for $b/a = 4/3$ and $b/a = 2$. Cyan patches indicate where the solver was unable to meet the integration tolerances and the outcome is hence undetermined. When the disks are close to perpendicular, collisions are not possible for as small values of $\tilde{\mathbf{w}}_{ab}$ as were observed for $b/a = 100$. Again, for small values of $\theta'_{a,in}$ the collision angle is similar to the initial relative angle between the disks and the numerically predicted collision boundary (7.52) provides a good approximation to the true collision boundary with the estimated velocity threshold for collision for $\theta'_{a,in} \leq 30^o$ being a maximum of 1.3 and 1.4 times smaller than the numerical velocity threshold for collision for $b/a = 4/3$, 2 respectively.

Next, we examine the collision angle and the collision boundary for $b/a = 1$. We first use a relative and absolute tolerance of 10^{-5}, as was used for $b/a = [4/3,\ 2,\ 100]$. Figure 8.12a shows the results. The phase plane for $b/a = 1$ has a patchy region of mixed collisions and no collisions around $10^{-2} \leq |\tilde{\mathbf{w}}_{ab}| \leq 10^{-1}$ and $45^o \leq \theta'_{a,in} \leq 70^o$. To test whether this region was a numerical artifact, both the relative and absolute tolerance were reduced from 10^{-5} to 10^{-8} to see if the region persisted. The phase

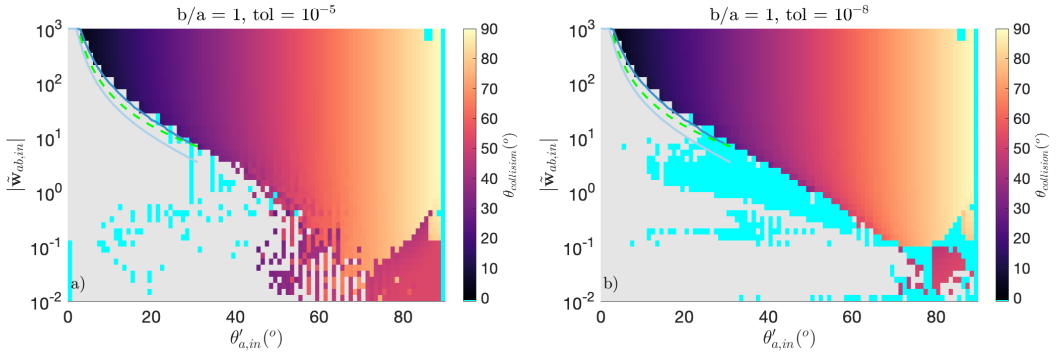

Figure 8.12: To test the robustness of the patchy region around $10^{-2} \leq |\tilde{\mathbf{w}}_{ab}| \leq 10^{-1}$ and $45^o \leq \theta'_{a,in} \leq 70^o$ for $b/a = 1$ we ran the same simulations but with both the absolute and relative tolerances set to 10^{-8} (panel b). This is compared to the original results for both tolerances set to 10^{-5} (panel a).

planes for a tolerance of 10^{-5} and 10^{-8} are shown in panels a and b respectively of Figure 8.12. The region where the solver struggled to meet the required tolerance substantially increased (see the larger cyan region in Figure 8.12b) and some collisions at larger values of $\theta'_{a,in}$ no longer occurred. Unfortunately reducing the tolerance by this amount leads to much slower computational run times so simulations had to be run with the higher tolerance of 10^{-5} over the remaining phase planes. This is likely to mean that the collision kernel calculated when the disks are similar in size will suffer some inaccuracies for the range of $\theta'_{a,in}$ and $|\tilde{\mathbf{w}}_{ab}|$ where the result changes with the solver tolerance. Increasing the tolerance for the other values of b/a has almost no effect suggesting that these results are more robust.

8.5.2 Calculation of the collision efficiency

We now proceed to calculate a collision efficiency due to hydrodynamic interactions. In §2.4.1 we explained that the collision kernel Γ_{ij} (2.52) is equal to the product of the encounter frequency $\mathcal{F}_{enc,ij}$ multiplied by the collision efficiency $C_{eff,ij}$, where collision efficiency was defined as the fractional reduction in the number of collisions due to particle-particle interactions were neglected (Daly, 1984). We have so far focussed on improving parametrisations for the encounter frequency in §4-6. Now

we calculate an expression for the collision efficiency.

A full expression for the collision efficiency due to hydrodynamic interactions would be given by (Wang and Ayala, and Kasprzak, and Grabowski, 2005),

$$C_{eff,ab} = \frac{\mathcal{F}^{hydro}_{enc,ab}}{\mathcal{F}^{ballistic}_{enc,ab}} \tag{8.23}$$

where $\mathcal{F}^{ballistic}_{enc,ab}$ is the ballistic encounter frequency given by (6.5), with $\mathcal{K}_{coll,ab}$ equal to the ballistic collision kernel which was calculated in §6. The hydrodynamic encounter frequency $\mathcal{F}^{hydro}_{enc,ab}$ would also be calculated using (6.5) with $\mathcal{K}_{coll,ab}$ as the collision kernel due to hydrodynamic interactions.

However, we have only calculated the collision kernel due to hydrodynamic interactions for $\phi_a = \phi_b = w_{ab,\Phi} = 0$, meaning that we have neglected rotation and translation of the disks around one axis. Restricting this range of incident angles and velocities, $\mathcal{F}^{hydro}_{enc,ab}$ is instead given by,

$$\mathcal{F}^{hydro}_{enc,ab} = \frac{4\pi r^2_{max,ab}}{V}\int_0^{\pi/2} \mathrm{d}\Theta^L \int_{-\infty}^{\infty} \mathrm{d}w^L_{ab,r} \int_{-\infty}^{\infty} \mathrm{d}w^L_{ab,\Theta} \int_{-\pi/2}^{\pi/2} \mathrm{d}\theta'^L_a \int_{-\pi/2}^{\pi/2} \mathrm{d}\theta'^L_b \sin\Theta^L \times$$
$$\rho(w^L_{ab,r})\rho(w^L_{ab,\Theta})\rho(\theta'^L_a)\rho(\theta'^L_b)\rho(\Theta^L)\mathcal{K}_{hydro,ab}(\Theta^L, \theta'^L_a, \theta'^L_b, w^L_{ab,r}, w^L_{ab,\Theta})|w^L_{ab,r}|, \tag{8.24}$$

which sums over the possible configurations of relative position, orientation and velocity in the $x'-z'$ plane. Hence, to calculate the collision efficiency, we instead set

$$\mathcal{F}^{ballistic}_{enc,ab} = \frac{4\pi r^2_{max,ab}}{V}\int_0^{\pi/2} \mathrm{d}\Theta^L \int_{-\infty}^{\infty} \mathrm{d}w^L_{ab,r} \int_{-\infty}^{\infty} \mathrm{d}w^L_{ab,\Theta} \int_{-\pi/2}^{\pi/2} \mathrm{d}\theta'^L_a \int_{-\pi/2}^{\pi/2} \mathrm{d}\theta'^L_b \sin\Theta^L \times$$
$$\rho(w^L_{ab,r})\rho(w^L_{ab,\Theta})\rho(\theta'^L_a)\rho(\theta'^L_b)\rho(\Theta^L)\mathcal{K}_{ballistic,ab}(\Theta^L, \theta'^L_a, \theta'^L_b, w^L_{ab,r}, w^L_{ab,\Theta})|w^L_{ab,r}|, \tag{8.25}$$

which considers ballistic collision over the same range of configurations as the hydrodynamic simulations.

Collisions do not occur in finite time under the lubrication approximation for $\theta'_a = \theta'_b = \Theta_L = 0$. Collisions may be possible for $|\tilde{\mathbf{w}}_{ab}| > 1000$ when $\Theta \neq 0$ and $\tilde{x}_a \neq \tilde{x}_b$, however the probability of the crystals having these velocities for

$\epsilon < 10^{-1}$ m^2 s^{-3} is $\ll 10^{-10}$ and hence the encounter frequency will be very close to zero. Collisions are necessary for the supercooling temperature to reduce at a fast enough rate to match observations. If secondary nucleation is the dominant source of nuclei, the collision rate will be too low if we assume $\rho(\theta'_a) = \delta(\theta'_a)$ and $\rho(\theta'_b) = \delta(\theta'_b)$, therefore, we will only calculate the collision efficiency for the case of $\rho(\theta_a) = \rho(\theta_b) = 1/\pi$ where collisions are possible at lower velocities. As in §6 we assume $\rho(w^L_{ab,r})$ and $\rho(w^L_{ab,r})$ are given by (6.9) and (6.10) respectively.

8.5.2.1 Calculation of the collision kernel

As in §6 we calculate the collision kernels $\mathcal{K}_{hydro,ab}$ and $\mathcal{K}_{ballistic,ab}$ for Θ^L, θ'^L_a, θ'^L_b spaced by 1^o and then integrate these kernels to obtain the encounter frequencies, where θ'^L_a, θ'^L_b are the orientations of the crystal in the $x' - z'$ plane and Θ^L is the angle between the z'-axis and the the line joining the centre of mass of crystal A and crystal B. For the simulations with hydrodynamics included, we calculate whether a collision occurs for initial values of the dimensionless variables Θ, θ'_a, $\tilde{w}_{ab,r}$ and $\tilde{w}_{ab,\Theta}$. Therefore, for each value of Θ^L, θ'^L_a, θ'^L_b we use the mapping in §E.7 between Θ^L and Θ, θ'^L_a and θ'_a, θ'^L_b and θ'_b, $w^L_{ab,r}$ and $\tilde{w}_{ab,r}$, and $w^L_{ab,\Theta}$ and $\tilde{w}_{ab,\Theta}$, in order to find the corresponding values of Θ, θ'_a, $\tilde{w}_{ab,r}$ and $\tilde{w}_{ab,\Theta}$. We relate this to the collision kernel in terms of dimensionless variables, $\mathcal{K}_{hydro,ab} = \mathcal{K}_{hydro,ab}(\Theta, \theta'_a, \tilde{w}_{ab,r}, \tilde{w}_{ab,\Theta})$.

To obtain $\mathcal{K}_{hydro,ab}(\Theta, \theta'_a, \tilde{w}_{ab,r}, \tilde{w}_{ab,\Theta})$ hydrodynamic simulations were run for $10^{-4} \leq |\tilde{\mathbf{w}}_{ab}| \leq 100$, with the relative velocity increasing logarithmically. We chose $-85^0 \leq \theta_u \leq 85^0$ with θ_u increasing in 5^o increments (see Figure 6.1 for a sketch of θ_u, which is the angle the relative velocity makes with the $-z'$ axis) and $\Theta = [0, 10, 20, 30, 40, 50, 60, 70, 80, 85]^o$. We chose $-90^o \leq \theta_a \leq 90^o$ with θ_a increasing in 5^o increments for $|\theta_a| > 20^o$ and 1^o increments for $|\theta_a| \leq 20^o$ as we found the collision boundary to be most sensitive to the initial angle. Next we found the velocity intervals bracketing the collision boundary at each value of θ_u, θ_a and Θ and then refined the resolution to determine the collision boundary with 0.005 accuracy in $\tilde{w}_{ab,r}$. We then constructed $\mathcal{K}_{hydro,ab}(\Theta, \theta'_a, \tilde{w}_{ab,r}, \tilde{w}_{ab,\Theta})$ across the

range of simulated Θ, θ_a, $\tilde{w}_{ab,r}$ and $\tilde{w}_{ab,\Theta}$. To find the collision kernel for Θ^L, $\theta_a'^L$ and $\theta_b'^L$, we have to find phase planes for θ_a' and Θ spaced by 1^o. To calculate this we linearly interpolated the phase planes in θ_a-Θ space to determine the collision kernel at the intermediate values. In some cases this meant that the hydrodynamic collision kernel was between 0 and 1. In reality the hydrodynamic collision kernel should only be 0 or 1 so future work should focus on refining the collision kernel when it is between 0 and 1. The ballistic collision boundary can be calculated analytically so does not suffer from this issue (see §E.8).

In some of the simulations (see for example the blue squares in Figure 8.11), the Matlab solver was unable to meet the integration tolerances, so the simulation produced no result. In these cases we calculated whether a collision would have occurred if the simulation was ballistic. If a collision would not have occurred we set $\mathcal{K}_{hydro,ab}(\Theta, \theta_a', \tilde{w}_{ab,r}, \tilde{w}_{ab,\Theta}) = 0$. This effectively assumes that in cases where a ballistic collision does not occur, a collision would also not occur if hydrodynamic interactions were included. In the simulations where a ballistic collision did occur we calculated one hydrodynamic collision kernel setting $\mathcal{K}_{hydro,ab}(\Theta, \theta_a', \tilde{w}_{ab,r}, \tilde{w}_{ab,\Theta}) = 1$ and another setting $\mathcal{K}_{hydro,ab}(\Theta, \theta_a', \tilde{w}_{ab,r}, \tilde{w}_{ab,\Theta}) = 0$, in order to explore the sensitivity to the non-converged results.

We define

$$\mathcal{T}_{ab}^{\alpha} = \frac{2}{\langle |w_{ab,r}(r_{c,ab})| \rangle} \int_0^{\pi/2} \mathrm{d}\Theta^L \int_{-\infty}^{\infty} \mathrm{d}w_{ab,r}^L \int_{-\infty}^{\infty} \mathrm{d}w_{ab,\Theta}^L \int_{-\pi/2}^{\pi/2} \mathrm{d}\theta_a'^L \times \int_{-\pi/2}^{\pi/2} \mathrm{d}\theta_b'^L \sin\Theta^L \rho(w_{ab,r}^L) \rho(w_{ab,\Theta}^L) \rho(\theta_a'^L) \rho(\theta_b'^L) \rho(\Theta^L) \times \mathcal{K}_{\alpha,ab}(\Theta^L, \theta_a'^L, \theta_b'^L, w_{ab,r}^L, w_{ab,\Theta}^L) |w_{ab,r}^L|, \quad (8.26)$$

with $\alpha = \{\text{hydro, ballistic}\}$ such that $C_{eff,ab} = \mathcal{T}_{ab}^{\text{hydro}} / \mathcal{T}_{ab}^{\text{ballistic}}$. We calculate $\mathcal{T}_{ab}^{\text{hydro}}$ and $\mathcal{T}_{ab}^{\text{ballistic}}$ for $\epsilon = 0.034\ \text{m}^2\,\text{s}^{-3}$ (the turbulent kinetic energy dissipation rate in the experiment of Schneck et al., 2019) and hence obtain $C_{eff,ab}$.

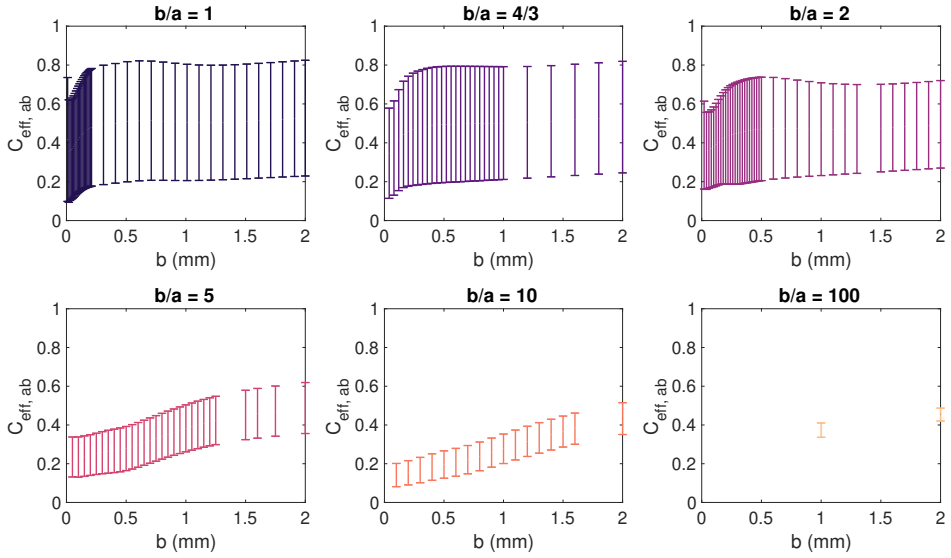

Figure 8.13: Maximum and minimum values of the collision efficiency for the value of b/a given in the title of each panel. The maximum values are obtained when we set $\mathcal{K}_{hydro,ab}(\Theta, \theta'_a, \tilde{w}_{ab,r}, \tilde{w}_{ab,\Theta}) = 1$ for cases where the solver failed but a collision occurred in the ballistic case, and the minimum values are obtained when we set $\mathcal{K}_{hydro,ab}(\Theta, \theta'_a, \tilde{w}_{ab,r}, \tilde{w}_{ab,\Theta}) = 0$ for cases where the solver failed but a collision occurred in the ballistic case.

Figure 8.13 shows the range of expected values for $C_{eff,ab}$ for $b/a = [1,\ 4/3,\ 2,\ 5,\ 10,\ 100]$. There is much larger uncertainty in $C_{eff,ab}$ for the smaller disk-size ratios where the solver struggled more. For values where $b/a \geq 5$, the collision efficiency increases with b. This is because at larger values of b the initial relative speed is faster (see Figure 8.6) so more collisions are possible. In all cases the collision efficiency is less than 1.

Using the values of $C_{eff,ab}$ shown in Figure 8.13 we use the Matlab scattered interpolation function to find the maximum and minimum collision efficiency for the values of a and b used in our model. Figure 8.14 shows $C_{eff,ab}$, $\mathcal{T}_{ab}^{\text{hydro}}$ and $\mathcal{T}_{ab}^{\text{ballistic}}$ for the two methods used to calculate the collision kernel, which were outlined above. In the top row (panels a-c) the collision kernel is set to 1 in cases where the solver failed and a ballistic collision occurred for that value of $\Theta, \theta'_a, \tilde{w}_{ab,r}, \tilde{w}_{ab,\Theta}$. In this case we find $0.08 \leq C_{eff,ab} \leq 0.42$ for $\epsilon = 0.034\ \text{m}^2\,\text{s}^{-3}$. In the bottom row (panels d-f) the collision kernel is set to 0 in the same cases, and we find

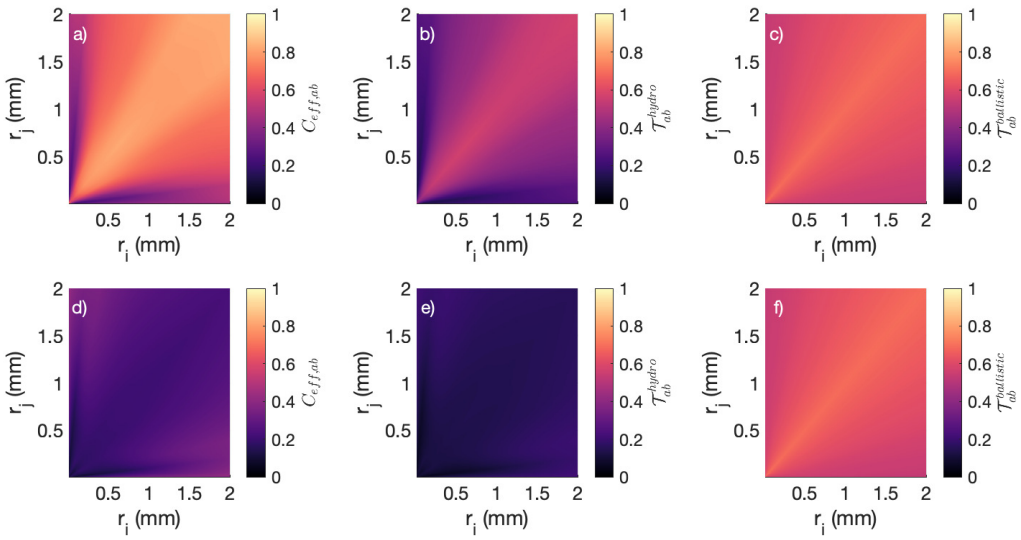

Figure 8.14: Calculation of the collision efficiency for radii of disks i and j with $\epsilon = 0.034$ $\mathrm{m^2 s^{-3}}$. In the top row (panels a-c) the collision kernel is set to 1 in cases where the solver failed and a ballistic collision occurred for that value of $\Theta, \theta_a', \tilde{w}_{ab,r}, \tilde{w}_{ab,\Theta}$. In the bottom row (panels d-f) the collision kernel is set to 0 in the same cases. Panels a and d are the collision efficiency, $C_{eff,ab} = \mathcal{T}_{ab}^{\mathrm{hydro}}/\mathcal{T}_{ab}^{\mathrm{ballistic}}$, Panels b and d are $\mathcal{T}_{ab}^{\mathrm{hydro}}$ and panels c and f are $\mathcal{T}_{ab}^{\mathrm{ballistic}}$, where $\mathcal{T}_{ab}^{\alpha}$ is given by (8.26) and reflects the fractional reduction in the number of collisions from the assumption that all crystals with a negative radial velocity entering a sphere of radius $r_{max,ab}$ collide.

$0.20 \leq C_{eff,ab} \leq 0.82$. There is a larger difference in the collision efficiencies as the disks become similar in size. We also note that $\mathcal{T}_{ij}$ is between 3 and 6 times greater here than $\mathcal{T}_{ij}$ calculated in §6 for the same probability density functions for θ_a and θ_b. This reflects the increase in the number of collisions due to setting $\tilde{w}_{ab,\Phi} = 0$ and $\phi_a' = \phi_b' = 0$ in this chapter whilst assuming a Gaussian distribution for $\tilde{w}_{ab,\Phi}$ and a uniform distribution for ϕ_a' and ϕ_b' in §6.

8.6 Conclusion

In this chapter we have calculated the effect of hydrodynamic interactions on the trajectories of the crystals in three spatial dimensions. To reduce computational expense, we only calculated the effect of hydrodynamic interactions for crystals with orientation varying in one plane (such that $\phi_a' = 0$ for crystal A). We also assumed that the velocity was only in the x'-z' plane and the setup was symmetric in y'. We calculated the pressure between the crystals using the lubrication approximation

and used this to find the forces and torques. We found that the resistive force was much weaker at steeper angles of approach when the velocity was manly due to vertical translation. This allowed for collisions of frazil ice crystals at these angles. Collisions generally occur with little rotation of either disk but when the disks are initially close to perpendicular, collisions are also possible at much lower initial speeds and occur after significant rotation of the top disk. We found that the two-dimensional criterion (7.52) still approximates the shape of the collision boundary well in the dimensions when the initial relative angle between the disks $\theta'_{a,in}$ is small. The boundary (7.52) is correct to within a factor of 1.53 for $\theta'_{a,in} \leq 30^o$. For larger values of $\theta'_{a,in}$ (7.52) is far from the true collision boundary as the 3D geometry of the disk becomes more important.

In §8.5.2 we calculated the collision efficiency due to hydrodynamic interactions. We estimated that if the relative angle between the two crystals is zero, hydrodynamic interactions lead to a negligible number of collisions. If the relative angle between the crystals follows a uniform distribution we found that hydrodynamic interactions reduced the number of collisions by a factor between 0.08 and 0.82 depending on the relative size of the crystals and uncertainty from the simulations that did not produce useful results. The large range is reflective of the difficulties the solver had when the crystals were of a similar size. When ratio of the crystal radii was greater or equal to 5 we found that the collision efficiency was between 0.08 and 0.62. The larger values of the collision efficiency occur for larger disks. If the larger disk has a radii of less than 0.5 mm the maximum collision efficiency is 0.4. Hence, hydrodynamic interactions might play an important role in accurately modelling collisions of frazil ice crystals.

To further understand the effect of hydrodynamic interactions several aspects could be explored. Firstly, the pressure between the crystals could be calculated using the full Stokes equations (Katopodes, 2019). This approach would be more computationally expensive but would yield more accurate results for cases with

intermediate relative angles $\theta'_a - \theta'_b$ where the lubrication approximation does not strictly apply. More accurate results could also be obtained by improving the solver to reduce the number of cases where the solver fails and by running at higher tolerances which proved prohibitively expensive here. We have also neglected the effects of crystal growth which would provide an additional flux due to the different densities of water and ice generating volumetric expansion in freezing.

For the observed supercooling for frazil ice production, the simple scale analysis in §E.4 suggests that growth generally acts on a significantly longer timescale than the time taken for the disks to collide. However, in some cases where the disks do not collide, the disks spend a long time close to each other at lower velocities in which case freezing might be important. A further simplification comes from the fact that we have chosen our setup to remain symmetric in y' such that we have set $w_{ab,y} = 0$ and $\phi'_a = \phi'_b = 0$. Therefore, it remains uncertain how successfully our calculation of the collision efficiency can be applied to cases where the ballistic collision rate consider all degrees of freedom.

The introduction of hydrodynamic interactions to calculate the collision efficiency also allows for several diagnostics to be obtained which might be useful in future models. In the model of Yang et al. (2023) flocculation only occurs for collisions occurring with velocity below a certain value. Hydrodynamic interactions enable a more accurate calculation of the collision velocity, which could be used to improve their model. Further, more complex parametrisations for secondary nucleation (for example Daly, 1984; Mercier, 1985 and Yang et al., 2023) rely on knowledge of the kinetic energy and velocity of each of the crystals when they collide, which again will be influenced by hydrodynamic interactions. Finally, hydrodynamic interactions allow us to calculate the pressure distribution across the crystal. This means that plate theory could be used to determine a fracture criteria for the crystals, which may allow more insight into the mechanics of the fracture process.

"By the seventh day God had finished the work he had been doing; so on the seventh day he rested from all his work. Then God blessed the seventh day and made it holy, because on it he rested from all the work of creating that he had done."

— Genesis 2:2 NIV

9 Conclusions

Contents

9.1 Overview of this thesis

This thesis has focussed on improving the parametrisation of frazil ice crystal collisions. Frazil ice crystals are small, roughly millimetre sized crystals that form in supercooled turbulent water. In the absence of seed nuclei from primary nucleation, secondary nucleation has been shown to be necessary to generate the large number of crystals needed for numerical models of frazil ice to match experimental data (Jones and Wells, 2018; Souillé et al., 2020; Svensson and Omstedt, 1998). However, all of these models have included tuning parameters to limit the number of collisions, such that the model results are a closer match to the experiments. Further, various processes are neglected, or incorrectly accounted for in the parametrisation of crystal

collisions. In this thesis we first identified these processes and then suggested how they can be parametrised. We began in §2 by comparing frazil ice models to crystal collision models in other settings. We found that typical frazil ice models:

1. Do not correctly calculate the relative velocity between crystals.
2. Only allow the collision radius to depend on the size of one crystal, when it should actually depend on the size of both colliding crystals.
3. Use the cylindrical formulation to estimate the encounter frequency, which assumes that the relative velocity in any instant is locally uniform over a spatial scale on the order of the collision radius, instead of the spherical formulation which does not make the same assumption.
4. Do not correctly redistribute the crystals between different size classes after a collision.
5. Do not fully account for the cylindrical shape of the crystals.
6. Ignore hydrodynamic effects.
7. Assume that the frazil ice crystals are homogenously distributed throughout the fluid.

In this thesis we addressed aspects of the first six of these concerns. Determining how the frazil ice crystals are distributed throughout the fluid remains a question for future research. At several points through the thesis we tested the effect of each of our changes using a simple frazil ice model where the crystal population only changed due to crystal collisions. We compared our results to the parametrisation for secondary nucleation used by Holland and Feltham (2005) which we termed the CP formulation. This model along with a mixed-layer model was introduced in §3. The results of these comparisons are summarised below.

In §4 we addressed the first three of the above concerns. We introduced a parametrisation for the mean radial relative velocity between frazil ice crystals

under the spherical formulation, where the number of crystals entering a sphere with radius equal to the collision radius is used to estimate the collision rate. The radial relative velocity was derived by combining the force on each crystal due to buoyancy and inertia. We also set the collision radius to be the sum of the radii of both of the colliding crystals rather than just one of the colliding crystals, to capture a wider range of configurations that lead to a collision. We found that these changes increased the crystal collision rate relative to the CP formulation for more quiescent flows with turbulent kinetic energy dissipation rate $\epsilon \leq 10^{-4}$ $\mathrm{m^2\,s^{-3}}$, and decreased the crystal collision rate relative to the CP formulation for $\epsilon > 10^{-4}$ $\mathrm{m^2\,s^{-3}}$. As tuning parameters in numerical models for frazil ice focus on changing the collision rate, these results suggests that the value of these parameters should also change, where used.

In §5 we addressed the fourth of the concerns above and derived a method to redistribute the crystals after a collision. The method distributes post collision crystal fragments into multiple size classes, not just the smallest size class and the size class of the crystal that collides. This led to a significant change in the mean crystal radius as the crystal population evolved, with the mean radius being much smaller than the mean radius calculated without the change in redistribution. The change to the collision rate was less than a factor of two. As the growth rate and mean buoyant rise velocity of frazil ice crystals depend on the mean radius of the crystal population, including the refined treatment of size redistribution is likely lead to further impacts on the results of more detailed numerical models of frazil ice suspensions. For example a smaller mean radius is likely to reduce the precipitation rate of frazil ice crystals.

In §6 we addressed the fifth of the above concerns and derived a method to account for the cylindrical shape of the crystals when calculating frequencies of ballistic collisions. We calculated the non-radial components of the relative velocity and the conditions for a collision to occur. We increased the collision radius to

the maximum separation between the crystals when they could still be in contact. We then calculated the reduction in the number of collisions for cases when the orientation of the crystals was random, and when the axis of the crystals was parallel to the gravitational field. For typical oceanographic turbulence levels, we found that the number of collisions reduced by a factor of between 0.17 and 0.99 depending on the crystal sizes, turbulence, and assumption made about the crystal orientation. The overall collision rate was between 3 and 10 times faster than in the CP model due to the larger collision radius. There was almost no change to the shape of the radius distribution of the crystal population. Again, as tuning parameters in numerical models for frazil ice focus on changing the collision rate, these results suggest that value of these parameters should also change where collisions schemes are updated.

In §7 and §8 we addressed the sixth of the above concerns by modelling the effect of hydrodynamic interactions as the crystals approach. In §7 we calculated the effect of hydrodynamic interactions when two plates approach close to parallel, using lubrication theory with an effectively two dimensional flow geometry. This provided an expression (7.52) for the velocity required for the plates to collide. We found that this initial velocity is at least an order of magnitude larger than the likely velocity of millimetre-sized frazil ice crystals in typical oceanographic conditions, suggesting collisions when crystals approach close to parallel are unlikely. We also tested whether fracture of the crystals via elastic bending is possible in cases where they do not collide. We again found that the velocity required for fracture is at least an order of magnitude larger than the likely velocity of millimetre sized frazil ice crystals in typical oceanographic conditions. As the results of §7 did not rule out the possibility of collision at larger angles, and were also calculated for two-dimensional plates instead of three-dimensional disks, in §8 we calculated the effect of hydrodynamic interactions as three-dimensional disk-shaped crystals approach at all angles. We again used the lubrication approximation, noting that it is not strictly applicable at steeper angles but is likely to be accurate to within an order of magnitude

(Cawthorn and Balmforth, 2010). We found that collisions were now possible at steeper approach angles. Using these results we than obtained an estimate for the collision efficiency, which is the fraction of crystal encounters that result in a collision. We found that the collision efficiency was between 0.08 and 0.82. The collision efficiency is dependent on the relative size of the crystals, with larger relative crystal sizes generally leading to a higher collision efficiency. The range in values for the collision efficiency is also influenced by uncertainty from the simulations that did not produce useful results. The results suggest that hydrodynamic interactions could be very important for accurately parametrising crystal collisions, but further work needs to be done to reduce the uncertainty in the collision efficiency.

9.2 Comparison with experimental results

We now use the mixed-layer model introduced in §3 to test our parametrisation for secondary nucleation against the experimental results of Schneck et al. (2019). We initialise the model with the reported values found at the maximum supercooling observed in the freshwater experiment ($t/t_c = 1$ in Figure 3. of Schneck et al., 2019). We set the supercooling to 0.0847^oC, the frazil ice crystal number density to 0.648cm^{-3}, the mean radius to 0.65 mm and standard deviation of the crystal population distribution to 0.28 mm. Schneck et al. (2019) reported that the crystal population retained a lognormal distribution throughout the experiment so we initialise with a lognormal distribution. In line with their observations, we set the cooling rate from external sources to $-2 \times 10^{-4}\ \text{K}\,\text{s}^{-1}$. We initialise with a uniform spacing in radial space between 200 size classes, with the crystal radii ranging from 0.01 mm to 2 mm. The rest of the model parameters are unchanged from those described in §3.

We compare four different parametrisations for secondary nucleation which we term as the CP, (SDR, E), (SDR, E1) and (SDR E0) parametrisations. In the CP parametrisation we use the parametrisations for secondary nucleation used by Holland and Feltham (2005). In the (SDR, E) parametrisation we use the

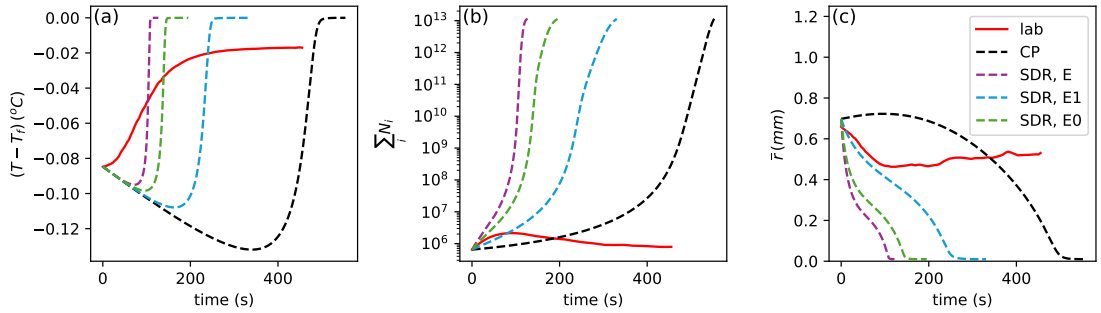

Figure 9.1: Comparison of the four parametrisations for secondary nucleation introduced in this thesis (dashed lines) against the laboratory results of Schneck et al. (2019) (solid red line). In CP parametrisation we use the parametrisations for secondary nucleation used by Holland and Feltham (2005). In (SDR, E) we use the parametrisations for secondary nucleation that includes the improvements made in §4-§6. In (SDR, E1), (SDR, E0) we use the same improvements from §4-§6 as well as including the upper and lower bound on the collision efficiency from §8 in (SDR, E1) and (SDR, E0) respectively. The results are obtained using the mixed-layer model introduced in §3 and show a) the supercooling, b) the total number of crystals, c) the mean crystal radius.

parametrisations for secondary nucleation that includes the improvements made in §4-§6. The spherical formulation is used to calculate the relative velocity, the collision radius depends on the size of both crystals, the crystals are redistributed after a collision using the method described in §5, and the cylindrical shape of the crystals as well as the non-radial components of the velocity are accounted for. As the flow is very turbulent, $\epsilon = 0.034\ \mathrm{m^2\,s^{-3}}$, we assume that the orientation of the crystals is likely to be random, so we take the collision frequency calculated using this assumption, ($\mathcal{F}^{A}_{enc,ij}$) from §6. In the (SDR, E1) and (SDR, E0) parametrisations we use the same improvements from §4-§6 as well as including the upper and lower bound on the collision efficiency from §8 in (SDR, E1) and (SDR, E0) respectively.

Figure 9.1 compares the results using the different parametrisations for secondary nucleation. Panel a compares the supercooling against observations, panel b compares the total number of crystals against observations and panel c compares the mean radius of the crystal population against observations. All of the parametrisations lead to an initial decrease in the temperature, whilst the results of Schneck et al. (2019) suggest that the temperature should initially increase. The discrepancy

is largest in the CP model, suggesting that although results with the implemented parameters do not mimic the observed initial temperature change, they do better than the old model. The time when the temperature starts to increase reflects the timescale over which collisions occur in each of these parametrisations for secondary nucleation, with collisions happening slowest in the CP parametrisation and fastest in the (SDR, E) parametrisation. In all models the temperature then increases more rapidly than was observed. In all cases, the total number of crystals also increases to be several orders of magnitude higher than what is observed by Schneck et al. (2019). Finally, in all cases the mean crystal radius tends to the radius of the smallest size class whilst the mean radius observed by Schneck et al. (2019) seems to plateau at a larger value. In the CP model the mean radius initially increases, whilst in all the other formulations the mean radius initially decreases in line with observations. This again suggests that our parametrisations for secondary nucleation may be favourable to the prior approach.

Although, the results in Figure 9.1 are still a poor fit with the observations of Schneck et al. (2019), they do allow useful insights into how parametrisations of crystal interactions could be improved and which processes should be included. Firstly, Schneck et al. (2019) report that 'the total volume of frazil ice particles was between 0.3 % and 1 % of the total volume of flocs'. Therefore, flocs are likely to play an important role in the temperature increase and not including flocs is probably the most significant reason why the results disagree. In particular, this may explain why the temperature in our experiments initially decreased. Further, the very presence of crystal flocs suggests that flocculation cannot be assumed to be negligible in frazil ice models. Therefore, some crystal collisions should be parametrised to result in flocculation. Letting some crystal collisions result in flocculation would also reduce the total number of crystals and increase the mean crystal size, which may lead to the modelled total number concentrations matching more closely with the observations.

As an additional test of our model, we compare the crystal population size distribution at the temperatures given in the titles of the panels in Figure 9.2. We compare the model results with the observed size distribution. For $T - T_f = 0.1[T(0) - T_f]$, the temperature in the experiment did not reach this value so we compare to the population distribution at the end of the experiment. As the temperature increases the modelled size distribution becomes increasingly less log-normal. This is reflective of the rapid increase in the number of crystals in the smallest size class due to collisions. These crystals then grow into the other size classes but at too low a rate for the crystal population to remain log-normal. The relative number of crystals in the smallest size classes is largest for the (SDR, E) parametrisation where the collision rate is highest.

Again, although, these results are inconsistent with the observations of Schneck et al. (2019), they do allow useful insights into the model could be improved. Parametrising collisions to produce large number of crystals of the smallest size class leads to great difficulty in maintaining the observed log-normal distribution as the crystals cannot grow quickly enough into the other size classes to maintain the distribution. This suggests that it would perhaps be more appropriate for collisions to result in crystals fracturing into a range of size classes. The number of crystals in the smallest size class could also be reduced if flocculation is much faster for smaller crystals, again suggesting that the model may show closer agreement to experiment if flocculation were included.

9.3 Ideas for further work

9.3.1 Parametrisation of secondary nucleation

Although, this thesis has improved the way crystal collisions are parametrised there are still many unanswered questions, and the results in §9.2 suggest that improvements can still be made to how secondary nucleation is included in models. Firstly, we have not addressed the weakness that comes from assuming that the frazil ice crystals are homogenously distributed. A homogenous distribution is

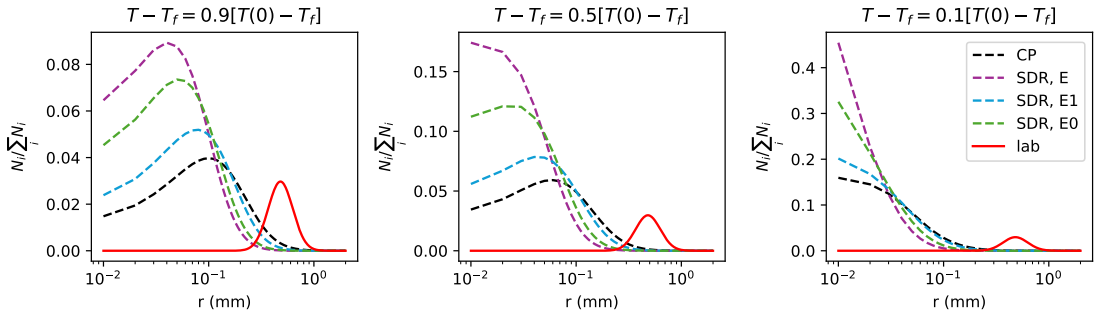

Figure 9.2: Same model runs as Figure 9.1 but comparing the crystal population distribution when the temperatures reach the value given in the title of each panel. The temperature at time zero is denoted $T(0)$. Time increases from left to right panels, but the actual times are different for each parametrisation (see Figure 9.1).

unlikely to be the case in turbulent flow because it has been shown (Varaksin, 2019) that particles lighter than the fluid have a tendency for increased particle concentration in areas of low vorticity due to the action of the centrifugal force. The opposite case is true when the particles are denser than the fluid. This effect has been shown to increase the collision frequency of heavy particles by one to two orders of magnitude (Sundaram and Collins, 1997; Wang et al., 2000a). Therefore, assuming the crystals are homogenously distributed within a turbulent flow means we are potentially underestimating the collision rate by a significant amount.

Secondly, there are still unanswered questions above the correct choice of probability density function for the relative velocity and the crystal orientation. In the ballistic case we have found that the collision rate can be up to a factor of three times faster, depending on the choice of probability density function for the crystal orientation. It would be useful to have experimental observations of the choice of probability density function for the crystal orientation.

Thirdly, our calculation of the effect of hydrodynamics was limited by computational resources. With unbounded computational resources this calculation would have ideally been done using full Stokes flow, for all possible crystal orientation with the velocity varying in all three directions. Therefore, our present results for the

collision efficiency need to be treated with some caution. The pressure distribution due to hydrodynamics could also be used to calculate the elastic deflection of the crystals as they approach in three-dimensions, which would provide interesting insight into the fracture mechanism.

Fourthly, we have only obtained results assuming the crystals have an aspect ratio of 50, whilst in reality a range of aspect ratios has been observed (Souillé et al., 2023). We would expect the aspect ratio to change over time if the ratio of radial verses axial growth is not constant. Further, once fracture occurs the aspect ratio of the fractured disk should change which is not accounted for in our model.

Finally, one big assumption made in our model is that all collisions always result in the production of a crystal of the smallest size class. This assumption leads to difficulties in maintaining the observed log-normal population distribution suggesting that a more appropriate choice might be to fracture the crystals into a range of different sizes.

9.3.2 Parametrisation of other processes

The results in §9.2 and the observations of Schneck et al. (2019) suggest that flocculation cannot be ignored in frazil ice models. Although this thesis has focussed on secondary nucleation, the ideas introduced could also be used to parametrise flocculation. Instead of assuming that all collisions result in fracture, a flocculation criteria could be implemented. Depending on how the crystals collide, they would either fracture, flocculate or remain unchanged. Lubrication forces slow down crystal evolution and increase the time for crystals to move apart when they approach but do not collide. This means that there is more time for the crystals to freeze together. Lubrication forces may also generate the apparent flocculation of crystal clusters that are not directly bonded but are slow to separate (i.e. hydrodynamically metastable clusters). One mechanism to calculate a flocculation criteria could be to introduce freezing into the hydrodynamic calculation. The collision velocity would then be a

combination of the velocity of the crystal and the crystal growth rate. As is the case in the model of Yang et al., 2023, flocculation could be parametrised to occur in cases where the collision velocity was below a certain value and nucleation when the collision velocity was above this value. The difference here is that the collision velocity would be calculated more accurately due to inclusion of hydrodynamic forces. The inclusion of freezing would also enable insight into the dynamics of the flocculation process. However, the calculations in §7 showed that all collisions produce a sharp enough pressure peak to cause fracture in 2D. Therefore, reconciling the results from lubrication theory with current models would need more detailed consideration of the mechanism of the fracture and flocculation process.

9.3.3 Introduction into a depth-dependent model

The code written for the simple frazil model and the mixed-layer model is easily adapted to modelling a depth dependent frazil crystal population with buoyant rise included. It would be interesting to see how inclusion of these processes affect crystal collisions. We have found that in quiescent conditions the collision rate is larger when crystals of different sizes interact. In more turbulent conditions the collision rate is larger for crystals of larger sizes. With buoyant rise included, the larger crystals are likely to rise to the surface faster than the smaller crystals. This is likely to reduce the collision rate in the quiescent case and in the turbulent case lead to more collisions closer to the surface, as long as the number of crystals at each depth is similar.

9.4 Implications of this thesis

This thesis has led to an improved understanding of secondary nucleation of frazil ice crystals and the important physical processes governing the rate at which frazil ice crystals collide. In particular, the choice of collision radius was seen to significantly alter the collision rate. Not completely accounting for the cylindrical shape of the crystals, and failing to include crystal interactions can lead to an overestimate of the number of encounters that result in a collision. The choice of parametrisation for secondary nucleation has been demonstrated to significantly

affect the evolution of the water temperature. In oceans and rivers, growth of frazil ice crystals produces heat and, in saline conditions, salt fluxes. Therefore, incorrectly parametrising secondary nucleation could lead to errors in the density of the water which would then propagate to larger scale processes such as convection. Further, we have demonstrated the need for further work in observing frazil ice collisions and parametrising flocculation. Many of our results, depend on the choice made to parametrise certain variables for example the probability distribution of the crystal orientation and the relative velocity. This demonstrates the need for experimental observations of these quantities. Further, comparison of our model with the observations of Schneck et al. (2019) suggests that future work should focus on parametrising flocculation which we postulate is important. Finally, although this thesis has focussed on frazil ice crystals, some of the results could be used as a basis to parametrise fracture of plate-like crystals in other settings. For example, after applying density modifications, the equation (7.52) for the collision boundary could be applied to estimate a minimum velocity for the fracture of plate-like ice crystals in clouds (Sheikh et al., 2022; Diedenhoven et al., 2020) or of plate-like crystals in industrial crystallisers (Besenhard et al., 2017).

Appendices

A
Nomenclature

Table A.1 defines some important symbols used in this thesis. Some cases where the symbol is only used a few times and in close proximity to where it is defined are not listed. The values or equation numbers listed in the final column correspond to the values or equations used in the numerical frazil ice model used to obtain the results in this thesis. In cases where the quantity is not used in the final model the relevant section referring to the quantity is listed instead.

Table A.1: Nomenclature.

Name	**Symbol**	**Unit**	**Value/ equation**
Area of the crystal that freezes	A_F	m^2	§2.3.1
Scaled added mass of particle p	A_p		(4.9)
Scaled buoyancy of particle p	b_p^*		(4.9)
Added mass coefficient	C_{add}		§4.2.1
Crystal drag coefficient	C_D		§3.2.1.4
Volume concentration of crystal of size class i	C_i		$n_i V_i$
Collision efficiency between particles of sizes i and j	$C_{eff,ij}$		(8.23)
Specific heat capacity	c_w	$\mathrm{J\,kg^{-1}\,K^{-1}}$	3974
Thickness of plate i	D_i	m	§7

Continued on next page

Table A.1: Nomenclature. (Continued)

Aspect ratio of crystals of size class i	d_i		50
Mean collision energy of crystals of size class j and k	$E_{coll,jk}$	J	§2.3.4
Total collision frequency of particles of size class i	$\mathcal{F}_{coll,i}$	s^{-1}	(4.53)
Drag force on a particle of size class i	$\mathbf{F}_i^d$	N	(2.11)
Encounter frequency of particles of size i with particles of size j	$\mathcal{F}_{enc,ij}$	s^{-1}	(4.46)
Rate at which crystals are added to size class i per unit volume from flocculation	$\mathcal{F}_{floc,i}$	$m^{-3}s^{-1}$	§2.3.4.2
Total production rate of crystals of size class i due to crystals of size class j per unit volume	$\mathcal{F}_{prod,ij}$	$m^{-3}s^{-1}$	§2.3.4
Flocculation rate	F	ms^{-1}	§2.3.4.2
Flocculation rate of crystals of size class $i-1$ into size class i	F_{i-1}	s^{-1}	§2.3.4.2
Flocculation rate of crystals out of size class i	f_i	s^{-1}	§2.3.4.2
Collision frequency of a single crystal of size class j with crystals of size class k	$f_{coll,jk}$	s^{-1}	(2.51)
Growth rate	G	ms^{-1}	(1.1)
Acceleration due to gravity	g	ms^{-2}	9.81
Radial distribution function	$g_{ij}(r_{c,ij})$		(2.55)
Gap thickness	h	m	
Minimum gap thickness	h_{min}	m	
Liquid thermal conductivity	k_l	$Wm^{-1}K^{-1}$	0.512
Length of plate i	L_i	m	7
Rate at which crystals melt out of size class i into the neighbouring size class	$\mathcal{M}_i$	s^{-1}	(2.8)
Crystal mass	m	kg	
Mass of crystal i	m_i	kg	$\rho_I \pi r_i^2 w_i$
Number of size classes	N		200
Number of nuclei produced per unit collision energy	N_E	J^{-1}	§2.3.4

Continued on next page

Table A.1: Nomenclature. (Continued)

Primary nucleation rate	$\dot{N}_I$	$\mathrm{m}^{-3}\mathrm{s}^{-1}$	§2.3.2
Flocculation rate	$\dot{N}_F$	$\mathrm{m}^{-3}\mathrm{s}^{-1}$	(2.1)
Secondary nucleation rate	$\dot{N}_T$	$\mathrm{m}^{-3}\mathrm{s}^{-1}$	(1.1)
Average collision rate between particles of size class i and j	$\langle \mathcal{N}_{ij} \rangle$	s^{-1}	(2.51)
Nusselt number	Nu		1
Number of crystals per unit volume	$\overline{n}$	m^{-3}	
Number of crystals of size class i per unit volume	n_i	m^{-3}	
Limit on the number density to reduce the collision rate	n_{max}	m^{-3}	§2.3.4
Number of crystals per unit length in radius space per unit volume	n_r	m^{-4}	(1.1)
Pressure	p	Pa	
Particle Reynolds number	Re_p		(2.12)
Crystal radius	r	m	
Radius of crystals of size class i	r_i	m	$10^{-5} - 0.002$
Critical radius	r_c	m	(1.1)
Contribution to the collision radius from a particle of size class i	$r_{c,i}$	m	
Collision radius between particles of size classes i and j	$r_{c,ij}$	m	$r_{c,i} + r_{c,j}$
Maximum possible separation between the centre of masses whilst the crystals are in contact	$r_{max,ij}$	m	§6.3
Equivalent radius for crystal of size class i	r_i^e	m	(2.38)
Reference salinity	S_0	psu	34.5
Stokes number	St		τ_p/τ_f
Fluid temperature	T	^{o}C	
Reference temperature	T_0	^{o}C	-2
Freezing temperature of ice	T_f	^{o}C	(3.3)
Time	t	s	
Average squared fluid velocity	u'^2	ms^{-1}	$\langle u^2 \rangle$
Fluid velocity	$\mathbf{u}$	ms^{-1}	

Continued on next page

Table A.1: Nomenclature. (Continued)

Velocity of a particle	$\mathbf{u}_p$	ms^{-1}	§4.2.1
Velocity of particle i	$\mathbf{u}_{pi}$	ms^{-1}	§4.2.1
Mean velocity of particle of size class i	$\langle \mathbf{u}_{pi} \rangle$	ms^{-1}	§2.3.4.1
Mean crystal volume	$\overline{V}$	m^3	
Volume of a crystal of size class i	V_i	m^3	$\pi r_i^2 w_i$
Volume of particle p	V_p	m^3	
Volume of a crystal with radius r	V_r	m^3	
Volume removed from an individual crystal in a single collision	V_{rem}	m^3	ζV_1
Rise velocity	v_g	ms^{-1}	§2.3.3
Rise velocity of a crystals of size class i	$v_{i,g}$	ms^{-1}	§3.2.1.4
Thickness of a crystals of size class i	w_i	m	$2r_i/d_i$
Relative rise velocity of two particles of size classes i and j	$w_{ij,g}$	ms^{-1}	$v_{i,g} - v_{j,g}$
Radial component of the relative velocity between the two particles of size classes i and j separated by a distance $r_{c,ij}$	$w_{ij,r}(r_{c,ij})$	ms^{-1}	(4.2)
Mean absolute radial component of the relative velocity between the two particles of size classes i and j separated by a distance $r_{c,ij}$	$\langle \lvert w_{ij,r}(r_{c,ij}) \rvert \rangle$	ms^{-1}	(4.46)
Relative velocity between the two particles of size classes i and j separated by a distance $r_{c,ij}$	$\mathbf{w}_{ij}(r_{c,ij})$	ms^{-1}	(4.1)
Mean relative velocity between the two particles of size classes i and j separated by a distance $r_{c,ij}$	$\langle \mathbf{w}_{ij}(r_{c,ij}) \rangle$	ms^{-1}	(4.18)
Relative velocity of crystals of size class i from turbulent motion	$w_{i,turb}$	ms^{-1}	(2.39), (2.40)
Depth	z	m	
Rate of production of crystals of size class i due to collisions with a single crystal of size class j	α_{ij}	s^{-1}	(2.24), (2.36)
Difference crystal rise area for crystal drag calculation	β		§2.3.3

Continued on next page

Table A.1: Nomenclature. (Continued)

Secondary nucleation rate of crystals out of size class i into size class 1	β_{i1}	s^{-1}	(2.41)
Salinity expansion coefficient	β_S	psu^{-1}	7.86×10^{-4}
Temperature expansion coefficient	β_T	$^oC^{-1}$	3.87×10^{-5}
Whether flocculation occurs for crystals of size class i	$\beta_{floc,i}$		(2.48)
Turbulent kinetic energy dissipation rate	ϵ	m^2s^{-3}	$10^{-8} - 0.034$
Rate at which crystals grow out of size class i into the neighbouring size class	Γ_i	s^{-1}	(2.6)
Collision kernel between particles of sizes i and j.	Γ_{ij}	m^3s^{-1}	(2.52)
Curvature of plate i	κ_i	m^{-2}	§7
Latent heat of solidification	$\mathcal{L}$	Jkg^{-1}	3.35×10^5
Kolmogorov lengthscale	η_K	m	$(\nu^3/\epsilon)^{1/4}$
Fluid dynamic viscosity	η	Pas	1.9×10^{-3}
Fluid kinematic viscosity	ν	m^2s^{-1}	1.95×10^{-6}
Frazil particle diffusivity	ν_c	m^2s^{-1}	(1.1)
Angle the vector joining the centre of mass of two crystals makes with the x axis within the $x-y$ plane	Φ	radians	
Angle the axis of crystal a makes with the x axis within the $x-y$ plane	ϕ_a	radians	
Angle the relative velocity makes with the x axis within the $x-y$ plane	ϕ_u	radians	
Fluid density	ρ	kgm^{-3}	(3.12)
Probability density function of x	$\rho(x)$		
Reference density	ρ_0	kgm^{-3}	1030
Ice density	ρ_I	kgm^{-3}	920
Particle density	ρ_p	kgm^{-3}	
Standard deviation of the radial velocity fluctuations	$\sigma_{ij}(r_{c,ij})$		(4.40), (4.41)
Angle the vector joining the centre of mass of two crystals makes with the z axis	Θ	radians	

Continued on next page

Table A.1: Nomenclature. (Continued)

Angle the axis of crystal a makes with the z axis	θ_a	radians	
Angle the relative velocity makes with the $-z$ axis	θ_u	radians	
Proportion of collisional energy transferred to the crystals	τ_{coll}		§2.3.4.1
Kolmogorov timescale	τ_K	s	$\sqrt{\nu/\epsilon}$
Particle relaxation time	τ_p	s	(4.5)
Number of crystals of size class 1 broken off per collision	ζ		1

B

Appendices for §4

Contents

B.1 Expression for $\langle u_{pi,x}^2(\mathbf{x})\rangle$ and $\langle u_{pi,x}(\mathbf{x})u_{pj,x}(\mathbf{x})\rangle$

In this appendix we briefly explain how the expression for the radial velocity correlation of particles i and j is obtained.

We use the expressions (A6) and (A7) in Chan et al. (2023) for $\mathcal{A}_i$ and $\mathcal{B}_{ij}$. To calculate $\mathcal{A}_i$ and $\mathcal{B}_{ij}$, Chan et al. (2023) express $\langle u_{pj,i}(\mathbf{x})^2\rangle$ and $\langle u_{pj,i}(\mathbf{x})u_{pk,i}(\mathbf{x})\rangle$ using a Fourier integral and relate the Fourier coefficients to the equivalent coefficients in the fluid Eulerian energy spectrum. The full derivation for these terms is found in Chan et al. (2023).

They obtain,

$$\langle u_{pi,x}^2 \rangle = \mathcal{A}_i \langle u_x^2 \rangle \tag{B.1}$$

$$\langle u_{pi,x} u_{pj,x} \rangle = \mathcal{B}_{ij} \langle u_x^2 \rangle. \tag{B.2}$$

where

$$\mathcal{A}_i = \frac{\zeta}{\zeta - 1} \left[\frac{1 + A_{pi}^2 \tau_{pi}^* / T_{fl}}{1 + \tau_{pi}^* / T_{fl}} - \frac{1 + A_{pi}^2 \zeta \tau_{pi}^* / T_{fl}}{\zeta (1 + \zeta \tau_{pi}^* / T_{fl})} \right], \tag{B.3}$$

$$\mathcal{B}_{ij} = 1 + \frac{\zeta}{(\zeta - 1)(\tau_{pi}^{*-1} + \tau_{pj}^{*-1})} \left[\frac{(A_{pi} - 1)(\tau_{pi}^{*-1} + \tau_{pj}^{*-1} A_{pj})}{1 + \tau_{pi}^{*-1} T_{fL}} + \frac{(A_{pj} - 1)(\tau_1^{*-1} + \tau_{pj}^{*-1} A_{pi})}{1 + \tau_{pj}^{*-1} T_{fL}} - \frac{(A_{pi} - 1)(\tau_{pj}^{*-1} + \tau_{pi}^{*-1} A_{pj})}{\zeta + \tau_{pi}^{*-1} T_{fL}} - \frac{(A_{pj} - 1)(\tau_{pi}^{*-1} + \tau_{pj}^{*-1} A_{pi})}{\zeta + \tau_{pj}^{*-1} T_{fL}} \right]. \tag{B.4}$$

Here $\zeta = 2(T_{fl}/\tau_L)^2$, where the Lagrangian time scale $\tau_L^2 = 2u'^2/(1.16\epsilon^{3/2}\nu^{-1/2})$ and T_{fl} is the fluid Lagrangian integral time scale (which gives a rough measure of the time taken by the particle velocity to become decorrelated with its initial state (Di Bernardino et al., 2020)). T_{fl} is related to the Eulerian longitudinal integral length scale L_f by $T_{fl} = 0.4 L_f / u'$.

We estimate L_f using a scaling analysis: $L_f = 0.5u'^3/\epsilon$ (Schröder et al., 2024). Therefore,

$$T_{fl} = \frac{u'^2}{5\epsilon}, \tag{B.5}$$

$$\zeta = \frac{0.0464 u'^2}{(\epsilon\nu)^{1/2}}. \tag{B.6}$$

B.2 Explanation for the increase in the mean radius as the turbulence increases

In this appendix we explain why the size class distribution shifts more to the smaller size classes when the turbulence reduces.

When most of the crystals are in size class 1, the dominant collisions are those between crystals of each size class and crystals of size class 1. In this case the

encounter frequency is found using (4.58) for quiescent flow and (4.56) for turbulent flow.

In turbulent flow, the ratio of the collision rate of larger particles with particles of size class 1 to the collision rate of smaller particles with particles of size class 1 is equal to r_l^3/r_s^3 where r_s is the radius of the smaller particle and r_l is the radius of the larger particles.

In quiescent flow, the ratio of the collision rate of larger particles with particles of size class 1 to the collision rate of smaller particles with particles of size class 1 is equal to $r_l^2 w_{g,l}/(r_s^2 w_{g,s})$. From Figure 3.1 we see that for particles smaller than 0.5mm, the rise velocity is calculated using the Stokes approximation, giving $w_{g,s} = g(1-\rho_I/\rho)2r_s^2/(32d\nu)$ and for particles larger than 0.5mm the rise velocity is roughly 10^{-3}m/s. We find that the ratio of the collision rate of larger particles with particles of size class 1 to the collision rate of smaller particles with particles of size class 1 is approximately equal to $0.001/r_s(r_l/r_s)^3$. Therefore, as $r_l \sim 1$mm the collision rates between smaller and larger particles are more different in quiescent flow, suggesting that the size class distribution will shift more to the smaller size classes for quiescent flow.

C

Derivation of the lubrication approximation

Contents

C.1 The lubrication approximation

The lubrication approximation is derived by considering which terms of the Navier-Stokes equation dominate for viscous flows where variation in one-direction is significantly larger than the others.

C.1.1 Dimensional analysis of the Navier-Stokes equation

We start off by considering the Navier-Stokes equation,

$$\frac{\partial \mathbf{v}}{\partial t} + (\mathbf{v} \cdot \nabla) = -\frac{1}{\rho}\nabla p + \nu \nabla^2 \mathbf{v}, \tag{C.1}$$

where $\mathbf{v} = (u_x, u_y, u_z)$ is the velocity of the fluid, ρ is the density of the fluid, p is the pressure and ν is the kinematic viscosity. We can write (C.1) in terms

of scaled variables, $u_x = U\tilde{u}_x$, $u_y = V\tilde{u}_y$, $u_z = W\tilde{u}_z$, $x = L_x\tilde{x}$, $y = L_y\tilde{y}$, $z = H\tilde{z}$, $t = T\tilde{t}$, $p = \Delta p\tilde{p}$.

$$\frac{L_x}{TU}\frac{\partial\tilde{u}}{\partial\tilde{t}} + \left(\tilde{u_x}\frac{\partial\tilde{u_x}}{\partial\tilde{x}} + \frac{VL_x}{UL_y}\tilde{u_y}\frac{\partial\tilde{u_x}}{\partial\tilde{y}} + \frac{WL_x}{UH}\tilde{u_z}\frac{\partial\tilde{u_x}}{\partial\tilde{z}}\right) = \\ -\frac{1}{\rho}\frac{\Delta p}{U^2}\frac{\partial\tilde{p}}{\partial\tilde{x}} + \nu\frac{L_x}{U}\left(\frac{1}{L_x^2}\frac{\partial^2\tilde{u_x}}{\partial\tilde{x}^2} + \frac{1}{L_y^2}\frac{\partial^2\tilde{u_x}}{\partial\tilde{y}^2} + \frac{1}{H^2}\frac{\partial^2\tilde{u_x}}{\partial\tilde{z}^2}\right). \quad \text{(C.2)}$$

and likewise for the y and z components.

C.1.2 Approximations

We consider a thin film, where the distance H between the surfaces is much larger than the length of the surfaces in the x and y directions,

$$\epsilon \sim \frac{H}{L_x} \sim \frac{H}{L_y} \ll 1 \quad \text{(C.3)}$$

Further we assume that the fluid is incompressible,

$$\nabla\cdot\vec{v} = \frac{U}{L_x}\frac{\partial\tilde{u_x}}{\partial\tilde{x}} + \frac{V}{L_y}\frac{\partial\tilde{u_y}}{\partial\tilde{y}} + \frac{W}{H}\frac{\partial\tilde{u_y}}{\partial\tilde{z}} = 0. \quad \text{(C.4)}$$

Performing a scale analysis we see $W \sim HU/L_x \sim HV/L_y \sim \epsilon U \sim \epsilon V \ll U, V$. We also assume one advective characteristic timescale $T \sim L_x/U$, and lengthscale $L_x, L_y \sim L$ and that the quantity,

$$\frac{H^2}{L^2}Re \ll 1. \quad \text{(C.5)}$$

Re-writing (C.2) in terms of ϵ, U, L_x and the Reynolds number, $Re = UL/\nu$ and choosing a characteristic pressure scale $\Delta p \sim \eta U/L(H/L)^2$,

$$\epsilon^2 Re\left(\frac{\partial\tilde{u}}{\partial\tilde{t}} + \tilde{u_x}\frac{\partial\tilde{u_x}}{\partial\tilde{x}} + \tilde{u_y}\frac{\partial\tilde{u_x}}{\partial\tilde{y}} + \tilde{u_z}\frac{\partial\tilde{u_x}}{\partial\tilde{z}}\right) = -\frac{\partial\tilde{p}}{\partial\tilde{x}} + \left(\epsilon^2\frac{\partial^2\tilde{u_x}}{\partial\tilde{x}^2} + \epsilon^2\frac{\partial^2\tilde{u_x}}{\partial\tilde{y}^2} + \frac{\partial^2\tilde{u_x}}{\partial\tilde{z}^2}\right). \quad \text{(C.6)}$$

For flows with $\epsilon^2 Re \ll 1$ and $\epsilon \ll 1$, the x-component of the dimensional Navier-Stokes equation simplifies to,

$$\frac{\partial p}{\partial x} = \eta\frac{\partial^2 u_x}{\partial z^2}. \quad \text{(C.7)}$$

D

Derivation of the forces and torques used in §7 for the cases of incomplete overlap and $\theta > 0$.

Contents

D.1 Dimensionless forces and torques for full overlap

In this section we calculate the pressure integrals required to determine the dimensionless forces and torques in §7.4.4. Applying the non-dimensionalisation in

§7.4.3.1 we obtain, $\tilde{F} = F/(12\eta L_a/T)$, $\tilde{\tau} = \tau/(12\eta L_a^2/T)$, and (7.22) (7.24) become,

$$-\tilde{F}_{bx} = \tilde{F}_{ax} = -\left[\frac{\phi}{2}\int_0^1 \tilde{p}d\tilde{x} + \frac{1}{12}(\tilde{u}_{ax}^t - \tilde{u}_{bx}^t - \tilde{\omega}_a\tilde{z}_a)\int_0^1 \frac{1}{\tilde{h}}d\tilde{x} + \frac{L_c}{12L_a}\tilde{\omega}_a\right], \quad \text{(D.1)}$$

$$-\tilde{F}_{bz} = \tilde{F}_{az} = \int_0^1 \tilde{p}d\tilde{x}, \quad \text{(D.2)}$$

$$\tilde{\tau}_a = \left[\int_0^1 (\tilde{x} - \tilde{x}_a)\tilde{p}d\tilde{x}\right], \quad \text{(D.3)}$$

$$\tilde{\tau}_b = \left[\int_0^1 (\tilde{x} - \tilde{x}_b)\tilde{p}d\tilde{x}\right]. \quad \text{(D.4)}$$

Dropping the tildes we can calculate the integrals in these expressions. Recalling that $p = Vp_V + \Omega p_\Omega$ and $h = h_{min} + \phi x$ we obtain,

$$\int_0^1 \frac{1}{h}\mathrm{d}x = \frac{1}{\phi}\ln\left[\frac{h_{min}+\phi}{h_{min}}\right], \quad \text{(D.5)}$$

$$\int_0^1 p_V\mathrm{d}x = \frac{1}{\phi^3}\left[\ln\left(\frac{h_{min}}{h_{min}+\phi}\right) + \frac{2\phi}{2h_{min}+\phi}\right], \quad \text{(D.6)}$$

$$\int_0^1 p_\Omega\mathrm{d}x = \frac{1}{2\phi^3}\left[\frac{2h_{min}\left(\frac{3h_{min}}{\phi}+2\right)\ln\left(\frac{h_{min}}{h_{min}+\phi}\right) + 6h_{min} + \phi}{2h_{min}+\phi}\right], \quad \text{(D.7)}$$

$$\int_0^1 xp_V\mathrm{d}x = \frac{1}{2\phi^4}\left[\frac{2h_{min}(3h_{min}+2\phi)\ln\left(\frac{h_{min}+\phi}{h_{min}}\right) - \phi(6h_{min}+\phi)}{2h_{min}+\phi}\right], \quad \text{(D.8)}$$

$$\int_0^1 xp_\Omega\mathrm{d}x = \frac{1}{2\phi^3}\left[\frac{\frac{h_{min}^2}{\phi^3}\ln\left(\frac{h_{min}}{h_{min}+\phi}\right)\left[(h_{min}+\phi)^2\ln\left(\frac{h_{min}+\phi}{h_{min}}\right) - 2\phi(4h_{min}+3\phi)\right] - \frac{7h_{min}^2}{\phi} - h_{min} + \frac{\phi}{4}}{2h_{min}+\phi}\right]. \quad \text{(D.9)}$$

These expressions contain singularities at $\phi = 0$, which present numerical difficulties when applied to the numerical solution of the equations of motion.

Hence, for $\phi \ll 1$, we make use of asymptotic expansions for small ϕ,

$$\int_0^1 \frac{1}{h}\mathrm{d}x = \frac{1}{h_{min}}\left[1 - \frac{\phi}{2h_{min}} + \frac{1}{3}\left(\frac{\phi}{h_{min}}\right)^2 + \mathcal{O}\left(\frac{\phi}{h_{min}}\right)^3\right], \tag{D.10}$$

$$\int_0^1 p_V \mathrm{d}x = -\frac{1}{12h_{min}^3}\left[1 - \frac{3\phi}{2h_{min}} + \frac{33}{20}\left(\frac{\phi}{h_{min}}\right)^2 + \mathcal{O}\left(\frac{\phi}{h_{min}}\right)^3\right], \tag{D.11}$$

$$\int_0^1 p_\Omega \mathrm{d}x = \frac{1}{24h_{min}^3}\left[1 - \frac{17\phi}{10h_{min}} + \frac{41}{20}\left(\frac{\phi}{h_{min}}\right)^2 + \mathcal{O}\left(\frac{\phi}{h_{min}}\right)^3\right], \tag{D.12}$$

$$\int_0^1 x p_V \mathrm{d}x = -\frac{1}{24h_{min}^3}\left[1 - \frac{17\phi}{10h_{min}} + \frac{41}{20}\left(\frac{\phi}{h_{min}}\right)^2 + \mathcal{O}\left(\frac{\phi}{h_{min}}\right)^3\right], \tag{D.13}$$

$$\int_0^1 x p_\Omega \mathrm{d}x = \frac{1}{45h_{min}^3}\left[1 - \frac{15\phi}{8h_{min}} + \frac{1093}{448}\left(\frac{\phi}{h_{min}}\right)^2 + \mathcal{O}\left(\frac{\phi}{h_{min}}\right)^3\right]. \tag{D.14}$$

To avoid numerically induced errors, we transition from the full analytical solutions, given by (D.5)-(D.9), which we call $G(h,\phi)_{full}$, to the approximation (D.10)-(D.14) for small ϕ, which we call $G(h,\phi)_{small\phi}$. We do this by writing each expression as $G(h,\phi) = G(h,\phi)_{full} f(h,\phi) + G(h,\phi)_{small\phi}[1 - f(h,\phi)]$ where $f(h,\phi)$ is a switching function given by

$$f(h,\phi) = \begin{cases} 0, & \phi < \phi_{min}, \\ \frac{(\phi-\phi_{min})^k}{(\phi-\phi_{min})^k + (\phi_{max}-\phi)^k}, & \phi_{min} < \phi < \phi_{max}, \\ 1, & \phi > \phi_{max} \end{cases} \tag{D.15}$$

where $k = 3$, $\phi_{min} = \min[10^{-3}, h_{min}/100]$, $\phi_{max} = \min[10^{-3}, h_{min}/10]$.

D.2 Incomplete overlap

This appendix summarises treatment of cases when the plates do not fully overlap and $\theta < 0$. The pressure deviation is assumed to be non-zero only between $\tilde{x}_1$ and $\tilde{x}_2$, where

$$\tilde{x}_1 = \max[0, \tilde{x}_b - 1/(2\gamma)], \tag{D.16}$$

$$\tilde{x}_2 = \min[1, \tilde{x}_b + 1/(2\gamma)]. \tag{D.17}$$

The minimum height perpendicular to plate B is given by

$$\tilde{h}_{min} = \tilde{z}_a - \tilde{z}_b - \phi(\tilde{x}_a - \tilde{x}_1). \tag{D.18}$$

We now solve (7.15) for $\tilde{p}_V$ and $\tilde{p}_\Omega$ but with the boundary conditions $\tilde{p}_V(\tilde{x}_1) = \tilde{p}_V(\tilde{x}_2) = 0$ and $\tilde{p}_\Omega(\tilde{x}_1) = \tilde{p}_\Omega(\tilde{x}_2) = 0$. We then integrate $\tilde{x}\tilde{p}_V$, $\tilde{x}\tilde{p}_\Omega$, $\tilde{p}_V$, $\tilde{p}_\Omega$ and $1/\tilde{h}$ between $\tilde{x}_1$ and $\tilde{x}_2$ to obtain the components necessary to calculate the torques and forces between the disks in the case when they do not overlap. As in §D.1 we also calculate the integrals in the limit when $\phi \ll 1$ and switch between the results with the switching function (D.15). The calculations are performed using Mathematica, and yield lengthy expressions not stated here.

D.3 Forces and torques when $\theta > 0$

In this section we discuss how the forces and torques are calculated for $\theta > 0$. The forces and torques for $\theta > 0$ can be calculated from the results for the forces and torques derived in §7.4 and section D.2 for and angle $-\theta$, with $\theta < 0$. To do this we reflect the coordinate system into a frame where the results for $\theta < 0$ can be applied, and then use symmetry arguments to calculate the forces and torques for $\theta > 0$. To do this transformation we first transform to a frame where plate B is horizontal and set the centre of mass of plate A to be at $\tilde{x} = -1/2$. In this frame $\tilde{x}_1$ and $\tilde{x}_2$ in §D.2 become $\tilde{x}_1 = \max[-1, \tilde{x}_b - 1/(2\gamma)]$, $\tilde{x}_1 = \min[0, \tilde{x}_b + 1/(2\gamma)]$. Then we let $\tilde{x} \mapsto -\tilde{x}$ such that $\tilde{x}_2 \mapsto -\tilde{x}_1$ and $\tilde{x}_1 \mapsto -\tilde{x}_2$. We have now transformed to a coordinate system such that we can use the integrals calculated for $\phi = |\theta|$ and $\tilde{x}_a = -\tilde{x}_b$, $\tilde{x}_b = -\tilde{x}_a$.

Therefore, the forces and torques for $\theta = \pm|\theta|$ will be related to each other by a parity inversion. The components of the forces and torques have the same sign if the terms in each integral have even parity, $f(\tilde{x}) = f(-\tilde{x})$. The components have the opposite sign if the terms in each integral have odd parity $f(\tilde{x}) = f(-\tilde{x})$. Because $p_V(\tilde{x}) = p_V(-\tilde{x})$, $p_\Omega(\tilde{x}) = -p_\Omega(-\tilde{x})$ and $h(\tilde{x}) = h(-\tilde{x})$, the resulting integrals will have the sign change detailed in Table D.1.

Integral for $\theta < 0$	Equivalent integral for $\theta > 0$
$\int p_V dx$	$\int p_V dx$
$\int p_\Omega dx$	$-\int p_\Omega dx$
$\int x p_V dx$	$-\int x p_V dx$
$\int x p_\Omega dx$	$\int x p_\Omega dx$
$\int 1/h dx$	$\int 1/h dx$

Table D.1: Sign change of the integrals for $\theta \mapsto -\theta$.

D.4 Boundary conditions

In this section we demonstrate that the equations in (7.28) are recovered when we apply the boundary conditions for beams with no shear force or bending moment at the ends. Integrating (7.36) over the length of plate A and applying the boundary conditions (7.37) for no shear force and no bending moment at the ends gives,

$$\frac{d^2\tilde{z}_a}{d\tilde{t}^2} = \int_0^1 \tilde{p} d\tilde{x} = \tilde{F}_{az}. \tag{D.19}$$

Integrating $(\tilde{x} - \tilde{x}_a)\times$ (7.36) to obtain the torque, we find,

$$\frac{d^2\tilde{\theta}_a}{d\tilde{t}^2} = -12 \int_0^1 (\tilde{x} - \tilde{x}_a)\tilde{p} d\tilde{x} = 12\tilde{\tau}_a. \tag{D.20}$$

Similarly, integrating (7.36) over the length of plate B, using (7.38) and noting that $D_a L_a/(D_b L_b) = m_a/m_b$ gives,

$$\frac{d^2\tilde{z}_b}{d\tilde{t}^2} = -\frac{m_a}{m_b}\int_0^1 \tilde{p} d\tilde{x} = \frac{m_a}{m_b}\tilde{F}_{bz}, \tag{D.21}$$

and integrating $(\tilde{x} - \tilde{x}_b)\times$ (7.36) we have,

$$\frac{d^2\tilde{\theta}_b}{d\tilde{t}^2} = 12\frac{L_a^2 m_a}{L_b^2 m_b}\int_0^1 (\tilde{x} - \tilde{x}_b)\tilde{p} d\tilde{x} = 12\frac{L_a^2 m_a}{L_b^2 m_b}\tilde{\tau}_b. \tag{D.22}$$

Hence we recover the equations in (7.28).

D.5 Location of the maximum curvature when $\theta_{in} = 0$

In this section we find the x location of the maximum curvature when $\theta_{in} = 0$. For configurations starting with $\theta_a = \theta_{in} = 0$, $\tilde{u}_{az}^t = \tilde{v}_{in}$, $\tilde{z}_a = 1$ and all the

other initial conditions set as zero, all other parameters apart from $\tilde{z}_b$ and $\tilde{u}^t_{bz}$ will remain zero throughout the trajectory such that $\Omega = 0$ and $\tilde{h}(x,t) = \tilde{h}_{min}(t)$. Therefore, the curvature is given by,

$$\tilde{\kappa}_a = V\tilde{\kappa}_{a,V}, \qquad \tilde{\kappa}_b = \frac{D_a V}{D_b}\tilde{\kappa}_{b,V}. \tag{D.23}$$

When $\theta = 0$, solving (7.36) using $\tilde{p} = V\tilde{p}_V$ from (7.16), and applying (7.37) and (7.38) for $\tilde{w}_{a,V}$ gives,

$$\tilde{\kappa}_{a,V} = \frac{(\tilde{x}-1)^2\tilde{x}^2}{24\tilde{h}^3} \tag{D.24}$$

which has a maximum value of $1/(384\tilde{h}^3)$ at $\tilde{x} = 1/2$.

Likewise, solving for $\tilde{\kappa}_{b,V}$ gives,

$$\tilde{\kappa}_{b,V} = \begin{cases} \frac{1}{96\tilde{h}^3\gamma}(-1+\gamma-2\gamma\tilde{x})^2, & \frac{1}{2} - \frac{1}{2\gamma} \le x < 0, \\ \frac{1}{96\tilde{h}^3\gamma}\{1+\gamma[-2+\gamma+4\tilde{x}(\tilde{x}-1)(\gamma-1-\tilde{x}+\tilde{x}^2)]\}, & 0 \le x \le 1, \\ \frac{1}{96\tilde{h}^3\gamma}(1+\gamma-2\gamma\tilde{x})^2, & 1 < x \le \frac{1}{2} + \frac{1}{2\gamma}. \end{cases} \tag{D.25}$$

where the ends of plate B are located at $M = (1-1/\gamma)/2$ and $P = (1+1/\gamma)/2$ and the curvature has a maximum value of $(4-3\gamma)/(384\gamma\tilde{h}^3)$ at $\tilde{x} = 1/2$.

E

2D setup

Contents

E.1 Derivation for the height of disk A above disk B and the location of edges of disk A

In this section we derive the expressions for the height of the surface of disk A above disk B and the position of the edges of disk A as a function of ϕ, where $\phi = -\theta_a$ and θ_a is the angle disk A have rotated about the y-axis (see Figure 8.2 for a sketch of how ϕ is related to θ_a).

When $\phi = 0$, in frame S the two edges of disk A are given by $(x-a)^2 + y^2 = a^2$, $z = h_{min}$, and $(x-a)^2 + y^2 = a^2$, $z = h_{min} + w_a$. We first work out a new expression for the edges of disk A and the height of the lower planar face of disk A when the planar face of disk A is at an angle ϕ to the x-axis. We keep the minimum perpendicular distance between disk A and disk B the same.

We first translate the position of disk A, such that the lowest point is at $x, z = 0$, $x \mapsto x$, $z \mapsto z - h_{min}$. Then we rotate disk A anti-clockwise by an angle ϕ about the $y-$axis such that $x \mapsto x\cos\phi - z\sin\phi$, $z \mapsto x\sin\phi + z\cos\phi$. We define $x = x'\cos\phi - z'\sin\phi$ and $z = x'\sin\phi + z'\cos\phi$. The lower edge of disk A is at $z = 0$ and the upper edge of disk A is at $z = w_a$. Therefore, at the lower edge, $0 = x'\sin\phi + z'\cos\phi$, giving $x = x'/\cos\phi$ and at the upper edge $w_a = x'\sin\phi + z'\cos\phi$, giving $x = (x' + w_a\sin\phi)/\cos\phi$. Substituting x' in we find new expressions for the edges of disk A,

$$x = (a \pm \sqrt{a^2 + y^2})\cos\phi, \tag{E.1}$$

$$x = -w_a\sin\phi + (a \pm \sqrt{a^2 + y^2})\cos\phi, \tag{E.2}$$

where (E.1) corresponds to the position of the lower edge and (E.2) corresponds to the position of the upper edge. The lower planar surface is at $z = x\tan\phi$ and translating $z \mapsto z + h_{min}$ gives $h(x, y) = h_{min} + x\tan\phi$ for $x \geq 0$.

We now find an expression for the height of the lower faces of disk A. For $x \geq 0$ the relevant face is the lower planar surface of disk A which we have found to satisfy

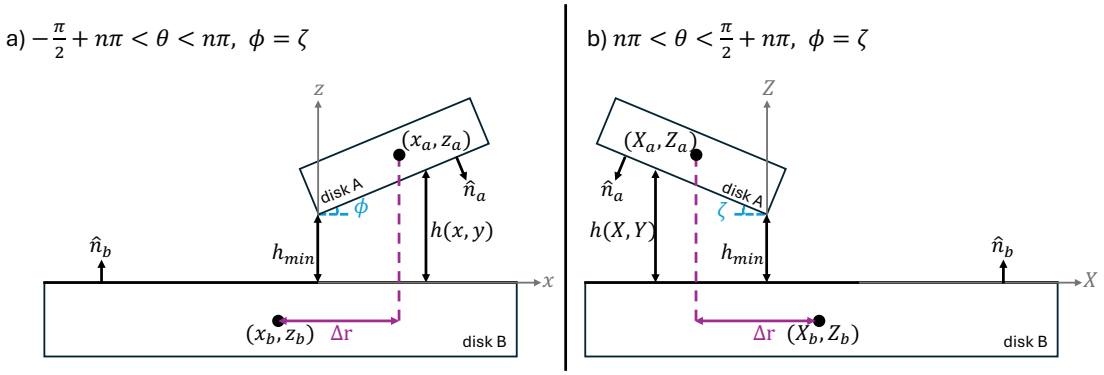

Figure E.1: To calculate the forces and torques for $0+n\pi<\theta<\pi/2+n\pi$, we use the co-ordinate transformation described in §E.2 such that the geometry is symmetric to the case when $-\pi/2+n\pi\theta<0+n\pi$. We set $\phi=\zeta$

$h(x,y)=h_{min}+x\tan\phi$. To find an expression for the curved face we consider the geometry when $\phi=\pi/2$. In this case the equation for the curved face is given by $z-(a+h_{min})^2+y^2=a^2$. Again we translate disk A such that the lowest point is at $x,z=0$, $x\mapsto x$, $z\mapsto z-h_{min}$. When we rotate disk A clockwise by an angle ψ about the $y-$axis such that $x\mapsto x\cos\psi+z\sin\psi$, $z\mapsto x-\sin\psi+z\cos\psi$. Noting that we can write $\phi=\pi/2-\psi$, the rotation can be expressed as $x\mapsto x\sin\phi+z\cos\phi$, $z\mapsto x-\cos\phi+z\sin\phi$. Therefore, translating by h_{min}, the new expression for the curved edge of the disk is given by $z\sin\phi+x\cos\phi-(a+h_{min})^2+y^2=a^2$, such that,

$$h(x,y)=\begin{cases}h_{min}-x\cot\phi+(a\pm\sqrt{a^2-y^2})/\sin\phi, & x<0\\ h_{min}+x\tan\phi, & x\geq 0.\end{cases} \tag{E.3}$$

E.2 Case when the lower planar face of the upper disk is to the right of the minimum point

In this section we solve for the forces and torques for the case when the lower planar face of disk A is to the right of the minimum point. In the case when the angle between the disks satisfies $\pi/2+n\pi<\theta_a<\pi+n\pi$, for $n\in\mathbb{Z}$, such that the geometry corresponds to cases B and D in Figure 8.2, we use the results of the calculation for the forces and torques we found in §8.3 where $-\pi/2+n\pi\leq\theta_a\leq 0+n\pi$. Considering the case discussed for $\theta_a<0$ in Figure 8.3 in §8.3 and repeated in Figure E.1a, we setup the symmetric case (Figure E.1b) such that Figure E.1a is

related to Figure E.1b by a reflection in the z axis.

To ensure symmetry, we set $\zeta = \phi$ where ζ is the acute angle between the flat face of disk A and the x-axis (see Figure 8.2). For $\pi/2 + n\pi < \theta_a < \pi + n\pi$, we apply a different x-co-ordinate transformation to the one given by (8.1) but the same z-co-ordinate transformation (8.2), we set

$$x = \cos\theta_b'(x' - x_a') - \sin\theta_b'(z' - z_a') - \left(a\cos\zeta - \frac{w_a}{2}\sin\zeta\right), \tag{E.4}$$

$$z = \sin\theta_b'(x' - x_b') + \cos\theta_b'(z' - z_b') - \frac{w_b}{2}, \tag{E.5}$$

such that we again the location of the lowest point of disk A is at $x = 0$. Under this transformation we can use the results for $\theta_a \mapsto -\theta_a$ and $x \mapsto -x$. The forces and torques in the reflected frame are related to the forces and torques in the original frame using the transformations in Table D.1.

E.3 Case of incomplete overlap

In this section we describe how the forces, torques and minimum distance between the plates changes when the disks do not fully overlap.

When the disks no longer fully overlap we set the pressure to be zero at points on the surface of disk A and B where there is no overlap. The integrals (see §E.6) to calculate the forces and torques are the same as in the case of complete overlap. The expression (8.3) for $h(x, y)$ is still used to calculate $h(x, y)$ but with h_{min} equal to the distance between the lowest point of disk A and $z = 0$ and the minimum distance is not necessarily equal to the vertical distance between the lowest point of disk A and the upper surface of disk B (see below).

In the case when the disks fully overlap the minimum distance between the disks is always the distance parallel to axis of disk B between the lowest point on the surface of disk A to the upper surface of disk B. However, when the disks do not fully overlap, this might not be the case (see panels a, b, e, f, g, h, k and l of

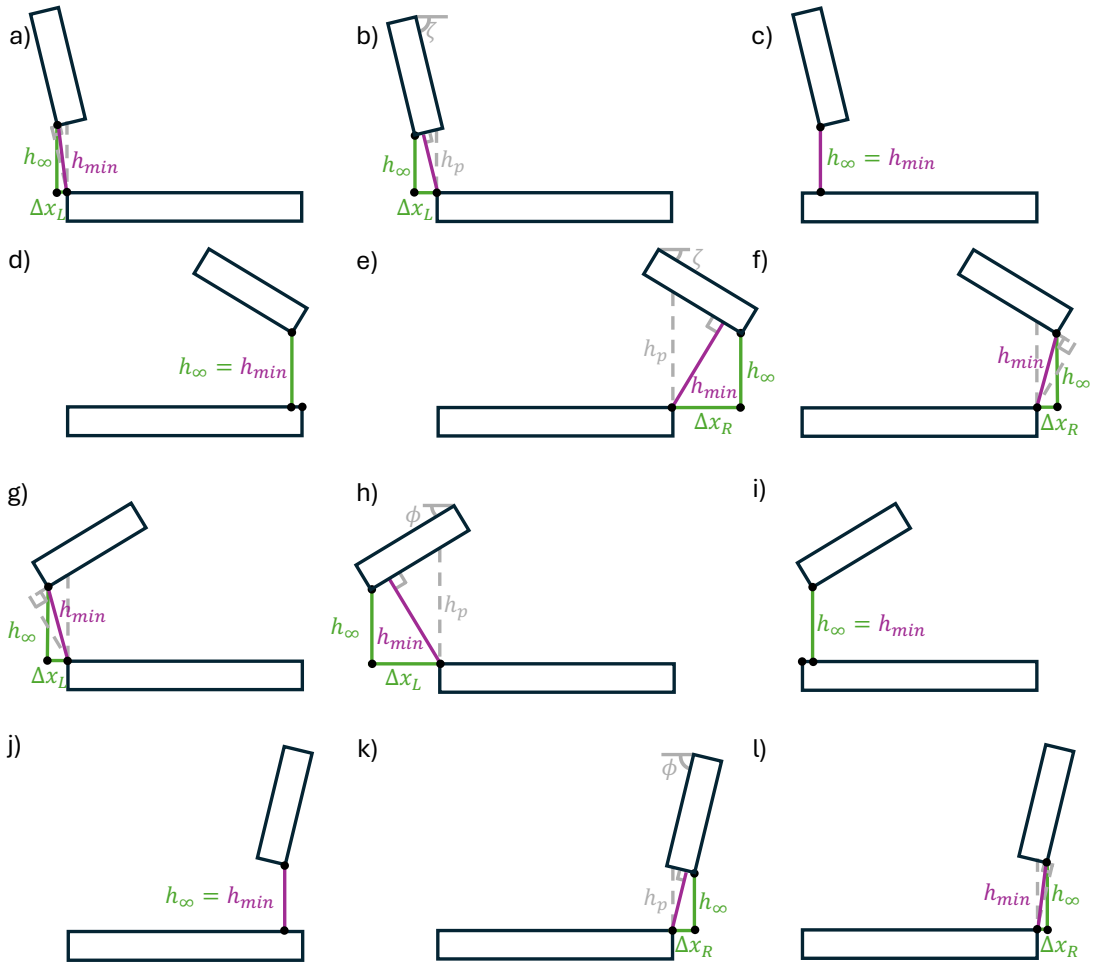

Figure E.2: The minimum distance between disks A and B in the case when the disks do not fully overlap. We define the vertical distance between the lowest point on the surface of disk A and z co-ordinate the upper surface of disk B as h_∞. Δx_L (Δx_R) are the minimum horizontal distance between the edge of disk B and the lowest point on the surface of disk A, when the centre of mass of disk A is to the left (right) of the centre of mass of disk B. In panels c, d, i and j the minimum distance, $h_{min} = h_\infty$. In panels b, e, h and k the minimum distance is the distance between the edge of disk B to the bottom surface of disk A along a line parallel to the normal to disk A. In panels a, f, g and l the minimum distance is the distance between the lowest point on the surface of disk A and the edge of disk B. Expressions for h_{min} are given in (E.8) and (E.7).

Figure E.2). Working in the frame where disk B is horizontal, we define h_{min} as the minimum distance between disks A and B, h_∞ as the vertical distance between the lowest point on disk A and the $z-$co-ordinate of the upper surface of disk B ($z = w_b/2$). We also set Δx_L (Δx_R) as the minimum horizontal distance between the edge of disk B and the lowest point on the surface of disk A when the centre of mass of disk A is to the left (right) of disk B. The acute angle between the lower planar face of disk A and the x-axis is given by ϕ for $0 + n\pi \leq \theta_a \leq \pi/2 + n\pi$, and by ζ for $-\pi/2 + n\pi \leq \theta_a \leq 0 + n\pi$ for $n \in \mathbb{Z}$. The minimum distance changes depending on the value of h_∞, Δx_L, Δx_R, ϕ and ζ. We define x_{LP} as the $x-$coordinate of the lowest point on disk A where,

$$x_{LP} = \begin{cases} x_\epsilon, & 2n\pi \leq \theta_a < \pi/2 + 2n\pi, \\ x_\alpha, & \pi/2 + 2n\pi \leq \theta_a < \pi + 2n\pi, \\ x_\beta, & \pi + 2n\pi \leq \theta_a < 3\pi/2 + 2n\pi, \\ x_\gamma, & 3\pi/2 + 2n\pi \leq \theta_a < 2\pi + 2n\pi, \text{ for } n \in \mathbb{Z}. \end{cases} \tag{E.6}$$

(See Figure 8.2 for locations of x_ϵ, x_α, x_β, x_γ). Note that $\Delta x_R = x_{LP} - (x_b + b)$ and $\Delta x_L = (x_b - b) - x_{LP}$.

For $n\pi \leq \theta_a < \pi/2 + n\pi$,

$$h_{min} = \begin{cases} \sqrt{h_\infty^2 + \Delta x_L^2}, & x_{LP} < x_b - b - (h_\infty + \Delta x_L \cot\zeta)\sin\zeta\cos\zeta, \\ (h_\infty + \Delta x_L \cot\zeta)\sin\zeta, & x_b - b - (h_\infty + \Delta x_L \cot\zeta)\sin\zeta\cos\zeta \leq x_{LP} < x_b - b, \\ h_\infty, & x_b - b \leq x_{LP} < x_b + b, \\ (h_\infty + \Delta x_R \tan\zeta)\cos\zeta, & x_b + b \leq x_{LP} < (h_\infty + \Delta x_R \tan\zeta)\cos\zeta\sin\zeta, \\ \sqrt{h_\infty^2 + \Delta x_R^2}, & x_{LP} > (h_\infty + \Delta x_R \tan\zeta)\cos\zeta\sin\zeta, \end{cases} \tag{E.7}$$

where h_{min} in the first line calculated using pythagoras theorem and h_{min} in the second line is calculated using $h_{min} = h_p \sin\zeta$ where $h_p = h_\infty + x_L \cot\zeta$. In the second line the lower bound on x is at $x = x_b - b - h_{min}\cos\zeta$. Similar arguments can be used to derive the bounds on x and h_{min} for the other choices of θ_a, x_a and x_b. The configuration for each choice of h_{min} for the top to bottom case in (E.8) is shown in panels a-f of Figure E.2.

For $n\pi - \pi/2 \leq \theta_a < n\pi$,

$$h_{min} = \begin{cases} \sqrt{h_\infty^2 + \Delta x_L^2}, & x_{LP} < x_b - b - (h_\infty + \Delta x_L \tan\phi)\sin\phi\cos\phi, \\ (h_\infty + \Delta x_L \tan\phi)\cos\phi, & x_b - b - (h_\infty + \Delta x_L \tan\phi)\sin\phi\cos\phi \leq x_{LP} < x_b - b, \\ h_\infty, & x_b - b \leq x_{LP} < x_b + b, \\ (h_\infty + \Delta x_R \cot\phi)\sin\phi, & x_b + b \leq x_{LP} < (h_\infty + \Delta x_R \cot\phi)\cos\phi\sin\phi, \\ \sqrt{h_\infty^2 + \Delta x_R^2}, & x_{LP} > (h_\infty + \Delta x_R \cot\phi)\cos\phi\sin\phi. \end{cases} \tag{E.8}$$

The configuration for each choice of h_{min} for the top to bottom case in (E.7) is shown in panels g-l of Figure E.2.

E.4 Justification for neglecting freezing of the crystals

In this section we justify why the effects of freezing of the ice crystals can be neglected.

If the water is supercooled the gap thickness will also tend to decrease due to disk growth by freezing as well as due to the disks moving towards each other. If the rate at which the gap decreases due to freezing is given by v_{freeze}, the total change in gap thickness is then given by

$$\frac{\partial h}{\partial t} = u_{az} - u_{bz} - u_{ax}\frac{\partial h}{\partial x} - v_{freeze}. \tag{E.9}$$

Because the density of ice is lower than that of water, freezing also results in an additional fluid flux out of the gap. Using mass conservation we obtain,

$$\frac{\partial h}{\partial t} = -\nabla \cdot \mathbf{q} - \frac{\rho_I}{\rho} v_{freeze}. \tag{E.10}$$

Eliminating $\partial h/\partial t$ from (E.10) using (E.9) yields a result that differs by $(1 - \rho_I/\rho)v_{freeze}$ from the equivalent combination of (7.9) and (8.4) used in §8.3.2 .

Assuming that the growth is only radial, the maximum value of v_{freeze} occurs when the top disk is perpendicular to the bottom disk. In this case $v_{freeze} = dr/dt$, where r is the radius of the top disk. We calculate the growth rate by assuming

only radial growth in (2.4) and using the suggestion for f made by Rees Jones and Wells, 2015. We find for an isolated ice crystal of thickness $2r/d$

$$\frac{dr}{dt} = \frac{Nu\, k_l \Delta T d}{2\rho_I \mathcal{L}} \frac{1}{0.9008 - 0.2634 \ln(1/d)} \frac{1}{r}. \tag{E.11}$$

This is an approximation as the presence of another crystal will mean that the temperature field is different to that experienced by an isolated ice crystal, which is likely to reduce the thermal gradient driving growth. Further, the increase in pressure due to the crystals approaching will increase the melting temperature of the ice (Wagner et al., 1994), making it harder for it to freeze. Therefore, this method is likely to underestimate the growth rate.

Expressing $v_{growth} = (a/T)\tilde{v}_{growth}$ in the dimensionless form using the non-dimensionalisation in §7.4.3.1 and §8.3.2.2 we find that the maximum dimensionless value of $\tilde{v}_{growth}$ is equal to,

$$\tilde{v}_{growth} = \frac{Nu\, k_l \Delta T \pi}{24 \eta \mathcal{L}} \frac{1}{0.9008 - 0.2634 \ln(1/d)} \times \frac{a}{r(t)}, \tag{E.12}$$

Assuming $a/r(t) \approx 1$ and using the values of Nu, k_l, d, η and $\mathcal{L}$ in Table 3.1 and setting $\eta = 1.9 \times 10^{-3} \mathrm{kg\,m^{-1}\,s^{-1}}$ (ITTC, 2011). We find, $\tilde{v}_{growth} < 10^{-4}\Delta T$. As we expect $\Delta T \leq 10^{-2}$ ^{o}C, the growth rate of the crystal is significantly slower than the initial relative velocity between the crystals (see Figure 8.6) and hence it seems reasonable to neglect crystal growth. However, growth could still be important at late stages near the collision boundary where $|\tilde{\mathbf{w}}_{ab}| \to 0$.

E.5 Solution for the pressure

In this section we describe the method used to solve for the pressure. Before describing the numerical method, we first derive an analytical expression for the pressure in the limit when the disks are close to parallel (ϕ is close to 0). This analytical expression allows us to test the numerically calculated forces and torques.

E.5.1 Analytical solution: limit where the disks approach close to parallel

In the limit when the disks fully overlap and are close to parallel we can obtain an analytical estimate for the pressure. For small ϕ, the system is close to being radially symmetric. We choose to set $\tilde{x}, \tilde{y} = 0$ to correspond to the centre of the circular face of disk A and we use a small angle approximation for the slope of the disk such that we replace $\tilde{x} \mapsto \tilde{x} - 1 + \mathcal{O}(\phi^2)$ in the calculation set out in §7.4.2. Thus in this co-ordinate system,

$$\tilde{h} \sim \tilde{h}_0 + \phi\tilde{x} = \tilde{h}_0(1 + \Phi\tilde{x}), \tag{E.13}$$

where $\tilde{h}_0$ is the height of the centre of the circular face of disk A ($\tilde{h}_0 = \tilde{h}_{min} + \phi$) and $\Phi = \phi/\tilde{h}_0$, which we shall assume is small. In this limit, (8.13)-(8.15) become,

$$\frac{\partial}{\partial\tilde{x}}\left\{[\tilde{h}_0(1+\Phi\tilde{x})]^3\frac{\partial\tilde{p}_\Omega}{\partial\tilde{x}}\right\} + \frac{\partial}{\partial\tilde{y}}\left\{[\tilde{h}_0(1+\Phi\tilde{x})]^3\frac{\partial\tilde{p}_\Omega}{\partial\tilde{y}}\right\} = -\tilde{x} + 1, \tag{E.14}$$

$$\frac{\partial}{\partial\tilde{x}}\left\{[\tilde{h}_0(1+\Phi\tilde{x})]^3\frac{\partial\tilde{p}_V}{\partial\tilde{x}}\right\} + \frac{\partial}{\partial\tilde{y}}\left\{[\tilde{h}_0(1+\Phi\tilde{x})]^3\frac{\partial\tilde{p}_V}{\partial\tilde{y}}\right\} = 1, \tag{E.15}$$

$$\frac{\partial}{\partial\tilde{x}}\left\{[\tilde{h}_0(1+\Phi\tilde{x})]^3\frac{\partial\tilde{p}_U}{\partial\tilde{x}}\right\} + \frac{\partial}{\partial\tilde{y}}\left\{[\tilde{h}_0(1+\Phi\tilde{x})]^3\frac{\partial\tilde{p}_U}{\partial\tilde{y}}\right\} = -\phi. \tag{E.16}$$

and the boundary of disk A is at $\tilde{x} = \pm\sqrt{1-\tilde{y}^2}\cos\phi$. Because ϕ is a constant $\tilde{p}_U = -\tilde{p}_V\phi$.

We assume $\Phi \ll 1$, and solve using a perturbation series expanding the pressure in powers of Φ,

$$\tilde{p}_i = \frac{1}{\tilde{h}_0^3}\sum_{n=0}^{\infty}\Phi^n p_{n,i} = \frac{1}{\tilde{h}_0^3}\left(p_{0,i} + \Phi p_{1,i} + \Phi^2 p_{2,i} + \ldots\right). \tag{E.17}$$

Substituting the series expansion for the pressure into (E.14)-(E.16) gives

$$\frac{\partial}{\partial\tilde{x}}\left[(1+\Phi\tilde{x})^3\frac{\partial}{\partial\tilde{x}}\left(\sum_{n=0}^{\infty}\Phi^n p_{n,\Omega}\right)\right] + \frac{\partial}{\partial\tilde{y}}\left[(1+\Phi\tilde{x})^3\frac{\partial}{\partial\tilde{y}}\left(\sum_{n=0}^{\infty}\Phi^n p_{n,\Omega}\right)\right] = -\tilde{x} + 1, \tag{E.18}$$

$$\frac{\partial}{\partial\tilde{x}}\left[(1+\Phi\tilde{x})^3\frac{\partial}{\partial\tilde{x}}\left(\sum_{n=0}^{\infty}\Phi^n p_{n,V}\right)\right] + \frac{\partial}{\partial\tilde{y}}\left[(1+\Phi\tilde{x})^3\frac{\partial}{\partial\tilde{y}}\left(\sum_{n=0}^{\infty}\Phi^n p_{n,V}\right)\right] = 1, \tag{E.19}$$

$$-p_{n,V}\phi = p_{n,U}. \tag{E.20}$$

Comparing powers of Φ up to $\mathcal{O}(\Phi^1)$ and dropping the tildes we obtain,

$$\frac{\partial^2 p_{0,\Omega}}{\partial x^2} + \frac{\partial^2 p_{0,\Omega}}{\partial y^2} = -x + 1, \tag{E.21}$$

$$\frac{\partial^2 p_{0,V}}{\partial x^2} + \frac{\partial^2 p_{0,V}}{\partial y^2} = 1, \tag{E.22}$$

$$\frac{\partial^2 p_{1,i}}{\partial x^2} + \frac{\partial^2 p_{1,i}}{\partial y^2} = -3\frac{\partial p_{0,i}}{\partial x} - 3x\left(\frac{\partial^2 p_{0,i}}{\partial x^2} + \frac{\partial^2 p_{0,i}}{\partial y^2}\right). \tag{E.23}$$

Boundary condition

We require p to satisfy the boundary conditions $p(\tilde{x} = \pm\sqrt{1-\tilde{y}^2}\cos\phi) = 0$ on the edge of the disk. Dropping the tildes and expanding in increasing powers of ϕ,

$$0 = p\left[x = \pm\sqrt{1-y^2}\left(1 - \frac{\phi^2}{2} + \ldots\right)\right], \tag{E.24}$$

$$= p\left(x = \pm\sqrt{1-y^2}\right) \mp \frac{\phi^2}{2}\sqrt{1-y^2}\left.\frac{\partial p}{\partial x}\right|_{x=\pm\sqrt{1-y^2}} + \ldots. \tag{E.25}$$

Individually imposing the boundary condition on each component of the pressure such that $p_V = p_\Omega = p_U = 0$ on the boundary. As long as $\Phi^1 \gg \phi^2$ or equivalently $1 \gg \phi(\tilde{h}_{min} + \phi)$, then to order Φ^1 the pressure boundary condition becomes,

$$p_{0,i}\left(x = \pm\sqrt{1-y^2}\right) + \Phi p_{1,i}\left(x = \pm\sqrt{1-y^2}\right) = 0. \tag{E.26}$$

so that $p_{0,i}$ and $p_{1,i}$ are individually zero at each order of expansion.

Method to solve for the pressure

To solve for the pressure, we split $p_{n,i} = \tilde{p}_{n,i} + P_{n,i}$ a particular integral and homogeneous solution, where each $\tilde{p}_{n,i}$ satisfies (E.18)-(E.20) respectively and $\nabla^2 P_{n,i} = 0$. In polar co-ordinates ($x = r\cos\theta$, $y = r\sin\theta$) solving $\nabla^2 P_{n,i} = 0$ gives,

$$P_{n,i} = \sum_{m=1}^{\infty} r^m \left(A_m \cos m\theta + B_m \sin m\theta\right) + A_0 + B_0\theta, \tag{E.27}$$

where we have ignored the $1/r^m$ and the $\ln r$ terms as the pressure remains finite at the centre of the disk. To satisfy the boundary conditions,

$$0 = \tilde{p}_{n,i}(r = 1) + P_{n,i}(r = 1). \tag{E.28}$$

When enforcing the boundary conditions, we use De Moivre's theorem to rewrite $\cos^n\theta$ in terns of $\cos k\theta$ and then convert back to polynomials in x and y using properties of the Chebyshev polynomials. For example, Solving (E.22) we obtain, $\tilde{p}_{0,V} = (x^2+y^2)/4 = r/4$. Therefore, to satisfy the boundary condition we require $P_{0,V} = -1/4$. Thus, $p_{0,V} = (x^2+y^2-1)/4$.

Solution for the pressure

Overall we find,

$$p_{0,V} = (x^2+y^2-1)/4, \tag{E.29}$$

$$p_{1,V} = -(9/16)x(x^2+y^2-1), \tag{E.30}$$

$$p_{n,U} = -p_{n,V}\phi, \tag{E.31}$$

$$p_{0,\Omega} = -(1/8)(x-2)(x^2+y^2-1), \tag{E.32}$$

$$p_{1,\Omega} = (1/64)(3-36x+19x^2-y^2)(x^2+y^2-1). \tag{E.33}$$

E.5.2 Numerical solution for the pressure

We now discuss the numerical method to solve for the pressure. We solve for $\tilde{p}_\Omega$, $\tilde{p}_V$ and $\tilde{p}_U$ for $10^{-6} \le \tilde{h}_{min} \le 10^4$, $0 \le \phi \le \pi/2$, $-(b-a) \le \tilde{x}_a - \tilde{x}_b \le b-a$ using a finite difference scheme of second-order accuracy applying Dirichlet boundary conditions in the non-overlapping regions. We initially set $\tilde{h}_{min} = 10^4$ and use 501×501 grid points to solve (8.13)-(8.15) for the components of the pressure. We set $\tilde{h}_{min}$ to decrease logarithmically with 41 values between $\tilde{h}_{min} = 10^4$ and $\tilde{h}_{min} = 10^{-6}$. At each new value of $\tilde{h}_{min}$ we then add a region of refined grid with 501×501 new grid in the region $0 \le \tilde{x}, \tilde{y} \lesssim \tilde{h}_{min}^{1/2}$.

When ϕ is close to $\pi/2$ (the disks are close to perpendicular). We additionally solve for the pressure assuming that the top disk can be approximated as an approaching parabolic prism (see Figure E.3a). In this setup we refine the grid to grow around the midpoint of the curved face of the top disk ($\tilde{x} = 0$ in the parabolic geometry is at $\tilde{x} = -(\pi/2-\phi)\tilde{w}_a/2$ in frame S) such that the height of the top disk

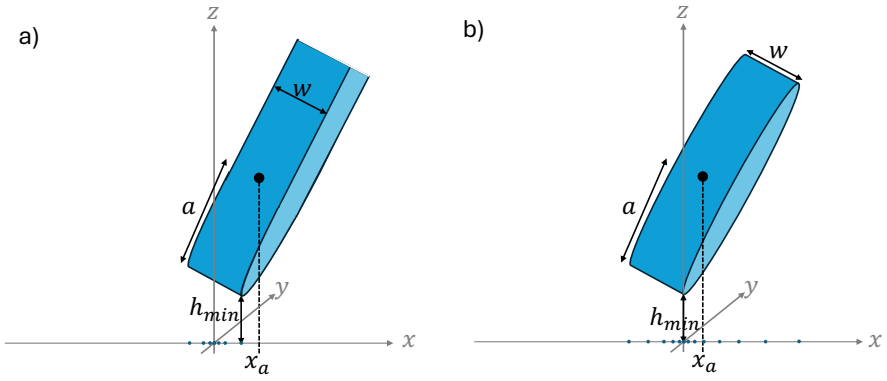

Figure E.3: When the disks are close to perpendicular we also calculate the pressure due to an approaching parabolic prism (panel a) with grid growing from $x = 0$, which is located halfway along the lowest edge of the curved surface. This is in contrast to the disk geometry (panel b), where $x = 0$ is located at the lowest point of the upper disk.

in the parabolic geometry is given by $\tilde{h} = \tilde{h}_{min} + (\tilde{x} + \tilde{w}_a/2)(\pi/2 - \phi) + \tilde{y}^2/2$. This will be used as an additional solution for the forces and torques when the disks are close to perpendicular and will allow us to compare two different numerical approaches.

E.6 Calculation of the forces and torques

In this section we discuss the numerical method to calculate the dimensionless forces and torques. We compare the numerical solution to the analytical solution when the disks are close to parallel. Using the non-dimensionalisation in §7.4.3.1, §D.1 and §8.3.2.2 we find that the dimensionless forces and torques are given by,

$$\tilde{F}_{ax} = -\iint_{S_a} \left[\frac{\tilde{p}}{2} \frac{\partial \tilde{h}}{\partial \tilde{x}} + \left(\tilde{u}^t_{ax} - \tilde{u}^t_{bx} - \tilde{\omega}_a z_a - \frac{\tilde{\omega}_b \tilde{w}_b}{2} \right) \frac{1}{12\tilde{h}} + \frac{\tilde{\omega}_a}{12} \right] \mathrm{d}\tilde{x}\mathrm{d}\tilde{y} \tag{E.34}$$

$$\tilde{F}_{az} = \iint_{S_a} \tilde{p}\, \mathrm{d}\tilde{x}\mathrm{d}\tilde{y} \tag{E.35}$$

$$\tilde{\tau}_a = -\hat{y} \iint_{S_a} (\tilde{x} - \tilde{x}_a)\tilde{p}\, \mathrm{d}\tilde{x}\mathrm{d}\tilde{y} \tag{E.36}$$

$$\tilde{\tau}_b = \hat{y} \iint_{S_a} (\tilde{x} - \tilde{x}_b)\tilde{p}\, \mathrm{d}\tilde{x}\mathrm{d}\tilde{y}. \tag{E.37}$$

Recalling $\tilde{p} = V\tilde{p}_V + U\tilde{p}_U + \Omega\tilde{p}_\Omega$ we integrate each component of the pressure over the surface of the overlapping disks to find the forces and torques. To do

this we calculate each component of the pressure, $\tilde{x}$ and $\partial\tilde{h}/\partial\tilde{x}$ at each point on the grid and integrate over the grid.

E.6.1 Analytical estimates for the forces and torques when the disks overlap and are close to parallel

In the limit when $\phi \ll 0$ we can obtain the dimensionless forces and torques by integrating the analytical estimates for the pressure found in §E.5.1. Letting $\partial h/\partial x = \phi$ we integrate (E.29)-(E.33) to find,

$$\iint_{S_a} \tilde{p}_V \,\mathrm{d}\tilde{x}\mathrm{d}\tilde{y} \approx -\frac{\pi}{8\tilde{h}_0^3}, \tag{E.38}$$

$$-\iint_{S_a} (\tilde{x}-\tilde{x}_a)\tilde{p}_V \,\mathrm{d}\tilde{x}\mathrm{d}\tilde{y} \approx -\frac{3\pi\phi}{64\tilde{h}_0^4}, \tag{E.39}$$

$$-\iint_{S_a} \frac{\tilde{p}_V}{2}\frac{\partial\tilde{h}}{\partial\tilde{x}} \,\mathrm{d}\tilde{x}\mathrm{d}\tilde{y} \approx \frac{\pi\phi}{16\tilde{h}_0^3}, \tag{E.40}$$

$$\iint_{S_a} \tilde{p}_\Omega \,\mathrm{d}\tilde{x}\mathrm{d}\tilde{y} \approx -\frac{\pi}{8\tilde{h}_0^3}\left(1+\frac{3\phi}{8\tilde{h}_0}\right) \tag{E.41}$$

$$-\iint_{S_a} (\tilde{x}-\tilde{x}_a)\tilde{p}_\Omega \,\mathrm{d}\tilde{x}\mathrm{d}\tilde{y} \approx -\frac{\pi}{8\tilde{h}_0^3}\left(\frac{1}{12}+\frac{3\phi}{8\tilde{h}_0}\right), \tag{E.42}$$

$$-\iint_{S_a} \frac{\tilde{p}_\Omega}{2}\frac{\partial\tilde{h}}{\partial\tilde{x}} \,\mathrm{d}\tilde{x}\mathrm{d}\tilde{y} \approx \frac{\pi\phi}{16\tilde{h}_0^3}\left(1+\frac{3}{8\tilde{h}_0}\right), \tag{E.43}$$

$$\iint_{S_a} \tilde{p}_U \,\mathrm{d}\tilde{x}\mathrm{d}\tilde{y} \approx \frac{\pi\phi}{8\tilde{h}_0^3}, \tag{E.44}$$

$$-\iint_{S_a} (\tilde{x}-\tilde{x}_a)\tilde{p}_U \,\mathrm{d}\tilde{x}\mathrm{d}\tilde{y} \approx \frac{3\pi\phi^2}{64\tilde{h}_0^4}, \tag{E.45}$$

$$-\iint_{S_a} \frac{\tilde{p}_U}{2}\frac{\partial\tilde{h}}{\partial\tilde{x}} \,\mathrm{d}\tilde{x}\mathrm{d}\tilde{y} \approx -\frac{\pi\phi^2}{16\tilde{h}_0^3}. \tag{E.46}$$

where $\tilde{h}_0 = \tilde{h}_{min} + \phi$. We note in the limit where the disks are exactly parallel and not rotating ($\phi = \tilde{\omega}_a - \tilde{w}_b = 0$), $\tilde{\tau}_a = 0$ as would be expected by symmetry. In this limit, $\int 1/\tilde{h}\mathrm{d}\tilde{x}\mathrm{d}\tilde{y} = \pi/\tilde{h}_{min}$.

E.6.2 Comparison to the numerical solution

To test the accuracy of our numerical solution for the forces and torques we compare to the analytical solution from §E.6.1 in Figure E.4. We expect the analytical solution to closely match the numerical solution when $\phi/(\tilde{h}_{min} + \phi)$ is small. Looking at the plots of $|\iint \tilde{p}_i \mathrm{d}\tilde{x}\mathrm{d}\tilde{y}|$ and $|\iint \tilde{p}_i \partial\tilde{h}/\partial\tilde{x}\, \mathrm{d}\tilde{x}\mathrm{d}\tilde{y}|/2$ in panels a-f of Figure E.4 (where $i = V, U, \Omega$) we see that the numerical solution (solid lines) closely matches the analytical solution (dotted lines) at small ϕ. The analytical solution and the numerical solution obtained with the disk geometry agree to within a factor of 3, with the largest disagreement found at the smallest value of h_{min} for $|\iint \tilde{p}_U/2\partial\tilde{h}/\partial\tilde{x}\mathrm{d}\tilde{x}\mathrm{d}\tilde{y}|$. The vertical component of the force given by $|\iint \tilde{p}_V \mathrm{d}\tilde{x}\mathrm{d}\tilde{y}|$ is postulated to dominate the motion. For this integral, the analytical solution and the numerical solution obtained with the disk geometry agree to within a factor of 2. This suggests that the numerical solution captures the forces well. Looking at the numerically calculated torques (panels g-i) we see that the numerically calculated torques closely match the analytical estimates when $\phi > 10^{-3}$. However, the numerically calculated U and V component of the torque on disk A does not go to zero as ϕ goes to zero (which we would expect to be the case as the system is symmetric at $\phi = 0$). We suspect this is due to the grid not being centred on the maximum of the pressure distribution and as a result when the pressure is very sharply peaked, points slightly different distances from the pressure peak are captured leading to a finite torque being calculated. This inaccuracy means that we use the analytical solution at small values of ϕ to calculate the forces and torques.

We also compared how close the numerical solution calculated using the parabolic prism is to the solution obtained using the full disk geometry. We again found very close agreement with the forces but the numerically calculated torques did not go to zero as ϕ approached $\pi/2$ in the disk geometry. As the parabolic prism setup was centred on the mid-point of the rounded surface, the torques in this co-ordinate system did go to zero. Therefore, the solution for the forces and torques due to the parabolic prism can be used when the disks are close to perpendicular.

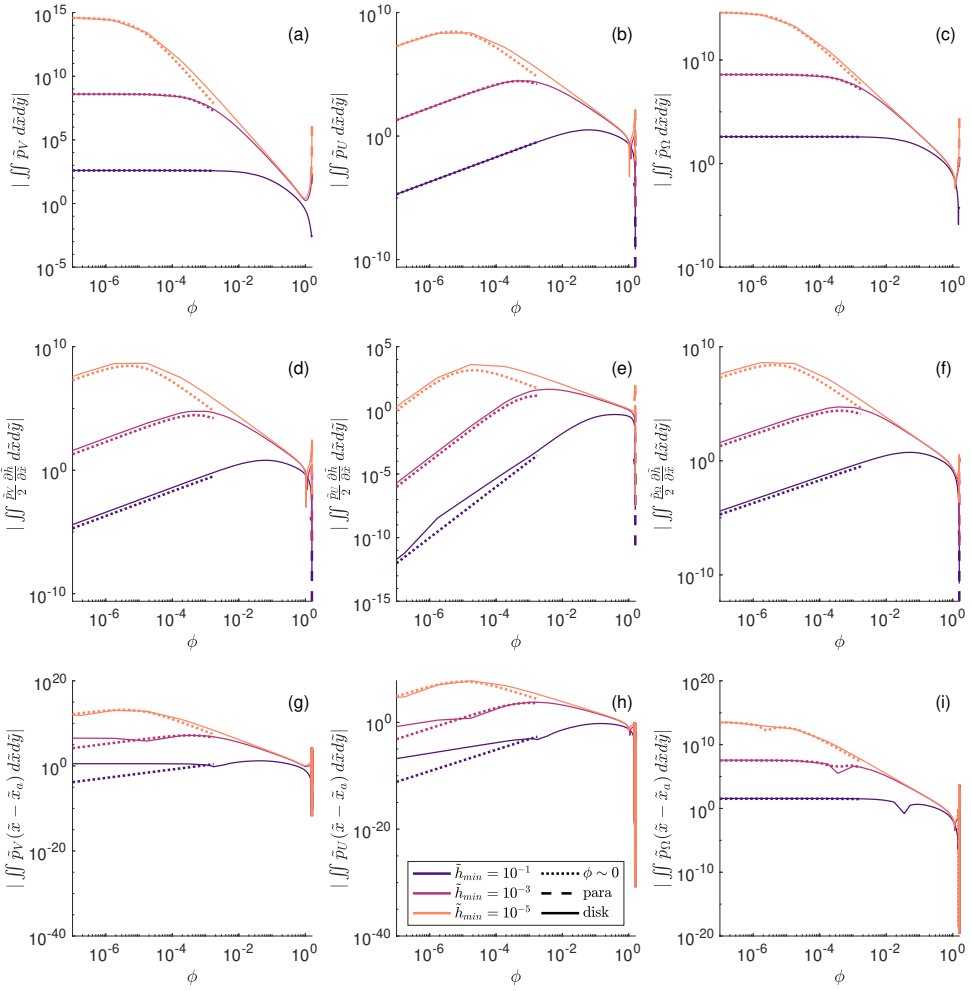

Figure E.4: Comparison of the components of the forces and torques obtained by the numerics to the analytical solutions given in §E.6.1. The solutions are compared for $\tilde{h}_{min} = [10^{-5}, 10^{-3}, 10^{-1}]$ with a different line colour for each value of $\tilde{h}_{min}$. The solid line is the numerical solution obtained with the disk geometry. The dashed line is the numerical solution obtained with the parabolic prism geometry. The dotted line is the analytical solution obtained using the equations in §E.6.1.

E.6.3 Combined forces and torques

As was noted in §E.6.2, the full numerical solution works well when the disks are far from being either parallel or perpendicular, but fails to capture the torques correctly when the disks approach parallel or perpendicular. Therefore, when the disks fully overlap we switch between the analytic, the numerical solution with disk geometry and the numerical solution with parabolic prism geometry to calculate the forces and the torques. Denoting $\tilde{F}_V = \iint \tilde{p}_V \, \mathrm{d}\tilde{x}\mathrm{d}\tilde{y}$. When the disks do not overlap we set,

$$\tilde{F}_V = \tilde{F}_{V,\phi\ll 0}[1 - f_0(\phi)] + \tilde{F}_{V,disk} f_0(\phi)[1 - f_{\pi/2}(\phi)] + \tilde{F}_{V,para} f_{\pi/2}(\phi). \tag{E.47}$$

where $\tilde{F}_{V,\ll 0}$ is the analytical solution (E.38), $\tilde{F}_{V,disk}$ is the numerical solution with the disk geometry, $\tilde{F}_{V,para}$ is the numerical solution with the parabolic prism geometry. The functions $f_i(\phi)$ transition smoothly between each of the regimes, and are given by

$$f_i(\phi) = \begin{cases} 0, & \phi < \phi_{i,min}, \\ \frac{(\phi-\phi_{i,min})^3}{(\phi-\phi_{i,min})^3+(\phi_{i,max}-\phi)^3}, & \phi_{i,min} < \phi < \phi_{i,max}, \\ 1, & \phi > \phi_{i,max}, \end{cases} \tag{E.48}$$

where $\phi_{0,min} = \min\{\pi/1800, \tilde{h}_{min}/3\}$, $\phi_{0,max} = \min\{\pi/180, 10\tilde{h}_{min}/3\}$, $\phi_{\pi/2,min} = \pi/2 - \pi/1800$, $\phi_{\pi/2,max} = \pi/2$. We use the same switching method with the other integrals listed in §E.5.1. When the disks do not overlap, the system is not symmetric at $\phi = 0$ or $\pi/2$ so the torque does not go to zero and we use the numerical solution with the disk geometry.

E.7 Relationship between the angles used to calculate the collision kernel and the initial angles in our simulation

In §8.4.2 we noted that the full range of initial conditions needed to calculate the collision efficiency can be obtained by running simulations for a reduced range of parameters. In this section we relate the full set of parameters used to obtain the collision kernel, Θ^L, $\theta_a'^L$, $\theta_b'^L$, $w^L_{ab,r}$, w^L_{ab,Θ^L} to the initial conditions in our simulations.

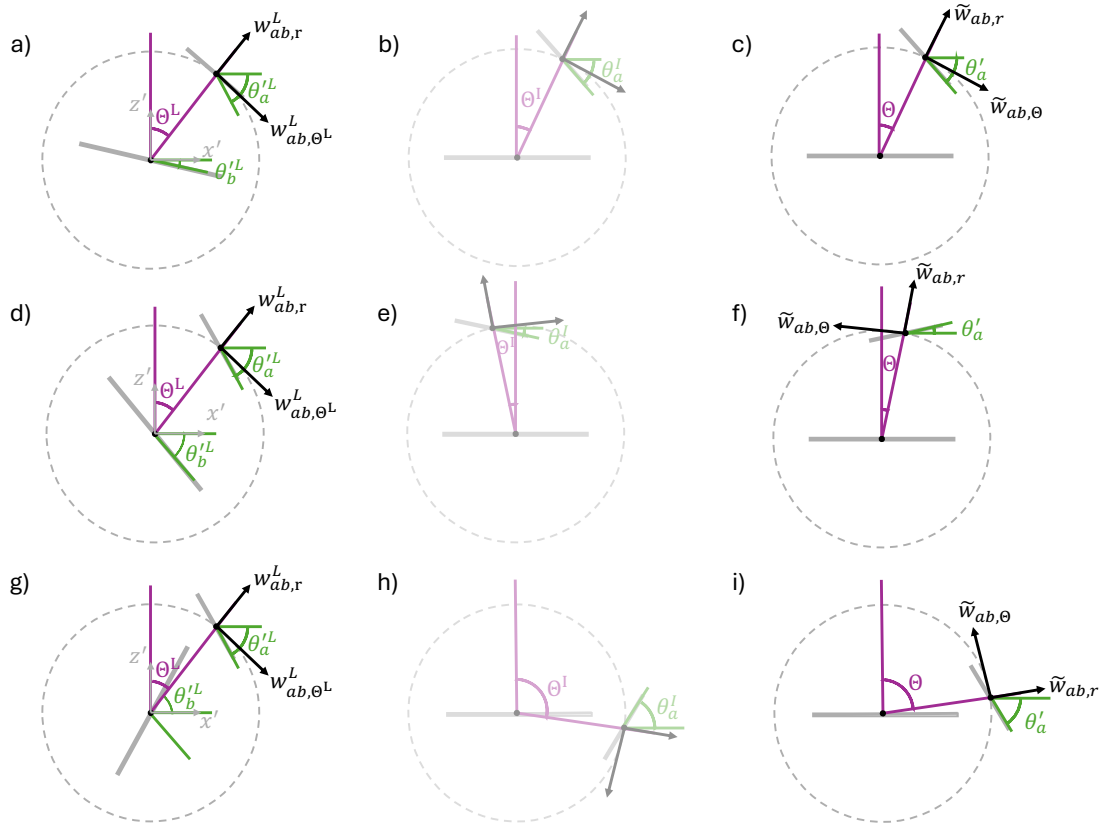

Figure E.5: Initial setup used in the simulation and how the initial conditions in the laboratory frame Θ^L, $\theta_a'^L$, $\theta_b'^L$, $w^L_{ab,r}$ and w^L_{ab,Θ^L} are related to Θ, θ_a', θ_b', $\tilde{w}_{ab,r}$ and $\tilde{w}_{ab,\Theta}$ for three different initial conditions. We initialise with the distance between the centre of mass of each crystal equal to $r_{max,ab}$. In panels a, d and g we sketch three different initial choices for Θ^L, $\theta_a'^L$, $\theta_b'^L$, $w^L_{ab,r}$ and w^L_{ab,Θ^L}. In panels b, e and h we transform the sketch in panels a, d and g respectively such that the planar surface of disk b is parallel to the x axis. In panel h we have let $\theta_a^I \mapsto \theta_a^I - \pi$. In panels c, f and i we sketch the corresponding values of Θ, θ_a', θ_b', $\tilde{w}_{ab,r}$ and $\tilde{w}_{ab,\Theta}$, which are obtained by symmetry, and are to be used in the simulation for the initial parameters in panels a, d and g.

Panels a, d and g of Figure E.5 show three different initial values of for Θ^L, $\theta_a'^L$, $\theta_b'^L$, $w^L_{ab,r}$ and w^L_{ab,Θ^L}. The simulations set $\theta_b' = 0$ so we initially rotate all angles by $\theta_b'^L$ such that we reach intermediate angles $\theta_a^I = \theta_a'^L - \theta_b'^L$, $\theta_b^I = \theta_b'^L - \theta_b'^L = 0$, $\Theta^I = \Theta^L - \theta_b'^L$ shown in panels b, e and h for the initial conditions in a, d and g respectively. The simulations use initial conditions $-\pi/2 \leq \theta_a' \leq \pi/2$, $0 \leq \Theta \leq \pi/2$. In some cases the rotation by $\theta_b'^L$ makes θ_a^I and/or Θ outside of this range. We

Θ^I	Θ	θ'_a	$\tilde{w}_{ab,\Theta}$	$\tilde{w}_{ab,r}$
$0 \leq \Theta^I \leq \pi/2$	$\Theta = \Theta^I$	$\theta'_a = \theta^I_a$	$\tilde{w}_{ab,\Theta} = \frac{w_{ab,\Theta^L}(\Theta^L)}{6\eta d/(\pi\rho_I a)}$	$\tilde{w}_{ab,r} = \frac{w_{ab,r}(\Theta^L)}{6\eta d/(\pi\rho_I a)}$
$-\pi/2 \leq \Theta^I < 0$	$\Theta = \lvert\Theta^I\rvert$	$\theta'_a = -\theta^I_a$	$\tilde{w}_{ab,\Theta} = -\frac{w_{ab,\Theta^L}(\Theta^L)}{6\eta d/(\pi\rho_I a)}$	$\tilde{w}_{ab,r} = \frac{w_{ab,r}(\Theta^L)}{6\eta d/(\pi\rho_I a)}$
$\pi/2 < \Theta^I < \pi$	$\Theta = \pi - \Theta^I$	$\theta'_a = -\theta^I_a$	$\tilde{w}_{ab,\Theta} = -\frac{w_{ab,\Theta^L}(\Theta^L)}{6\eta d/(\pi\rho_I a)}$	$\tilde{w}_{ab,r} = \frac{w_{ab,r}(\Theta^L)}{6\eta d/(\pi\rho_I a)}$

Table E.1: Relationship between Θ and Θ^I, θ'_a and θ^I_a, $\tilde{w}_{ab,\Theta}$ and w_{ab,Θ^L} and $\tilde{w}_{ab,r}$ and $w_{ab,r}$. The transformation for the top, middle and bottom rows of the table is sketched in the top, middle and bottom rows of Figure E.5.

first ensure $-\pi/2 \leq \theta^I_a \leq \pi/2$ by setting

$$\theta^I_a \mapsto \begin{cases} \pi + \theta^I_a, & -3\pi/2 \leq \theta^I_a < -\pi/2, \\ \theta^I_a, & -\pi/2 \leq \theta^I_a \leq \pi/2, \\ \theta^I_a - \pi, & \pi/2 < \theta^I_a \leq 3\pi/2. \end{cases} \tag{E.49}$$

We then transform Θ^I such that $0 \leq \Theta^I \leq \pi/2$. In doing so this changes θ^I_a and $\tilde{w}_{ab,\Theta}$ in some cases, with the transformations given in Table E.1. Panels c, f and i of Figure E.5 sketch the value of Θ, θ'_a, θ'_b, $\tilde{w}_{ab,r}$ and $\tilde{w}_{ab,\Theta}$ corresponding to the initial choice of Θ^L, θ'^L_a, θ'^L_b, $w^L_{ab,r}$ and w^L_{ab,Θ^L} in panels a, d and g of Figure E.5.

E.8 Calculation of the ballistic collision kernel

In this section we discuss how the ballistic collision kernel is calculated.

To calculate the ballistic collision kernel we use a different method to calculate the collision kernel as was used in §6 as we wish to calculate the kernel as a function of $\tilde{w}_{ab,r}$ and $\tilde{w}_{ab,\Theta}$ so that we can combine it with the hydrodynamic collision kernel. In §6 we stated that disks will collide if the orientation of the relative velocity is within a range of angles $\theta_{u,min} \leq \theta_{u,max}$ where $\theta_{u,min}$ and $\theta_{u,max}$ depended on ϕ_a and ϕ_b. For $\phi_a = \phi_b = 0$ we can calculate an expression for $\theta_{u,min}$ and $\theta_{u,max}$. Consider two disks separated by $r_{max,ab} = \sqrt{a^2 + (w_a/2)^2} + \sqrt{b^2 + (w_b/2)^2}$ at an angle Θ from the z axis (see Figure E.6). We calculate the angles between the maximum and minimum values of x on the edge of the disks (arrows joining the black circles in Figure E.6). The maximum and minimum angle are the angles between each of the blue arrows and the z axis. If the angle the relative velocity

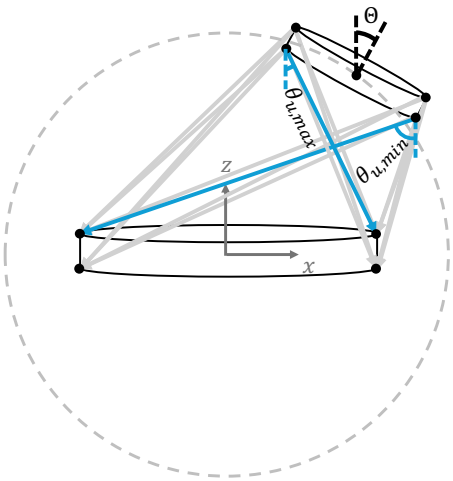

Figure E.6: Method to calculate the range of angles the relative velocity can make with the -z axis for a collision to occur. A collision occurs if the angle that the relative velocity makes with the -z axis, θ_u is between $\theta_{u,max}$ and $\theta_{u,min}$. To calculate $\theta_{u,max}$ and $\theta_{u,min}$ lines are drawn connecting each of the points at the maximum and minimum values of x (black circles) on on the edge of the disks and the angle between each line and the -z axis is calculated. The maximum and minimum angle correspond to $\theta_{u,max}$ and $\theta_{u,min}$ and the corresponding lines are coloured blue.

makes with the $z-$axis is between the maximum and minimum of these angles, a collision will occur. The collision criteria is therefore,

$$\theta_{u,min} \leq \arctan\left(\frac{\tilde{w}_{ab,x}}{-\tilde{w}_{ab,z}}\right) \leq \theta_{u,max}. \tag{E.50}$$

To determine if a collision occurs for a certain value of $\tilde{w}_{ab,r}$ and $\tilde{w}_{ab,\Theta}$ we first find $\tilde{w}_{ab,x}$ and $\tilde{w}_{ab,z}$ and then calculate whether they are within the collision region.

"Therefore everyone who hears these words of mine and puts them into practice is like a wise man who built his house on the rock."

— Matthew 7:24 NIV

References

Anand, P., Ray, S., & Subramanian, G. (2020). Orientation dynamics of sedimenting anisotropic particles in turbulence. *Phys. Rev. Lett.*, *125*, 034501.

Audoly, B. (2011). Localized buckling of a floating elastica. *Phys. Rev. E*, *84*, 011605.

Auguste, F., Magnaudet, J., & Fabre, D. (2013). Falling styles of disks. *Journal of Fluid Mechanics*, *719*, 388–405.

Ayala, O., Rosa, B., & Wang, L.-P. (2008). Effects of turbulence on the geometric collision rate of sedimenting droplets. part 2. theory and parameterization. *New Journal of Physics*, *10*(9), 099802.

Barrette, P. (2021). Understanding frazil ice: The contribution of laboratory studies. *Cold Regions Science and Technology*, *189*, 103334.

Besenhard, M., Neugebauer, P., Scheibelhofer, O., & Khinast, J. (2017). Crystal engineering in continuous plug-flow crystallizers. *Crystal Growth & Design*, *17*(12), 6432–6444.

Bokhari, A., Mahomed, F., & Zaman, F. (2012). Invariant boundary value problems for a fourth-order dynamic Euler-Bernoulli beam equation. *Journal of Mathematical Physics*, *53*(4), 043703.

Bradtke, K., & Herman, A. (2023). Spatial characteristics of frazil streaks in the Terra Nova Bay polynya from high-resolution visible satellite imagery. *The Cryosphere*, *17*(5), 2073–2094.

Brown, R., Hubert, W., & Daly, S. (2011). A primer on winter, ice, and fish: What fisheries biologists should know about winter ice processes and stream-dwelling fish. *Fisheries*, *36*(1), 8–26.

Cawthorn, C., & Balmforth, N. (2010). Contact in a viscous fluid. Part 1. a falling wedge. *Journal of Fluid Mechanics*, *646*, 327–338.

Challabotla, N., Zhao, L., & Andersson, H. (2015). Orientation and rotation of inertial disk particles in wall turbulence. *Journal of Fluid Mechanics*, *766*, R2.

Champney, J., Dobrovolskis, A., & Cuzzi, J. (1995). A numerical turbulence model for multiphase flows in the protoplanetary nebula. *Physics of Fluids*, *7*(7), 1703–1711.

Chan, T., Ng, C. S., & Krug, D. (2023). Bubble–particle collisions in turbulence: Insights from point-particle simulations. *Journal of Fluid Mechanics*, *959*, A6.

Chen, Y., Lian, J., Zhao, X., Guo, Q., & Yang, D. (2023). Advances in frazil ice evolution mechanisms and numerical modelling in rivers and channels in cold regions. *Water*, *15*(14).

Chen, Y., Lian, J., Zhao, X., & Yang, D. (2024). Parameter optimization of frazil ice evolution model based on NSGA-II genetic algorithm. *Water*, *16*(9).

Chen, Z., Elektorowicz, M., An, C., & Tian, X. (2023). Entrainment and enrichment of microplastics in ice formation processes: Implications for the transport of microplastics in cold regions. *Environmental Science amp; Technology*, *57*(8), 3176–3186.

Clark, S., & Doering, J. (2009). Frazil flocculation and secondary nucleation in a counter-rotating flume. *Cold Regions Science and Technology*, *55*(2), 221–229.

Clark, S., & Doering, J. (2008). Experimental investigation of the effects of turbulence intensity on frazil ice characteristics. *Canadian Journal of Civil Engineering*, *35*(1), 67–79.

Daly, S. (1984). *Frazil ice dynamics*. Cold Regions Research; Engineering Laboratory (U.S.)

Daly, S. (1994).

Daly, S., & Barrette, P. (2023). Prevention of water intake blockage by ice during supercooling events. *Journal of Cold Regions Engineering*, *37*(1), 03122001.

Daly, S., & Ettema, R. (2006). Frazil ice blockage of water intakes in the great lakes. *Journal of Hydraulic Engineering*, *132*(8), 814–824.

Devenish, B., Bartello, P., Brenguier, J.-L., Collins, L., Grabowski, W., IJzermans, R., Malinowski, S., Reeks, M., Vassilicos, J., Wang, L.-P., & Warhaft, Z. (2012). Droplet growth in warm turbulent clouds. *Quarterly Journal of the Royal Meteorological Society*, *138*(667), 1401–1429.

Di Bernardino, A., Monti, P., Leuzzi, G., & Querzoli, G. (2020). Eulerian and lagrangian time scales of the turbulence above staggered arrays of cubical obstacles. *Environmental Fluid Mechanics*, *20*(4), 987–1005.

Dodin, Z., & Elperin, T. (2002). On the collision rate of particles in turbulent flow with gravity. *Physics of Fluids*, *14*(8), 2921–2924.

Dolata, B., & Zia, R. (2021). Faxén formulas for particles of arbitrary shape and material composition. *Journal of Fluid Mechanics*, *910*, A22.

Dormand, J., & Prince, P. (1980). A family of embedded Runge-Kutta formulae. *Journal of Computational and Applied Mathematics*, *6*(1), 19–26.

Eames, I., & Gilbertson, M. A. (2004). The settling and dispersion of small dense particles by spherical vortices. *Journal of Fluid Mechanics*, *498*, 183–203.

Ettema, R., Karim, M., & Kennedy, J. (1984). Laboratory experiments on frazil ice growth in supercooled water. *Cold Regions Science and Technology*, *10*(1), 43–58.

Ettema, R., Kirkil, G., & Daly, S. (2009). Frazil ice concerns for channels, pump-lines, penstocks, siphons, and tunnels in mountainous regions. *Cold Regions Science and Technology*, *55*(2), 202–211.

Evans, T., Sarofim, A., & Margolis, G. (1974). Models of secondary nucleation attributable to crystal-crystallizer and crystal-crystal collisions. *AIChE Journal*, *20*(5), 959–966.

Findheisen, W. (1939). Zur frage der regentropfenbildung in reinem wasserwolken. *Meteor. Z.*, *56:365-368*.

Frazer, E., Langhorne, P., Leonard, G., Robinson, N., & Schumayer, D. (2020). Observations of the size distribution of frazil ice in an ice shelf water plume [e2020GL090498 10.1029/2020GL090498]. *Geophysical Research Letters*, *47*(21), e2020GL090498.

Galton-Fenzi, B., Hunter, J., Coleman, R., Marsland, S., & Warner, R. (2012). Modeling the basal melting and marine ice accretion of the Amery Ice Shelf. *Journal of Geophysical Research: Oceans*, *117*(C9).

Gebre, S., Alfredsen, K., Lia, L., Stickler, M., & Tesaker, E. (2013). Review of ice effects on hydropower systems. *Journal of Cold Regions Engineering*, *27*(4), 196–222.

Gere, J., & Goodno, B. (2009). Stresses in beams (basic topics). In *Mechanics of materials* (7th ed., p. 361, Vol. 1). Cengage Learning.

Golledge, N., Keller, E., Gossart, A., Malyarenko, A., Bahamondes-Dominguez, A., Krapp, M., Jendersie, S., Lowry, D., Alevropoulos-Borrill, A., & Notz, D. (2025). Antarctic coastal polynyas in the global climate system. *Nature Reviews Earth amp; Environment*, *6*(2), 126–139.

Gosink, J., & Osterkamp, T. (1983). Measurements and analyses of velocity profiles and frazil ice-crystal rise velocities during periods of frazil-ice formation in rivers. *Annals of Glaciology*, *4*, 79–84.

Gustavsson, K., Sheikh, M., Naso, A., Pumir, A., & Mehlig, B. (2021). Effect of particle inertia on the alignment of small ice crystals in turbulent clouds. *Journal of the Atmospheric Sciences*, *78*(8), 2573–2587.

Hamid, A., Shakaib, M., Molina, J., Qasim, D., Fareed, B., Uzair, M., & Yamamoto, R. (2024). Direct numerical simulations of suspension of disk-shaped particles. *Physics of Fluids*, *36*(4), 043339.

Hammar, L. (1994).

Heorton, H., Nikhil, R., & Feltham, D. (2017). A model of sea ice formation in leads and polynyas. *Journal of Physical Oceanography*, *47*(7), 1701–1718.

Herman, A., Dojczman, M., & Świszcz, K. (2020). High-resolution simulations of interactions between surface ocean dynamics and frazil ice. *The Cryosphere*, *14*(11), 3707–3729.

Hewitt, H., Fox-Kemper, B., Pearson, B., Roberts, M., & Klocke, D. (2022). The small scales of the ocean may hold the key to surprises. *Nature Climate Change*, *12*(6), 496–499.

Hewitt, I., Balmforth, N., & De Bruyn, J. (2015). Elastic-plated gravity currents. *European Journal of Applied Mathematics*, *26*(1), 1–31.

Holland, P., & Feltham, D. (2005). Frazil dynamics and precipitation in a water column with depth-dependent supercooling. *Journal of Fluid Mechanics*, *530*, 101–124.

Hosoi, A., & Mahadevan, L. (2004). Peeling, healing, and bursting in a lubricated elastic sheet. *Phys. Rev. Lett.*, *93*, 137802.

Ito, M., Fukamachi, Y., Ohshima, K., & Shirasawa, K. (2020). Observational evidence of supercooling and frazil ice formation throughout the water column in a coastal polynya in the Sea of Okhotsk. *Continental Shelf Research*, *196*, 104072.

Ito, M., Ohshima, K., Fukamachi, Y., Mizuta, G., Kusumoto, Y., & Kikuchi, T. (2021). Underwater frazil ice and its suspension depth detected from ADCP backscatter data around sea ice edge in the Sea of Okhotsk. *Cold Regions Science and Technology*, *192*, 103382.

Ito, M., Ohshima, K., Fukamachi, Y., Simizu, D., Iwamoto, K., Matsumura, Y., Mahoney, A., & Eicken, H. (2015). Observations of supercooled water and frazil ice formation in an Arctic coastal polynya from moorings and satellite imagery. *Annals of Glaciology*, *56*(69), 307–314.

ITTC. (2011). ITTC – recommended procedures fresh water and seawater properties. In *ITTC – recommended procedures fresh water and seawater properties*. https://ittc.info/media/4048/75-02-01-03.pdf

Jeong, H., Lee, S.-S., Park, H.-S., & Stewart, A. (2023). Future changes in antarctic coastal polynyas and bottom water formation simulated by a high-resolution coupled model. *Communications Earth amp; Environment*, *4*(1).

Jones, R., & Wells, A. (2018). Frazil-ice growth rate and dynamics in mixed layers and sub-ice-shelf plumes. *The Cryosphere*, *12*(1), 25–38.

Katopodes, N. (2019). Chapter 5 - viscous fluid flow. In N. D. Katopodes (Ed.), *Free-surface flow* (pp. 324–426). Butterworth-Heinemann.

Kelly, A., Rodemann, T., Meiners, K., Auman, H., Moreau, S., Fripiat, F., Dellile, B., & Lannuzel, D. (2024). Microplastics in Southern Ocean sea ice: A pan-Antarctic perspective. *Water Emerging Contaminants Nanoplastics*, *3*(4).

Kolev, N. I. (2012). Drag, lift, and virtual mass forces. Springer Berlin Heidelberg.

Lal, D., Mason, R., & Strickland-Constable, R. (1969). Collision breeding of crystal nuclei. *Journal of Crystal Growth*, *5*(1), 1–8.

Liu, F., Li, H., Zhao, X., & Chen, Y. (2024). Study on the spatiotemporal evolution pattern of frazil ice based on CFD-DEM coupled method. *Water*, *16*(23).

Manohar, R. (1936). XLVI. application of Bessel functions to the solution of problem of motion of a circular disk in viscous liquid. *The London, Edinburgh, and Dublin Philosophical Magazine and Journal of Science*, *21*(141), 546–564.

Martin, S. (1981). Frazil ice in rivers and oceans. *Annual Review of Fluid Mechanics*, *13*(Volume 13, 1981), 379–397.

Matousek, V. (1992). An analysis of example. *Proceedings of the 11th International Symposium on Ice*, *1*(1), 1–22.

Maxey, M., & Riley, J. (1983). Equation of motion for a small rigid sphere in a nonuniform flow. *The Physics of Fluids*, *26*(4), 883–889.

McFarlane, V., Loewen, M., & Hicks, F. (2014). Laboratory measurements of the rise velocity of frazil ice particles. *Cold Regions Science and Technology*, *106-107*, 120–130.

McFarlane, V., Loewen, M., & Hicks, F. (2015). Measurements of the evolution of frazil ice particle size distributions. *Cold Regions Science and Technology*, *120*, 45–55.

McFarlane, V., Loewen, M., & Hicks, F. (2017). Measurements of the size distribution of frazil ice particles in three Alberta rivers. *Cold Regions Science and Technology*, *142*, 100–117.

McFarlane, V., Loewen, M., & Hicks, F. (2019). Field measurements of suspended frazil ice. part II: Observations and analyses of frazil ice properties during the principal and residual supercooling phases. *Cold Regions Science and Technology*, *165*, 102796.

Mercier, R. (1985). *The reactive transport of suspended particles : Mechanisms and modeling* [Doctoral dissertation, Massachusetts Institute of Technology]. http://hdl.handle.net/1721.1/15232

Meyer, C., & Deglon, D. (2011). Particle collision modeling – a review. *Minerals Engineering*, *24*(8), 719–730.

Mittelstedt, C. (2023). *Theory of plates and shells*. Springer Vieweg.

Monin, A., Yaglom, A., & Lumley, J. (2007). Mathematical description of turbulence. spectral functions. In *Statistical fluid mechanics. vol. 2: Mechanics of turbulence* (pp. 23–25). Dover Publications.

Morse, B., & Richard, M. (2009). A field study of suspended frazil ice particles. *Cold Regions Science and Technology*, *55*(1), 86–102.

Moy, A., Borca-Tasciuc, D., & Tichy, J. (2017). Squeezing flow between rigid tilted surfaces: A general solution and case study for MEMS. *Lubrication Science*, *29*, 531–539.

Nakata, K., Ohshima, K., & Nihashi, S. (2021). Mapping of active frazil for Antarctic coastal polynyas, with an estimation of sea-ice production [e2020GL091353 2020GL091353]. *Geophysical Research Letters*, *48*(6), e2020GL091353.

Naumann, A., Notz, D., Håvik, L., & Sirevaag, A. (2012). Laboratory study of initial sea-ice growth: Properties of grease ice and nilas. *The Cryosphere*, *6*(4), 729–741.

Ngo-Cong, D., Nguyen, A. V., & Tran-Cong, T. (2018). Isotropic turbulence surpasses gravity in affecting bubble-particle collision interaction in flotation. *Minerals Engineering*, *122*, 165–175.

Nguyen, A., An-Vo, D.-A., Tran-Cong, T., & Evans, G. (2016). A review of stochastic description of the turbulence effect on bubble-particle interactions in flotation. *International Journal of Mineral Processing*, *156*, 75–86.

Ohshima, K., Fukamachi, Y., Ito, M., Nakata, K., Simizu, D., Ono, K., Nomura, D., Hashida, G., & Tamura, T. (2022). Dominant frazil ice production in the Cape Darnley polynya leading to Antarctic bottom water formation. *Science Advances*, *8*(42), eadc9174.

Opfergelt, S., Gaspard, F., Hirst, C., Monin, L., Juhls, B., Morgenstern, A., Angelopoulos, M., & Overduin, P. (2024). Frazil ice changes winter biogeochemical processes in the Lena River. *Communications Earth amp; Environment*, *5*(1).

Osterkamp, T. (1975). Frazil ice nucleation mechanisms.

Pei, C., Yang, J., She, Y., & Loewen, M. (2024). Measurements of frazil ice flocs in rivers. *The Cryosphere*, *18*(9), 4177–4196.

Poole, D., Barenghi, C., Sergeev, Y., & Vinen, W. (2005). Motion of tracer particles in He II. *Phys. Rev. B*, *71*, 064514.

Pope, S. (2000). The scales of turbulent motion. In *Turbulent flows* (pp. 182–195). Cambridge University Press.

Portela, E., Rintoul, S., Herraiz-Borreguero, L., Roquet, F., Bestley, S., van Wijk, E., Tamura, T., McMahon, C., Guinet, C., Harcourt, R., & Hindell, M. (2022). Controls on Dense Shelf Water Formation in Four East Antarctic Polynyas [e2022JC018804 2022JC018804]. *Journal of Geophysical Research: Oceans*, *127*(12), e2022JC018804.

Pradhan, K., & Chakraverty, S. (2019). Chapter one - overview of functionally graded materials. In K. K. Pradhan & S. Chakraverty (Eds.), *Computational structural mechanics* (pp. 3–6). Academic Press.

Qin, D., Yao, T., Ding, Y., & Ren, J. (2020). Establishment and significance of the scientific system of cryospheric science. *Bulletin of Chinese Academy of Sciences*, *35*(4).

Radia, N. (2014). *Frazil ice formation in the polar oceans* [Doctoral dissertation, University College London (University of London)].

Rani, S., Dhariwal, R., & Koch, D. (2014). A stochastic model for the relative motion of high Stokes number particles in isotropic turbulence. *Journal of Fluid Mechanics*, *756*, 870–902.

Rees Jones, D., & Wells, A. (2015). Solidification of a disk-shaped crystal from a weakly supercooled binary melt. *Phys. Rev. E*, *92*, 022406.

Reynolds, O. (1886). IV. on the theory of lubrication and its application to Mr. Beauchamp Tower's experiments, including an experimental determination of the viscosity of olive oil. *Philosophical Transactions of the Royal Society of London*, *177*, 157–234.

Rosevear, M., Gayen, B., Vreugdenhil, C., & Galton-Fenzi, B. (2025). How does the ocean melt Antarctic ice shelves? *Annual Review of Marine Science*, *17*(Volume 17, 2025), 325–353.

Roy, A., Gupta, A., & Ray, S. (2018). Inertial spheroids in homogeneous, isotropic turbulence. *Phys. Rev. E*, *98*, 021101.

Saffman, P., & Turner, J. (1956). On the collision of drops in turbulent clouds. *Journal of Fluid Mechanics*, *1*(1), 16–30.

Schneck, C., Ghobrial, T., & Loewen, M. (2019). Laboratory study of the properties of frazil ice particles and flocs in water of different salinities. *The Cryosphere*, *13*(10), 2751–2769.

Schröder, M., Bätge, T., Bodenschatz, E., Wilczek, M., & Bagheri, G. (2024). Estimating the turbulent kinetic energy dissipation rate from one-dimensional velocity measurements in time. *Atmospheric Measurement Techniques*, *17*(2), 627–657.

Schubert, H. (1999). On the turbulence-controlled microprocesses in flotation machines. *International Journal of Mineral Processing*, *56*(1), 257–276.

Schulson, E., & Duval, P. (2009). Brittle compressive failure of unconfined ice. In *Creep and fracture of ice* (pp. 236–265). Cambridge University Press.

Sheikh, M., Gustavsson, K., Lévêque, E., Mehlig, B., Pumir, A., & Naso, A. (2022). Colliding ice crystals in turbulent clouds. *Journal of the Atmospheric Sciences*, *79*(9), 2205–2218.

Smedsrud, L. (2002). A model for entrainment of sediment into sea ice by aggregation between frazil-ice crystals and sediment grains. *Journal of Glaciology*, *48*(160), 51–61.

Smedsrud, L., & Jenkins, A. (2004). Frazil ice formation in an ice shelf water plume. *Journal of Geophysical Research: Oceans*, *109*(C3).

Smith, B., Fricker, H., Gardner, A., Medley, B., Nilsson, J., Paolo, F., Holschuh, N., Adusumilli, S., Brunt, K., Csatho, B., Harbeck, K., Markus, T., Neumann, T., Siegfried, M., & Zwally, J. (2020). Pervasive ice sheet mass loss reflects competing ocean and atmosphere processes. *Science*, *368*(6496), 1239–1242.

Smith, S., Muench, R., & Pease, C. (1990). Polynyas and leads: An overview of physical processes and environment. *Journal of Geophysical Research: Oceans*, *95*(C6), 9461–9479.

Souillé, F., Goeury, C., & Mouradi, R.-S. (2023). Uncertainty analysis of single- and multiple-size-class frazil ice models. *The Cryosphere*, *17*(4), 1645–1674.

Souillé, F., Taccone, F., & El Mertahi, C. (2020, October). A multi-class frazil ice model for shallow water flows. https://hdl.handle.net/20.500.11970/107443

Steinberg, A., Hamlington, P., & Zhao, X. (2021). Structure and dynamics of highly turbulent premixed combustion. *Progress in Energy and Combustion Science*, *85*, 100900.

Sundaram, S., & Collins, L. (1997). Collision statistics in an isotropic particle-laden turbulent suspension. part 1. direct numerical simulations. *Journal of Fluid Mechanics*, *335*, 75–109.

Svensson, U., & Omstedt, A. (1998). Numerical simulations of frazil ice dynamics in the upper layers of the ocean. *Cold Regions Science and Technology*, *28*(1), 29–44. https://www.sciencedirect.com/science/article/pii/S0165232X98000111

Svensson, U., & Omstedt, A. (1994). Simulation of supercooling and size distribution in frazil ice dynamics. *Cold Regions Science and Technology*, *22*(3), 221–233.

Taylor, G. (1935). Statistical theory of turbulence. *Proceedings of the Royal Society of London. Series A - Mathematical and Physical Sciences*, *151*(873), 421–444.

Thomas, D., Judd, S., & Fawcett, N. (1999). Flocculation modelling: A review. *Water Research*, *33*(7), 1579–1592.

Thompson, L., Smith, M., Thomson, J., Stammerjohn, S., Ackley, S., & Loose, B. (2020). Frazil ice growth and production during katabatic wind events in the Ross Sea, Antarctica. *The Cryosphere*, *14*(10), 3329–3347.

Tinklenberg, A., Guala, M., & Coletti, F. (2024). Turbulence effect on disk settling dynamics. *Journal of Fluid Mechanics*, *992*, A4.

Ushio, S., & Wakatsuchi, M. (1993). A laboratory study on supercooling and frazil ice production processes in winter coastal polynyas. *Journal of Geophysical Research: Oceans*, *98*(C11), 20321–20328.

van Diedenhoven, B., Ackerman, A., Fridlind, A., Cairns, B., & Riedi, J. (2020). Global statistics of ice microphysical and optical properties at tops of optically thick ice clouds [e2019JD031811 2019JD031811]. *Journal of Geophysical Research: Atmospheres*, *125*(6), e2019JD031811.

Varaksin, A. (2019). Collision of particles and droplets in turbulent two-phase flows. *High Temperature*, *57*(4), 555–572.

Voth, G., & Soldati, A. (2017). Anisotropic particles in turbulence. *Annual Review of Fluid Mechanics*, *49*(Volume 49, 2017), 249–276.

Wagner, T., & Vella, D. (2011). Floating carpets and the delamination of elastic sheets. *Phys. Rev. Lett.*, *107*, 044301.

Wagner, W., Saul, A., & Pruss, A. (1994). International equations for the pressure along the melting and along the sublimation curve of ordinary water substance. *Journal of Physical and Chemical Reference Data*, *23*(3), 515–527.

Wang, L.-P., Ayala, O., Kasprzak, S., & Grabowski, W. (2005). Theoretical formulation of collision rate and collision efficiency of hydrodynamically interacting cloud droplets in turbulent atmosphere. *Journal of the Atmospheric Sciences*, *62*(7), 2433–2450.

Wang, L.-P., Ayala, O., Scott, K., & Wojciech, G. (2005). Theoretical formulation of collision rate and collision efficiency of hydrodynamically interacting cloud droplets in turbulent atmosphere. *Journal of the Atmospheric Sciences*, *62*(7), 2433–2450.

Wang, L.-P., Wexler, A., & Zhou, Y. (1998). Statistical mechanical descriptions of turbulent coagulation. *Physics of Fluids*, *10*(10), 2647–2651.

Wang, L.-P., Wexler, A., & Zhou, Y. (2000a). Statistical mechanical description and modelling of turbulent collision of inertial particles. *Journal of Fluid Mechanics*, *415*, 117–153.

Wang, L.-P., Wexler, A., & Zhou, Y. (2000b). Statistical mechanical descriptions of turbulent coagulation of inertial particles. *Journal of Fluid Mechanics*, *415*, 117–153.

Wang, S., & Doering, J. (2005). Numerical simulation of supercooling process and frazil ice evolution. *Journal of Hydraulic Engineering*, *131*(10), 889–897.

Wilkinson, A., Pradas, M., & Wilkinson, M. (2023). Lubrication dynamics of a settling plate. *Journal of Fluid Mechanics*, *977*, A28.

Yang, D., Lian, J., Zhao, X., Hou, Q., Chen, Y., & Zhang, Y. (2023). A mathematical model for supercooling process and its application to frazil ice evolution. *Scientific Reports*, *13*(1), 5801.

Ye, S., Doering, J., & Shen, H. (2004). A laboratory study of frazil evolution in a counter-rotating flume. *Canadian Journal of Civil Engineering*, *31*(6), 899–914.

Yuu, S. (1984). Collision rate of small particles in a homogeneous and isotropic turbulence. *AIChE Journal*, *30*(5), 802–807.

Zaichik, L., Alipchenkov, V., & Avetissian, A. (2005). Modelling turbulent collision rates of inertial particles. In W. Rodi & M. Mulas (Eds.), *Engineering turbulence modelling and experiments 6* (pp. 959–968). Elsevier Science B.V.

Zaichik, L., & Alipchenkov, V. (2003). Pair dispersion and preferential concentration of particles in isotropic turbulence. *Physics of Fluids*, *15*(6), 1776–1787.

Zaichik, L., & Alipchenkov, V. (2010). Modelling of transport and dispersion of arbitrary-density particles in turbulent flows. *International Journal of Heat and Fluid Flow*, *31*(5), 850–861.

Zhang, Z., Sun, D.-W., Zhu, Z., & Cheng, L. (2015). Enhancement of crystallization processes by power ultrasound: Current state-of-the-art and research advances. *Comprehensive Reviews in Food Science and Food Safety*, *14*(4), 303–316.